Search for Shape Transitions in Neutron-rich W isotopes

and

Optimizing Hole Mobilities for Gamma-Ray Tracking

BY

VIKRAM SINGH PRASHER

M.S. UNIVERSITY OF MASSACHUSETTS LOWELL (2012)

SUBMITTED IN PARTIAL FULFILLMENT OF THE REQUIREMENTS

FOR THE DEGREE OF DOCTOR OF PHILOSOPHY

DEPARTMENT OF PHYSICS AND APPLIED PHYSICS

UNIVERSITY OF MASSACHUSETTS LOWELL

Signature of
Author: _____ Date: _12-16-2015_
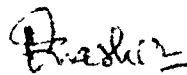
Signature of Dissertation Chair: _____
Name: Prof. Partha Chowdhury
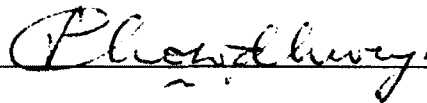
Signatures of Other Dissertation Committee Members
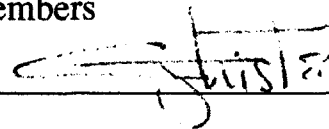
Committee Member Signature: _____
Name: Prof. Christopher J. Lister
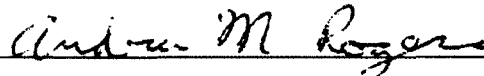
Committee Member Signature: _____
Name: Prof. Andrew M. Rogers

ProQuest Number: 10016321

ProQuest 10016321

Search for Shape Transitions in Neutron-rich W isotopes

and

Optimizing Hole Mobilities for Gamma-Ray Tracking

BY

VIKRAM SINGH PRASHER

ABSTRACT OF A DISSERTATION
SUBMITTED TO THE FACULTY OF THE
DEPARTMENT OF PHYSICS AND APPLIED PHYSICS
IN PARTIAL FULFILLMENT OF THE REQUIREMENTS

FOR THE DEGREE OF
DOCTOR OF PHILOSOPHY
PHYSICS
UNIVERSITY OF MASSACHUSETTS LOWELL
2015

Thesis Supervisor: Partha Chowdhury, Ph.D.
Professor, Department of Physics and Applied Physics

Abstract

Nuclear structure studies are intimately tied to advanced detector arrays, both current and emerging. The present work describes two independent projects that have advanced detector arrays in common. The first explores the physics of nuclear shapes and shape evolution with angular momentum in the A~180 region using Gammasphere, arguably the world's most advanced 4π array for high-resolution gamma-ray spectroscopy at present, coupled to CHICO2, a state-of-the-art position-sensitive detector for heavy-ions in binary reactions near the Coulomb barrier. The second involves simulations and analysis for GRETINA, a next-generation segmented gamma-ray tracking array which can resolve the interaction position of a gamma-ray to a few mm, and is slated to evolve into the germanium shell GRETA, for use at the national Facility for Rare Isotope Beams.

The reasonably rare phenomenon of a transition from prolate collective to oblate collective rotation along the yrast line, long predicted and possibly observed recently in ^{180}Hf, are expected to occur at even lower spins in ^{186}W. Prompt collective excitations in ^{186}W were populated via inelastic excitation using a ^{136}Xe beam from the ATLAS accelerator at Argonne incident on a thin ^{186}W target.

Emitted γ-rays were detected using Gammasphere, coincident with the binary reaction fragments detected in the heavy-ion counter CHICO2. Level schemes were extended in ^{186}W, although experimental constraints limited the observation of states above 14^+. The observed γ-ray yields were compared to Coulomb excitation predictions. A large staggering between the even- and odd-spin members of the γ-vibrational band suggests increased triaxiality in this nucleus. Transfer reaction products were also analyzed, and the yrast band in ^{185}W extended to higher spins. A sudden increase in signature splitting in the ground state band of ^{187}W, compared to ^{185}W suggests a boundary for the onset of gamma softness.

The GRETINA array consists of "quad" modules of segmented position- sensitive Ge crystals, each with a central contact along the cylindrical axis that collects the electrons and 36 contacts along the cylindrical surface which collect the "hole" current pulse generated by a γ ray interaction inside the crystal. A signal decomposition algorithm is used to fit the observed waveform from each crystal contact with a linear combination of stored basis signals to localize the γ-ray interaction within the detector volume. In this work, the sensitivity of the hole mobility parameter for position reconstruction in GRETINA is investigated. Calibration data on position resolution is analyzed, together with simulations that isolate the signal decomposition dependence from electronics cross-talk. The chi-square fits exhibit a shallow minimum for $\pm 15\%$ variation in the hole mobility, effectively excluding it as a parameter in play for addressing remaining challenges in reconstructing γ-ray interaction points in GRETINA.

Acknowledgements

This thesis is as much the culmination of my academic career as it is a lesson in teamwork. Without the combined effort of my professors, labmates, mentors and family, this work would not have been possible.

It was by extraordinary chance that I happened on Prof. Partha Chowdhury one evening working late in Olney Hall. By the next day, I was fortunate enough to be known as member of his esteemed research group. For affording me the unique opportunity to work on arguably one of the most innovative, demanding and exciting problems currently encountered in the field of nuclear physics, as well as for guiding and challenging me along the way, I am forever grateful.

Later, in that same research group, I was introduced to Prof. Christopher. J. Lister, whose expertise in detector development further diversified my knowledge of radiation detection. The combination of these two influences has indisputably molded my understanding of science and will unquestionably shape and bolster my future career.

I would also like to share my appreciation for Dr. Edana Merchan, whose software proficiency immensely contributed to my overall research project.

To my esteemed colleagues at the Lawrence Berkeley National Lab, specifically, Heather Crawford, Andreas Wiens, Christopher Campbell, Augusto Macchiavelli, I. Y. Lee, and especially Mario Cromaz, your input, supervision, faith and round-the-clock support was invaluable during my GRETINA project. For that, as well as the opportunity to work on such an exceptional and stimulating project, I thank you. Mario, your help was instrumental in the completion of this project and I am sincerely thankful for your advice and direction.

Additionally, I must mention the wonderful team at the University of Rochester for providing me the opportunity to learn hands-on while installing and commissioning the upgraded CHICO2 Detector; also for allowing me to be the first one to gather and analyze the data set taken with this unique combination of CHICO2 and Gammasphere. This includes: Doug Cline, Adam Hayes and Ching-yen Wu. On the same note, I would like to extend my sincere thanks to our collaborators at the Physics Division at the Argonne National Laboratory for their support during this experiment.

It is impossible to properly thank my mother and late father for their unwavering confidence and support. It is because of their influence that I am where I am today. To my sister, Alka, the girl who followed me around the world, I could not be more proud of you. There is no one with whom I'd have rather taken this grad school journey with. I would also like to thank my wife Shilpa for her support, encouragement, and quiet patience, which helped me through the last leg of the work.

Finally, for being my "home away from home", I thank my dear friend Laura Dewhirst and her family. I owe you one.

Contents

List of Figures

xiv

xvi

List of Tables

Chapter 1

Introduction

The shape of an atomic nucleus is a fundamental property reflecting the spatial distribution of the nucleons. It is governed by the interplay of macroscopic, liquid-drop like properties of the nuclear matter and microscopic shell effects. Nuclei can be either spherical or deformed in their ground state. Closed-shell nuclei are always spherical in their ground state whereas in a nucleus with partially filled shells the valence nucleons tend to polarize the core towards a deformed mass distribution.

In some areas of the nuclear chart the shape is very sensitive to structural effects and can change from one nucleus to its neighbor. In addition to shape changes with proton or neutron number, the shape can also change with excitation energy or angular momentum within the same nucleus. Nuclear shapes and their evolution as a function of spin offer insight into the complex correlations between constituent nucleons. While most quadrupole-deformed nuclei have prolate

shapes, a small number, particularly near shell closures, have oblate deformations. Whereas collective oblate shapes at low spins and non-collective oblate shapes at high spins have been established in many nuclei, the observation of collective oblate rotation at high spins is quite rare.

The first half of this thesis involves the study of rotational bands in deformed neutron-rich nuclei with $A \approx 180$, around the W (Z = 74) region, which exhibit distinctive characteristics which should enable a transition from prolate to oblate collective rotation at high spins. In this mass region, collective oblate rotation, aided by nucleon alignments at lower rotational frequencies, is predicted to be favored over prolate shapes at high spins [1]. A recent study by the UMass Lowell research group reported possible experimental evidence for collective oblate rotation becoming favored at spins around $20\hbar$ in the rigid, well deformed, axially symmetric ^{180}Hf nucleus, at the highest end of angular momentum populated [2]. Theoretical calculations in this region predict a prolate to oblate shape transition in ^{184,186}W nuclei at a lower range of angular momentum than observed in the ^{180}Hf nucleus. The primary focus of this project was to extend the structure of ^{186}W to such spins that would allow a clean observation of the predicted shape transition.

Current nuclear structure studies such as the ones presented in this work primarily involve the techniques of gamma-ray spectroscopy in conjunction with auxiliary detectors. High-resolution germanium (Ge) detector arrays have been deployed in this field for over three decades. The first half of this thesis utilizes Gammasphere, an array of over 100 Compton-suppressed germanium detectors,

2

arguably still the world's best high-resolution gamma-array at present [3]. In the second half of this thesis, the focus shifts from physics to instrumentation with next generation position-sensitive Ge detector arrays.

The reconstruction of the original direction and energy of gamma rays through locating their interaction points in solid state detectors is a crucial evolving technology for nuclear physics, space science and homeland security. New arrays such as AGATA in Europe and GRETINA in the U.S. have been built for nuclear science based on highly segmented germanium crystals. With radioactive beam facilities, such as FRIB, coming on-line in the near future, these gamma-ray tracking arrays promises orders-of-magnitude improvement in weak signal detection for nuclear spectroscopy. Improvements in the sensitivity of the detection system are essential to the success of such scientific program.

The capability of reconstructing the position of the interaction with a resolution at the level of a few millimeters is a fundamental requirement for reliable tracking. It is, therefore, important to understand and quantify the limiting factors of position resolution. Improvements in signal decomposition algorithms, which depend on pulse shape analysis to determine the interaction points, can be realized by better modeling the crystals. Specifically, we need a better understanding of drift velocity anisotropy, which causes considerable differences in pulse shape rise time depending on the position of the spatial charge carrier creation.

The research objective of the second part of this thesis work was to systematically investigate crystal properties, such as charge transport, of a closed-ended

coaxial germanium semiconductor GRETINA detector. Specifically, the focus was to study the effect of uncertainties in hole mobility on pulse shape formation and also on algorithms which determine the gamma-ray interaction position in the crystal, with the final goal of improving tracking performance of the array.

The thesis is divided into two parts, each starting with introducing key theories and concepts, upon which the two individual projects are based.

Part 1

Search for Shape Transitions in Neutron-rich W isotopes

Chapter 2

Theoretical Background

This chapter summarizes the important points and theoretical concepts used in this thesis with references to literature where more details may be found.

2.1 Independent particle spherical shell model

The study of nuclear properties shows evidence of nuclear shells analogous to those observed in atoms. Extra stability certain numbers of neutrons and protons indicate closed shells. These "magic" numbers are 2, 8, 20, 28, 50, 82 and 126 for both neutrons or protons. While electronic shells in atoms arise from the motion of electrons in the central Coulomb potential of the nucleus, the nuclear shell structure has no such external potential but the nucleons move in the potential created by themselves.

The nuclear shell model [4] describes the energy levels for protons and neu-

trons in an attractive central potential with strong spin-orbit coupling

$$V_{tot} = V_{cent} - V_{ls} < l.s >$$ (2.1)

where V_{tot} is the total potential of the nucleus, V_{cent} is the attractive central poten-

tial dependent on the number of nucleons, and $V_{ls} < l.s >$ is the potential due to

the coupling between orbital angular momentum l, and spin, s. The energy levels

calculated for nuclei with such a potential exhibit large energy gaps in the single

particle spectrum, each corresponding to a magic number which represents the

cumulative number of nucleons filling the lower levels. Nuclei with protons and

neutrons near magic numbers are spherical in shape; however, away from closed

shells, nuclei can be deformed.

2.2 Nuclear Deformation and Shapes

Nuclei in specific regions of the nuclear chart, such as the rare earth

$(150 < A < 190)$ and actinide $(A > 220)$ regions, are known to be deformed in

their ground states. A deformed nuclear volume can be described by modeling the

nucleus as an incompressible nuclear fluid with a sharp surface, a liquid drop. One

way to parameterize the nuclear surface is with the length of radius vector from

the origin to the surface, given by [5]

$$R(\theta,\phi) = R_0 \left(1 + \sum_{\infty}^{\infty} \sum^{\lambda} \alpha_{\lambda\mu} Y_{\lambda\mu}(\theta,\phi) \right)$$ (2.2)

$$R(\theta,\phi) = R_0 \left| 1 + \sum^{\infty} \sum^{\lambda} \alpha_{\lambda\mu} Y_{\lambda\mu}(\theta,\phi) \right.$$

where $R_0 = r_0 A^{1/3}$ is the average radius and $\alpha_{\lambda\mu}$ are the coefficients of spherical harmonics $Y_{\lambda\mu}(\theta, \phi)$ of order λ. The lowest multiple, $\lambda = 2$ and $\mu = 0$, corresponds to quadrupole deformation (spheroidal shape) [6]. The next multipole, $\lambda = 3$ and $\mu = 0$, represents octupole deformation (pear shaped) stemming from reflection-asymmetry in the nuclear shape [7].

Most deformed nuclei are axially symmetric in their ground state, and the potential has a minimum at $\gamma = 0°$, where γ gives the degree of axial asymmetry. The relation between β, which gives a measure of the extent of the deformation, to γ and the nuclear radii are given as

$$\delta R_x = \sqrt{\frac{5}{4\pi}} R_0 \beta \cos(\gamma - \frac{2\pi}{3}) \tag{2.3}$$

$$\delta R_y = \sqrt{\frac{5}{4\pi}} R_0 \beta \cos(\gamma + \frac{2\pi}{3}) \tag{2.4}$$

$$\delta R_z = \sqrt{\frac{5}{4\pi}} R_0 \beta \cos\gamma \tag{2.5}$$

where β and γ are defined as:

$$\alpha_{20} = \beta \cos\gamma, \tag{2.6}$$

$$\alpha_{22} = \alpha_{2-2} = \frac{1}{\sqrt{2}} \beta \sin\gamma, \tag{2.7}$$

with $\alpha_{21} = \alpha_{2-1} = 0$. A common convention to describe the range of shapes for $\lambda = 2$ in terms of the β and γ variables is the Lund convention [8]. Fig. 2.1 shows

the various shapes that result from quadrupole deformation and places them in the $(\beta - \gamma)$ plane. In this convention the relationship between β, γ and the nuclear radii can be observed from the change in nuclear radius in Cartesian coordinates as a function of β and γ. For $\gamma = 0°$, the nucleus is elongated in one direction and compressed equally in the other two; this is called a prolate (American football) shape, as shown in Fig. 2.1. For nuclei with $\gamma = 60°$, it is compressed in one direction and extended equally in the other two, and is called an oblate (disk-like) shape. A triaxial nucleus has $\gamma = 30°$ where all three axes have different lengths.
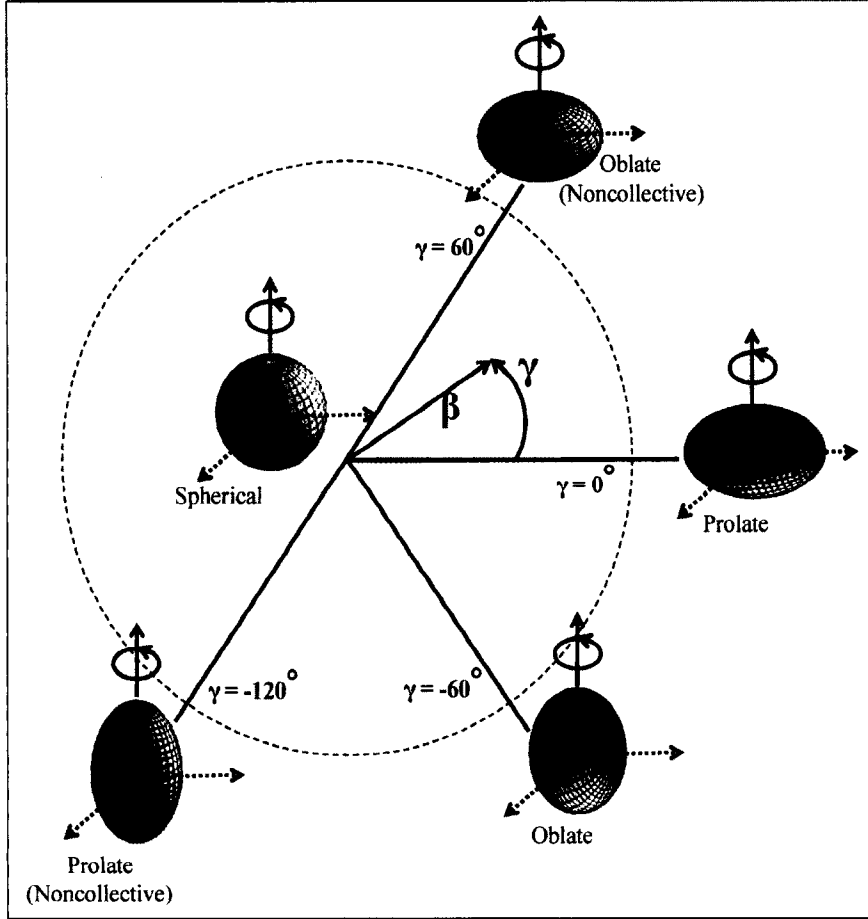
Figure 2.1: Nuclear shapes for deformation parameters β and γ using the Lund convention.

Many other complex axial asymmetric shapes can also be generated by varying γ. An important property of a quadrupole deformed nucleus is its quadrupole moment. The intrinsic quadrupole moment, in terms of β, is given as

$$Q_0 \approx \frac{3}{\sqrt{5\pi}} Z R_0^2 \beta (1 + 0.1\beta) \qquad (2.8)$$

2.2.1 The Nilsson model : Deformed shell model

In a deformed shell model, one considers the effects of deformation on single-particle energies. The Nilsson model provides a description of single-particle motion in a non-spherical potential. This model provides a microscopic basis for macroscopic collective phenomena such as rotations and vibrations of deformed (non-spherical) nuclei. An additional frequency term, dependent on the quadrupole deformation (β or ϵ or δ, based on the shape parameterization considered), is included in the modified harmonic oscillator potential (or in any other potential such as Woods-Saxon) to incorporate the effect of the deviations from the spherical symmetry. The Hamiltonian is given by [9],

$$H_{Nils} = \frac{P^2}{2m} + \frac{1}{2}m\left[\omega_x(x^2 + y^2) + \omega_z z^2\right] - Cl.s - Dl^2 \qquad (2.9)$$

where ω_x and ω_z are one dimensional oscillator frequencies in the x and z directions and m and P are the mass and momentum of the particle respectively. The oscillator frequencies are related to the deformation parameter δ ($\delta \sim 0.95\beta$), as

$$\omega_x^2 = \omega_y^2 = \omega_0^2\left(1 + \frac{2}{3}\delta\right) \qquad (2.10)$$

$$\omega_z^2 = \omega_0^2\left(1 - \frac{4}{3}\delta\right) \qquad (2.11)$$

where ω_y is the one-dimensional oscillator frequency in the y direction and ω_0 is the oscillator frequency for a spherical potential with $\delta = 0$. The l^2 and $l.s$ terms

ensure the proper order and energies of the single-particle levels in the spherical limit ($\beta = 0$). Positive values of deformation (β or ϵ or δ) represent prolate shapes and the negative values corresponds to oblate shapes.

A Nilsson diagram gives energies of various orbits as a function of deformation. A Nilsson orbit is labeled as:

$$\Omega^{\pi}[N n_z \Lambda] \tag{2.12}$$

where N is the principal quantum number (denoting the major shell), π is the parity and n_z is the number of nodes in the wave function in the z direction. And, Ω and Λ are defined, as shown in a schematic coupling of the collective angular momentum and the intrinsic angular momentum of the valence nucleon in a deformed nucleus (Fig. 2.2). In Fig. 2.2, angular momenta are labeled R for the rotational angular momentum and $J = \sum_{n=1}^{A} j_n$ for the sum of the intrinsic angular momenta of the valence nucleons outside the deformed core. R and J sum up to the total angular momentum, $\vec{I} = \vec{J} + \vec{R}$.
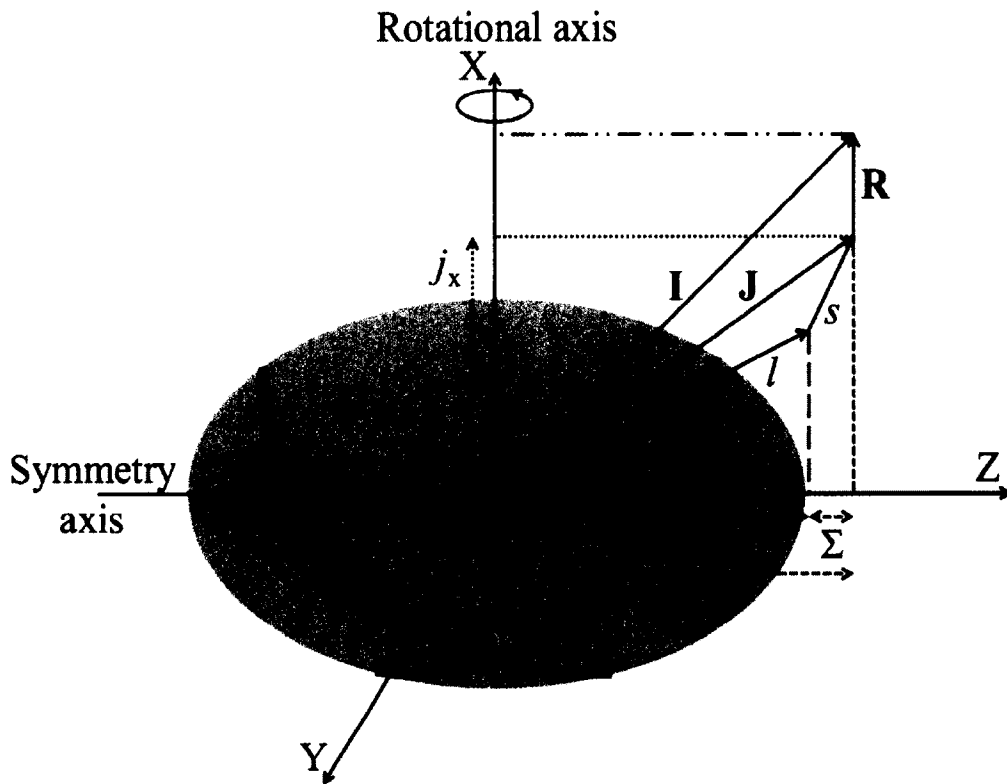
Figure 2.2: The asymptotic quantum numbers for deformed shell model.

For a valence nucleon in a single j orbit; we define

• Ω the projection of the single-particle angular momentum on the symmetry axis (z axis).

• Λ the component of the orbital angular momentum of the particle along the symmetry axis.

• K the projection of the total angular momentum, since the rotational angular momentum of axially symmetric nuclei is perpendicular to the symmetry axis, it

contributes nothing to K and therefore K is the sum of all Ω values of individual unpaired nucleons.

- Σ projection of the intrinsic nucleon spin on the symmetry axis, (therefore $K = \Lambda + \Sigma = \Lambda \pm \frac{1}{2}$).

The energy of the states now depends upon the projection of j onto the symmetry axis, Ω (shown in Fig. 2.2), for which there are $(2j+1)$ values for each j. Fig. 2.3 shows Nilsson single-particle energies for neutrons in the $82 \leq Z \leq 126$ region. There is a relation between the permissible values of n_z and Λ such that their sum must be even if N is even (positive parity) and odd if N is odd (negative parity). For example, the Nilsson states for the $i_{13/2}$ orbital are 1/2[660], 3/2[651], 5/2[642], 7/2[633], 9/2[624], 11/2[615], 13/2[606].
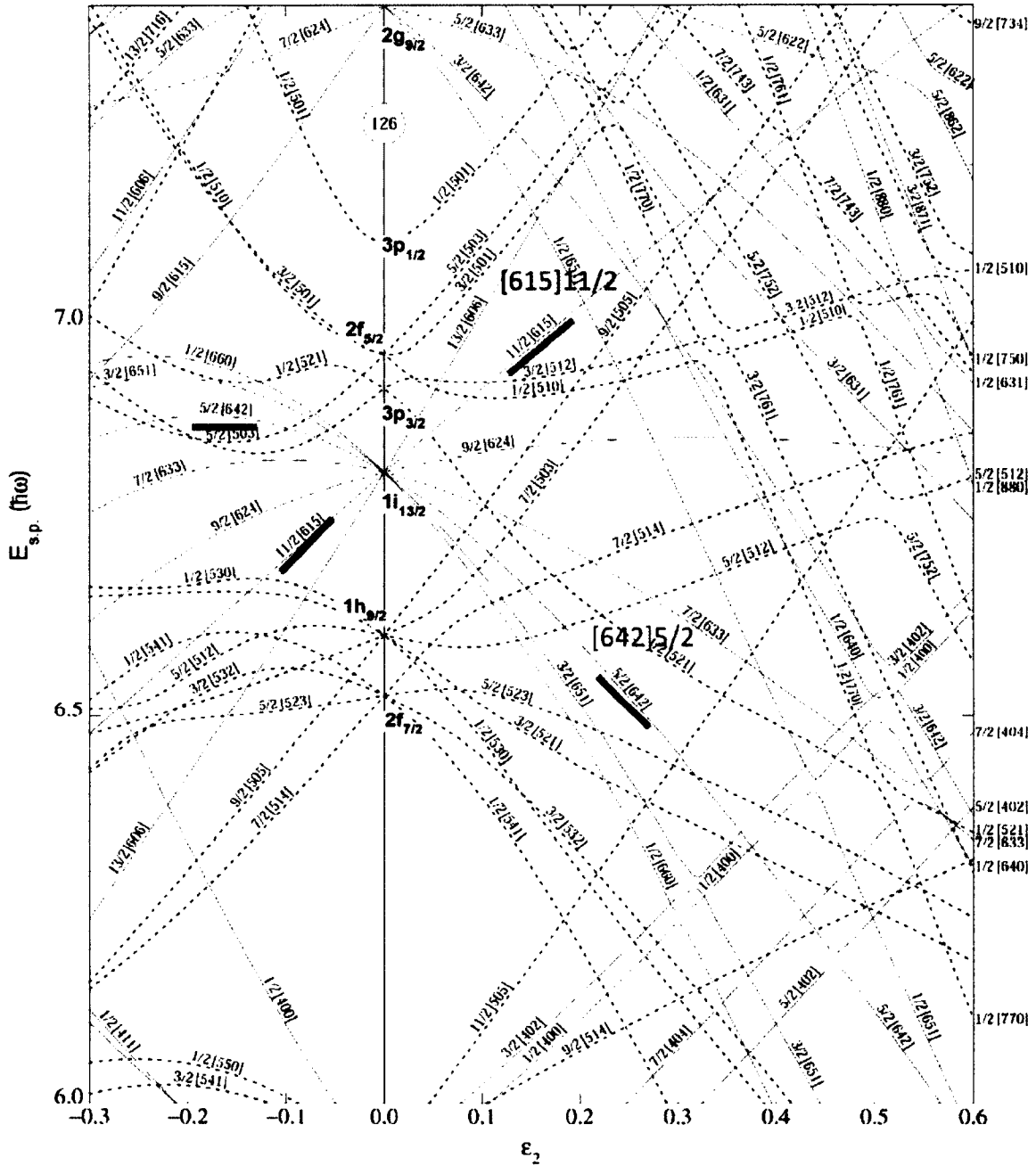
Figure 2.3: Nilsson diagram for neutrons, $82 < N < 126$. The ordinate axis is labeled in units of $\hbar\omega_0 = 41A^{-1/3}$ MeV] [10]. Highlighted orbitals are used as illustrative examples in text.

For example, an orbit having total angular momentum $I = \dfrac{13}{2}$ can have val-

15

ues of Ω ranging from $\dfrac{1}{2}$ to $\dfrac{13}{2}$. The angle made by each orbital plane with the symmetry axis is $\theta = \sin^{-1}(\Omega/I)$. From the Nilsson diagram, it is apparent that for the same value of Ω, the orientation of an orbital is different for prolate and oblate deformations (Fig. 2.3).

For example in Fig. 2.3, the orbital 11/2[615] ($N = 6$, $I = \dfrac{13}{2}$, with $\Omega^\pi = \dfrac{11^+}{2}$) is occupied at lower energy on the oblate side ($\epsilon_2 < 0$) than the prolate ($\epsilon_2 > 0$). Oblate shapes exist only when the down-sloping high-Ω orbitals are occupied by the valence nucleons on the oblate side, leading to a lower value for a sum over their energies thus making them more favorable than the prolate configuration. This situation is observed only in the case of a few nuclei, and therefore prolate shapes are preferred in deformed nuclei across the periodic table.

2.2.2 The Cranking model

As the collective angular momentum increases, the centrifugal and Coriolis forces increasingly affect the intrinsic states. If the angular velocity of the collective rotation is not slow compared to the motion of the nucleons, then the cranking model is needed to calculate the centrifugal and Coriolis corrections to the intrinsic Hamiltonian. In the cranking model the nucleus is rotated, or "cranked" with some fixed frequency, ω, to investigate its properties [11]. This provides a direct way to understand this effect on collective rotational bands and high-spin single particle configurations, which are the two kinds of structure that are most impor-

tant in the vicinity of the yrast line (locus of states with lowest energy for a given angular momentum) at high spins.

The cranking model is a further extension to the deformed shell model, which introduces another degree of freedom, rotational frequency, $\hbar\omega$. Cranking models take into the account the response of nucleons to the rotation of the nuclear potential and the Hamiltonian can be expressed as [12],

$$H_\omega = H_0 - \vec{\omega}.\vec{I} \qquad (2.13)$$

where H_0 is the static Hamiltonian in the rotating frame. Our calculations use the single-particle Woods-Saxon Hamiltonian to find the single-particle states in the intrinsic frame. The term $\vec{\omega}.\vec{I}$ represents the effects of both centrifugal and Coriolis interactions, which will modify the single-particle orbital motion. Also, the pairing interaction is often included with the cranked hamiltonian H_ω [13],

$$H' = H_\omega - \Delta(P^+ + P) - \lambda N, \qquad (2.14)$$

where H' is the quasiparticle hamiltonian, Δ is the pairing gap, P^+/P are the quasiparticle pair creation/annihilation operators, λ the chemical potential, and N is the particle number operator, included to keep the total number of particles constant. Quasiparticles are mathematical constructs that describe excitations in terms of linear combinations of particle and hole occupation probabilities. Using the quasiparticle construct the particles can be replaced by non-interacting quasiparticles

17

whose energies are additive. For each single-particle level there are two quasi-particle levels, one positive and one negative, reflections of each other about the Fermi surface. The cranking calculations are presented in this thesis in the form of quasiparticle energies. The energies in the rotating frame are called Routhians, and are labelled by their parity and signature (π, α). Under rotation the nlj quantum numbers and Nilsson labels are no longer good quantum numbers, and a single (π, α) orbital will represent a mix of Nilsson configurations.

2.3 Collective excitation

A deformed nucleus can accommodate angular momentum either in the form of collective motion (rotation and vibration) or by individual angular momenta of the valence nucleons. In addition, there can be interplay between the individual and collective degrees of freedom, for example, nucleon pair breaking and the alignment of their individual angular momenta along the axis of collective rotation [14]. This work involves the study of nuclear rotations and vibrations, which are explained in the following sections.

2.3.1 Rotational motion in nuclei

Deformation is a prerequisite to collective rotation of a quantum system since an orientation cannot be defined for a spherical system. Rotational bands, therefore, indicate the existence of a deformation in a nucleus. The Hamiltonian for a

rotating rigid body can be written as [5],

$$H_{rot} = \frac{\hbar^2}{2\Im}\mathrm{R}^2 \qquad (2.15)$$

where R is the angular momentum of the rotating core and $\Im$ is the moment of inertia. Fig. 2.2 shows the coupling scheme of the nuclear angular momenta in the deformation-aligned case. If the total angular momentum of the system is due to the rotating core only, which refers to the collective motion of all nucleons in the nucleus (as is normally true for deformed even-even nuclei) then the total angular momentum I = R, and the energies of the rotational levels are given by

$$E_{rot}(\mathrm{I}) = \frac{\hbar^2}{2\Im}\mathrm{I}(\mathrm{I}+1) \qquad (2.16)$$

where only even I are allowed for an axially symmetric shape. Then the γ-ray energies observed between adjacent levels will be E2 transitions. When nuclear rotational motion is superimposed on an intrinsic excitation characterized by projection K, we find $\mathrm{R} = \sqrt{\mathrm{I}(\mathrm{I}+1) - K^2}$ and the energy of the state is given by

$$E_{rot}(\mathrm{I}) = \frac{\hbar^2}{2\Im}(\mathrm{I}(\mathrm{I}+1) - K^2) \qquad (2.17)$$

Thus, for an even-even nucleus, where $K = 0$ in the ground state, the ratio of the excitation energies of the $\mathrm{I}^\pi = 4^+$ and 2^+ states should be approximately 3.33. This is consistent for a large number of well deformed nuclei. For example, in ^{186}W

the $\dfrac{E_{4+}}{E_{2+}}$ ratio is equal to 3.24.

Experimentally, the energy E of a state is measured as a function of the total angular momentum I, i.e the rotating nucleus can be expressed in terms of its angular rotational frequency, ω, as

$$E_{rot}(\text{I}) = \frac{1}{2}\mathfrak{I}\omega^2. \tag{2.18}$$

From equation 2.16 and 2.18, ω in terms of I is

$$\mathfrak{I}\omega = \hbar\sqrt{\text{I}(\text{I}+1)}. \tag{2.19}$$

Also, the relation between experimentally observed $\Delta \text{I} = 2$ transition γ-rays and the rotational frequency ω is

$$\hbar\omega = \frac{dE(\text{I})}{d\text{I}_x} \approx \frac{dE_\gamma}{2} \tag{2.20}$$

i.e. half the γ-ray energy [15]. Here, $\text{I}_x = \sqrt{\text{I}(\text{I}+1) - K^2}$ is projection of the angular momentum along the rotation axis and is known as *aligned angular momentum* and E_γ is γ-ray energy between the rotational states of angular momenta I and I - 2, which by using equation 2.16 is given as

$$E_\gamma = E_\text{I} - E_{\text{I}-2} = \frac{\hbar^2}{2\mathfrak{I}}(4\text{I} - 2). \tag{2.21}$$

The information derived from the relationship between E, I, I_x and ω can be used

20

to compare experimental results with cranked shell model calculations [16].

The moment of inertia ($\Im$) can also be determined from the experimentally observed γ-rays or energy spacings, as shown in equation 2.21. The moment of inertia found in this way is called the kinematic moment of inertia ($\Im^{(1)}$) and in a more general way, it is defined as the ratio of I_x to the rotational frequency ω and is given as

$$\Im^{(1)} = \hbar\frac{I_x}{\omega} = \hbar^2 I_x \left[\frac{dE}{dI_x}\right]^{-1}. \tag{2.22}$$

The experimental alignment, I_x, can further be used to investigate the rotational properties of a nucleus. At a given rotational frequency, the difference in alignment between rotational bands will be due to the difference in the underlying particle configurations of the bands. To facilitate measuring the increase in alignment and the differences in alignment between bands, a rotating reference based on equation 2.16 is subtracted from the aligned spin to give the experimental alignment, i_x:

$$i_x(\omega) = I_x(\omega) - I_{x,ref}(\omega). \tag{2.23}$$

The rotational reference $I_{x,ref}(\omega)$ is given by

$$I_{x,ref}(\omega) = \omega(J_0 - J_1\omega^2), \tag{2.24}$$

where J_0 and J_1 are Harris parameters that characterize the rotational reference, and are chosen to give approximately zero experimental alignment for the ground state band at low rotational frequency.

21

2.3.2 Vibrational modes of excitation

Another way in which nuclei can generate collective angular momentum is by surface vibrations. According to the hydrodynamic model [17], which is usually applied to describe nuclear vibrations, the nucleus can undergo small oscillations about an equilibrium shape. These oscillations are characterized by modes (λ, μ) of frequency ω_μ, degenerate in μ, and that depend on the density, the surface tension, and the mean radius R_0 (equation: 2.2). The vibrational energy of each mode (λ, μ) is given by

$$E_{\lambda,\mu} = (n_{\lambda,\mu} + \frac{1}{2})\hbar\omega_\lambda \qquad (2.25)$$

and the total excitation energy above the ground state, by

$$E_{ex} = \sum_{n_\lambda} \hbar\omega_\lambda \qquad (2.26)$$

where $n_\lambda = \sum_\mu n_{\lambda,\mu}$ is the number of "phonons" of order λ, for this excited state of energy. In this case, vibrational quanta called "phonons" of multipolarity λ, carry the energy and the parity, π, of each phonon mode is given by $(-1)^\lambda$. For nuclear vibrations, it is usually assumed that there is no density variation ($\omega_0 = 0$), and no pure vibration ($\omega_1 = 0$). Dipole ($\lambda = 1$) vibrations correspond to translations of the centre of mass of the nucleus and therefore cannot be produced by internal forces if the protons and neutrons move together. A schematic illustration of the different modes of nuclear vibration for $\lambda = 0, 1, 2$ and 3 are shown in Fig. 2.4.

22
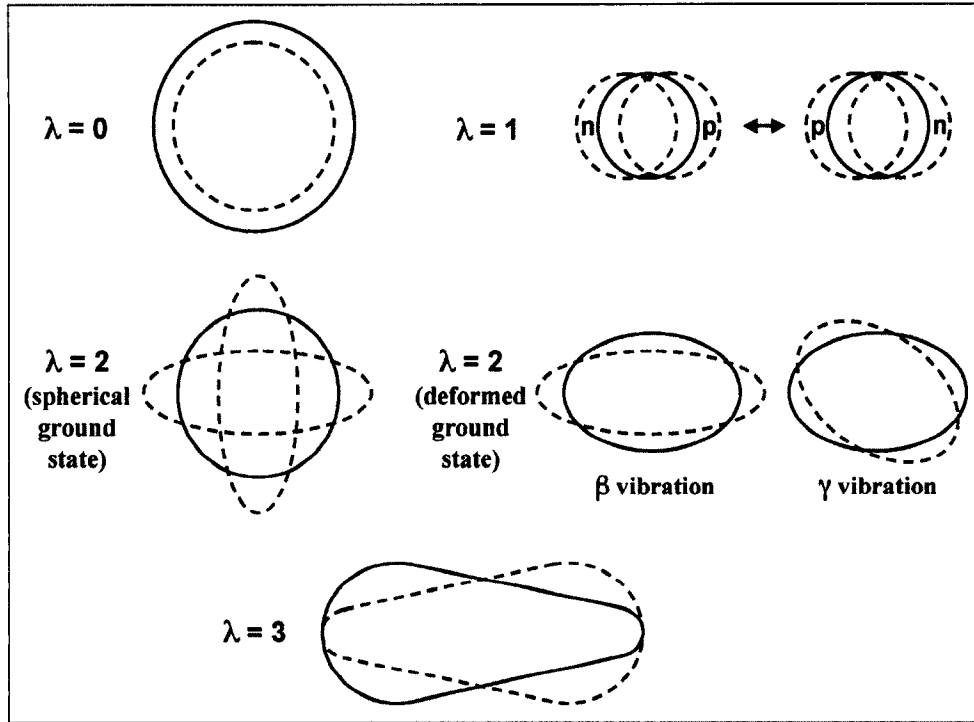
Figure 2.4: Schematic illustration of nuclear vibration modes [18].

Vibrational and rotational excitations can co-exist in a deformed nucleus [19]. This results in rotational states, characterized by a rotational band, built on a vibrational excitation. The most common rotational-vibrational states are, therefore, the lowest orders of vibrational modes for $\lambda = 2$ (quadrupole) and $\lambda = 3$ (octupole). Phonons of $\lambda = 2$ produce low-energy quadrupole vibrations which can take two forms, that is, β and γ vibrations. The names β and γ-vibration come from the fact that the β-vibration corresponds to fluctuation in the quadrupole deformation, while the γ-vibration corresponds to oscillation in γ.

The first, β-vibrations, are shape oscillations directed along the symmetry axis. The angular momentum vector for such oscillations is perpendicular to the

23

symmetry axis, therefore, such bands are based on $I^\pi = K^\pi = 0^+$ states. The second, produces a dynamical time-dependent deviation from axial symmetry and hence oscillations in the γ shape parameter, which governs the deformation at right angles to the β_2 deformation axis. Thus the angular momentum vector of γ vibrations points along the symmetry axis (assuming a mean γ of zero, the nuclei will on average be axially symmetric), which gives rise to bands based on $I^\pi = K^\pi = 2^+$ states. Octupole vibrations are associated with $\lambda = 3$ phonons, where the parity of the states in negative and the sequence of spins depend on the value of K. For $K = 0$, $I^\pi = 1^-$, 2^-, 3^- and higher. The relative energies of the even- and odd-spin members of the γ-vibrational band (signature splitting) give insight into the nature of the triaxiality of the nucleus [20] [21].

2.4 Gamma-Ray Emission

The study of γ-ray emission is of great importance in nuclear spectroscopy. Studying γ emission and its competing process, internal conversion, allows the determination of spin and parities of the excited states.

Selection rules

Excited nuclear states decay following an exponential decay time profile of the form ($e^{-\lambda t}$). Consider a γ transition from an initial excited state of energy E_i, angular momentum I_i and parity π_i to a final state E_f, I_f and π_f. The energy of

the γ-ray is given by [4]:

$$E_\gamma = E_f - E_i. \qquad (2.27)$$

The conservation of angular momentum imposes the following selection rule on the multipolarities of γ-ray transitions between two states, $I_i \rightarrow I_f$, such that,

$$|I_i - I_f| \leq L \leq |I_i + I_f|, \; (L \neq 0) \qquad (2.28)$$

where L denotes the transition multipolarity. The electromagnetic interaction is parity conserving, which imposes the additional selection rule,

$$\pi_i \pi_f = \pi_L. \qquad (2.29)$$

Whether a transition is electric (E) or magnetic (M) in nature depends on its multipolarity and the change in parity it represents,

$$\Delta \pi(EL) = (-1)^L, \quad \Delta \pi(ML) = (-1)^{L+1}. \qquad (2.30)$$

Considering only the lowest multipolarities, where the initial and final states have the same parity, the transition will be $E2$ or $M1$ in nature, and where there is a change in parity the transition will be $M2$ or $E1$. Transitions with the maximum change in angular momentum of the nuclear states are called "stretched" transitions.

25

Internal conversion

Internal conversion is a competing process to γ-ray decay, which occurs when an excited nucleus interacts electromagnetically with and ejects an orbital electron [22]. The energy of the internal conversion electron (ICE), E_{ICE}, is given as

$$E_{ICE} = E_{transition} - E_{b.e.} \qquad (2.31)$$

where $E_{transition}$ is the transition energy and $E_{b.e.}$ is the binding energy of the electron. The internal conversion coefficient, α, characterizes the competition between this decay process and γ-ray emission. It is the ratio of internal conversion decays, λ_{IC}, to the number of γ-ray decays, λ_γ. This coefficient is defined for each electron shell (i.e., the K, L, M shells etc), such that the total ratio $\alpha_{\text{total}} = \alpha_K + \alpha_L + \alpha_M +$ ... . The total decay probability between two given states then becomes,

$$\lambda_{\text{total}} = \lambda_\gamma + \lambda_{\text{IC}}, \quad \lambda_{\text{total}} = \lambda_\gamma(1 + \alpha_{\text{total}}). \qquad (2.32)$$

The experimentally determined γ-ray intensities were corrected for internal conversions, where conversion coefficients (α) were calculated using the BrIcc program from the Australian National University [23] [24].

Chapter 3

Motivation and Theoretical Calculations

In this chapter, a brief overview of previous theoretical and experimental studies which provide evidence for collective oblate rotation becoming favored at high spins in a rigid, well-deformed, axially symmetric ^{180}Hf nucleus is presented. In addition, theoretical calculations predicting the same physics phenomena in the neutron rich ^{186}W nucleus at lower spins is also presented.

3.1 Physics Motivation

The ground states of the nuclei in $A \approx 180$ region are characterized by axially symmetric prolate shapes. Both valence neutrons and protons occupy high-j orbitals, with high-Ω values for prolate shapes and low-Ω values for oblate deformation. Since nucleons in low-Ω orbitals are expected to align at lower rotational frequencies, both neutron and proton alignments are conducive to oblate shapes being favored over prolate ones at high spins. This distinctive characteristics of

neutron-rich, $A \approx 180$ nuclei has prompted us to look for rare transitions from prolate to oblate collective rotation at high spins.

An earlier theoretical calculation by Hilton and Mang [1] predicted a novel prolate to oblate shape change in ^{180}Hf. As shown in Fig. 3.1, where the excitation energy is plotted as a function of I(I+1), I being the spin, the predicted oblate band becomes "yrast" (lowest energy state for a given angular momentum) at a spin 26$\hbar$ and crosses the prolate ground state band.
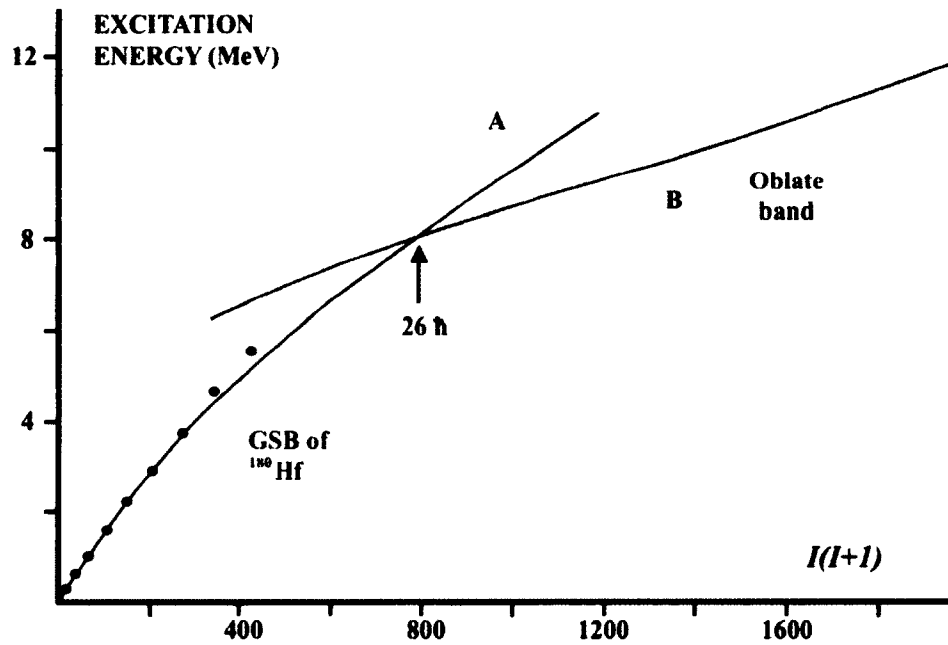
Figure 3.1: Prediction of prolate to oblate shape transition in ^{180}Hf [1]. Excitation energy as a function of I(I+1)), where I is the spin. Known levels in ^{180}Hf are indicated by dots (●).

Despite the difficulty of populating highly excited states in these neutron-rich nuclei, recent experimental and detection advances have made it possible to study

these nuclei through deep-inelastic and transfer reactions using heavy projectiles. The nuclear structure group at UMass Lowell conducted an experiment to investigate and study the prompt rotational structures in ^{180}Hf at high-spin using deep inelastic reactions. In this experiment [2], performed at Argonne National Laboratory, a 1300 MeV beam of ^{180}Hf was incident upon a ^{232}Th target ($\approx$20% above the Coulomb barrier). In these studies new transitions and collective states up to spin I = 20$\hbar$ were observed, extending on previously identified band structures [25], as shown in Fig. 3.2.

180Hf Level Scheme

1 **1a** **2**

5553 20⁺ 5665 20⁺ 20⁺ 5628

872 984 705

18⁺ 4922

4681 18⁺

868 654

16⁺ 4268

3812 16⁺ 456 592

1265 14⁺ 3676

808 673 549

3004 14⁺ 12⁺ 3128

731 1404 515

10⁺ 2612

2273 12⁺ 983 480

8⁺ 2132

643 1498 409

6⁺ 1723

1630 10⁺ 1050 4⁺ 315 408

547 1530 2⁺ 209 199

1083 8⁺ 1083

443 1493 1100

640 6⁺ 1415 1106

308 332 4⁺ 1315

93 215 2⁺

0 93 0⁺

180Hf
72 **108**

3

15⁺ 4322

717

13⁺ 3605

646

11⁺ 2959

1333

562

9⁺ 2398

1330 767 470

7⁺ 1928

5⁺ 371 1557

845

1315 3⁺ 266 1291

916

1288

983

1249

1198

4

(14⁺) 3970

966 671

(12⁺) 3299

687 570

1026 (10⁺) 2729

597 457

(8⁺) 2272

1098 371

(6⁺) 1901

1669

1189

1261

Figure 3.2: Partial level scheme for ¹⁸⁰Hf [2], showing the relevant collective structures.

Experimentally, the even-spin gamma-vibrational band (band 2) in ¹⁸⁰Hf was extended from I = 14ℏ → 20ℏ, and was observed to change its character beyond spin 10ℏ. The excitation energy (with a rigid rotor contribution subtracted) of ¹⁸⁰Hf bands (level scheme: Fig. 3.2), when plotted against spin (I), highlights this behavior as shown in Fig. 3.3. From Fig. 3.3, the interactions between these two bands are apparent in the region of the band crossing with the new band. The

odd-spin (band 3) partner of the gamma band continues to retain its vibrational character while the even-spin gamma band (band 2) is clearly crossed by a new band at spin $10\hbar$. In the level scheme diagram (Fig. 3.2.), there are connecting transitions (687 and 597 keV) between the quasi-vibrational band (band 4) and the even-spin gamma band. From the observed mixing of band 4 with the even-spin gamma band together with supporting theoretical predictions, a collective, oblate rotational character for band 2 at high spins was suggested [2, 26].

These studies are consistent with previously discussed theoretical predictions that nucleon alignments would favor oblate over prolate shapes at high spins in neutron-rich Hf isotopes. With this motivation theoretical calculations were carried out to explore more neutron-rich nuclei in this mass region, as presented in the next section.
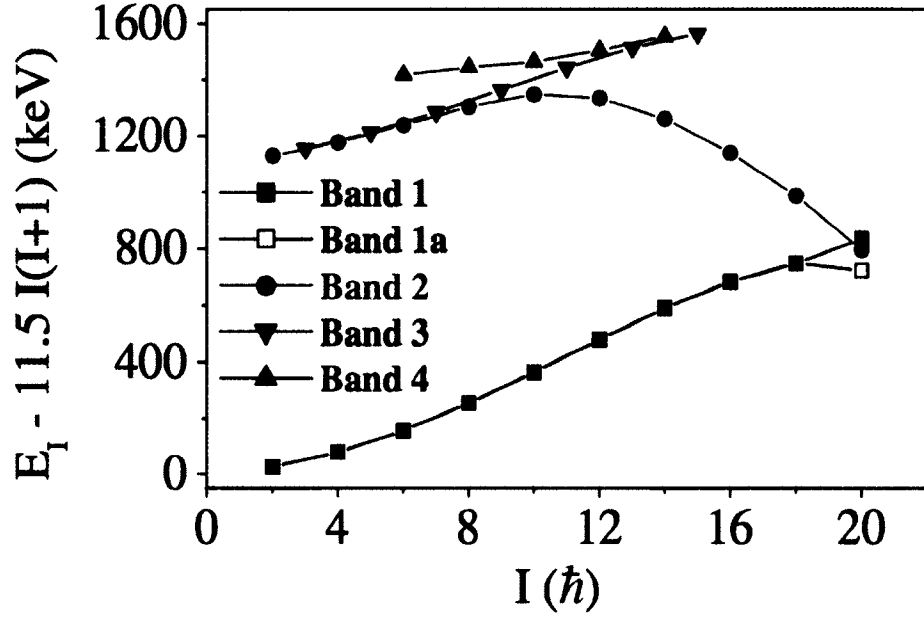
Figure 3.3: Excitation energy of the levels versus spin (I) for the ground state band, even and odd-spin gamma bands and low-K quasi-vibrational band in ^{180}Hf [26].

3.2 Theoretical Calculations for shape evolution in ^{186}W

Predictions of cranking calculations

Cranking calculations have been performed using standard Nilsson parameters in the ULTIMATE CRANKER (UC) code [27], where the modified harmonic oscillator potential is used with principal axis cranking. These total energy surface calculations allow the shape evolution to be studied as a function of spin. From these calculations the shape evolution with spin for various W (Z=74) isotopes is shown in Fig. 3.4. For the isotope ^{180}W (N = 106), oblate rotation is not preferred even at the highest spins. For ^{182}W (N = 108) and beyond, oblate shapes

are favored at successively lower spins, with increasing neutron number. The yrast rotational structure in the isotope ^{186}W (with N = 112) is expected to have a near-oblate ($\gamma = 40°$) shape, above I = $14\hbar$. The total energy surfaces in ^{186}W for the ground state and at I = $16\hbar$ are shown in Fig. 3.5. It is evident that ^{186}W (N = 112) offers the best opportunity for observation of both the prolate-to-oblate shape transition and observation of the (near)-oblate states over a significant range of spin. It should be noted that though an oblate shape is expected to be favored at higher spins in ^{184}W (above I = $18\hbar$) compared to ^{186}W, the triaxiality parameter in ^{184}W is predicted to be much closer to collective oblate ($\gamma = 60°$) than in ^{186}W, following the shape transition. Therefore, it is also desirable to study ^{184}W from this perspective.
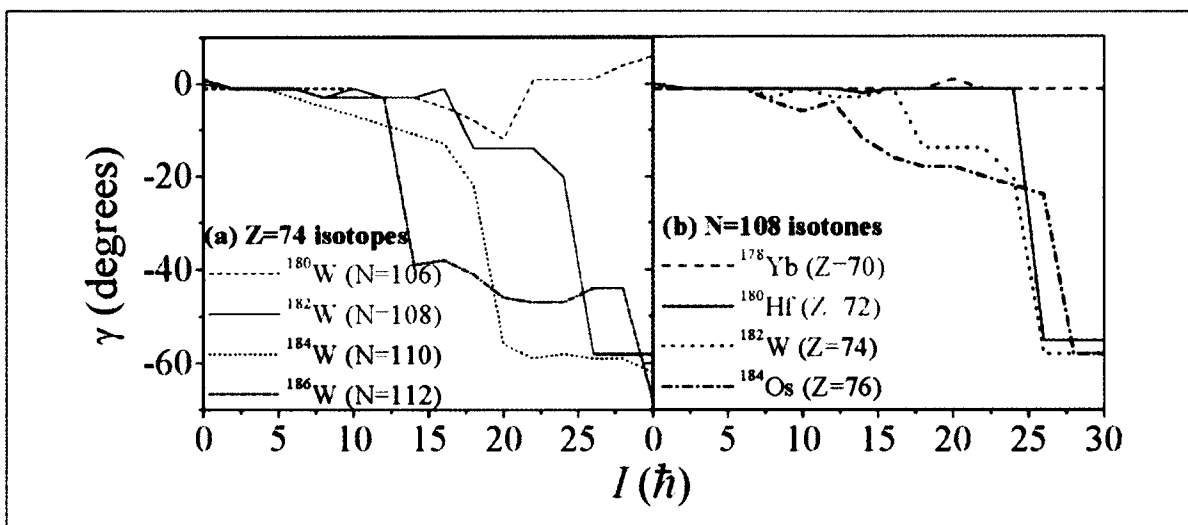
Figure 3.4: Predicted shape evolution for the yrast collective structures in the W isotopes. The variation in the triaxiality parameter (γ), as a function of spin for (a) Z = 74 isotopes, and (b) N=108 isotones.

Total energy surfaces generated using Ultimate Cranker

The total energy surfaces in ^{186}W for the ground state $I = 0\hbar$ and at $I = 16\hbar$ are shown in Fig. 3.5. The calculations predict an axially symmetric, prolate shape with $(\varepsilon_2, \gamma) = (0.20, 0°)$ for ground state and near-oblate shape with $(\varepsilon_2, \gamma) = (0.19, -40°)$ for $I = 16\hbar$. Here ε_2 is the deformation parameter and is related to β_2, to first order by $\beta_2 \approx 1.05\varepsilon_2$.
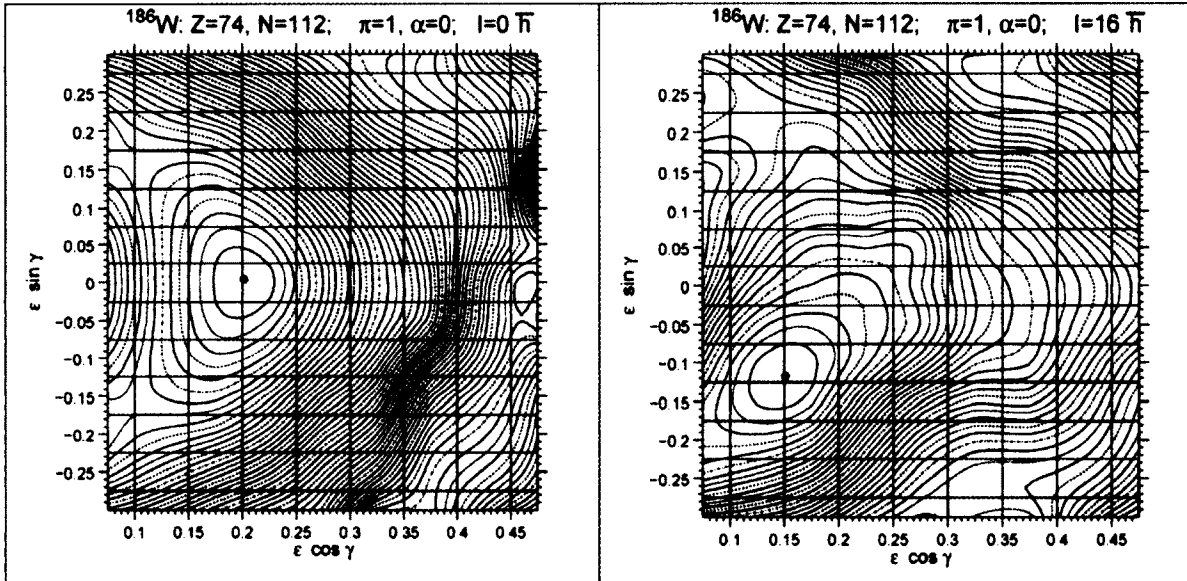
Figure 3.5: Shape evolution in ^{186}W from UC calculation. Total energy surfaces for the lowest, positive parity states in ^{186}W, at $I = 0\hbar$ (left) and at $I = 16\hbar$ (right), where lowest energy minimum is indicated by a dot.

Quasi-particle diagrams

In the Nilsson diagram (Fig. 2.3), the orbitals occupied by the valence neutrons in ^{186}W are highlighted (solid lines representing positive parity and positive

signature orbitals). On the prolate side ($\varepsilon_2 > 0$), the [642]5/2 high-Ω orbital is close to the Fermi level. For the oblate side ($\varepsilon_2 < 0$), the high-Ω orbital [615]11/2 is near the Fermi surface. The valence nucleons in the low-Ω orbitals typically align at lower frequencies if they are close to the Fermi level. Therefore, the alignment frequency is expected to be lower for the oblate deformed configuration.

The rotational frequency at which the first nucleon pair aligns can be calculated using the cranking model. The alignment frequencies have been calculated using a Wood-Saxon potential, and the results are presented in the quasi-particle diagram (Fig. 3.6). Where the energy E_μ of the particle(hole), relative to the Fermi level is plotted as a function of frequency.
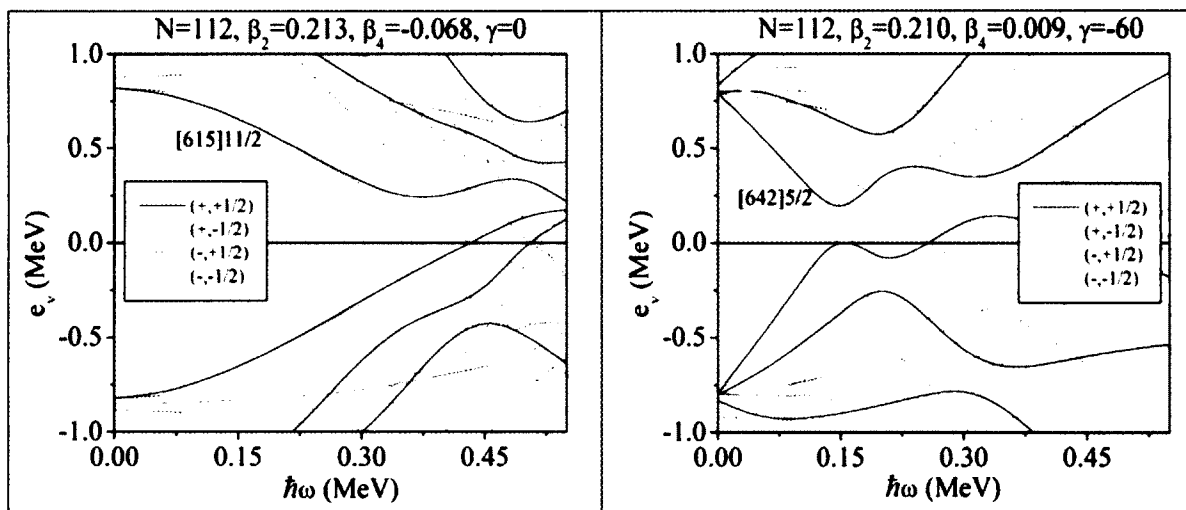
Figure 3.6: Neutron quasi-particle levels in ^{186}W, illustrating the difference between the crossing frequencies for prolate (0.38 MeV) and oblate (0.15 MeV) shapes.

For prolate shapes, the first $i_{13/2}$ neutron crossing is predicted at $\hbar\omega = 0.38$ MeV, for the [615]11/2 Nilsson orbital. For oblate shapes, the crossing is (as expected) at a much lower rotational frequency ($\hbar\omega = 0.15$ MeV), since the [642]5/2 Nilsson orbital (with lower-Ω) is involved. For the first $h_{11/2}$ proton crossing, a similar situation is predicted, with crossing frequencies of $\hbar\omega = 0.50$ MeV and $\hbar\omega = 0.22$ MeV for prolate and oblate shapes, respectively. With both neutron and proton alignments expected at much lower frequencies for oblate shapes than the first alignment for prolate deformation, the oblate aligned states, which are energetically favored by virtue of their large MOI, should become yrast.

From these calculations, it is evident that ^{186}W (with N = 112) offers an excellent opportunity for both the observation of prolate-to-oblate shape transition and observation of the near-oblate states over a significant range of spin.

3.3 Known prompt rotational structures in W isotopes

Nuclear structure properties along the W (Z = 74) isotopic chain have been investigated in previous studies of rotational band structures and shape transitions as well as K-isomeric states associated with well deformed prolate shapes. The ^{186}W nucleus is the heaviest stable isotope of tungsten, whose low-lying structure has been studied following β-decay of the neutron-rich parent ^{186}Ta [28, 29, 30, 31]. Also, tungsten nuclei were extensively studied using Coulomb excitation techniques using protons, ^{4}He, ^{16}O and ^{208}Pb beams to deduce nuclear structure infor-

mation [32, 33, 34, 35]. To establish the role of multi-quasiparticle configurations in the high-angular-momentum structure, high-spin isomers in ^{186}W target nuclei have also been studied by inelastic excitations using pulsed ^{238}U beams [36].

However, even though these nuclides have been studied in great detail at low spins, experimental information on the high spin yrast states of tungsten isotopes, specifically ^{185,186}W, is sparse due to the neutron-rich nature of these systems. The advent of heavy-ion accelerators and modern detector arrays now make it possible to extract new information about the high-spin excitations of such nuclei. The different techniques and detection technologies used to excite and study ^{185,186}W nuclei are described in the following chapter.

Chapter 4

Experimental Details

The investigation of nuclear structure properties of neutron-rich nuclei, specifically in A ~ 180 region with high N/Z ratio, has been a subject of long standing physics interest. Experimentally, with increase in neutron number, it becomes progressively more difficult to study these neutron rich nuclei with stable beam/target combinations. The challenges arise from limitations of the fusion-evaporation reaction mechanism, where fusing two lighter nuclei in order to populate high angular momentum nuclear states preferentially leads to neutron deficient nuclei. Recent advances in the production of heavy beams such as Xe, Pb and U with sufficient energies required to surpass the Coulomb barrier, have led to the increased use of deep-inelastic and transfer reactions on the heaviest stable isotopes in the neutron-rich A ~ 180 region and has proved to be an efficient mechanism for populating high-spin states.

The nuclear structure group at UMass Lowell has performed experiments in

the past to study high spin states in $^{180}_{72}\text{Hf}_{108}$ using similar techniques. This chapter will describe in detail the experimental technique and setup used in the current experiment conducted at Argonne National Laboratory, where accelerated ^{136}Xe ions were incident on a thin ^{186}W target. The working details of a large γ-ray detector array which was coupled with a heavy-ion counter to facilitate particle-γ coincidence techniques, will also be discussed.

4.1 Inelastic and Transfer Reactions

Inelastic and transfer reactions are general reaction mechanisms which can be used to excite neutron-rich nuclei to relatively high spin-states. A characteristic feature of these reactions is that they preserve the binary character of the system, so that the final fragments maintain some resemblance to the initial nuclei. These reactions involve a fast redistribution of protons and neutrons among colliding nuclei, which is governed by strong driving forces associated with the potential energy surface of the complex nucleus.
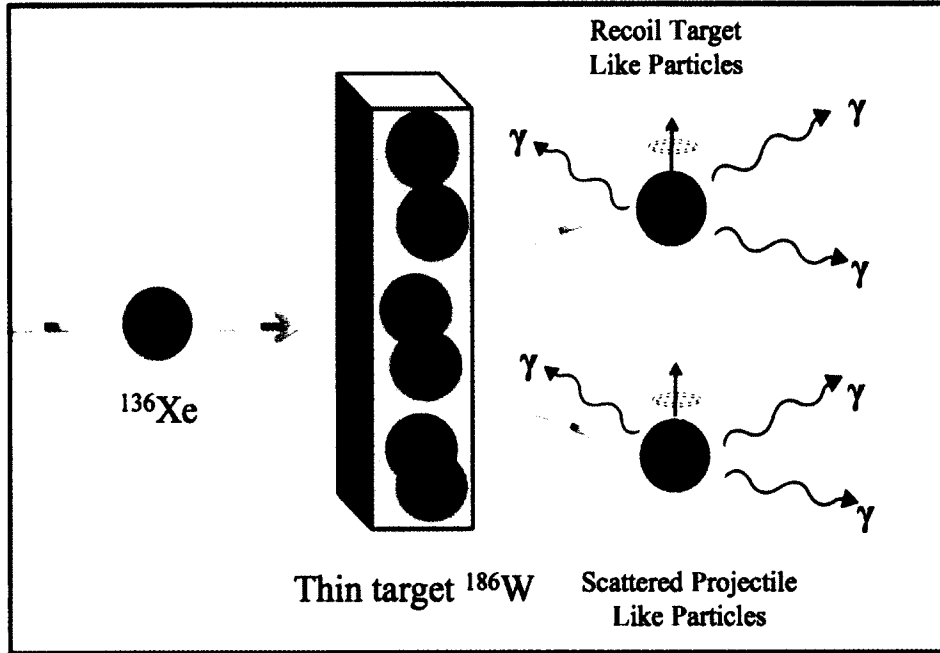
Figure 4.1: Schematic of deep inelastic collision.

The experiment was performed at Argonne National Laboratory (ANL). Prompt rotational structures in ^{186}W were populated using 725 and 800 MeV ^{136}Xe beam energies provided by Argonne Tandem Linac Accelerator System (ATLAS), incident on a thin enriched ^{186}W target. The Coulomb barrier energy in the laboratory frame for the chosen beam and target is estimated to be,

$$E_{Lab}^{Coulomb} = (1 + A_1/A_2)\frac{1.44Z_1Z_2}{1.16(A_1^{1/3} + A_2^{1/3} + 2)} \approx 669\text{MeV} \qquad (4.1)$$

The selected beam energies for ^{136}Xe are $\approx 9\%$ and $\approx 20\%$ above the Coulomb barrier, which would allow the population of sufficiently high spins, yet limit the background from other reaction channels. Following an inelastic or transfer reac-

tion, the recoiling nuclei (projectile- and target-like) recoil into vacuum and are detected using a position sensitive particle detector CHICO2 used in conjunction with Gammasphere, as discussed in the following sections.

4.1.1 Binary reaction kinematics

The following kinematic equations refer to the laboratory reference frame, where the nuclei in the target are considered at rest. If the reaction plane is defined by the direction of the incident beam and one of the outgoing particles, then conserving the component of momentum perpendicular to that plane shows immediately that the motion of the second outgoing particle must lie in the same plane, see Fig. 4.2.
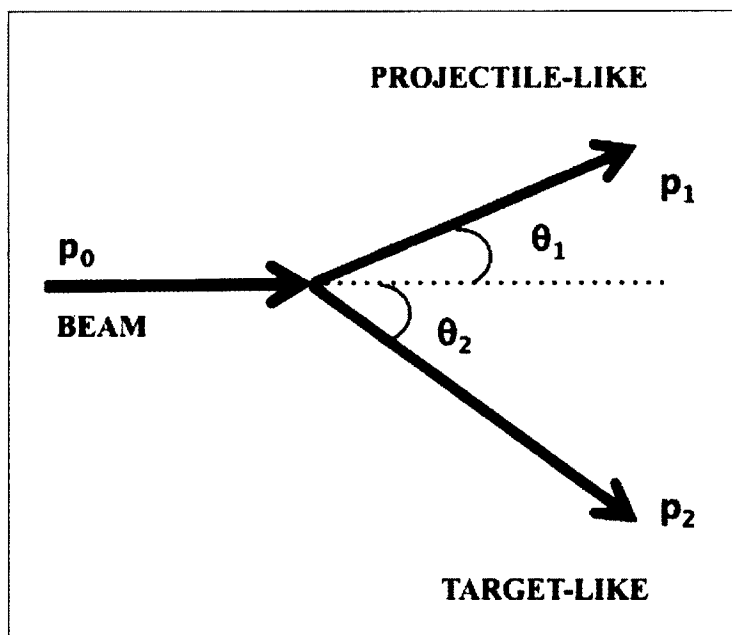
Figure 4.2: Reaction geometry. Projectile and target recoils define the plane of the binary reaction.

Conservation of linear momentum gives,

$$p_0 = p_1\cos\theta_1 + p_2\cos\theta_2 \quad and \quad 0 = p_1\sin\theta_1 - p_2\sin\theta_2$$

where p_0 is the initial momentum of beam, p_1, p_2, are the recoil momenta and θ_1, θ_2 are the scattering angles for the projectile and target nuclei respectively. From these equations, the relation of the recoil momenta to the initial beam momentum can be derived as,

$$p_{1,2} = p_0\frac{\sin(\theta_2,\theta_1)}{\sin(\theta_1 + \theta_2)}. \tag{4.2}$$

In a non-relativistic approximation the momentum is given by $p = m\beta c$, whereas the relativistic momentum is given by $p = m\beta c\gamma$ where m is the mass, β is the ratio of velocity of particle to the velocity of light and $\gamma = \frac{1}{\sqrt{1-\beta^2}}$. If an elastic collision is assumed, where the energy conservation can be given by Equation 4.1.1, then using Equations 4.2 and 4.1.1 for a given recoil angle, the recoil angle of the other fragment and the velocity of the recoils can be calculated using,

$$\frac{p_0^2}{2m_{beam}} = \frac{p_1^2}{2m_1} + \frac{p_2^2}{2m_2} \tag{4.3}$$

Fig. 4.3 shows the calculated velocities for the projectile and target recoils in the case of a ^{136}Xe beam at laboratory energy of 800 MeV impinging on a ^{186}W target. Gamma rays from nuclei recoiling at these velocities require Doppler correction techniques, as discussed in Section 5.2.2.
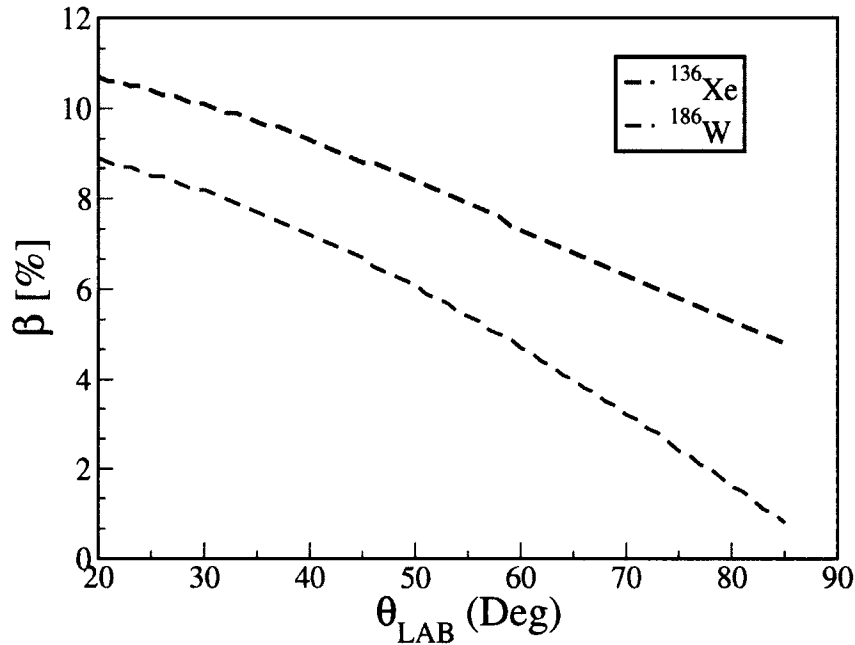
Figure 4.3: Calculated velocities of the projectile and the target recoils for a ^{136}Xe beam at 800 MeV in the laboratory frame impinging on a ^{186}W target. An elastic collision and simple two-body kinematics are assumed.

4.2 Beam and target production

The Argonne tandem-linac accelerator system (ATLAS) can accelerate stable isotopes of any element up to and including Uranium, with energies up to 17 MeV/u. For the current experiment a ^{136}Xe beam (at $\sim$ 5.5 MeV/u) was used as it is stable and can be reliably produced and accelerated by ATLAS. The choice of beam is also based on the need to (a) populate high spins and (b) keep the low-energy ($<$ 1 MeV) region of the spectrum relatively free of transitions from the

43

excitation of beam nuclei. This beam was also successfully used in earlier studies of ^{180}Hf. Suitable thin ^{186}W targets ($250\mu g/cm^2$) backed by a $110\mu g/cm^2$ carbon foil, were prepared in the Argonne Physics Division Accelerator target laboratory. As shown in Fig. 4.4, the gamma ray detector array Gammasphere, situated in Target area IV, and the CHICO2 particle detector placed in the Gammasphere target chamber were used in coincidence detection setup, as explained in the following sections.
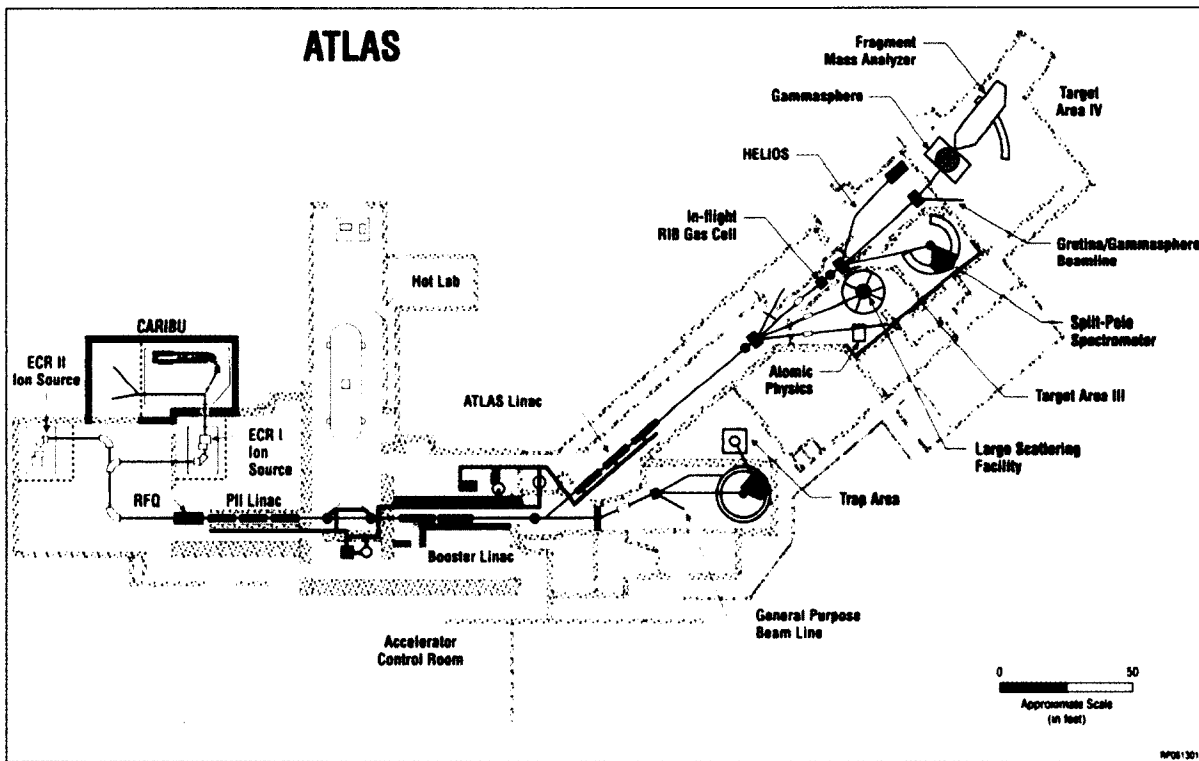
Figure 4.4: Layout of the Argonne tandem-linac accelerator system [37].

4.3 Detectors

4.3.1 Gammasphere

Gammasphere is the national gamma ray research facility currently at Argonne National Laboratory with the main focus on nuclear structure studies. The Gammasphere detector and data acquisition system, originally developed in the early 1990s consists of a close-packed spherical configuration of up to 110 Compton-shielded germanium (Ge) detectors with custom made electronics to measure gamma-ray energy and time [38] [39] (Fig. 4.6). Each germanium detector is about 7 cm in diameter and 8 cm long and is surrounded by bismuth germanate scintillator acting as a Compton suppression shield, as shown in Fig. 4.5, resulting in enhanced peak to Compton ratio in gamma-ray spectra.

There are several performance factors that contribute to the overall sensitivity of such a large array of Compton-suppressed Ge detector, which includes energy resolution, efficiency, peak-to-total, and rate [40]. These are defined as [41]:

- The ratio of counts in the full-energy peak to total counts in the entire spectrum (peak-to-total (P/T) ratio).

- The energy resolution, defined as the ratio of the full width at half-maximum (FWHM) of a given γ-ray peak, ΔE_γ, to the peak energy E_γ.

- The effective solid angle, which is a sum of all the individual detectors in the array.

45

A typical Gammasphere HPGe detector can achieve an energy resolution of about 2.2 keV FWHM for a 1.33MeV γ-ray, an efficiency of $\sim 75\%$ relative to that of a 7.62 cm x 7.62 cm NaI(Tl) detector, and a time resolution of ~ 8.5 ns FWHM for ^{60}Co. The P/T ratio for a Ge detector is about 25% without Compton suppression, and increases to better than 60% with suppression [41] [42]. The time resolution of one element of the BGO shield ranges from 2.5 ns to 4 ns, while its energy resolution is poor, of the order of a typical value of 8-10% for scintillation detectors [43].

Another important quantity to evaluate the performance of HPGe detectors is the resolution (or *resolving power* R), which in terms of FWHM and P/T ratio of a measured γ-ray is defined as [44]:

$$R = \left(\frac{SE_\gamma}{\Delta E_\gamma}\right) (P/T), \qquad (4.4)$$

where SE_γ is the average separation between γ-rays in a cascade. A controllable component in the resolving power of an array is ΔE_γ, which has the following contributing factors:

• The intrinsic resolution of the detector system, ΔE_I, which takes into account the individual properties of the detector.

• Doppler broadening due to the velocity and angular spread of recoils, ΔE_V and ΔE_R, respectively. Improvements can be made with kinematic corrections.

• Doppler broadening due to the opening angle of the detectors, ΔE_D. Clustering

46

and segmentation of detectors can improve this quality.

Thus, the final energy resolution of the detector array can be written as:

$$\Delta E_\gamma = \sqrt{\Delta E_I^2 + \Delta E_D^2 + \Delta E_V^2 + \Delta E_R^2}. \tag{4.5}$$

Gammasphere has been successfully used for almost 25 years now and its excellent performance has revealed many new nuclear physics phenomena. However, some aspects can still be improved and are already in progress, which can help improve its overall performance. Due to the use of BGO shielding the actual solid angle coverage of Ge detectors is only 46% of 4π sr. Next generation germanium detector arrays based on γ-ray tracking concept, which rely on higher segmentation and eliminates the use of Compton suppressers, would cover more solid angle. GRETA and AGATA [45] are being built based on this technology, where locating the first interaction point of a gamma ray in the detector would enable better event-by-event Doppler correction and hence higher resolving power compared with existing arrays.
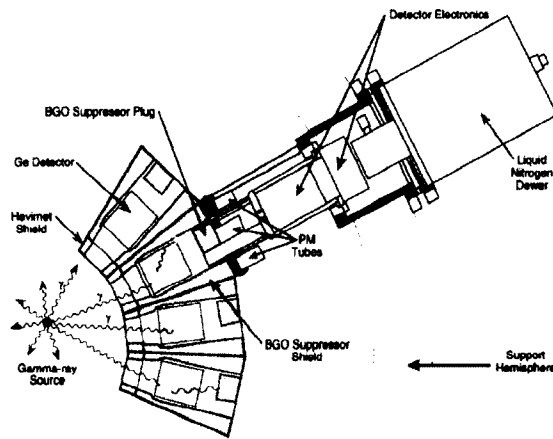
Figure 4.5: A schematic diagram of a Gammasphere detector module showing the Ge crystal (8cm long), the BGO/photomultiplier suppression system, the housing for the electronic control system and also the liquid-nitrogen dewars used to cool the Ge crystal in order to suppress random thermal signals [46].

With the need to cope with high counting rates (up to 20 kHz in each detector), a digital signal processing based data acquisition was recently developed for Gammasphere. Previously, the system used VXI based analog electronics, where the throughput of data was limited at high rates due to the conversion time of the ADC and the rate of data readout. At the center of this development are the GRETINA digitizer modules which digitize the Ge preamp signals at a 100MHz rate [47]. Initial tests with upgraded data acquisition have shown that the Ge count rate can be increased up to 50,000 counts/sec with digital pulse processing while maintaining the losses due to pileup below 10% per detector and preserving good

48

energy resolution [48]. The new DAQ, which is expected to significantly increase event throughput, was used to collect data in this experiment.

4.3.2 Heavy Ion Detector: CHICO2

The design of Gammasphere allows for the use of a wide variety of auxiliary detectors. These include external devices, which are designed to be placed inside the chamber [49] [50]. The CHICO (Compact Heavy Ion COunter) detector, a highly segmented 4π position-sensitive parallel-plate avalanche counter is designed to detect heavy-ion binary fragments, as shown in Fig. 4.6 (b). It was developed specifically for use with Gammasphere, to exploit the advantages of the kinematic coincident technique [51].

(a)   (b)
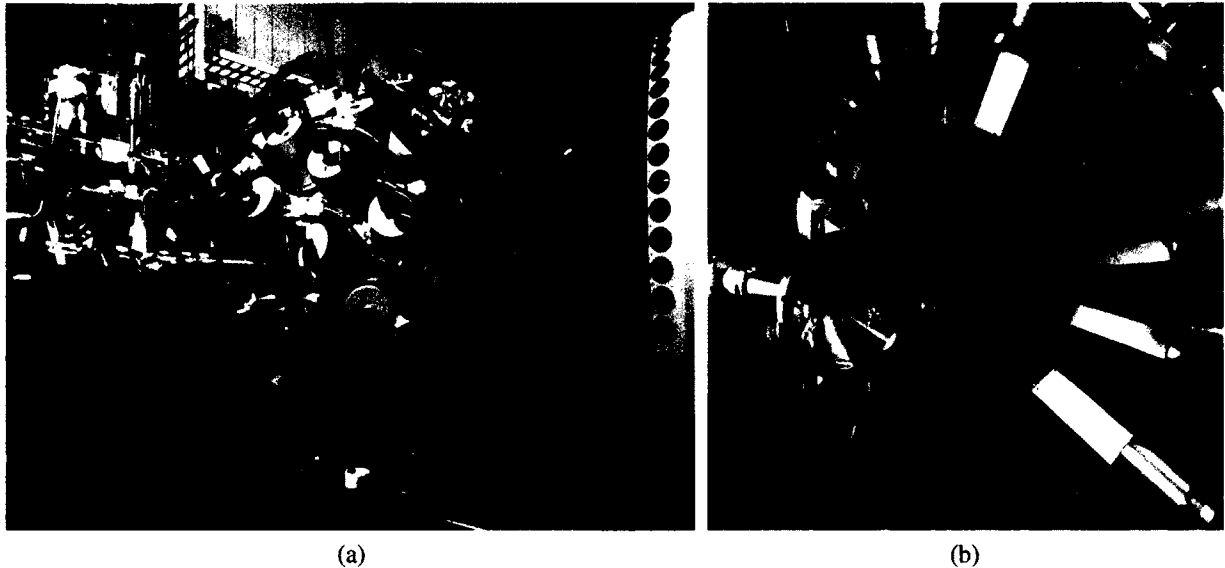
Figure 4.6: (a) The Gammasphere spectrometer. (b) Gammasphere (one hemisphere) and CHICO (one half) in their standard coupled mode.

An upgraded version of CHICO is CHICO2, which was developed for GRETINA, to improve θ,ϕ resolution in anticipation of "tracking". Like CHICO, the geometry of CHICO2 has each hemisphere containing ten θ-ϕ position-sensitive parallel-plate avalanche detector panels in a conical array. As shown in Fig. 4.7, the PPACs are housed in an (1.58 mm thick and 35.6 cm in diameter) aluminum hemisphere shell, each mounted in fixtures epoxied to the inside of the hemisphere. A pressure window made from 0.9 μm thick mylar contains the detector grade isobutane gas at 4 Torr from the high vacuum target chamber. All ten PPACs in a single hemisphere share a common gas volume.
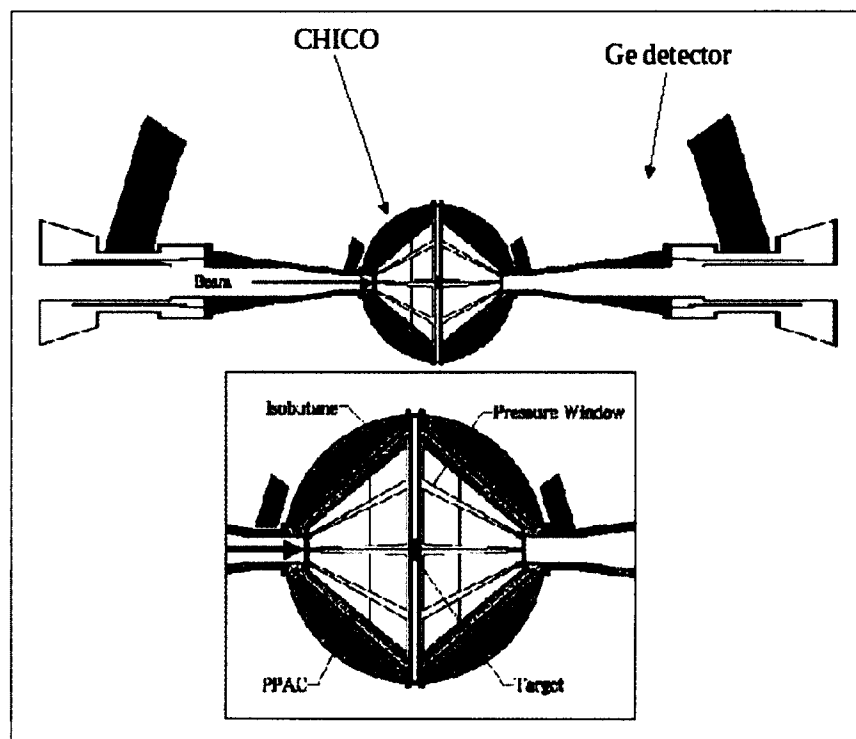
Figure 4.7: Schematic of the experimental setup. The PPAC array (CHICO) is shown with two representative Gammasphere Ge detectors [52].

In the upgraded hardware, each of the panels consists of a pixelated cathode board coupled with the delay-line readout for the position measurement and a 5-channel fast amplifier for processing both anode and cathode signals. As shown in Fig. 4.8, the cathode is segmented into $1°$ wide θ stripes for $12° < \theta < 85°$ and $95° < \theta < 168°$ while ϕ is segmented with $\pm 1.4°$ resolution.
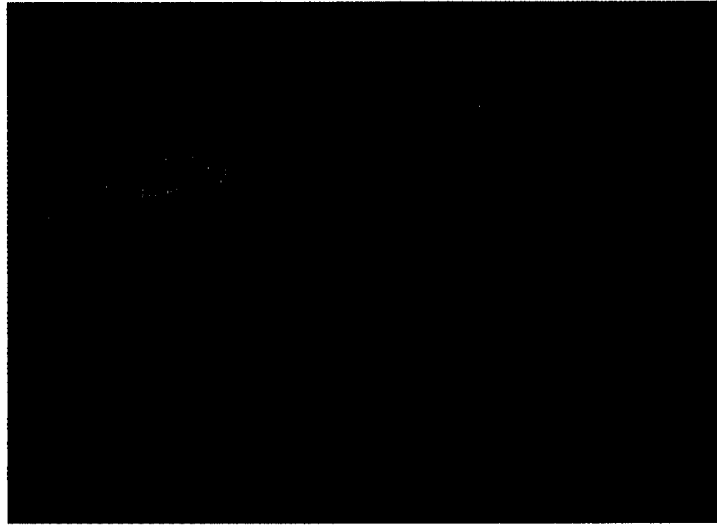
Figure 4.8: (Upper) Layout of cathode board pixelation, where 1475 pixels are arranged such that each θ slice is $0.5°$ wide and spaced every degree and the ϕ slices are mostly $1.4°$ wide in θ except at the smaller θ where they are wider. (Lower) Efficient delay line readouts which uses 4 output signals to identify and interpolate the 1475 pixels per board. Also seen are the transmission lines at the end of board, that carries the anode and cathode signals to the fast amplifiers which are outside of the gamma detector array [52].

Also upgraded is a $100\mu g/cm^2$ segmented aluminized stretched polypropylene anode, from which, in addition to the time, pulse height is also recorded for each event. The anode time resolution is $\approx 500ps$.

51

Figure 4.9: Mounting an anode frame in CHICO2 [52].

The detection solid angle for CHICO2 is 67% of 4π with a minimum flight path of 13 cm. The measured mass resolution is $\Delta m/m \approx 5\%$ for binary collisions. The firmware for the new VME-based data acquisition system has been developed in anticipation of CHICO2 serving as an auxiliary detector for GRETINA and Gammasphere. The present experiment was one of the first to use CHICO2 coupled to "Digital" Gammasphere.
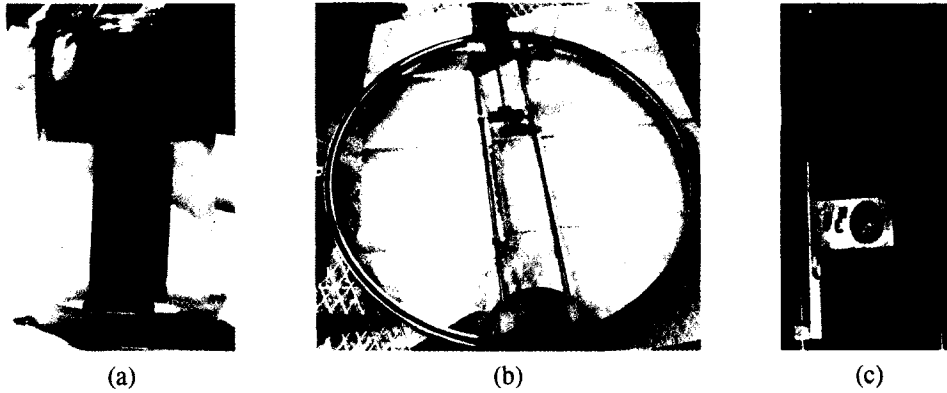
Figure 4.10: Photographs of target and target ladder. (a) An enriched ^{186}W thin target. (b) and (c) Target ladder and multiple targets positioned on the ladder.

Experiment description

In the present experiment, the front face of Gammasphere Ge crystals was fitted with 0.02" thick Ta and Cu absorbers to attenuate low energy photons and atomic x-rays. A total of 10 parallel plate avalanche counters (PPACs) were arranged in five co-plannar pairs in the forward hemisphere. The multi-parameter Gammapshere and CHICO2 data were collected event-by-event and saved in external hard drives. The acquisition master trigger required that at least one prompt γ-ray was detected in Gammasphere, together with two, co-planar binary fragments in CHICO2. Typical beam currents were approximately 0.25 pnA. For a rate of $\approx$ 1.5 kHz per CHICO2 PPAC and $\approx$ 1 kHz per Ge detector in Gammasphere, $\approx$ 6 GB of data were collected per hour. Analysis techniques used to extract the nuclear structure information from the raw data are discussed in the next chapter.

Chapter 5

Analysis of the GAMMASPHERE-CHICO2 Data

The data reduction of γ-ray spectroscopy experiments prior to physics interpretation involves the sorting of raw events into histograms, and analysis of the γ-ray coincidences. Raw events stored on disk were sorted for useful information using the DGSSort program [53] in combination with the CERN ROOT package [54]. In this chapter, a description of the data reduction techniques will be given. In particular, the procedures to calibrate the detectors, the kinematic reconstruction of binary-reaction events and Doppler correction techniques for the γ-rays emitted will be discussed.

5.1 Detector Calibration

5.1.1 Gammasphere calibration

Energy calibration

In order to extract energies and relative intensities of the γ-ray transitions, the response of the Ge detectors need to be calibrated. Calibration data were taken both at the beginning and end of the experiment, with γ ray sources (^{152}Eu and ^{243}Am) placed at the target position inside the reaction chamber of CHICO2. A detailed list of energies and intensities of γ-rays in those standard sources can be found in [55][56]. All the calibration events were sorted and binned into histograms by their raw pulse heights. The energy calibration, where the pulse heights from the Ge detectors were scaled such that the peaks in the histogram match the energies of the sources (known from the literature) was performed with GF3 (part of the RadWare suite of programs [57]). GF3 is used to perform least square fitting for each of the photo-peaks and these are compared with the reference values for these sources. The main goal of an energy calibration is to obtain a relationship between energy of the gamma ray and the ADC channel number.

Efficiency calibration

After the initial energy calibrations, "effit" (RadWare utility) was used to find the relative efficiency of the Gammasphere array as function of energy. The data

points from these measurements were fitted to a function:

$$\varepsilon = \exp\langle[(A + Bx + Cx^2)^{-G} + (D + Ey + Fy^2)^{-G}]^{-1/G}\rangle, \qquad (5.1)$$

where

$$x = \log\left(\frac{E_\gamma}{E_1}\right), \qquad (5.2)$$

and

$$y = \log\left(\frac{E_\gamma}{E_2}\right); \qquad (5.3)$$

E_γ is the γ-ray energy in keV; constants E_1 and E_2 are 100 keV and 1 MeV, respectively; parameters A, B, C fit the efficiency at low energies ($E_\gamma < 200$ keV) and D, E, F at high energies ($E_\gamma > 200$ keV); and the G is the parameter that fits the turnover between high and low energy regions.

Fig. 5.1 shows an efficiency curve obtained for the Gammasphere array in combination with CHICO2, with a maximum efficiency in the gamma ray energy region of 200 - 225 keV, which decreases in the low and high energy regions. The values of the parameters A through G in this fit are 5.246(22), 2.75(10), 0, 4.826(5), -0.589(15), -0.040(15) and 11.0(0), respectively. The γ-ray peak areas can then be corrected for this energy-dependent relative efficiency to obtain true relative intensities.
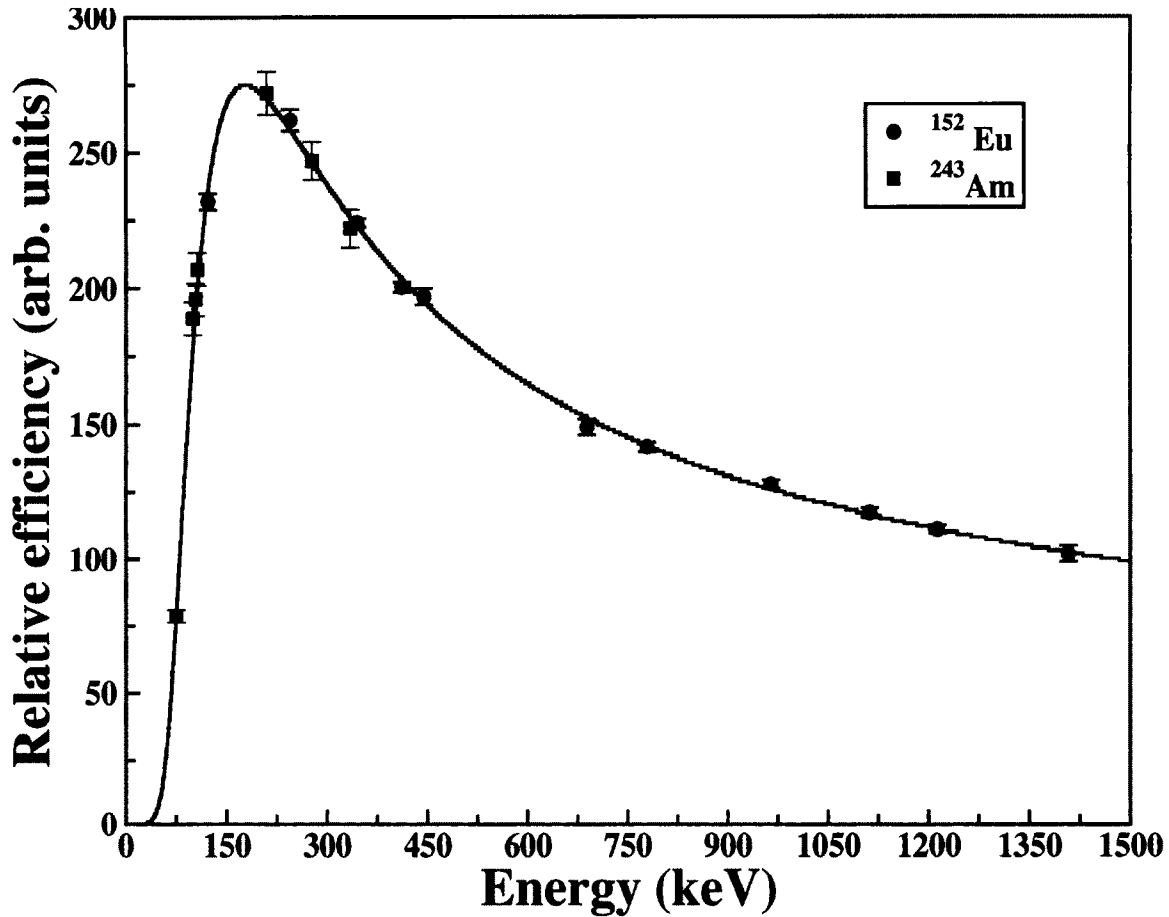
Figure 5.1: A relative efficiency curve for Gammasphere with CHICO2, where data points corresponds to [152]Eu and [243]Am sources.

5.1.2 CHICO2 calibration

The geometry and working of the cathode and anode plates for CHICO2 were discussed in Section 4.3.2. The PPACs of CHICO2 provide signals proportional to (a) time of ion arrival (inferred form the anode pulse) and (b) the (x, y) hit position on the PPAC (inferred from signals arriving at each end of a cathode delay line readout). These parameters can be mapped from t_{anode}, $t_{cathode, left}$,

$t_{cathode, right}$, $t_{cathode, up}$ and $t_{cathode, down}$ onto time (t) and azimuthal and polar angles of scattering (ϕ, θ) for the projectile-like and target-like particles.

When the raw data are histogrammed two calibration features can be seen: the end of the detector ($\theta = 18°$) and the pressure window support rib (59°). In order to apply the correct calibration to a cathode spectrum, two channel numbers corresponding to $\theta = 18°$ and 59° are written in a file, and the coefficients a and b are determined by solving the simultaneous equations for the two angles,

$$\theta° = a * channel\ number + b \tag{5.4}$$

The calibrated cathode spectrum is shown in Fig. 5.2. Here, a third feature at θ = 36° is seen, which corresponds to the scattering angle of xenon nuclei, when tungsten nuclei are blocked at 59° in the opposite PPAC.
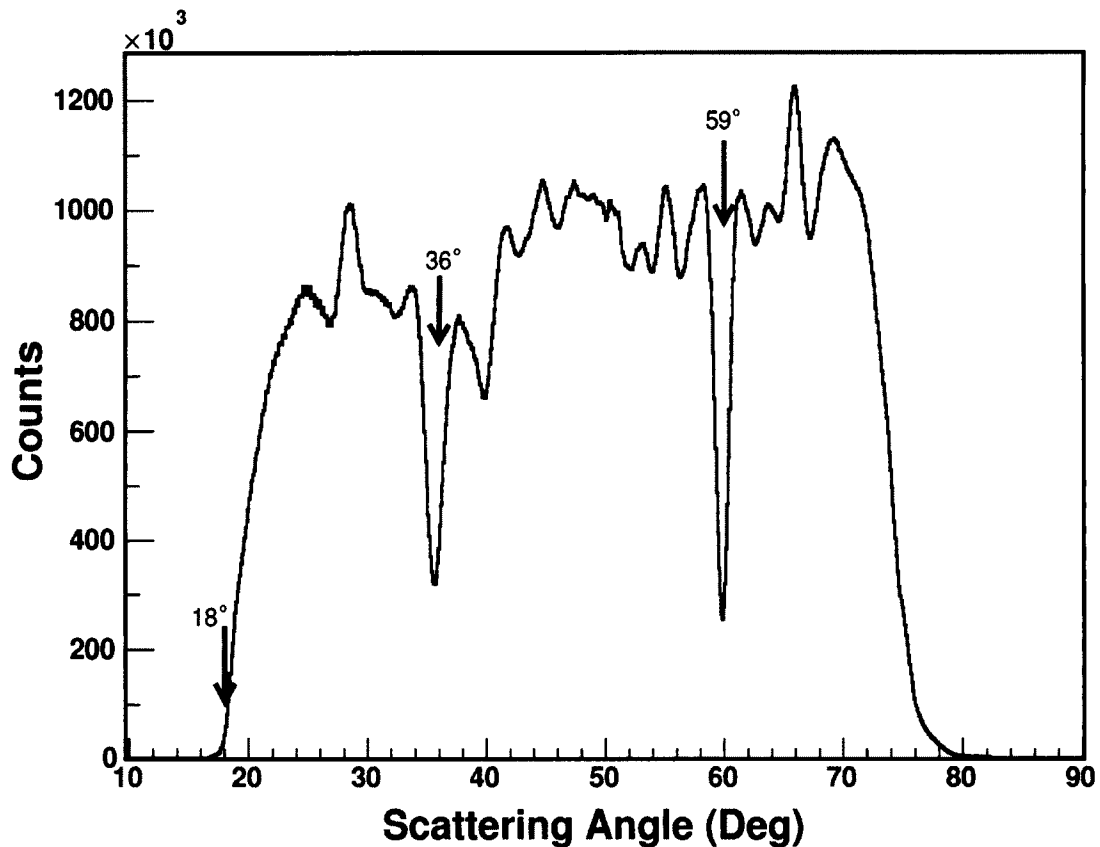
Figure 5.2: Calibrated recoil position spectrum generated from the signals detected in the cathode board of a CHICO2 PPAC.

5.2 Data Reduction and Off-line Analysis

5.2.1 Particle Identification

The first step in understanding each scattering event is to identify the gamma rays with their correct fragment type, i.e projectile-like-fragments (PLF) or target-like-fragments (TLF). For a binary reaction, conservation of momentum can be used to differentiate the two, by selecting the appropriate regions in the direct

59

measurement of time-of-flight difference (Δt) and scattering angle θ, as shown in Fig. 5.3.
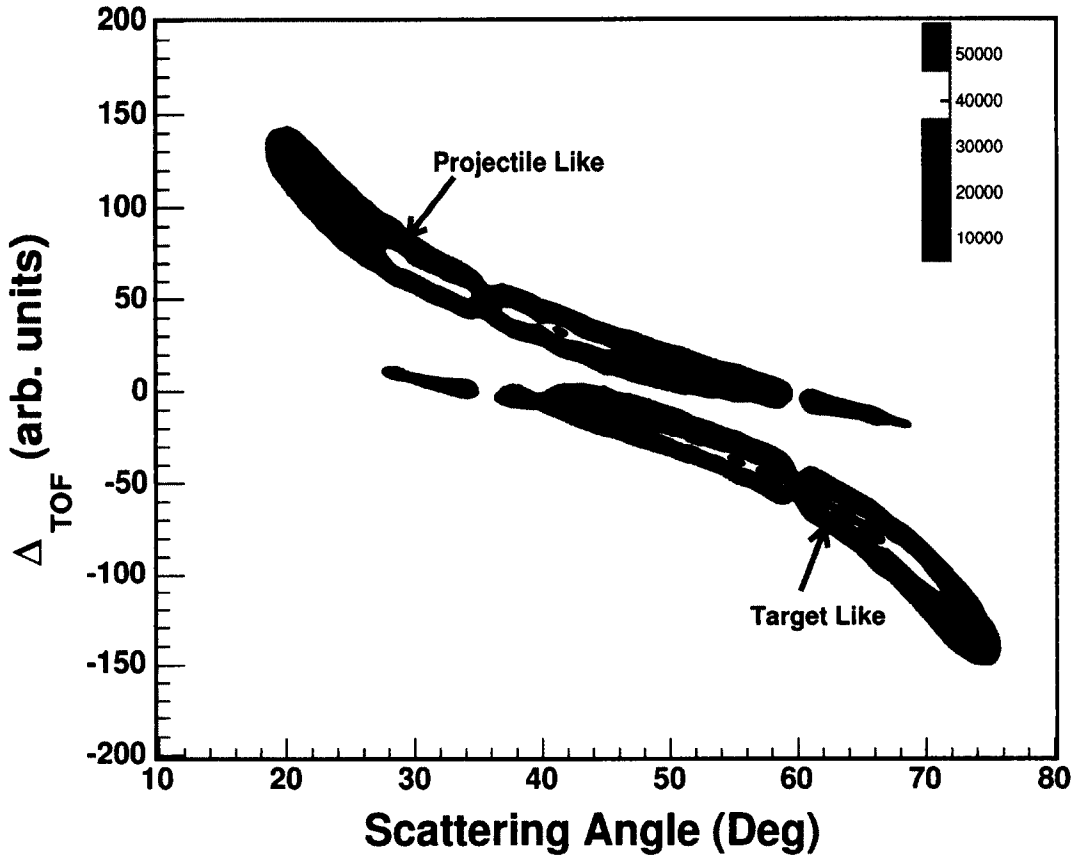
Figure 5.3: The time-of-flight difference between projectile-like-fragment and target-like-fragment vs. θ histogram with a lower limit at 10000 counts for clarity. The gap at $\theta = 59°$ is due to a support rib (see text).

Once this differentiation is made, their momenta can be defined from their scattered angular positions, again assuming two body kinematics (equation 4.2).

With this information, Δt vs. θ data was transformed into mass m vs. θ, as

$$m_1 = \frac{\Delta t + \frac{d_2}{p_2}(m_1 + m_2)}{\frac{d_1}{p_1} + \frac{d_2}{p_2}} \tag{5.5}$$

where p_i are the particle momenta and d_i are the flight distances to the PPAC planes. The flight distances from the target to the surface of the PPACs are given by

$$d(\theta, \phi) = \frac{d_{\perp}}{\cos\theta\sin\alpha + \sin\theta\cos\alpha \sin(\phi_{center})} \tag{5.6}$$

where $d_{\perp}$ is the minimum fight path from the target to the CHICO2 detector (about 13 cm), α is the polar angle of a normal to the PPAC extending through the target center, and ϕ_{center} is the azimuthal angle between the particle trajectory and the center of the PPAC. The mass transformation, as shown in Fig. 5.4, where linearized mass is plotted against scattering angle, helps in the setting of cleaner gates for particle identification.
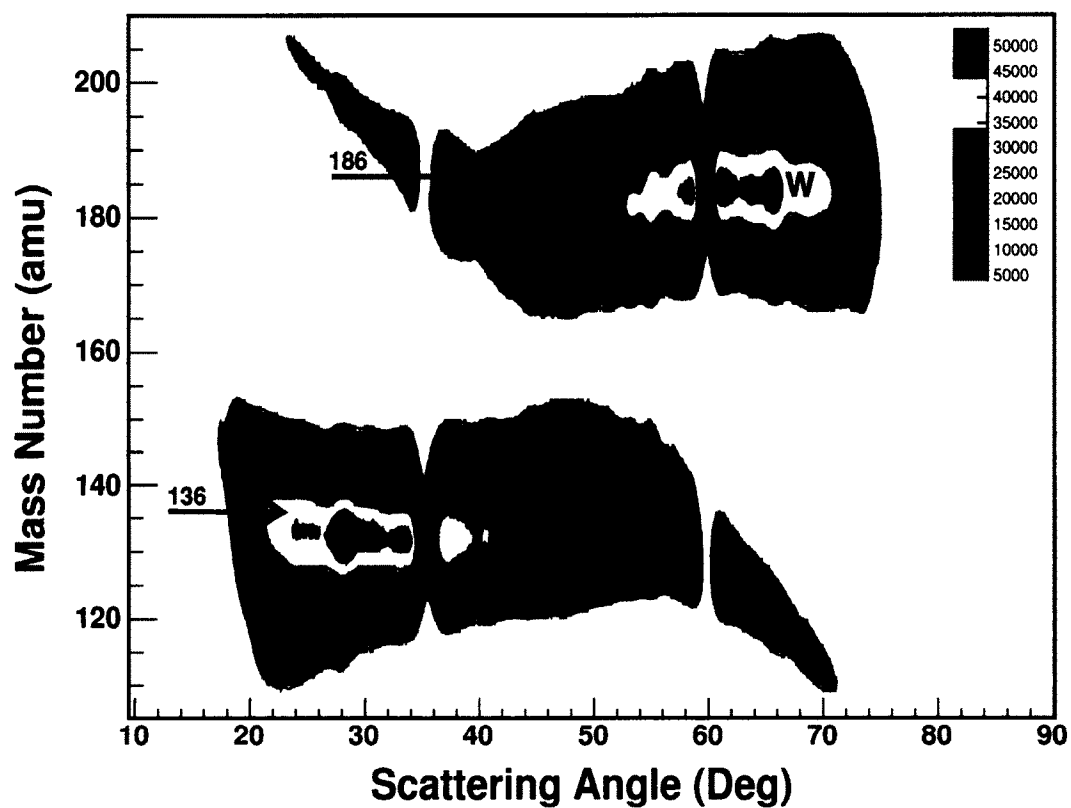
Figure 5.4: A mass (m) versus θ histogram with a lower threshold at 3000 counts for clarity.

The one dimensional projection of a 2D mass spectrum is shown in Fig. 5.5, where the Xe and W fragments are separated with a resolution of about $\approx 10\%$.
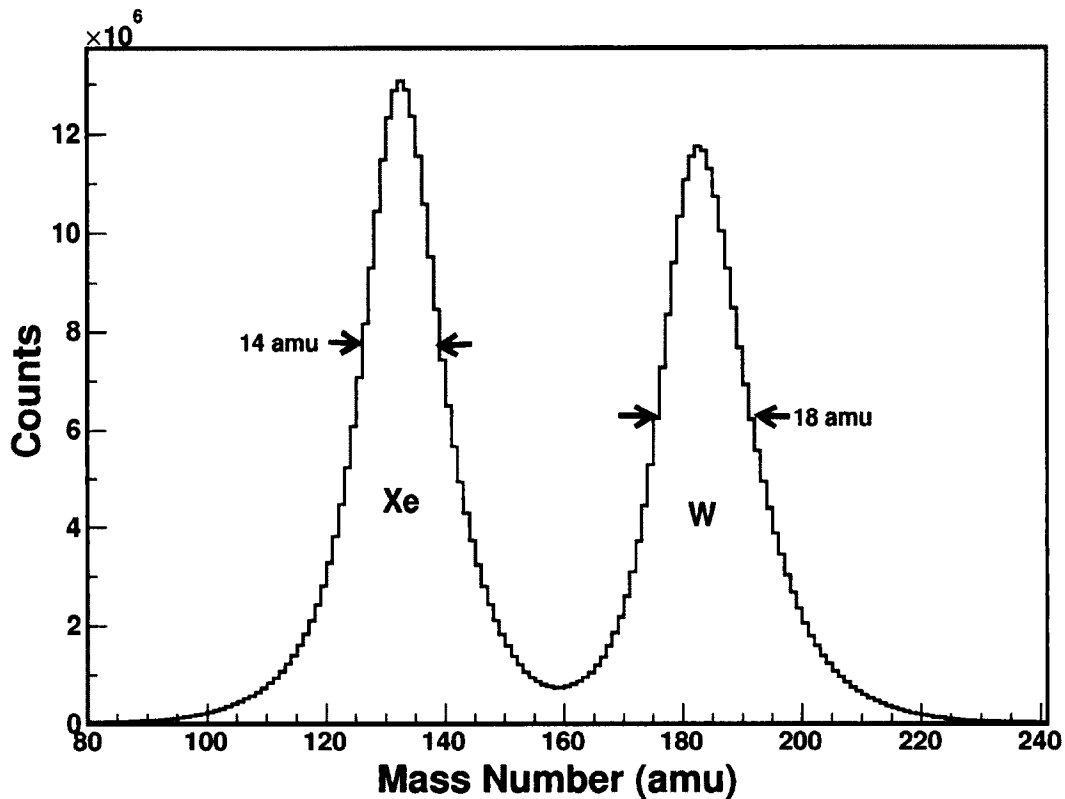
Figure 5.5: Mass resolution obtained from time-of-flight difference between projectile-like and target-like fragments.

5.2.2 Doppler Correction

In using thin targets the prompt γ-rays emitted in flight by the recoiling nuclei are significantly Doppler shifted. The maximum velocities of the binary partners in this experiment reaction are of the order of $\beta \approx 11\%$, as shown in Fig. 4.3. The prompt γ-ray energies can be Doppler corrected on an event-by-event basis using the polar angle deduced from the interaction position of the recoils, as measured by CHICO2. Assuming conservation of linear momentum for the scattered beam

and target,

$$p_{W,Xe} = \frac{p_0 \sin(\theta_{Xe,W})}{\sin(\theta_W + \theta_{Xe})}$$ (5.7)

where $p_W = m_W \beta_W c$ and $p_{Xe} = m_{Xe} \beta_{Xe} c$ are the momenta of the target nuclei and recoiling beam respectively; θ_W and θ_{Xe} are the laboratory scattering angles of the recoiling beam and target nuclei respectively and p_0 is the momentum of the incident beam. The Doppler shifted γ-rays are corrected according to,

$$E_\gamma = E_{\gamma'} \frac{1 - \beta \cos\Theta}{\sqrt{1 - \beta^2}}$$ (5.8)

where E_γ is the gamma-ray energy in the moving frame and Θ is the angle between the source vector and the detector, as shown in Fig. 5.6. The angle

$$\cos\Theta = \sin\theta_R \sin\theta_\gamma (\cos\phi_R \cos\phi_R + \sin\phi_R \sin\phi_\gamma) + \cos\theta_R \cos\theta_\gamma$$ (5.9)

where θ_R and ϕ_R are the scattering angles of the recoils (PLFs and TLFs) and θ_γ and ϕ_γ are the detection angles of the γ-rays in the Gammasphere.

64
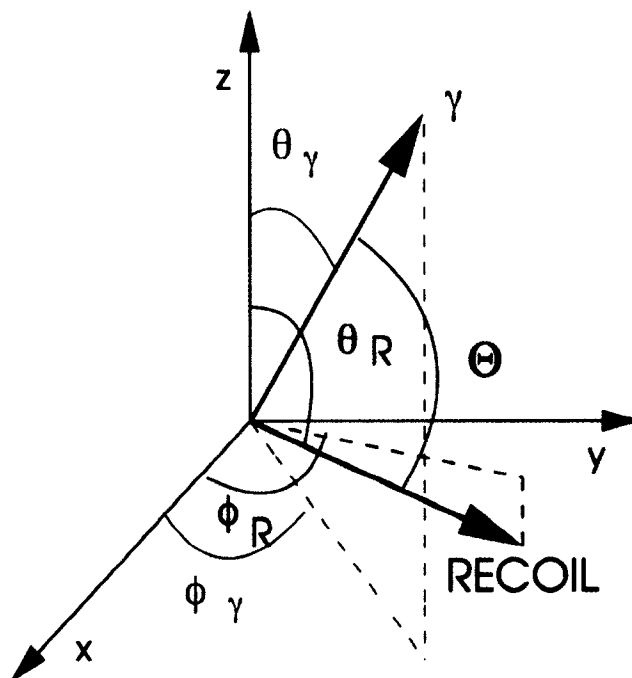
Figure 5.6: A schematic view of the reaction where the position vector and scattering angles of a recoil from the thin target along with the γ-ray it emits in flight is shown in spherical coordinates. The x-z plane is perpendicular to direction of beam, which is the along the y-axis. The opening angle between the recoil and the γ-ray trajectory, Θ, which is used in Doppler-broadening correction is also shown.

The γ-ray energies as measured in the laboratory frame can thus be Doppler corrected for the PLFs or TLFs by using their corresponding β values. Note that in each case only the γ-rays emitted by the nuclei for which the Doppler correction is made are sharper in the resulting spectrum, while those with the incorrect Doppler correction are smeared out (Fig. 5.7). This technique provides a powerful way of separating the γ-rays emitted from the PLFs and TLFs.
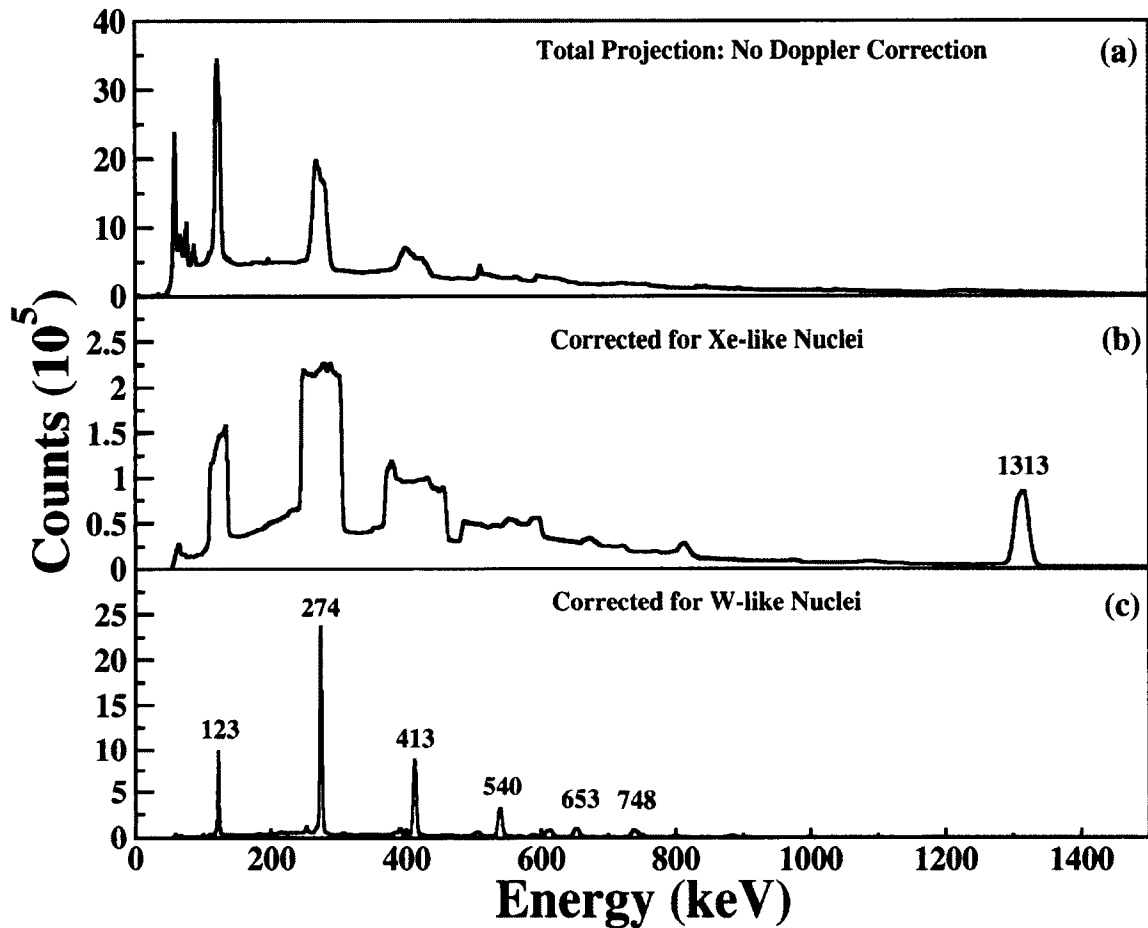
Figure 5.7: Effect of Doppler correction on spectra. Lines are sharpened when the correction for the appropriate recoiling ion is applied and broadened if the correction for the reaction partner is applied (see labeled peaks).

5.2.3 Gamma Coincidence Analysis

A nucleus can decay through many different intermediate states. Because of the multiple detectors in Gammasphere, it is possible to detect multiple γ-rays being emitted in coincidence, i.e within a specified time interval. In an ideal experiment each event should contain only γ-rays from a given decay sequence, but

realistically there are γ-rays detected from other sources. Compton scattering and time-random coincidences are the primary source of extra γ-rays.

In order to limit background contribution from events arising from time-random coincidences, a one-dimensional time-difference spectrum generated by plotting number of counts vs. the time-difference between subsequent decays is shown in Fig. 5.8. The time difference axis is presented in terms of channel number, with the conversion factor of 1 channel = 10 ns. When sorting the data into histograms, only those events within the peak were selected by defining a time cut of 25 channels on either side of the peak, resulting in a total selection of 50 channels, or an absolute time difference of 500 ns. This is to ensure inclusion of all low-energy gamma rays which typically have worse timing, as discussed further below.
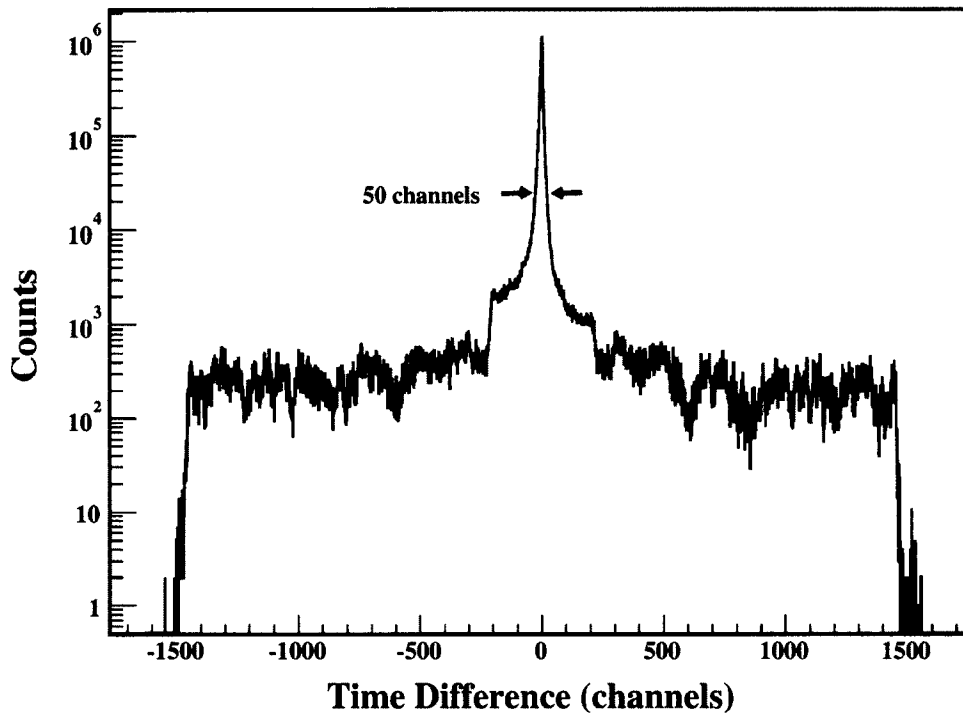
Figure 5.8: Spectrum shows the time difference between pairs of γ-rays ($t_{\gamma 1}$ - $t_{\gamma 2}$). Time calibration is 1 channel = 10 ns. Note the logarithmic scale.

Also, the time difference between the detection of a particle and a γ-ray, shown in Fig. 5.9, is used to determine whether or not they are correlated. In order to select the good events and to separate them from the random coincidences and background, a 2D matrix of the gamma ray energy versus time difference between particle and gamma was created, as shown in Fig. 5.10: the largest part of the events is concentrated in a limited region, around which an energy-dependent "sliding" time-energy coincidence window is placed. The gate was ± 25 ns wide at the high-energy end, where the FWHM of the time peak is ~ 30 ns, and ± 250 ns at the low-energy end of the spectrum. Events outside of this window can be

attributed to the correlation of a γ-ray with an scattered particle from a different collision to the one which caused the excitation.
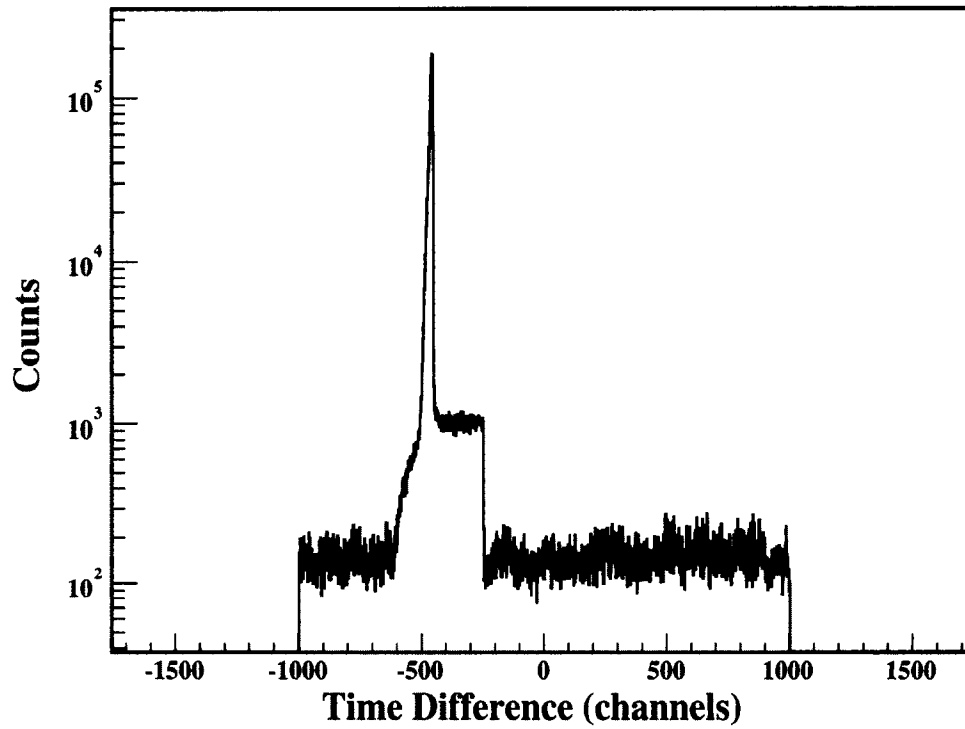
Figure 5.9: Spectrum of the particle-γ time difference ($t_{particle}$ - t_γ). Time calibration is 1 channel = 10 ns. Note the logarithmic scale.

2000

1500

1000

500

0

10^5

10^4

10^3

10^2

10

1

Energy (keV)

-600   -500   -400   -300   -200

Time Difference (channels)
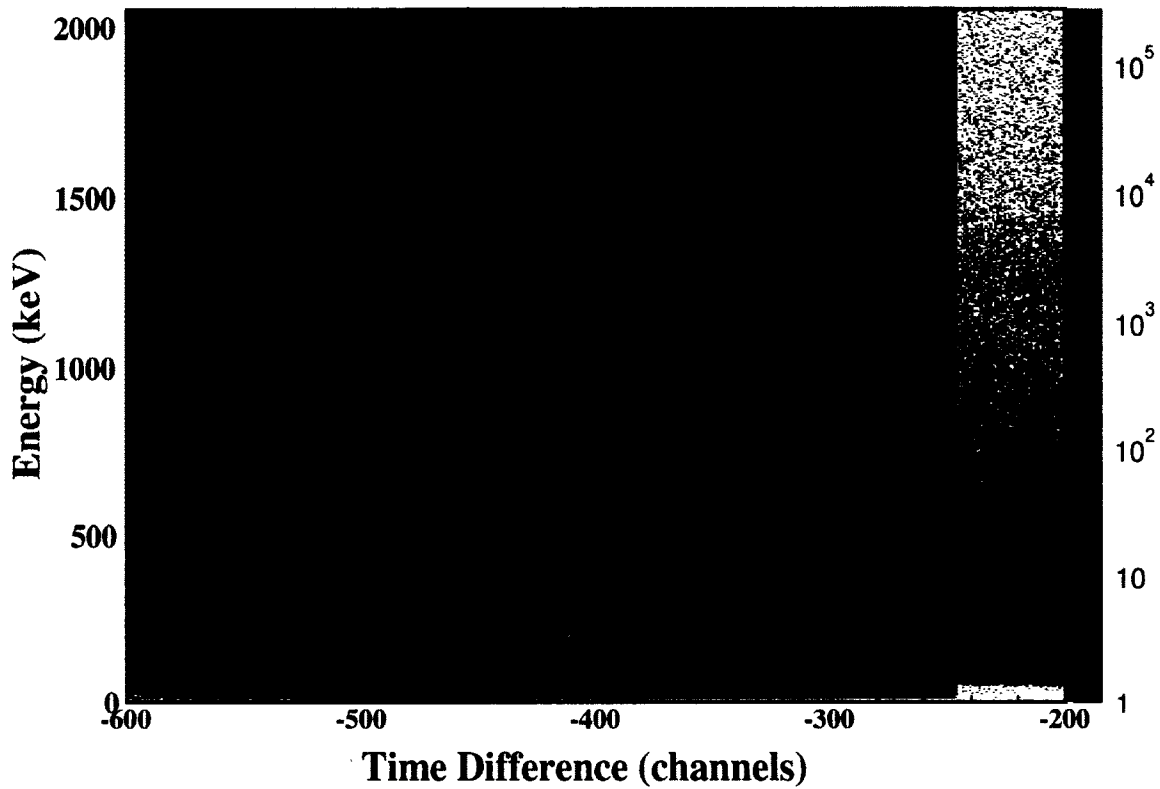
Figure 5.10: Energy versus particle-gamma time-difference matrix for the detectors. The two dimensional energy-dependent "sliding" gate applied is also shown.

The techniques described above allows cleaner particle-γ and γ γ correlated events. The further analysis to determine which specific γ-ray transitions appear in coincidence with each other, is achieved by creating 2-dimensional E_γ - E_γ matrices. These matrices are made by incrementing the number of counts at position (x, y) and (y, x) for every pair of coincident γ-rays, where x and y are the γ-ray energies. Such E_γ - E_γ matrices are symmetric about x = y.

As shown in Fig. 5.11 (a), consider three γ-rays with energies $E_{\gamma 1}$, $E_{\gamma 2}$ and $E_{\gamma 3}$, detected in coincidence with a single particle detected. The E_γ-E_γ matrix

70

would then be incremented at $(E_{\gamma 1}, E_{\gamma 2})$, $(E_{\gamma 2}, E_{\gamma 1})$, $(E_{\gamma 1}, E_{\gamma 3})$, $(E_{\gamma 3}, E_{\gamma 1})$, $(E_{\gamma 2}, E_{\gamma 3})$ and $(E_{\gamma 3}, E_{\gamma 2})$. This procedure is repeated for the each particle detected. Once all particles have been considered, it is possible to establish which γ-rays are coincident by placing energy 'gate' in one of the dimensions, say x, on the completed matrix.

Fig. 5.11 (b) shows the ideal spectra resulting from gates for sample level scheme is shown in (a). As shown, If the gate contains a photopeak at energy E_γ, projecting the contents of the energy gate onto the y axis results in a 1-dimensional spectrum showing the number of events coincident with E_γ over all γ-ray energies. Hence, gating E_γ-E_γ matrices creates a spectrum containing the γ-rays which are in coincidence with the transition chosen to be gate.
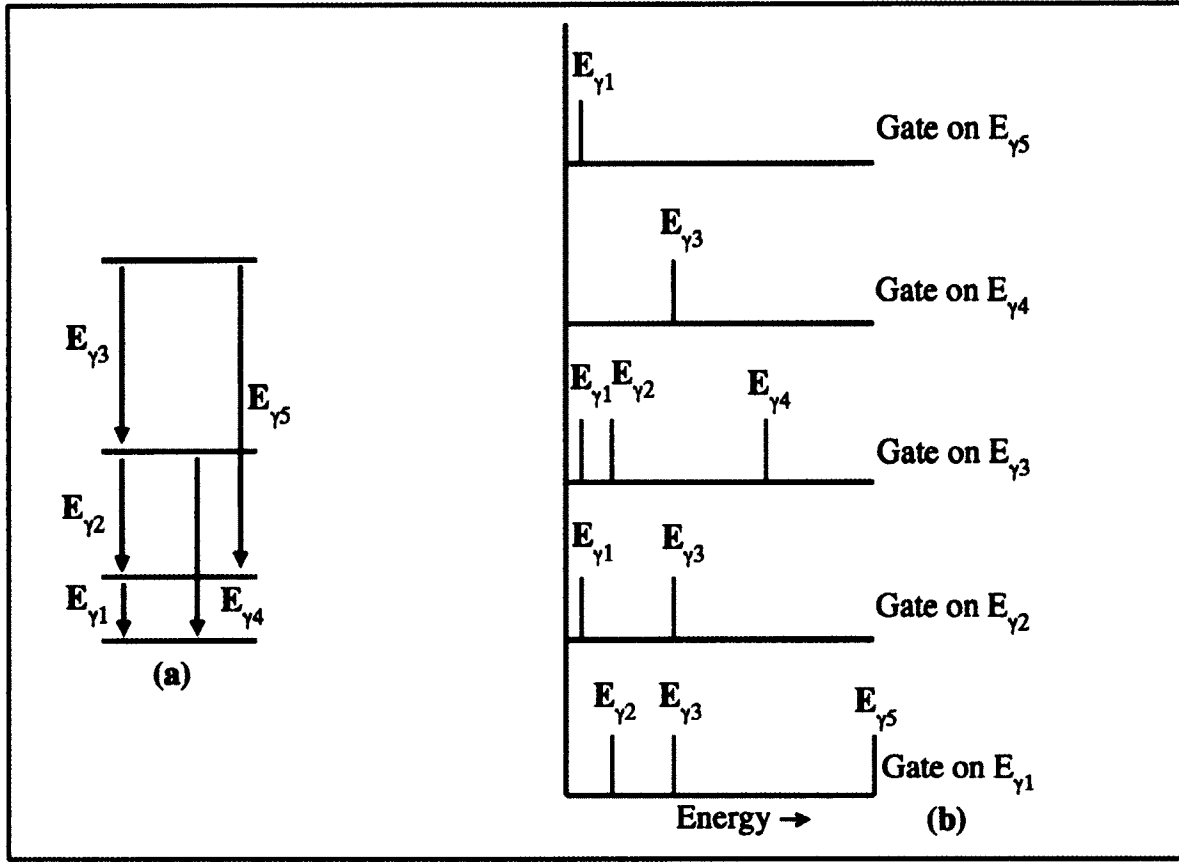
Figure 5.11: Schematic of (a) a sample level scheme and (b) spectra that result from various gates of a coincidence matrix.

The 2D gamma-gamma matrices generally consists of a high background level due to doublets or some residual contamination from other reaction channels. This issue can be overcome by creating a 3-dimensional energy histogram, namely E_γ-E_γ-E_γ cube. In a cube, the gated spectrum contains the coincidence events with two γ-ray transitions which are also in coincidence with each other. In reference to Fig. 5.11 (a), a "double gate" of $E_{\gamma 1}$ and $E_{\gamma 2}$ would result in projection showing $E_{\gamma 3}$ only. Although the triple coincidences in a γ-γ-γ cube contain significantly

lower statistics compared to double coincidences in a γ-γ matrix, they result in a cleaner analysis. A set of RADWARE programs [58]: *Escl8r* and *Levit8r* for inspecting matrices and cubes, respectively, and *xmgls* for building level scheme were used.

To obtain accurate γ-ray peak yields resulting from inelastic excitation Gammasphere and CHICO2 calibrations, Doppler correction files, a number of time difference conditions and gates were applied to the collected raw data while sorting.

5.2.4 Q-value of the Reaction

Assuming conservation of mass and energy, the Q-value of the reaction can be defined as,

$$Q = \frac{P_0^2}{2A_{beam}} - \left(\frac{P_1^2}{2A_{PLF}} + \frac{P_2^2}{2A_{TLF}} \right) \tag{5.10}$$

where A_{beam} is the mass of ^{136}Xe beam in amu, and the terms $A_{PLF,TLF}$ refer to the masses of the PLFs and TLFs, respectively. In this analysis, these masses were taken to be that of the beam and the target, since the masses of the PLF and the TLF fragments can only be determined approximately to ± 8 amu, due to a short time-of-flight for a target-to-PPAC distance of 13 cm.

Experimentally obtained Q-values are plotted against mass number in Fig. 5.12, which can be used to cleanly separate the two reaction partners. When the Q-value

is plotted against the scattering angle, it allows differentiation between inelastic collisions, corresponding to a region of large energy loss, and Coulomb reaction around a minimum Q-value loss. This capability was used in this data analysis, where separate γ-γ-γ cubes for the fragments corresponding to different Q-value regions were produced by placing appropriate two-dimensional gates, as discussed in more detail in Section 6.3.1.
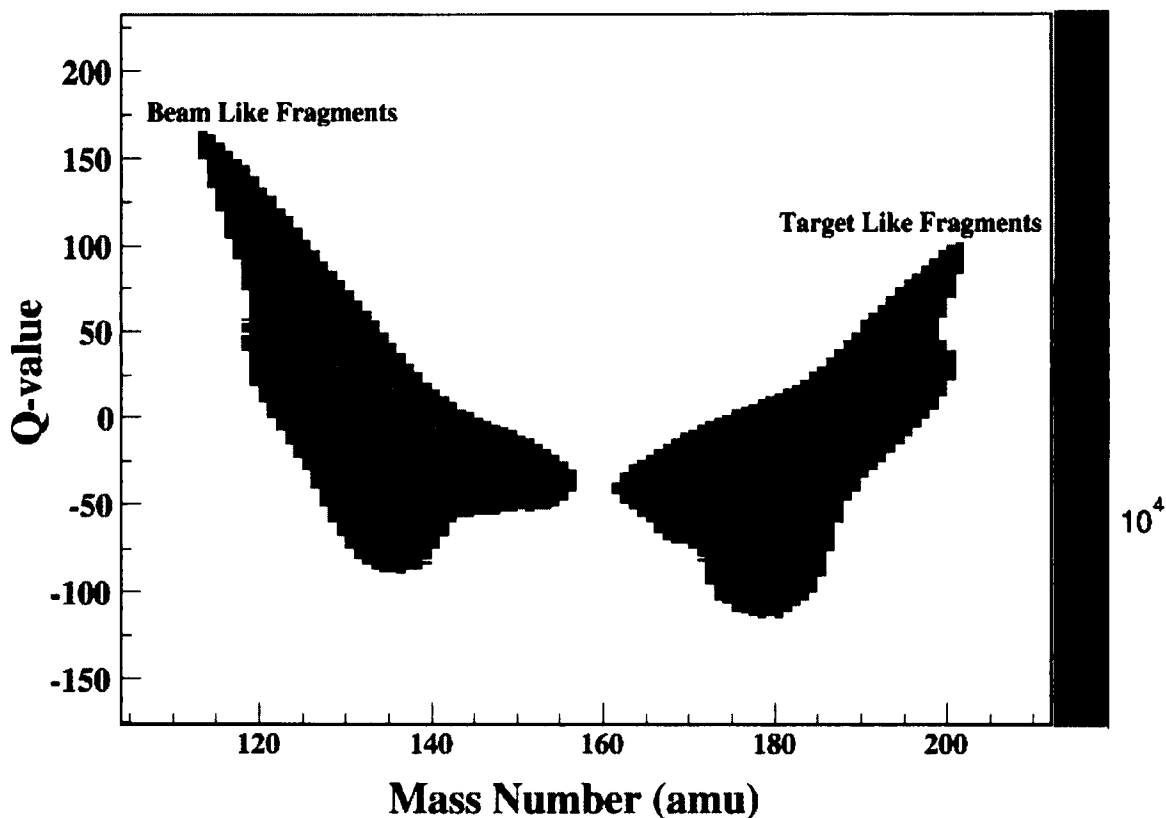
Figure 5.12: Q-value versus mass number for the two kinds of fragment.

To compare experimentally obtained yields, for events with Q-value near to

coulomb excitations, a program which is capable of computing Coulomb excitation yield, GOSIA was used [59]. This code is based on semiclassical theory of multiple Coulomb excitation, which was developed by Alder *et al.* in 1956 [60], and is a further manifestation of the first multiple Coulomb excitation computer program COULEX developed by Winther and de Boer in 1965 [61] [62]. This code was used to quantitatively calculate Coulomb excitation amplitudes using an assumed set of reduced electromagnetic matrix elements.

5.2.5 DCO ratios

A compound nucleus formed in a heavy ion fusion reaction is in a state with its angular momentum vector perpendicular to the axis of the beam direction as the angular momentum arises purely from the two body collision given a certain impact parameter. Even after the subsequent emission, the residual nucleus keeps a high degree of orientation for a long time (of the order of nanoseconds). If γ-rays are emitted from such a nucleus, the angular distribution of the relative intensities (with respect to the beam axis) depends on the multipolarity of the transitions.

The angular correlations of γ-γ coincidences depend on the spins of levels involved in these coincidence. With 4π γ-ray arrays, the information about the correlations are already available in the collected data, since the detectors are placed at various angles with respect to the beam direction. The method of directional correlations of γ-rays emitted from oriented states (DCO ratio method) was applied to establish the multipolarity of transitions [63]. In this experiment,

the measured DCO ratios were subsequently used to assign level spins and parities for the side bands in ^{186}W. The angle of a γ-ray was determined with respect to the emitting nucleus direction. Supplementary (i.e. forward and backward) angles are considered the same, since the beams are assumed to be unpolarized, and detectors insensitive to the polarization of γ-radiations.

Two angle-dependent γ-γ matrices were constructed for coincident gamma rays. One axis on each matrix was incremented by a γ-ray detected at any angle with respect to the recoiling nucleus. The second axis was incremented by a γ-ray detected at angles $0°$ - $20°$ with respect to the emitting recoils in one matrix, and those detected between $70°$ - $90°$ with respect to the emitting recoils in the other. Angle-dependent spectra were generated by gating on low-lying stretched quadrupole transitions in the ground state band on the angle-independent axis of the two matrices. Intensities, I_γ, for specific transition gamma rays were then extracted from the two angle-dependent spectra. The experimental DCO ratio R_{DCO} for a γ transition was calculated as:

$$R_{DCO(\gamma)} = \frac{I_\gamma(0° - 20°)}{I_\gamma(70° - 90°)} \qquad (5.11)$$

normalized to the average ratio for known stretched quadrupole transitions in the ground state band. With this prescription, stretched quadrupole transitions would cluster around R_{DCO} values around 1, while stretched dipoles would have $R_{DCO} <$ 0.85.

Chapter 6

Experimental Results and Interpretation

This chapter discusses the relevant aspects of neutron rich $^{182-187}$W isotopes emerging from the experimental observations and analysis of the present work, where ^{136}Xe beams of 725 and 800 MeV was used to inelastically excite ^{186}W targets. First, spectroscopic information gathered for inelastically excited ^{186}W nucleus is presented, followed by, neighboring W isotopes (^{182,183,184,185,187}W) which were populated via neutron transfer reactions. Subsequently, a discussion of the experimental results deduced from the present work in the context of previous experimental and theoretical predictions is presented, with the main focus on ^{185,186}W nuclei.

6.1 Collective Excitation in ^{186}W, Z = 74, N = 112

As discussed in section 3.3, rotational bands in ^{186}W established in prior experimental studies provide an important basis for the present work. Assignments

of new γ-rays observed in the present work to ^{186}W were based on coincidences with known ones. The final level scheme for ^{186}W deduced from this data is shown in Fig. 6.1. It consists of a ground state rotational and newly extended vibrational bands, where level placement was primarily determined using three-fold γ-ray data, as explained in section 5.2.3. A sum of double gates on the first five transitions in individual band generated from a cube was used for relative intensity measurements. The energies and relative γ-ray intensities, corrected for internal conversions and detection efficiencies, for the observed γ-rays are reported in Table: 6.1. The total internal conversion coefficients (α) for some transitions in ^{186}W are given in the Appendix (Table 12.1). Intensities were normalized to 1000 for the 123 keV $2^+ \rightarrow 0^+$ ground state band transition. Measured DCO ratios of a few key transitions are also included (Fig. 6.2 and Table 12.2 in the Appendix). Following comparison with transitions of known multipolarity, any transition with $R_{DCO} \geq 0.85$ was assigned as a quadrupole and with $R_{DCO} \leq 0.85$, as a dipole. The measured DCO ratios of the quadrupole GSB transitions range between 0.89 and 1.12.
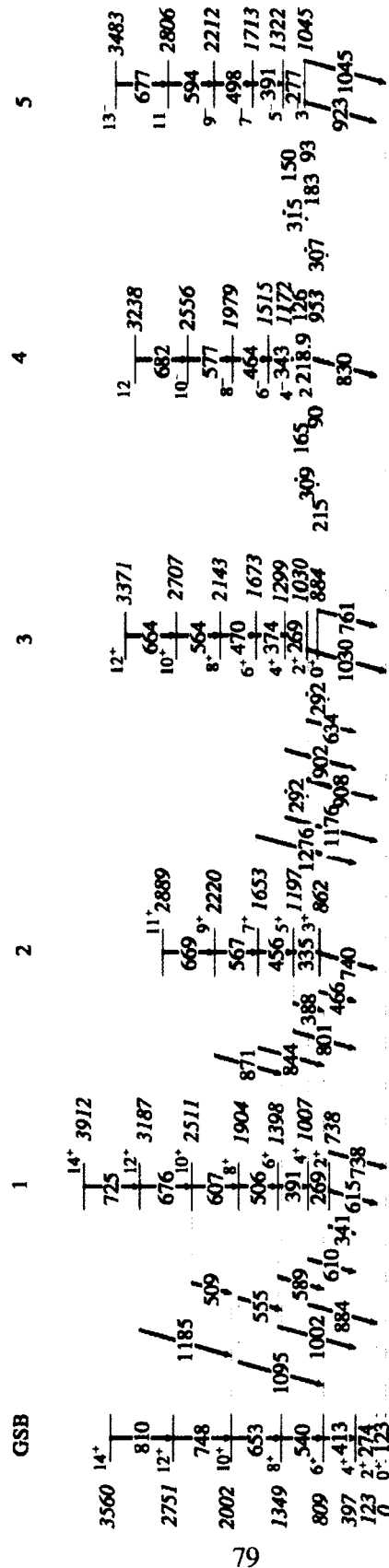
Figure 6.1: Level scheme of ^{186}W deduced from present work, showing ground state band, quasi-γ (bands 1 & 2), quasi-β (band 3) and octupole (band 4 & 5) vibrational bands.

Table 6.1: Tabulated are level energies, initial and final states, gamma-ray energy and its intensity observed in ^{186}W. Measured DCO ratio of a few specific transitions are included. Uncertainties in the transition energies are $\sim \pm 0.3$ keV.

E_γ (keV)	Band$_i$ → Band$_f$	E_i (keV)	I_i^π → I_f^π	I_γ	R_{DCO}
90.5	4 → 2	952.7	2^- → 3^+		
92.7	5 → 4	1045.4	3^- → 2^-		
122.6	GSB → GSB	122.6	2^+ → 0^+	1000(11)	0.916(4)
126.2	4 → 5	1171.6	4^- → 3^-		
146.6	3 → GSB	1030.2	2^+ → 0^+		
150.5	5 → 4	1322.1	5^- → 4^-		
164.9	4 → 1	1171.6	4^- → 4^+		
183.1	5 → 1	1045.4	3^- → 3^+		
214.8	4 → 1	952.7	2^- → 2^+		
218.9	4 → 4	1171.6	4^- → 2^-		
268.7	3 → GSB	1298.9	4^+ → 2^+		
268.8	1 → 1	1006.7	4^+ → 2^+	0.68(6)	
273.9	GSB → GSB	396.6	4^+ → 2^+	489(5)	0.893(4)
276.7	5 → 5	1322.1	5^- → 3^-		
292.2	3 → 1	1298.9	4^+ → 4^+		
292.3	3 → 1	1030.2	2^+ → 2^+		
307.4	5 → 1	1045.4	3^- → 2^+		
309.4	4 → 2	1171.6	4^- → 3^+		0.80(7)
315.4	5 → 1	1322.1	5^- → 4^+		0.68(6)
335.0	2 → 2	1197.3	5^+ → 3^+	0.84(6)	
343.0	4 → 4	1514.6	6^- → 4^-	1.6(1)	
373.6	3 → 3	1672.5	6^+ → 4^+	1.4(1)	
388.1	2 → GSB	1197.3	5^+ → 6^+		
391.4	1 → 1	1398.1	6^+ → 4^+	4.31(15)	1.08(3)
391.4	5 → 5	1713.5	7^- → 5^-	3.26(13)	
412.7	GSB → GSB	809.3	6^+ → 4^+	678(7)	1.000(3)
455.5	2 → 2	1652.8	7^+ → 5^+	1.13(8)	
464.3	4 → 4	1978.9	8^- → 6^-	0.98(8)	
465.8	2 → GSB	862.3	3^+ → 4^+		

Table 6.1 - continued

E_γ (keV)	Band$_i \to$ Band$_f$	E_i (keV)	$I_i^\pi \to I_f^\pi$	I_γ	R_{DCO}
470.2	$3 \to 3$	2142.7	$8^+ \to 6^+$	1.34(9)	
498.4	$5 \to 5$	2211.9	$9^- \to 7^-$	3.88(15)	
506.0	$1 \to 1$	1904.2	$8^+ \to 6^+$	5.21(18)	
509.6	$1 \to$ GSB	2516.0	$10^+ \to 10^+$		
540.0	GSB $\to$ GSB	1349.2	$8^+ \to 6^+$	571(6)	1.097(5)
558.8	$1 \to$ GSB	1904.0	$8^+ \to 8^+$		
564.3	$3 \to 3$	2707.0	$10^+ \to 8^+$	1.34(9)	
567.2	$2 \to 2$	2220.0	$9^+ \to 7^+$	0.92(7)	1.10(7)
576.7	$4 \to 4$	2555.6	$10^- \to 8^-$		
588.8	$1 \to$ GSB	1398.1	$6^+ \to 6^+$		
594.4	$5 \to 5$	2806.3	$11^- \to 9^-$	12.7(3)	
607.0	$1 \to 1$	2511.2	$10^+ \to 8^+$	19.04(43)	
610.2	$1 \to$ GSB	1006.7	$4^+ \to 4^+$		
615.4	$1 \to$ GSB	738.0	$2^+ \to 2^+$		
633.7	$3 \to$ GSB	1030.2	$2^+ \to 4^+$		
653.2	GSB $\to$ GSB	2002.4	$10^+ \to 8^+$	239(3)	1.124(24)
660.0	$3 \to 3$	3367.0	$12^+ \to 10^+$	0.77(7)	
667.1	$2 \to 2$	2887.1	$11^+ \to 9^+$	0.38(5)	
676.7	$5 \to 5$	3483.0	$13^- \to 11^-$	1.80(12)	
677.0	$1 \to 1$	3193.0	$12^+ \to 10^+$		
681.9	$4 \to 4$	3237.5	$12^- \to 10^-$		
725.0	$1 \to 1$	3912.2	$14^+ \to 12^+$		
737.0	$1 \to$ GSB	737.0	$2^+ \to 0^+$	1.45(10)	
739.7	$2 \to$ GSB	862.3	$3^+ \to 2^+$	1.52(11)	0.641(19)
748.5	GSB $\to$ GSB	2750.9	$12^+ \to 10^+$	69(1)	1.124(21)
761.0	$3 \to$ GSB	883.6	$0^+ \to 2^+$		
800.8	$2 \to$ GSB	1197.3	$5^+ \to 4^+$		0.641(13)
810.0	GSB $\to$ GSB	3560.9	$14^+ \to 12^+$	0.8(1)	1.02(8)
830.1	$4 \to$ GSB	952.7	$2^- \to 2^+$		
843.6	$2 \to$ GSB	1652.8	$7^+ \to 6^+$		
870.8	$2 \to$ GSB	11349.2	$9^+ \to 8^+$		
884.1	$1 \to$ GSB	1006.7	$4^+ \to 2^+$		1.00(4)

Table 6.1 - continued

E_γ (keV)	Band$_i$ → Band$_f$	E_i (keV)	$I_i^\pi \to I_f^\pi$	I_γ	R_{DCO}
902.4	3 → GSB	1298.9	$4^+ \to 4^+$		1.02(8)
907.6	3 → GSB	1030.2	$2^+ \to 2^+$		
922.8	4 → GSB	1045.4	$3^- \to 2^+$	2.22(14)	
1001.6	1 → GSB	1398.1	$6^+ \to 4^+$		1.02(2)
1030.2	3 → GSB	1030.2	$2^+ \to 0^+$		
1045.4	4 → GSB	1045.4	$3^- \to 0^+$		
1095.0	1 → GSB	1904.0	$8^+ \to 6^+$		
1166.8	1 → GSB	2516.0	$10^+ \to 8^+$		
1176.3	3 → GSB	1298.9	$4^+ \to 2^+$	0.62(7)	
1185.6	1 → GSB	3187.2	$12^+ \to 10^+$		
1276.4	3 → GSB	1672.9	$6^+ \to 4^+$	1.20(11)	
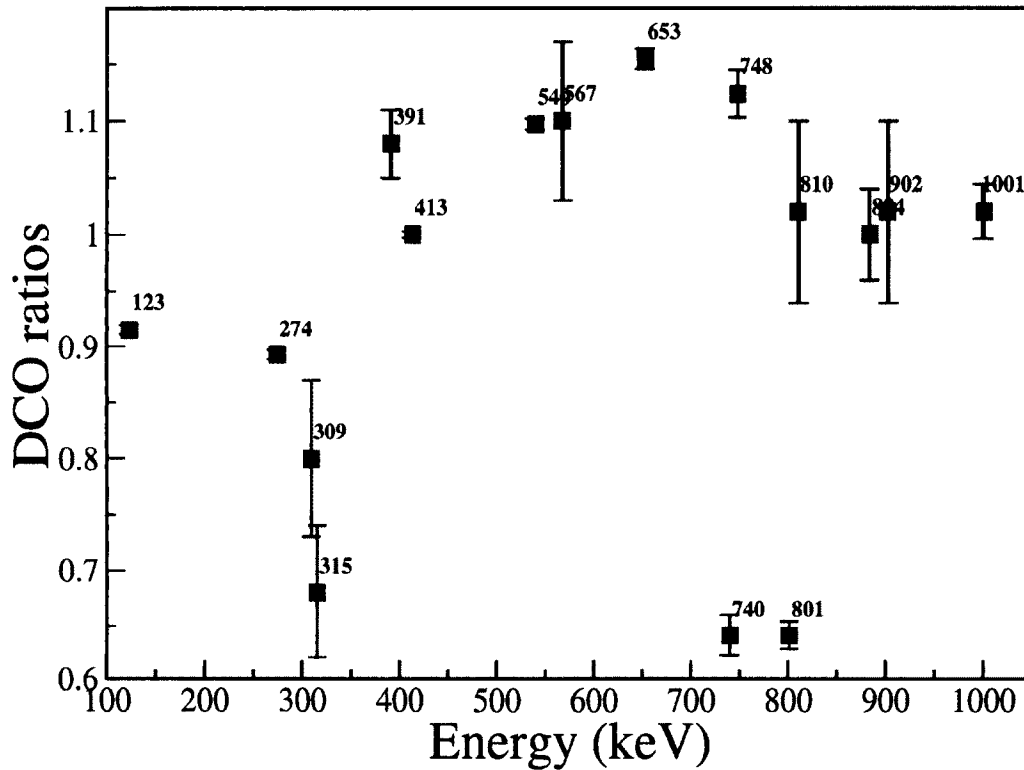
Figure 6.2: Measured DCO ratios of transitions in the decay scheme of ^{186}W.

6.1.1 The ground state rotational band (GSB)

The ground state band in ^{186}W was observed up to spin $I^\pi = 14^+$, as shown in Fig. 6.1. This is also the maximum spin observed in previous work [35]. In order to search for new higher-lying transitions in the ground state band of ^{186}W, both the data sets at 800 and 725 MeV beam energy were sorted together to make a E_γ-E_γ-E_γ cube. A triples coincidence spectrum with sum of double-gate combinations of all pairs of known transitions in ^{186}W GSB is shown in Fig. 6.3.
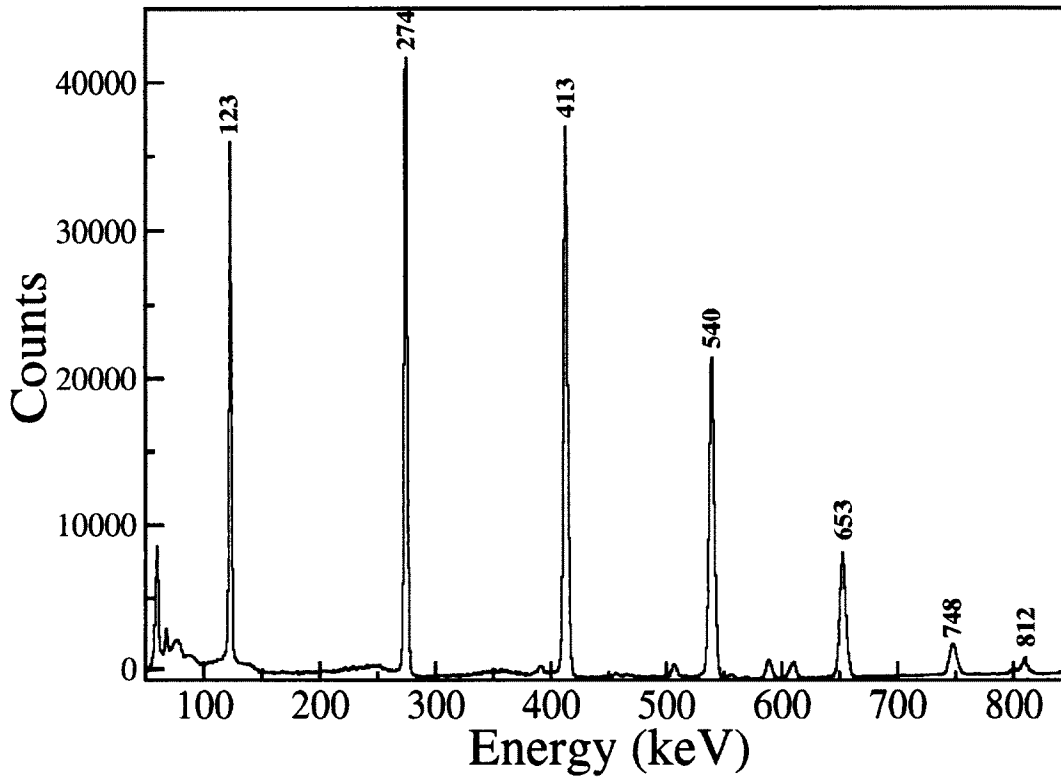
Figure 6.3: Triples coincidence spectrum with sum of double-gate combinations of all pairs of known transitions in ^{186}W GSB.

In order to cleanly look for high spin states in the GSB and avoid any contamination, a coincidence spectrum obtained by gating on 812 keV (14^+ -> 12^+), the highest transition in the GSB, is shown in Fig. 6.4. This clearly shows all of the known lower state γ-transitions in the ground state band of ^{186}W nucleus, with no new coincident gamma ray. Similarly, a coincidence spectrum is obtained by gating on the 653 keV (10^+ -> 8^+) ground-state band γ-transition. As shown in Fig. 6.5, this gate shows relatively strong 748, and 810 keV γ-transitions, but no

other clearly visible transition in coincidence.
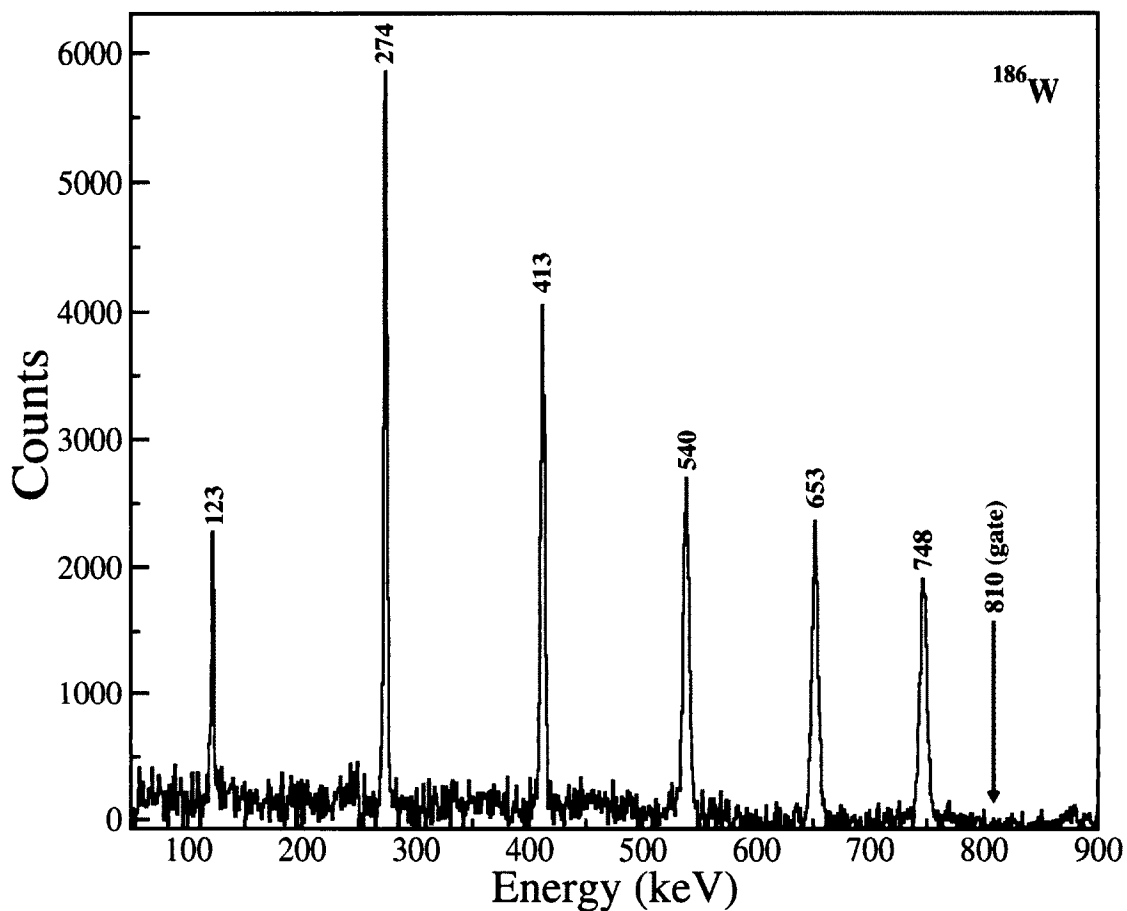
Figure 6.4: Spectrum of a single gate on the 810 keV transition in ^{186}W GSB.

With this clean gate, it can be seen that there is a sudden drop of intensity, about 20%, from the 748 keV to the 810 keV transition. This plot also highlights a marked area which was scanned for possible coincident gamma ray, if the next spin state would follow constant moment of inertia. Between the two limiting cases, the relative intensity of any peak is seen to be about 1% of that of 748 keV. Since the area under peak and hence the intensities are from a clean gate, this

comparison provide a quantitative confirmation that no higher spin transition is seen in this data.
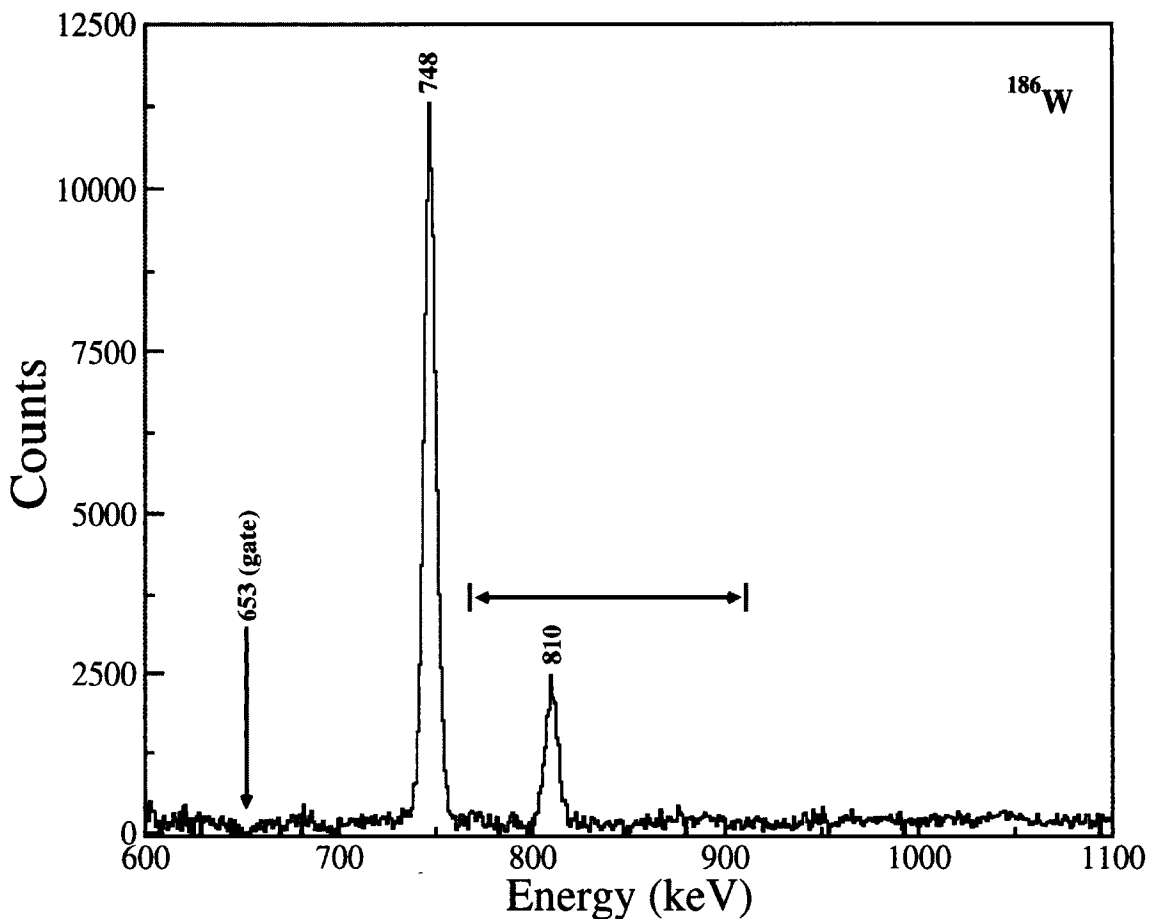
Figure 6.5: Spectrum obtained by setting a single gate on the 653 keV transition in ^{186}W GSB.

This rapid drop in the transition intensities, which prevented the observation of any higher-lying excited state, is also shown in Fig. 6.6,
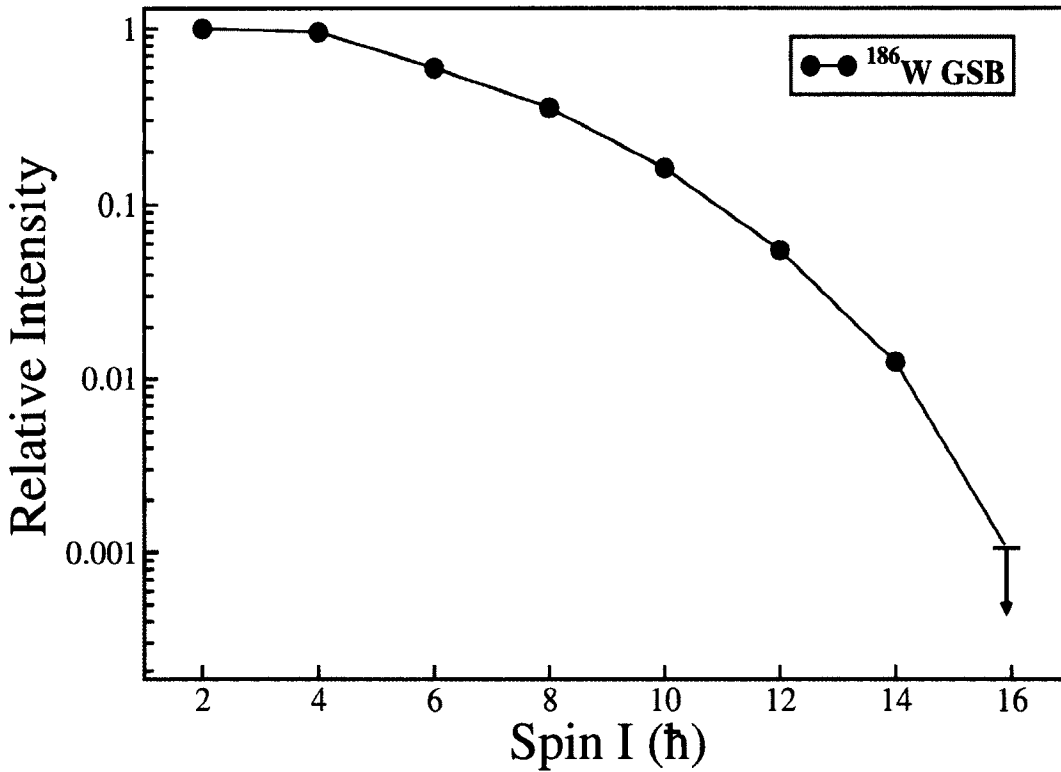
Figure 6.6: Relative transition intensities in the ^{186}W GSB. The last point corresponds to an upper limit from the marked area in Fig. 6.5.

6.1.2 The quasi γ-band

As shown in Fig. 6.1, band 1 which starts at $I^\pi = 2^+$, is a positive-parity even-spin sequence, which was previously identified as a quasi γ-band [35] up to a 12^+ level. This band is confirmed in the current coincidence data (Fig. 6.7 (a)), with an additional new 725 keV transition found linking 14^+ level to 12^+.

A previously assigned state with energy level of 1908 was found to be 4 keV

lower, making $8^+ \rightarrow 6^+$ transition to be 506 keV. Also, three additional intra-band transitions of 509, 1095 and 1185 keV connecting this bands 10^+ to 10^+ of GSB, 8^+ to 6^+ of GSB and 12^+ to 10^+ of GSB, respectively, have been found in this work. The DCO ratios of the 884- and 1002-keV transitions are consistent with their stretched quadrupole assignment of 4^+ to GSB 2^+ and 6^+ to GSB 4^+, respectively.

The positive-parity odd-spin sequence, band 2 in Fig. 6.1, was known ([35, 33, 34]) up to the (5^+) level at 1197 keV. In this work, three higher transitions of 456, 567 and 669 keV were identified extending it to $I^\pi = 11^+$ state, as shown in Fig. 6.7 (b). Two additional intra-band transition of 844 and 871 keV have been identified connecting 7^+ level to 6^+ level and 9^+ level to 8^+ level of ground state band, respectively. The DCO ratios of the 740- and 801-keV transitions are consistent with their stretched dipole assignment of 3^+ to the GSB 2^+ and 5^+ to the GSB 4^+ states, respectively.
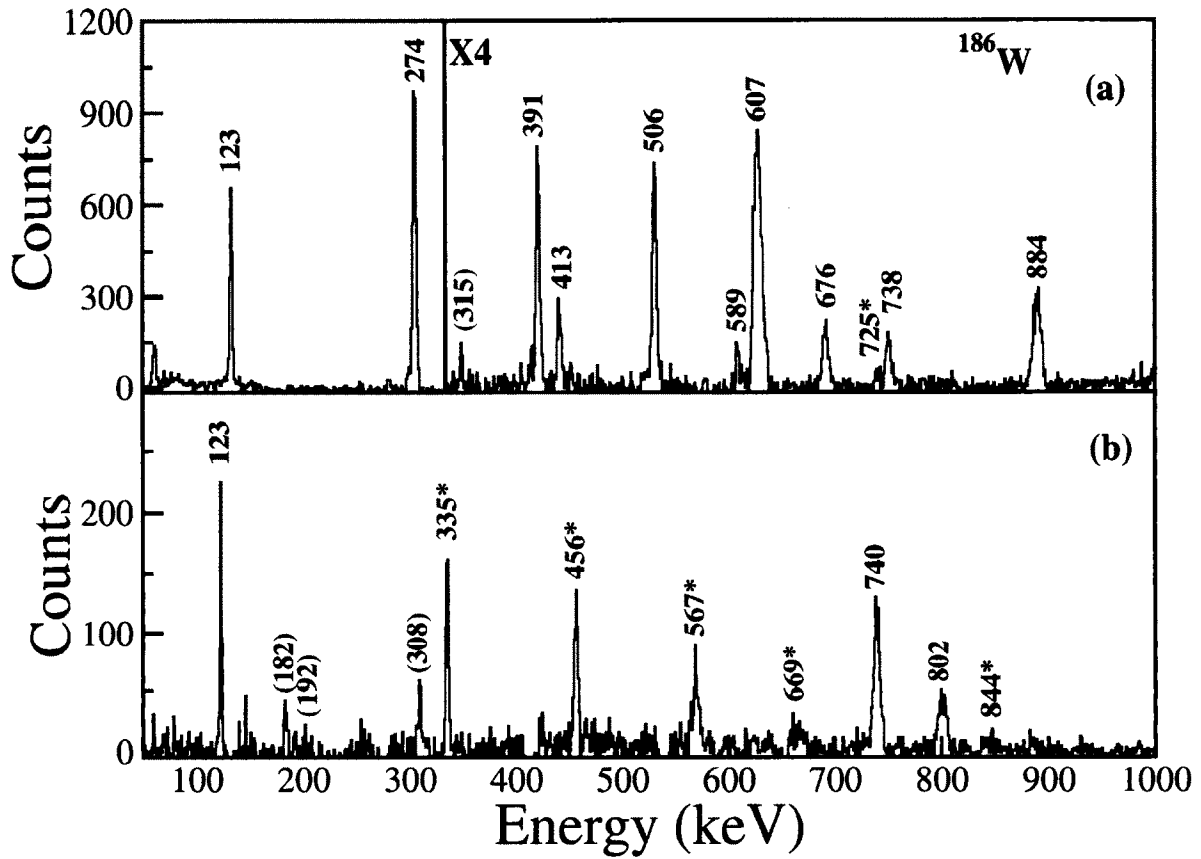
Figure 6.7: Summed coincidence spectra double-gated on transitions in band 1 and 2 of ^{186}W, is shown in (a) and (b) respectively. A combination of 391, 506 and 607 keV γ-ray energies was used for band 1, and 335, 455, 567 and 740 γ-ray energies was used for band 2. New gamma rays identified in the present work are indicated with asterisks.

6.1.3 The quasi β-band

As shown in Fig. 6.1, band 3 is built on the previously known state at 884 keV which decays to a GSB 2$^+$ state by a 761 keV transition. This band was identified

as a quasi β-band and was known up to 1299 keV (4^+) [34], which decays to the ground state band via 1176 keV (to 2^+) and 902 keV (to 4^+) transitions. Four new γ-rays of 374, 470, 564 and 664 keV are assigned to this band, which are shown in Fig. 6.8. An additional intra-band transition of 1276 keV energy is also identified as connecting 6^+ to 4^+ of the ground state band.
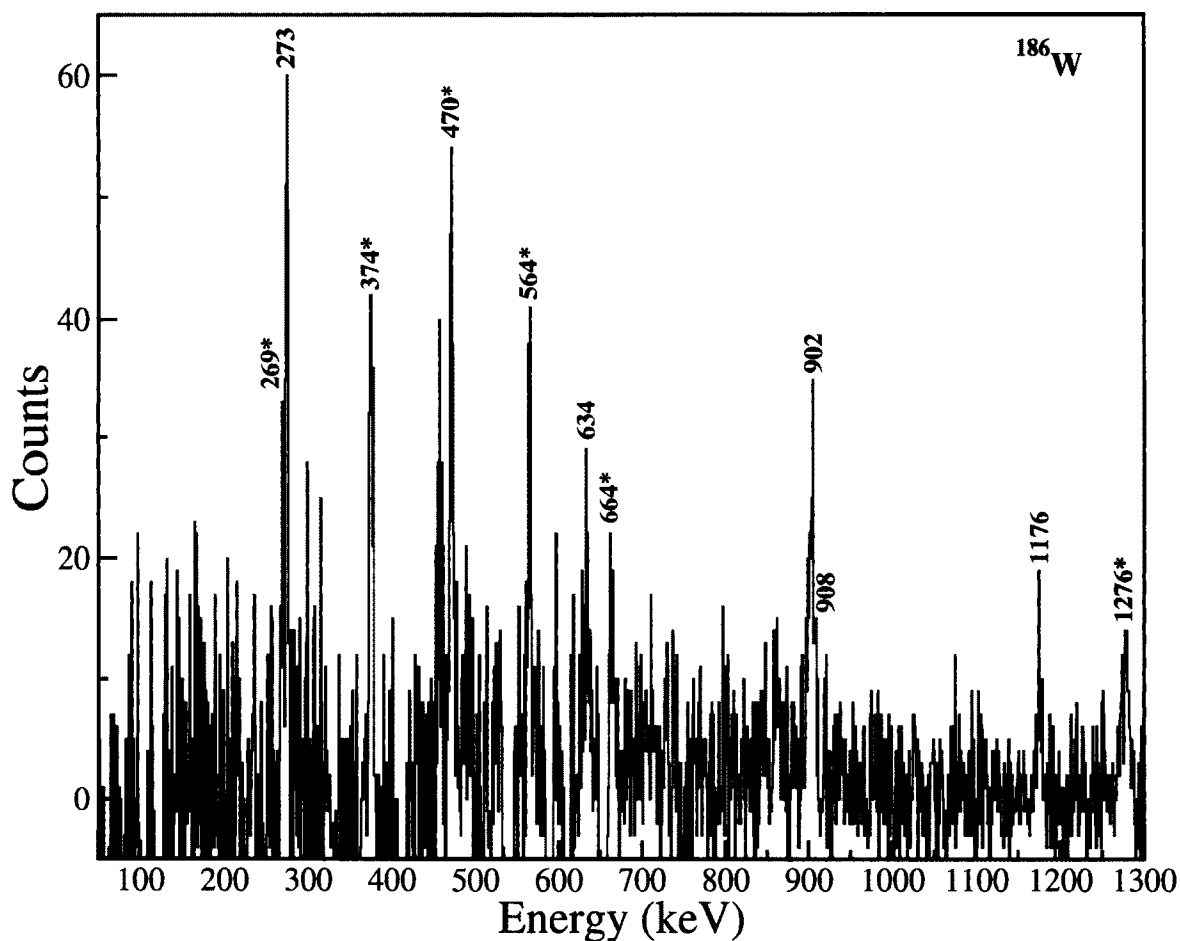
Figure 6.8: Summed coincidence spectrum double-gated on 374, 470, 564 and 902 keV transitions in band 3 of ^{186}W. New gamma rays identified in the present work are indicated with asterisks.

6.1.4 The octupole vibration band

As shown in Fig. 6.1, negative parity bands 4 and 5 were previously reported as signature partners of a $K^\pi = 2^-$, octupole-vibrational band [33]. Only the two lowest levels of each band, that is, 2^- at 953 keV and 4^- at 1172 keV for band 4, 3^- at 1045 keV and 5^- at 1322 keV for band 5, were known prior to this study. In this work, these bands have been observed up to $I^\pi = 12^-$ and 13^-, respectively. While the in-band transitions are strong, weak out-of-band transitions to the ground state band are seen from the low lying states. Representative spectra for these bands are shown in Fig. 6.9. The DCO ratios of the 315-keV transition is consistent with its stretched dipole assignment of 5^- to the 4^+ state of the gamma band.
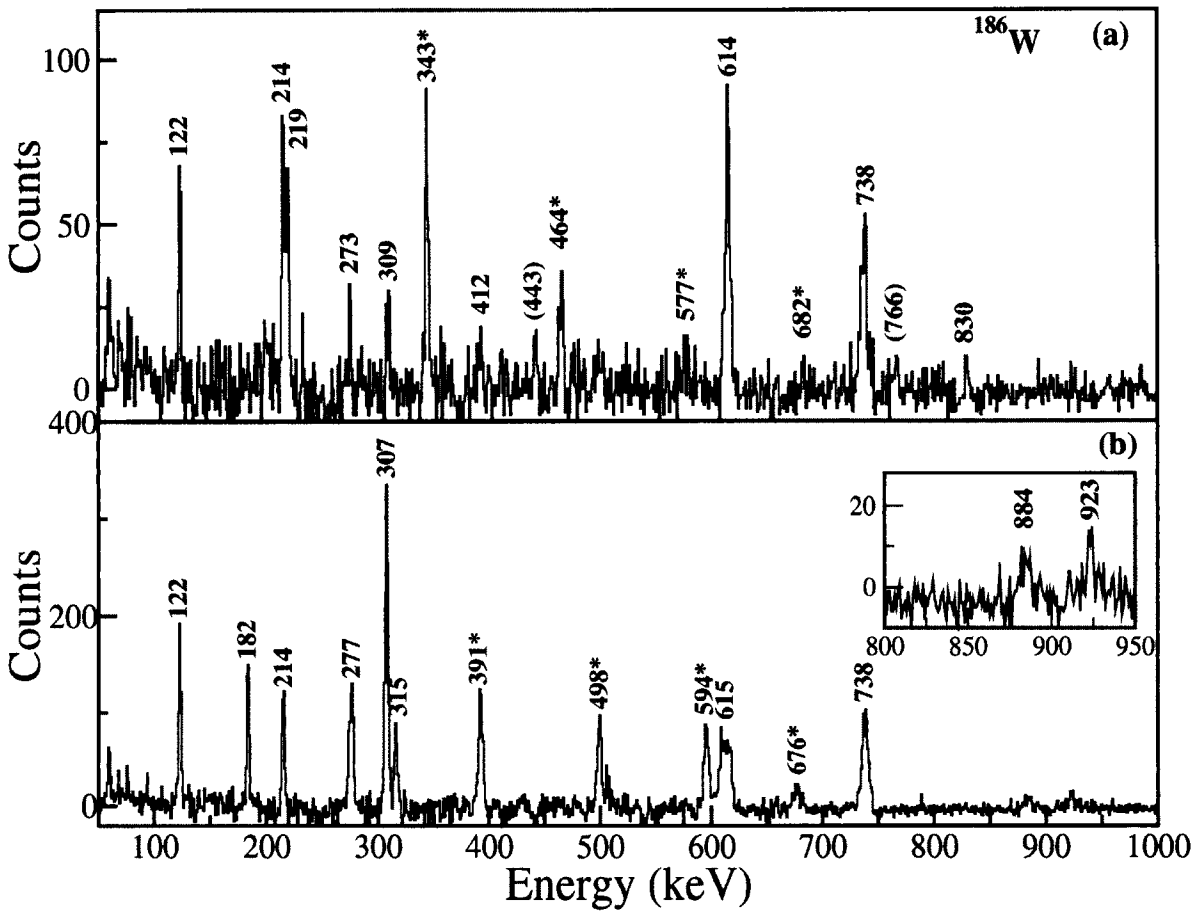
Figure 6.9: Summed coincidence spectra double-gated on transitions in (a) band 4 and (b) band 5 of ^{186}W respectively. A combination of 214, 219, 343 and 464 keV γ-ray energies was used for band 4, and 277, 391, 498, 594 and 676 γ-ray energies was used for band 5. New gamma rays identified in the present work are indicated with asterisks.

6.2 Neutron Transfer Reactions

Data analysis revealed neutron transfer reactions and production of nuclei with both more and less neutrons than the target nucleus ^{186}W. The following sections discuss structural information obtained for even-A (^{182,184}W) and odd-A

(^{183,185,187}W) tungsten isotopes, separately.

6.2.1   Ground state bands in ^{182,184}W

The ground states of even-even ^{182}W and ^{184}W nuclei have been well established in the previous studies [64] [65], up-to spin 20^+ and 16^+, respectively, as shown in Fig. 6.10. The sensitivity of the current detection setup and beam-target combination allows the observation of spins as high as 12^+ for both the 2n and 4n transfer channels, ^{182}W and ^{184}W nuclei, respectively. The spectra for ^{182}W and ^{184}W along with ^{186}W nuclei with sum of double gates in a γ-γ-γ cube for 800 MeV beam energy are shown in Fig. 6.10.

182W

20+ ——— 5428.4

738

18+ ——— 4690.7

781

16+ ——— 3909.9   184W

797   16+ ——— 4116.6

14+ ——— 3112.7   797

740   14+ ——— 3319.6

12+ ——— 2372.4   763

661   12+ ——— 2556.7

10+ ——— 1711.8   696

568   10+ ——— 1860.5

8+ ——— 1144.3   609

464   680.4   8+ ——— 1251.9

6+   504

4+ 351 329.4   6+ ——— 748.3

2+ 229 100.1   4+ 384 364.1

0+ 100   0.0   2+ 253 111.2

                             0+ 111   0.0
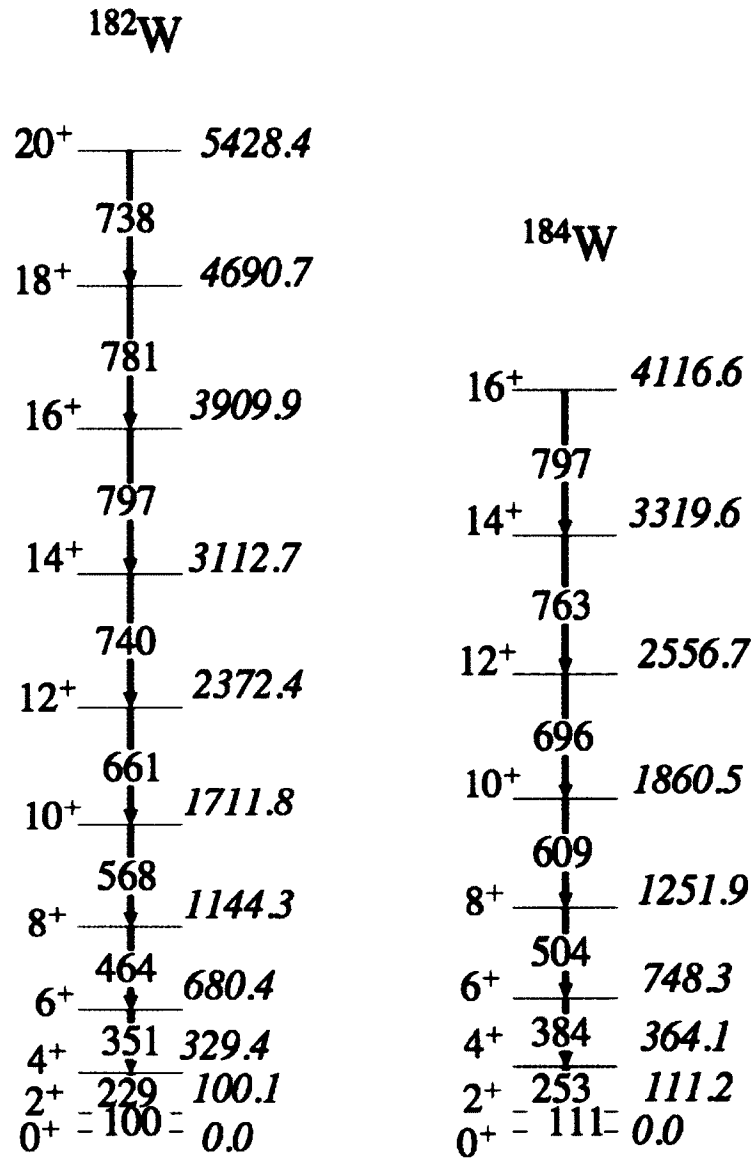
Figure 6.10: Partial level scheme of ^{182}W and ^{184}W, showing their ground state bands [64] [65].

The data allow a direct comparison of the population intensities of inelastic and transfer channels. The average counts in the bottom four transitions of each band (up to the 8^+ state) in a sum of their own double-gate combinations were compared, after correcting for efficiency and internal conversion. The 2n and 4n

transfer channels are seen to be populated at relative intensities of 2.2% and 1.1% of the inelastic channel at 800 MeV. This can be approximately verified by the peak counts in the double-gated spectra shown. The same ratios hold for the lower beam energy of 725 MeV, within statistical uncertainties.
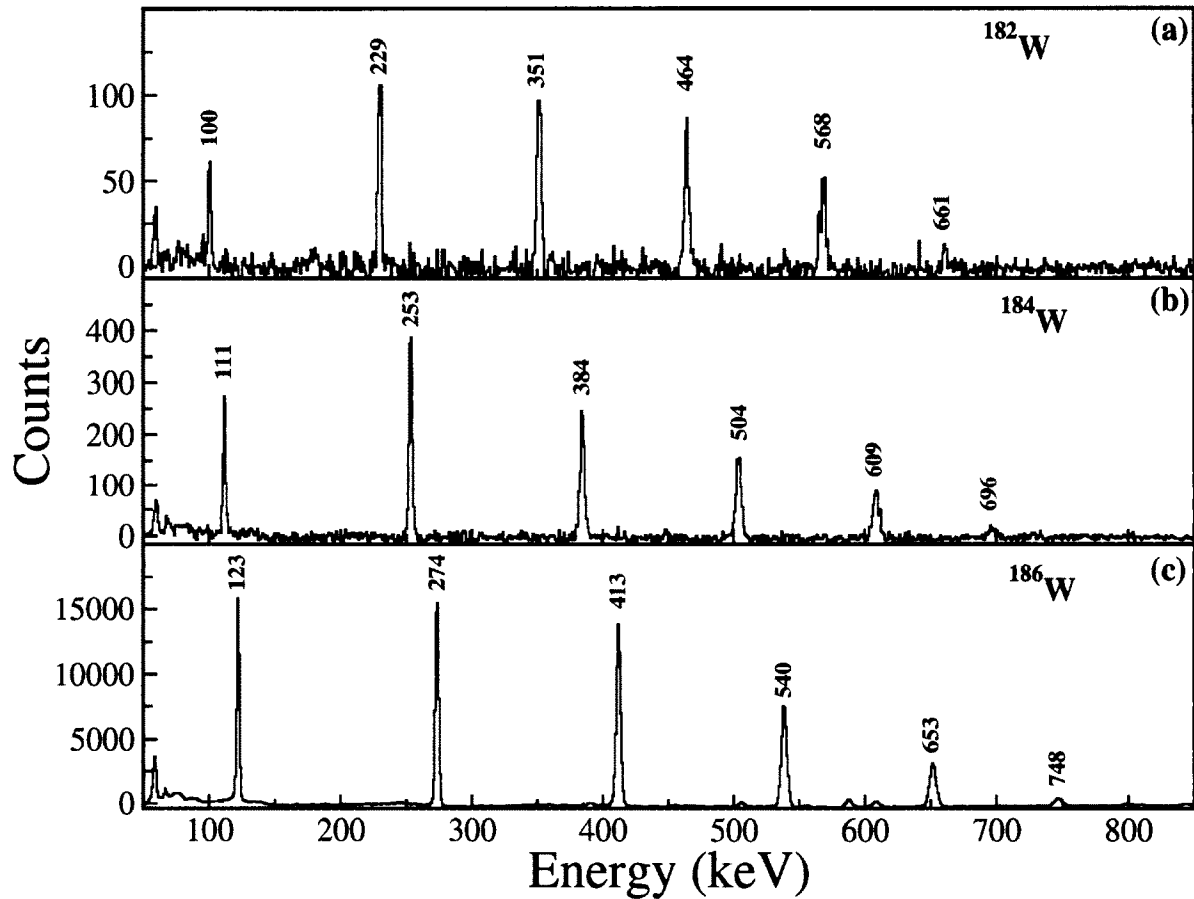
Figure 6.11: Coincidence spectra obtained by the sum of double gates of (a) the 100, 229, 351 and 464 keV transitions in the ^{182}W GSB, (b) the 111, 253, 384 and 504 keV transitions in the ^{184}W GSB, and (c) the 123, 274, 413 and 540 keV transitions in the ^{186}W GSB.

6.2.2 Ground state bands in ^{183,185,187}W

The odd-neutron transfer channels lead to odd-A nuclei, where the population intensities are typically fragmented over multiple bands. The ground state bands of 3n and 1n transfer from target to projectile are discussed, leading to ^{183}W and ^{185}W nuclei, respectively, together with the 1n transfer channel from projectile to target, leading to the ^{187}W nucleus.

Ground state band in ^{183}W, Z = 74, N = 109

In earlier work [66], the stable ground state of ^{183}W built on a $\nu 1/2^-[510]$ neutron orbital, was observed up to the $35/2^-$ state at 4043 keV. The level scheme deduced from these studies is shown in Fig. 6.12. With the current experiment, where ^{183}W was populated via 3n transfer from target to beam, states only up to $21/2^-$ at 1596 keV were cleanly observed.

35/2⁻ _____ 4043

33/2⁻ _____ 752⁻ 3707

31/2⁻ _777_____ 3291

29/2⁻ _____ 731 ─ 2930

27/2⁻ _708_____ 2560

25/2⁻ _____ 659 ─ 2222

23/2⁻ _627_____ 1901

21/2⁻ _____ 573 ─ 1596

19/2⁻ _533___ 1328
17/2⁻ ___266 _478 ─ 1062
15/2⁻ _431___ 850
13/2⁻ _219 375 ─ 631
11/2⁻ _322___ 475
9/2⁻ ___166 268 ─ 309
7/2⁻ _210 207
5/2⁻ ___108 161 99 46
3/2⁻ 1/2⁻ ___99___ 0
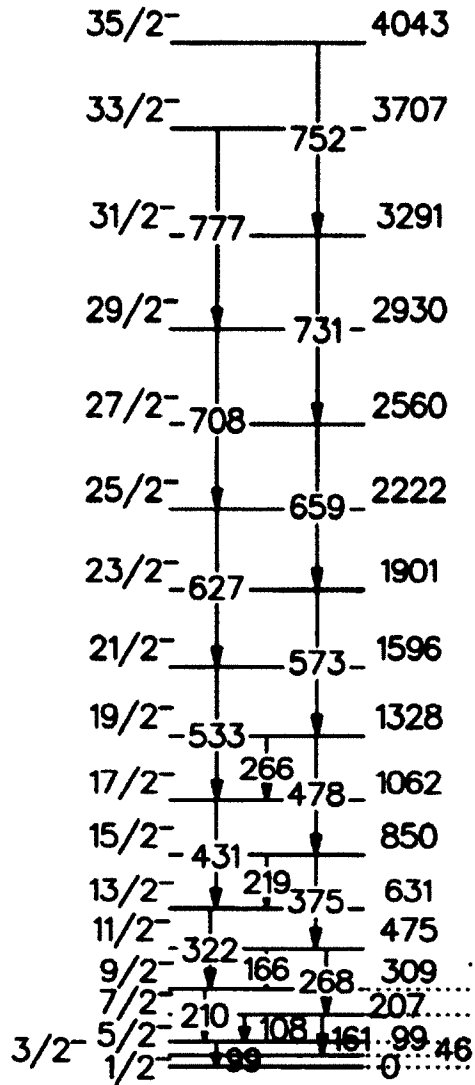
Figure 6.12: Partial level scheme for ^{183}W, as taken from Ref. [66]. All energies are in keV.

Fig. 6.13 shows a coincidence spectrum with sum of double gates, generated from a cube using data at both the beam energies, clearly showing the 533 keV $(21/2^- \rightarrow 19/2^-)$ transition in the ^{183}W.
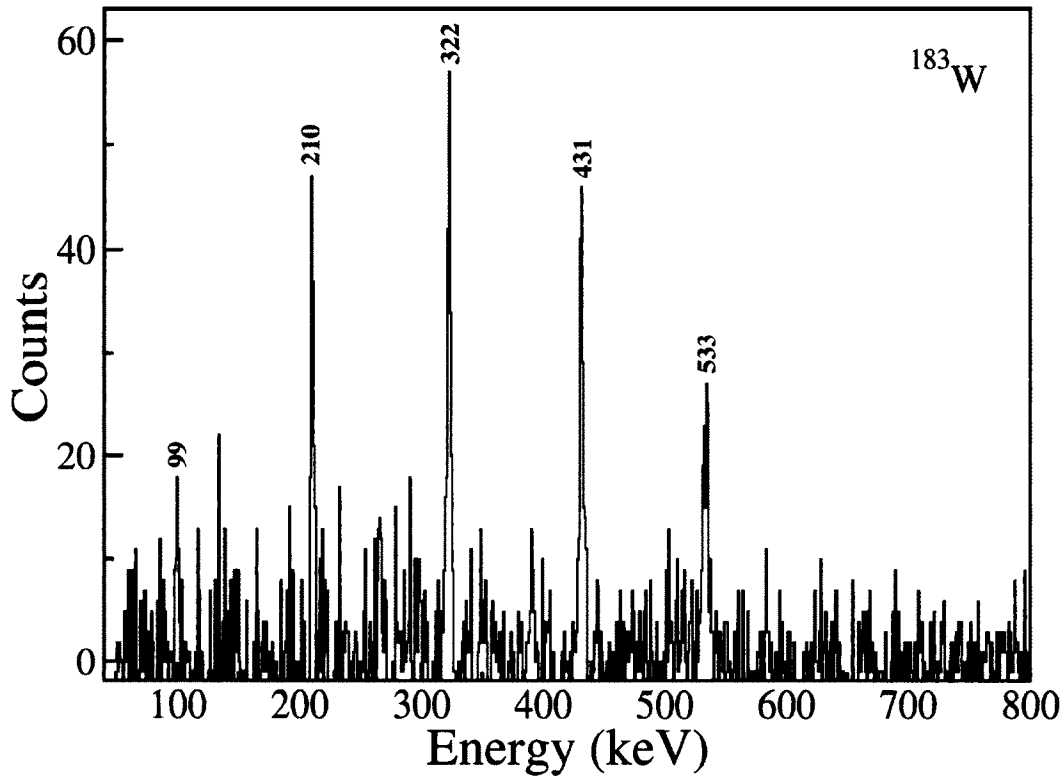
Figure 6.13: Triples coincidence spectrum with sum of double-gate combinations of 99, 210, 322, 431 and 533 keV transitions built on the $1/2^-$ ground state in ^{183}W.

Ground state band in ^{185}W, Z = 74, N = 111

Prior to the current study, the yrast band of ^{185}W was established only to spin $9/2^-$ built on a $\nu 3/2^-[512]$ neutron orbital, from decay measurements [67]. The level scheme of ^{185}W deduced from the present work is shown in Fig. 6.14, where seven new transitions have been assigned. This work extends band 1(a) and its signature partner band 1(b) to spin $19/2^-$ and $25/2^-$, respectively. Representative

coincidence spectra obtained from a cube, which included data at both the beam energies, for these two bands are shown in Fig. 6.15 (a) and (b). As can be seen in the coincidence spectrum, the two sequences of peaks are spaced characteristic of two rotational bands.
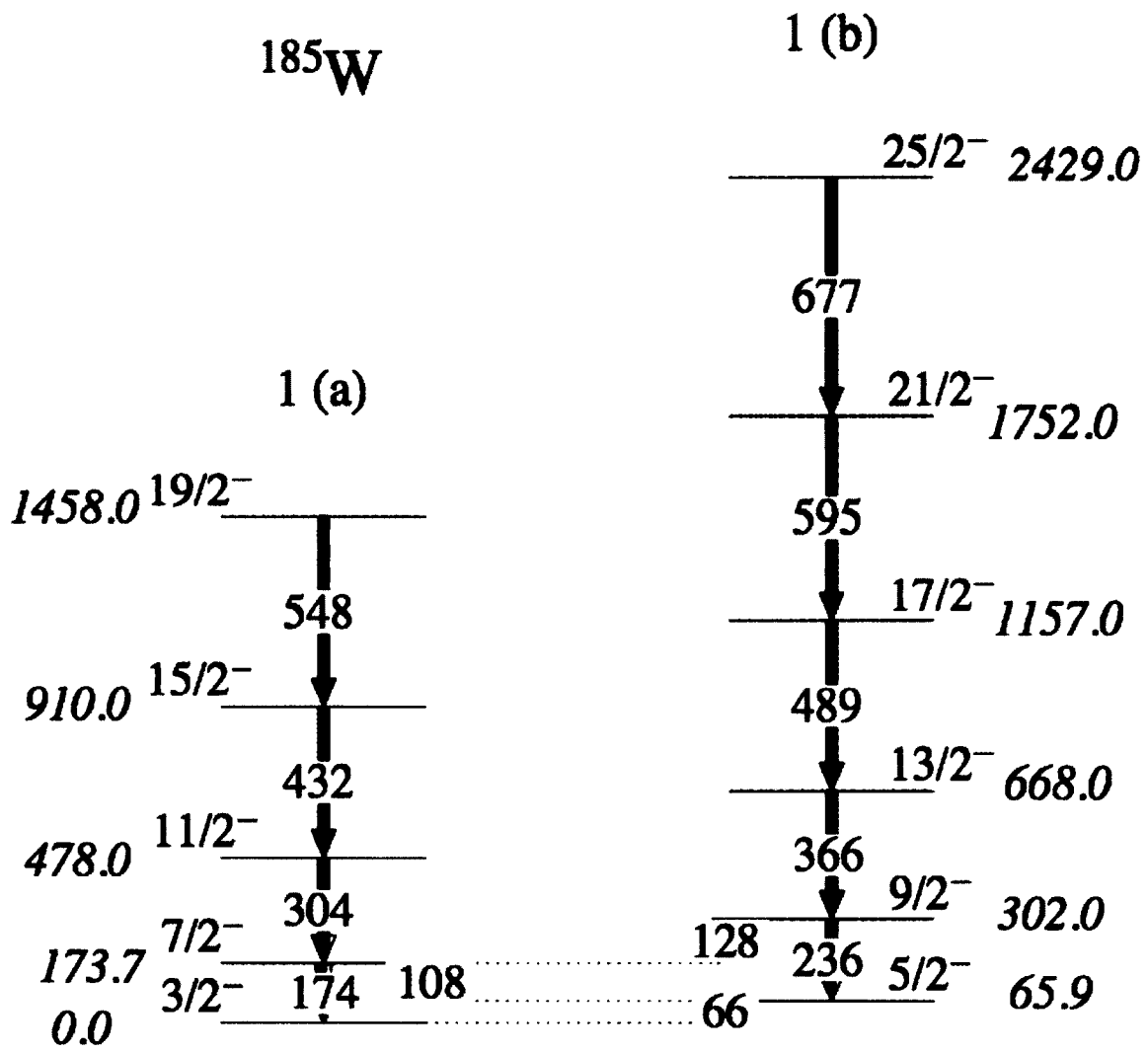
Figure 6.14: Partial level scheme for ^{185}W from the present work. All energies are in keV.
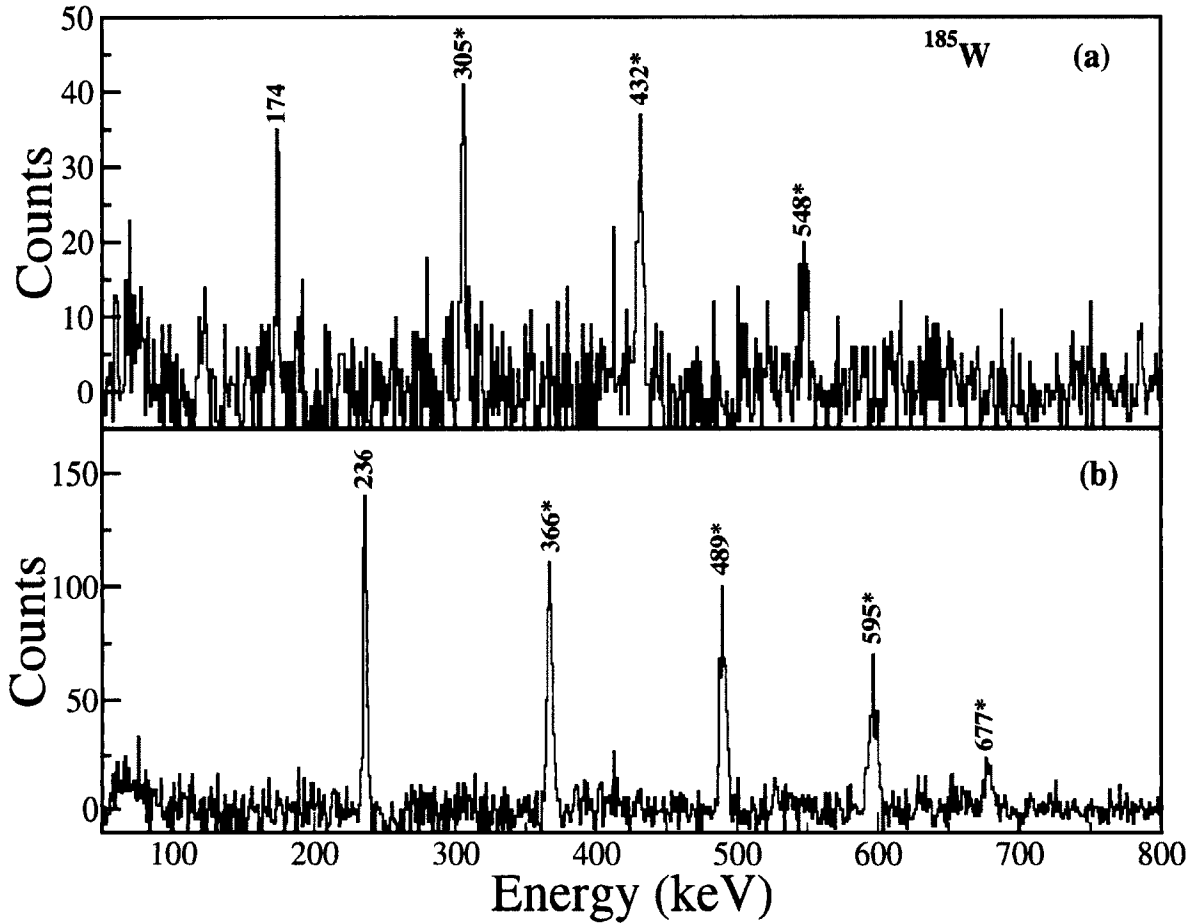
Figure 6.15: Triples coincidence spectrum with sum of double-gate combinations of all pairs of transitions in (a) band 1(a) and (b) band 1(b) for ^{185}W. New gamma rays identified in the present work are indicated with asterisks.

Ground state band in ^{187}W, Z = 74, N = 113

The previous studies in exploring the prompt excited states of ^{187}W have confirmed that the ground state band observed up to $21/2^-$ state at 1832.3 keV is built on a $\nu 3/2^-[512]$ neutron orbital [68] [69] [70]. The level scheme is shown in Fig. 6.16.
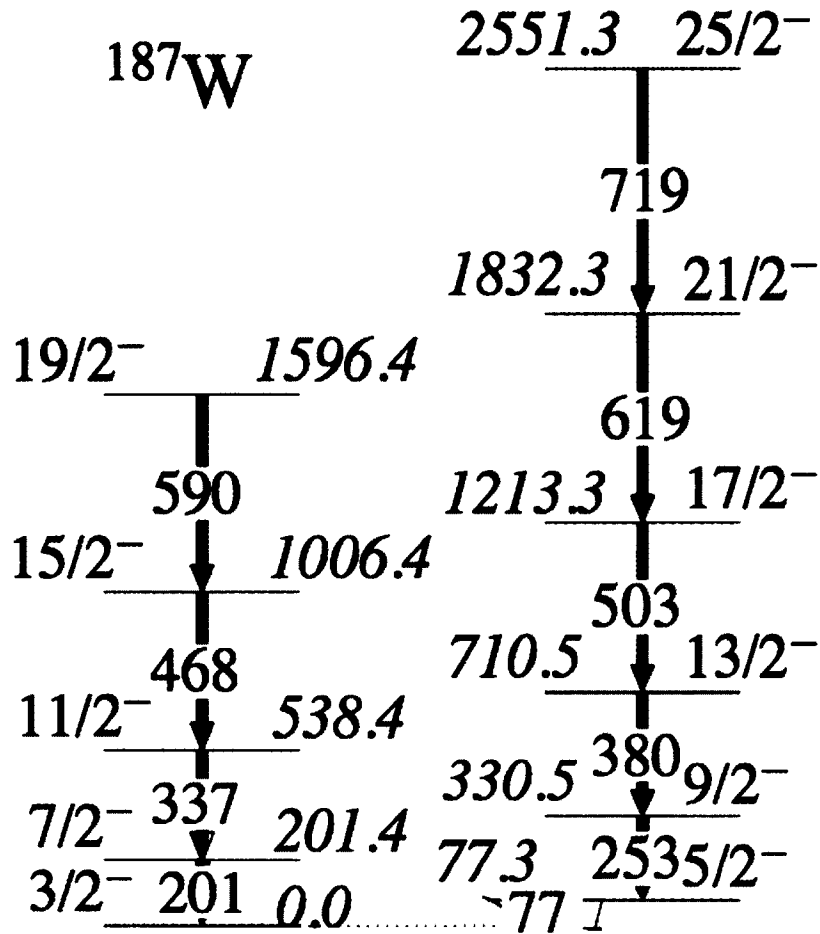
Figure 6.16: Partial level scheme for ^{187}W from the present work. All energies are in keV.

Whereas a transition from the $21/2^-$ state to the $17/2^-$ (1213.3 keV) state was tentatively placed previously, it is confirmed in the present data. Additionally, a new gamma ray of energy 719 keV is seen in coincidence and is placed above this state, as shown in Fig. 6.17, leading to a highest tentative spin assignment of $25/2^-$ for the new 2551-keV state.
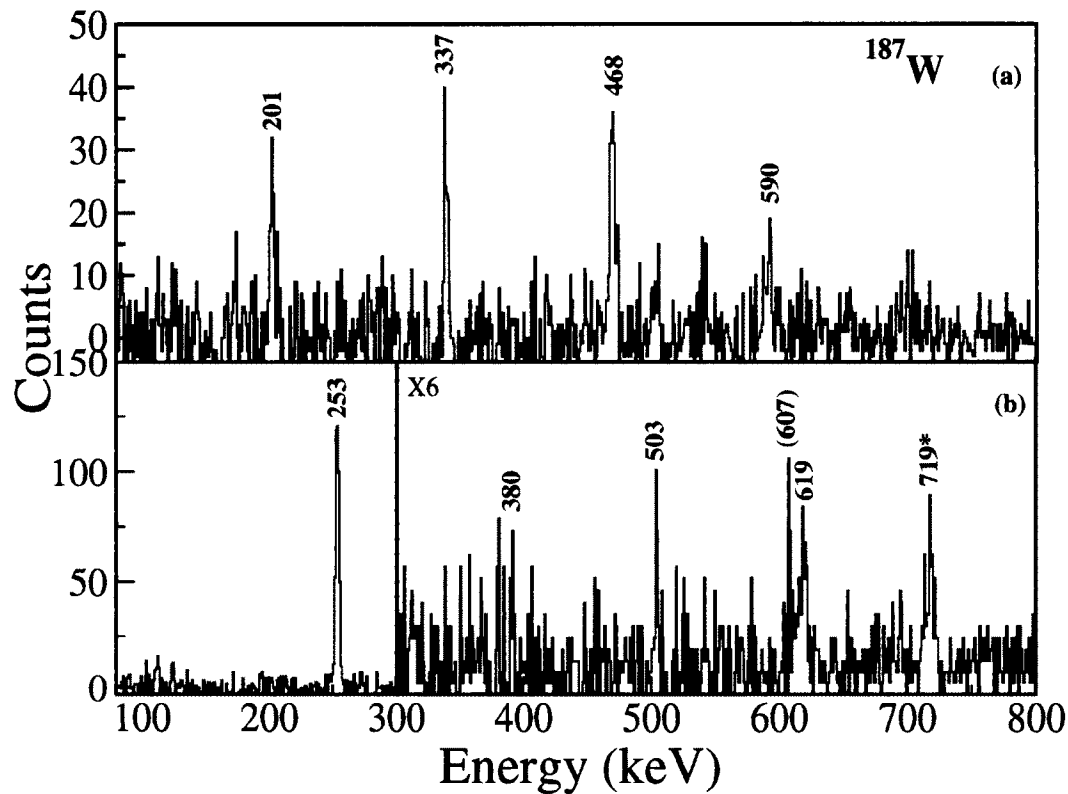
Figure 6.17: (a) Triples coincidence spectra with sum of double-gate combinations of (a) 201, 337, 468 and 590 keV transitions built on the 3/2⁻ ground state (b) 380, 503 and 619 keV transitions built on the 5/2⁻ state (77 keV). New gamma rays identified in the present work are indicated with asterisks.

6.3 Discussion of Band Structures in ^{186}W, Z = 74, N = 112

6.3.1 The ground state rotational band (GSB)

As noted in the Section 6.1, the experiment failed to reach spins higher than the previously observed maximum of $14\hbar$. The possibility of observing a prolate-

to-oblate shape transition is, thus, severely compromised, as this phenomenon was predicted at spins beyond $14\hbar$. The population intensities are analyzed in the following sections from a reaction mechanism perspective, through a comparison of Coulomb excitation calculations to experiment. In this section, the ground state band characteristics in ^{186}W is compared with neighboring even-W systematics, to scrutinize and discuss the structure evolution of ^{186}W up to the highest angular momenta observed in this experiment.

Woods-Saxon calculations presented in Section 3.2 predict a neutron alignment in the prolate minimum at $\hbar\omega$ = 0.38 MeV and in the oblate minimum at $\hbar\omega$ = 0.15 MeV. The ground state band is observed to approximately 0.4 MeV, and thus there should be some alignment indications at the highest spins. The evolution of kinematic moment of inertia $J^{(1)}$ as a function of rotational frequency $\hbar\omega$ = ($\frac{\Delta E}{2}$) for ^{182,184,186}W GSB bands is shown in Fig. 6.18, where ^{182}W has been observed up to $20\hbar$ in earlier studies. A sudden increase in moment of inertia and a backbend is seen in ^{182}W at I^{π} = 14^{+} and $\hbar\omega \approx 0.38$ MeV, and upbends at around the same rotational frequency can be noticed at I^{π} = 12^{+} for ^{184,186}W. The first nucleon alignment in the yrast band, where a pair of high-j $i_{13/2}$ neutrons unpair and align themselves with the spin of rotating core due to Coriolis force, agrees with calculations of quasi-particle levels using a prolate Woods-Saxon potential (Fig. 3.6), for ^{186}W. Unfortunately the data do not allow a mapping of the full alignment behavior across the critical rotational frequency.

Theoretical calculations performed using Ultimate Cranker predict that the

collective oblate minimum should become yrast or energetically favored at a spin of 16$\hbar$ (Fig. 3.5). The inability to experimentally observe any new higher lying spin-states above 14$\hbar$ in ^{186}W GSB, as discussed in section 6.1.1, is analyzed in the following section.
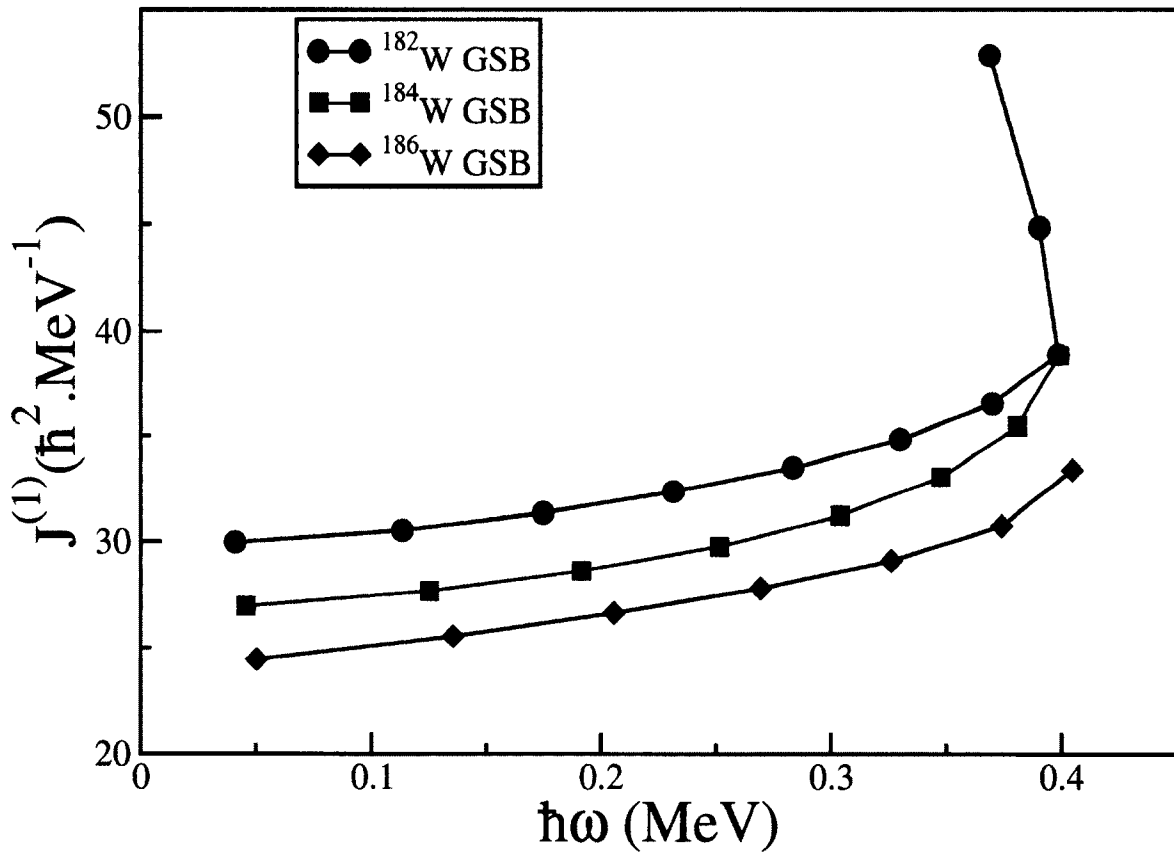
Figure 6.18: The kinematic moment of inertia $J^{(1)}$ versus rotational frequency $\hbar\omega$ for ^{182,184,186}W GSB bands.

Q-value: examining the reaction mechanism

In order to understand the failure to observe higher spin states, the various reaction mechanisms contributing to total cross-section for the deep-inelastic reaction, which depend on the beam energy and impact parameter, were explored. As explained previously (in section: 5.2.4), CHICO2 allows a determination of the reaction Q-value, which is defined as the difference between the initial and final energy of the system, on an event-by-event basis. The Q-value is positive for Coulomb excitation and real Q-value should be negative for quasi-elastic mechanisms. The Q-value when plotted as a function of scattering angle enables the differentiation between these different reaction mechanisms.
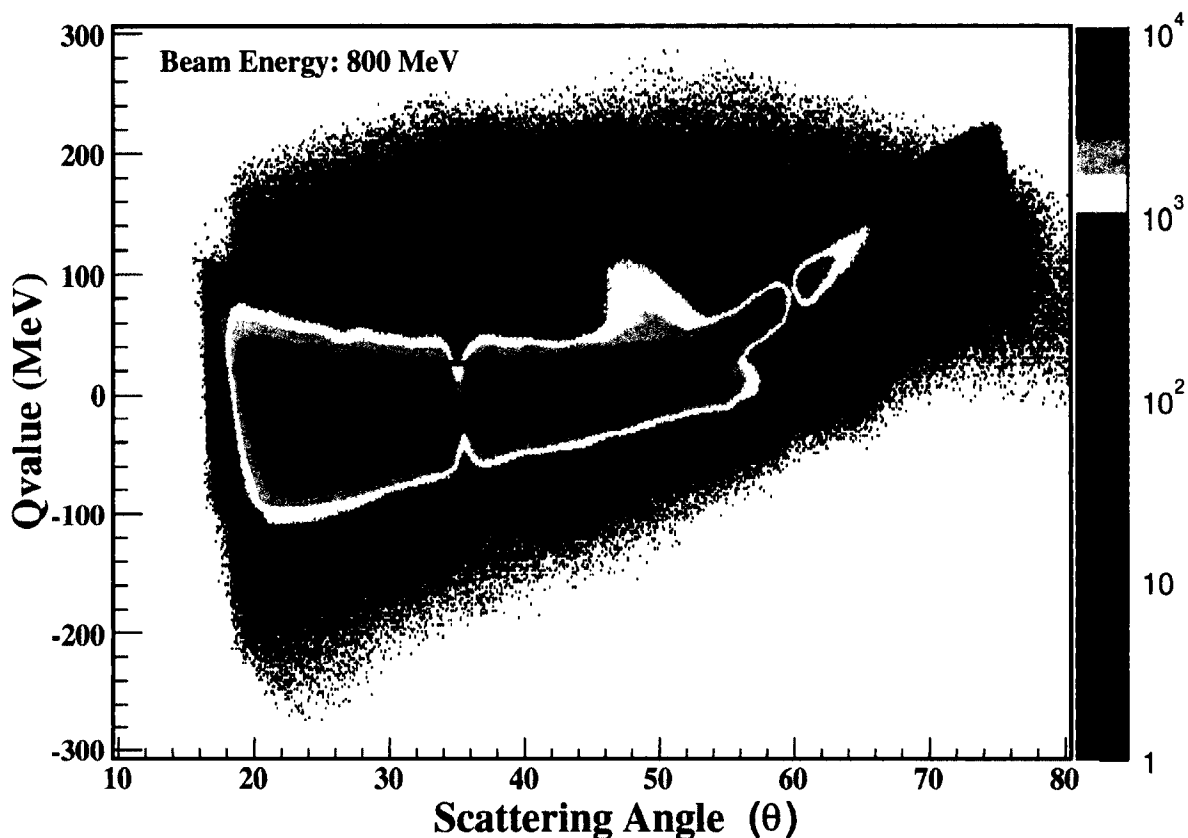
Figure 6.19: Deduced Q-value versus scattering angle for the TLFs (Traget Like Fragments) populated in the present reaction at 800 MeV beam energy. A 2-D graphical cut to restrict events selection to a particular range of Q-value and particle scattering angle is shown.

As shown in Fig. 6.19, a two dimensional gate on the Q-value, to restrict the events to lie between -25 to 25 MeV of Q-value, and scattering angles ($\theta_{lab} = 20°$ to $\theta_{lab} = 47°$) is used to try and improve the signal-to-noise for Coulomb excitation events, and to compare the experimental yields to calculations. The spectra obtained both with and without this Q-value condition, were analyzed. The condition on scattering angle is from a calculation of the maximum angle ^{186}W can have, if 800 MeV beam energy ^{136}Xe is used. In order to measure γ-ray yield

in inelastic channel, the data for both the beam energies, 800 and 725 MeV, was analyzed for the above conditions incorporated in the sorting routines to obtain a two-dimensional energy matrix. The extracted yield values are given in Table: 12.3 and 12.4 in the Appendix, and are compared with Coulomb calculations as discussed in the next section.

Coulomb Excitation calculations

The γ-ray yield for the ground state band in ^{186}W is also calculated directly using the multiple Coulomb-excitation code GOSIA [59]. For this calculation, information on the beam and target species, target thickness and its elemental composition, detection set-up along with beam energy and scattering angle were required to determine the kinematics. In addition, the nuclear-structure information, energy levels and matrix elements of the ^{186}W nucleus were taken from the available literature [71]. All previously known transitions for yrast states up to I^{π} = 14$^+$ are included in the calculations along with higher levels, which were estimated by keeping moment of inertia constant in rigid-rotor model of equation 2.16 and assuming that transition probabilities stay constant (B(E2) = 0.87 e^2b^2).

The value of electric quadrupole moment (Q) = -1.57b for the 2$^+$ energy level at 122.63 keV is used. All input information is given in Table 6.2, along with the values used for un-observed excited states. The partner nucleus requires no structure information, since it is assumed that no mutual excitation takes place.

107

Table 6.2: Input values to GOSIA calculations for ^{186}W yield calculations. The values of extrapolated energy levels above spin state 12^+ are given in the parenthesis.

E_i (keV)	E_γ (keV)	$I_i^\pi \to I_f^\pi$	B(E2) (W.u)	B(E2) (e^2b^2)
122.6	122.6	$2^+ \to 0^+$	111 (19)	0.70 (12)
396.6	273.9	$4^+ \to 2^+$	144 (10)	0.908 (63)
809.3	412.7	$6^+ \to 4^+$	187 (13)	1.179 (82)
1349.2	540.0	$8^+ \to 6^+$	178 (13)	1.123 (82)
2002.4	653.2	$10^+ \to 8^+$	151 (15)	0.952 (95)
2750.9	748.5	$12^+ \to 10^+$	189 (20)	1.192 (126)
3560.9	810	$14^+ \to 12^+$	138 (15)	0.87 0 (95)
(3600)	849	$14^+ \to 12^+$	138 (15)	0.87 0 (95)
(4550)	950	$16^+ \to 14^+$	138 (15)	0.87 0 (95)
(5600)	1050	$18^+ \to 16^+$	138 (15)	0.87 0 (95)
(6750)	1150	$20^+ \to 18^+$	138 (15)	0.87 0 (95)

The calculations were performed based on known matrix elements for all the known high spin transitions up to the highest excited 14^+ state, then integrating over the solid angle subtended by CHICO2 corresponding to acceptance of both scattered-beam and recoiling-target ($20°$ - $47°$) particles. The output results form these calculations, which were calculated for incident ^{136}Xe beam at two energies, 725 and 800 MeV, are given in the Table 12.5 and 12.6 in the Appendix, respectively. The obtained yield values are corrected for internal conversions (Table 12.1) and detection efficiencies. These corrected yields are then compared to the ones extracted from experimental data, as described in the previous section, where Q-value and scattering angle selection helps explore the Coulomb excitation reaction channel.

Fig. 6.20 show the relative yield of high-spin states in the ground state band of ^{186}W at two beam energies from the current experiment, with and without the Q-selection, along with that obtained from the Coulomb excitation GOSIA code. Relative population obtained with no Q-value condition seems to be similar at both the beam energies, whereas an appreciable difference is seen for the Coulomb excitation (i.e. with Q-value condition) events. Also, a comparison of relative population of high spin states in Coulomb excitation events from experiment and calculation establishes the fact that the higher beam energy (i.e. 800 MeV), which is further above the Coulomb barrier, brings in more angular momentum into this nucleus. An upper limit on the relative population of the 16^+ state extracted in all experiment cases are also plotted, as deduced from the non-observation of any gamma ray in the clean 653 keV gate.
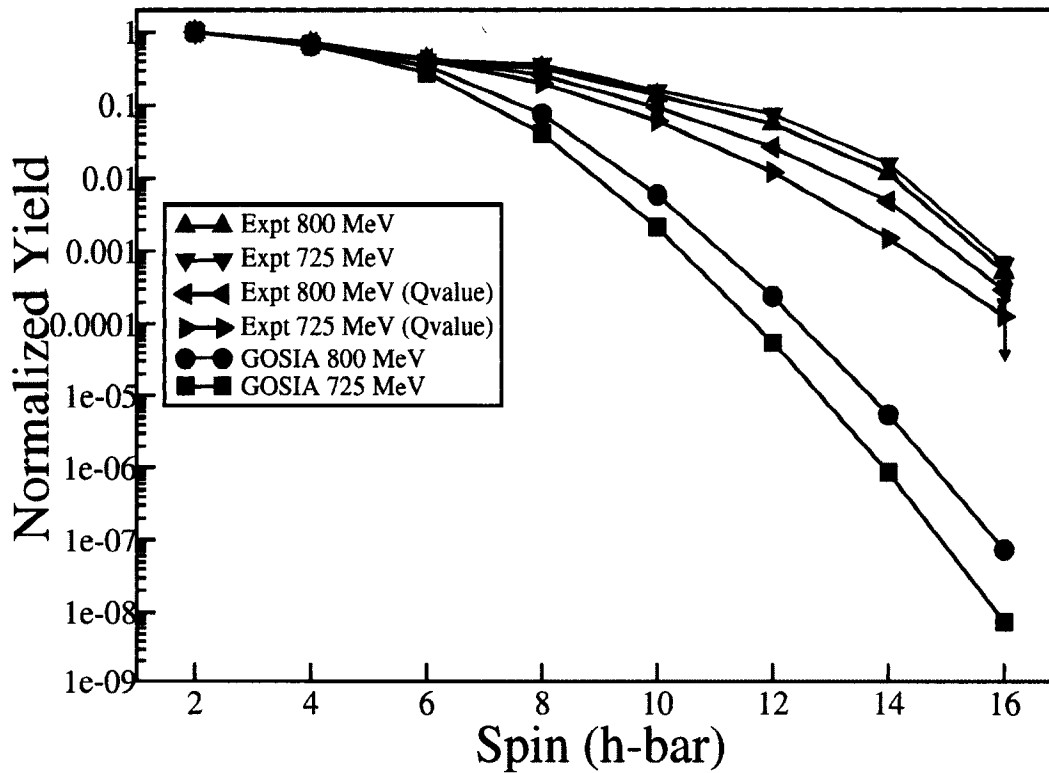
Figure 6.20: Comparison of gamma-ray yield of ground state transitions in ^{186}W at two beam energies from experiment (with and without Q-value condition) to that obtained from GOSIA calculations. Here the yields are corrected for efficiency and internal conversion and are normalized to the 2^+ to 0^+ transition yield.

The relative population of the higher spin states are seen to be significantly higher in the experiment than expected from Coulomb excitation calculations. Without any Q-value condition, the experimental yield ratios are even higher at higher spins. This was the primary reason to use beam energies significantly above the Coulomb barrier, such that non-Coulomb excitations could populate the highest spin states effectively.

110

The relative yields of the ground state band in ^{186}W from the present work is compared with that of ^{180}Hf from the prior experiment using Gammasphere and CHICO with the same ^{136}Xe beam at a beam energy of 750 MeV as shown in Fig. 6.21. The relative population curves as a function of angular momentum for the two seem to follow each other relatively well (within a factor 2) up to spin 14. A more detailed comparison of the actual counts in the two experiments reveals a significant difference in statistics. The sum of all single gates in the ground state band shows a factor of 20 lower statistics in the present experiment. Other comparisons with double-gated spectra confirm this more than an order of magnitude lower statistics. This is also consistent with the beam currents noted for the two experiments, where the Hf experiment had a 2 pnA beam while the W experiment again had a factor of 10 lower beam. These non-optimal conditions were partly predicated by the fact the W experiment was one of the first physics experiments after the commissioning of Digital Gammasphere and CHICO2, which led to significant teething problems and loss of effective beam time.

Better options for future experiments to populate higher spin states in ^{186}W are discussed below.
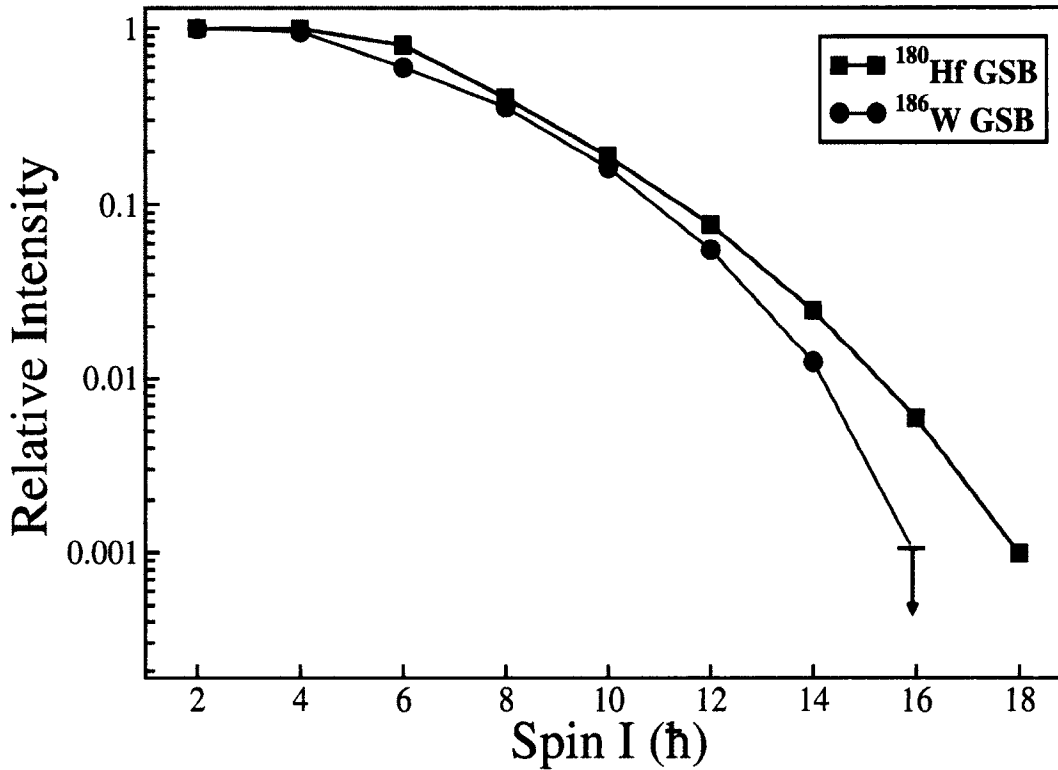
Figure 6.21: Relative yields of GSB transitions for ^{186}W and ^{180}Hf using ^{136}Xe beams at similar energies (see text), normalized to 1 for the 2^+ to 0^+ transition in each nucleus.

The calculations using this semi-classical Coulomb excitation code, not only helps in differentiating between relative angular momentum brought into the system for two beam energies of ^{136}Xe, it provides a tool to explore better beam-target combination for future experiments. With this motivation, various higher-Z stable beam options were explored. One option is stable ^{208}Pb, for which calculations were carried out for two beam energies: i.e 1404 and 1287 MeV which are 20% and 10% above Coulomb barrier for ^{208}Pb on ^{186}W combination, respectively. The

respective γ-ray yields are given in Table 12.7 and 12.8, in the Appendix. A comparison of these yields with that for ^{136}Xe beam at two energies, which were used for the current experiment, is shown in Fig. 6.22. This plot shows that for spins $14\hbar$ and $16\hbar$, a ^{208}Pb beam at 1404 MeV gives a factor of about 20 and 50 more yield as compared to ^{136}Xe beam at 725 MeV, respectively. These factors, coupled to the added factor of 20 to be gained from statistics mentioned above, suggest that a future experiment with Pb beams could yield 2 to 3 orders of magnitude higher counts around $14\hbar$, which would undoubtedly extend the level scheme by two or three units of spin.
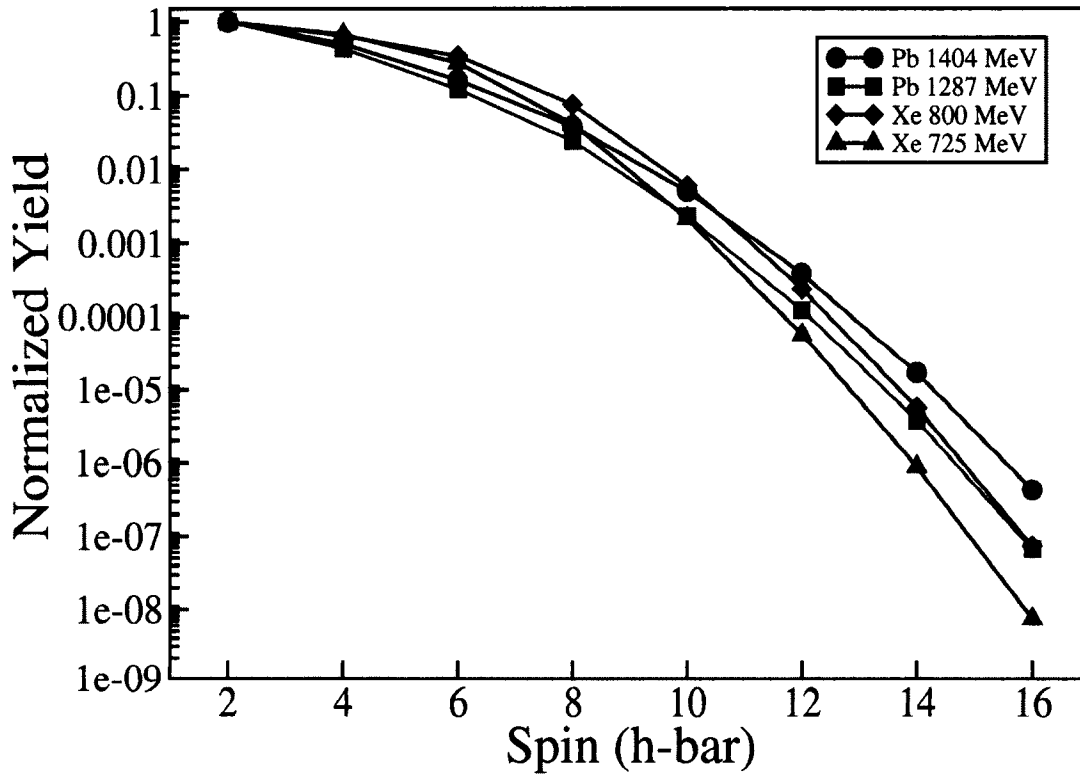
Figure 6.22: Gamma-ray yield of ground state transitions in [186]W from GOSIA calculations, when a [208]Pb beam of energy 1404 and 1287 MeV and [136]Xe beam of energy 800 and 725 MeV are used to excite [186]W target. Here the yields are corrected for efficiency and internal conversion and are normalized to the 2^+ to 0^+ transition yield.

Another comparison is possible with data from previous studies, where multiple Coulomb excitation of [186]W was performed using 1020 MeV [208]Pb beam, which is 15% lower than the Coulomb barrier [35]. The transitions observed within and between the ground state band and band 1 (γ-band) from this work along with the one deduced form the current work with [136]Xe beam 20% above

the Coulomb barrier is given in Fig. 6.23. This shows that this beam-target combination and reaction mechanism could bring enough momentum to observe transitions in the ground state band up to spin $14\hbar$ in ^{186}W. It should be noted that the side band, i.e the quasi γ-vibrational band 1 in ^{186}W, was traced up to spin $12^{+}\hbar$ in this experiment. This reinforces the results that if a heavier ^{208}Pb is beam is used above the Coulomb barrier, its more likely to excite high energy states in ^{186}W.

A heavier projectile, coupled with the requisite statistics that was planned for in the proposed experiment as described earlier in this section, should provide a better chance of accessing the primary physics thrust of this work.
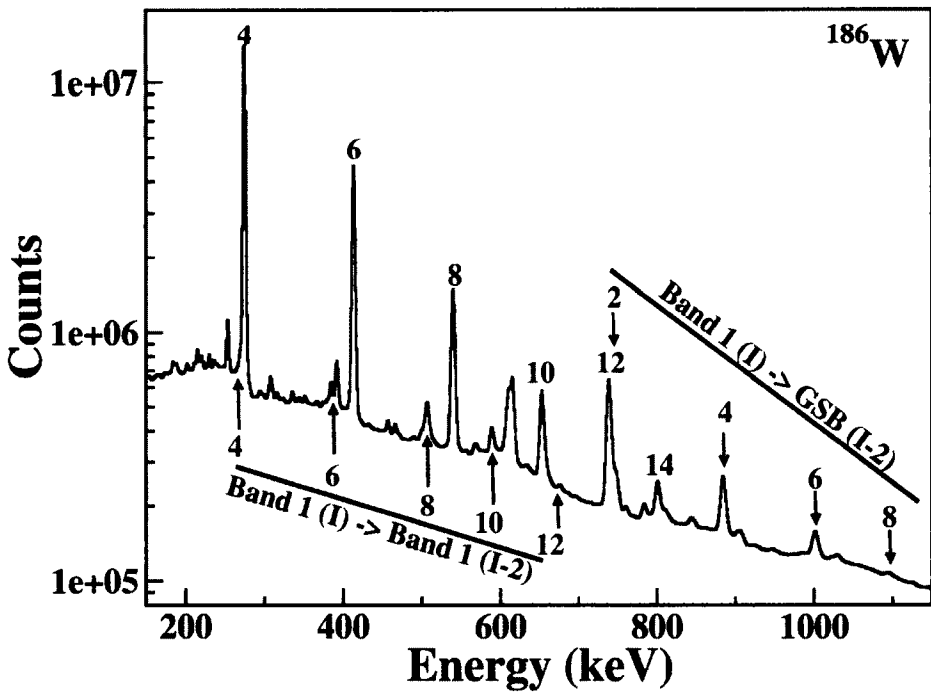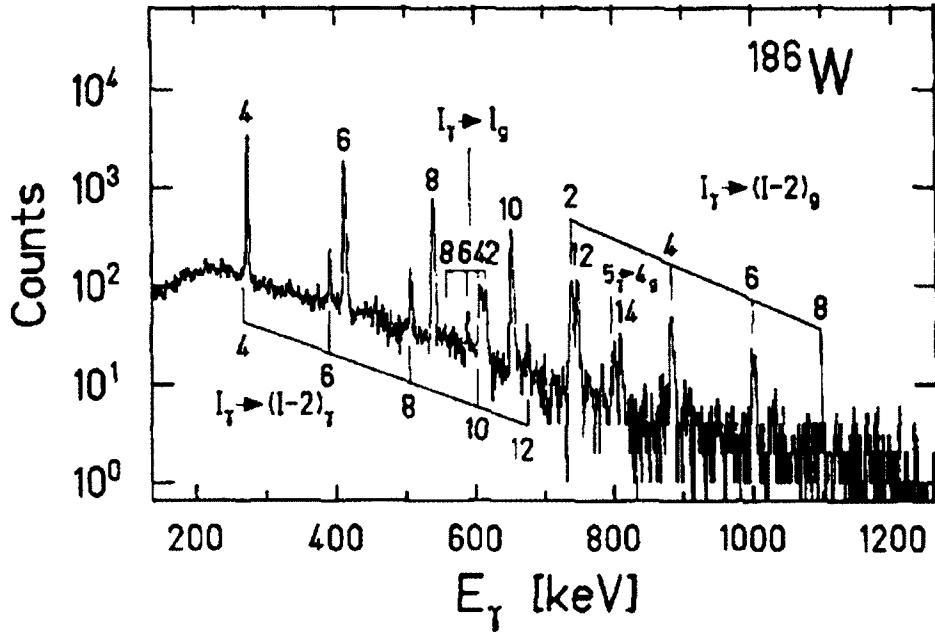
Figure 6.23: Comparing population of ground state band of ^{186}W, (Upper) for ^{208}Pb beam on ^{186}W thin target with beam energy $\approx$ 15% below the Coulomb barrier [35] and (Lower) ^{136}Xe on ^{186}W thin target with beam energy $\approx$ 20% above the Coulomb barrier (current work). Here transitions observed within and between the ground state band and band 1 (γ-band) are indicated.

116

6.3.2 Vibrational bands in ^{186}W

Although the prolate ground state band was not extended beyond 14^+, an oblate potential minimum co-existing with prolate at lower spins is a distinct possibility. This was the situation in ^{180}Hf, where one signature of the gamma vibrational band was observed to interact with a new band at low spins, to evolved into a band with oblate characteristics. Thus all collective side-bands need to be scrutinized for their specific characteristics.

Multiple new transitions are observed in bands 1 to 5 in ^{186}W, as shown in the level scheme: Fig. 6.1, which have the characteristics of one-phonon vibrational excitations. The level energies of these bands as a function of $I(I + 1)$, Fig. 6.24, shows an effective moment of inertia similar to that of GSB, consistent with their vibrational nature.
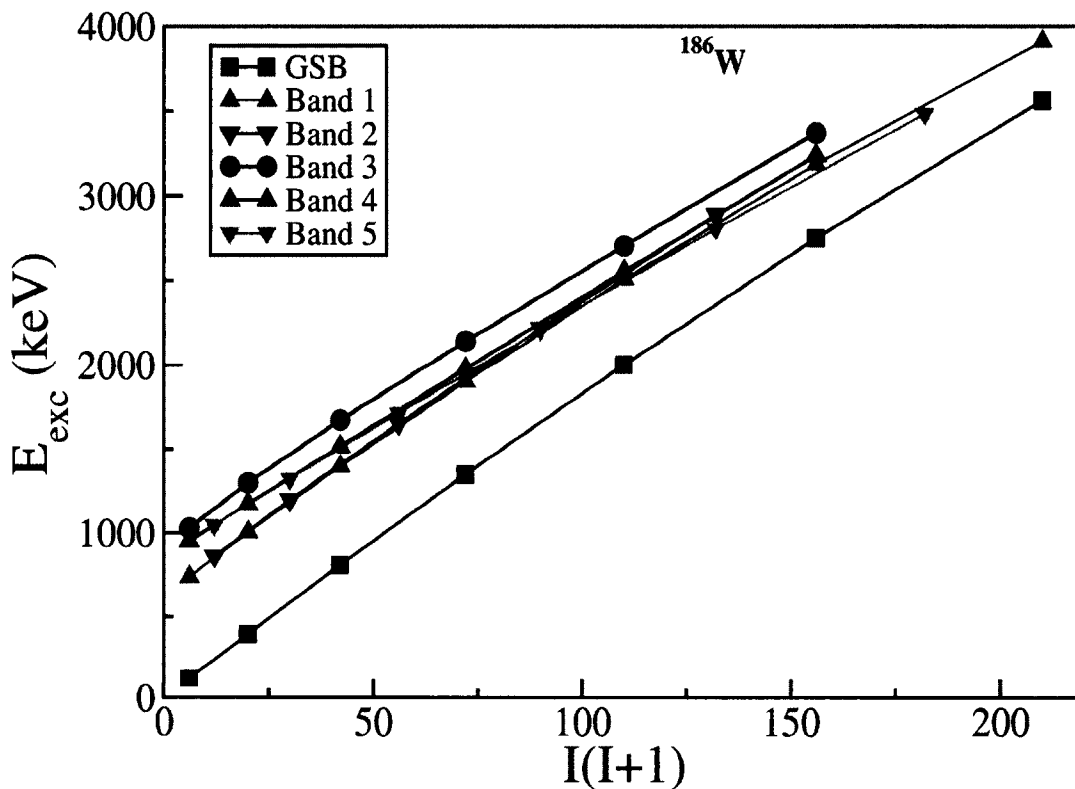
Figure 6.24: Excitation energies of levels as a function of I(I+1). New found levels are found to fit well with low-lying states built on the $K^\pi = 0^+$ (Band 3), 2^+ (Bands 1 and 2), 2^- (Bands 4 and 5) bands in ^{186}W.

The behavior of the ground state rotational band and quasi-gamma, quasi-beta and octupole vibration bands in ^{186}W are clearly visible in Fig. 6.25, where the excitation energies are plotted as a function of spin (I). For a better visibility and comparison, the energy of a reference rotor (E - 16.3*I(I + 1)) has been subtracted from the experimental excitation energies at each spin (I) value. For quasi-gamma bands built on $K^\pi = 2^+$ (band 1 and 2) and octupole $K^\pi = 2^-$ (band 4 and 5),

the slopes of the curves changes at spins higher then $I = 8\hbar$, indicating an onset of configuration change. This plot indicates that the odd and even-spin quasi-gamma vibrational bands follow each other very closely up to spin $8\hbar$. After this point, the odd-spin partner of the gamma band continues to retain its vibrational character however the even-spin gamma band clearly shows sign of interactions with some other band. This is the same behavior that was observed in ^{180}Hf, where the even signature partner of the gamma band interacted with a new band, and where it was conjectured that the higher spin members of this band can be attributed oblate character. Arguments for whether a similar situation is possible in ^{186}W is discussed below.
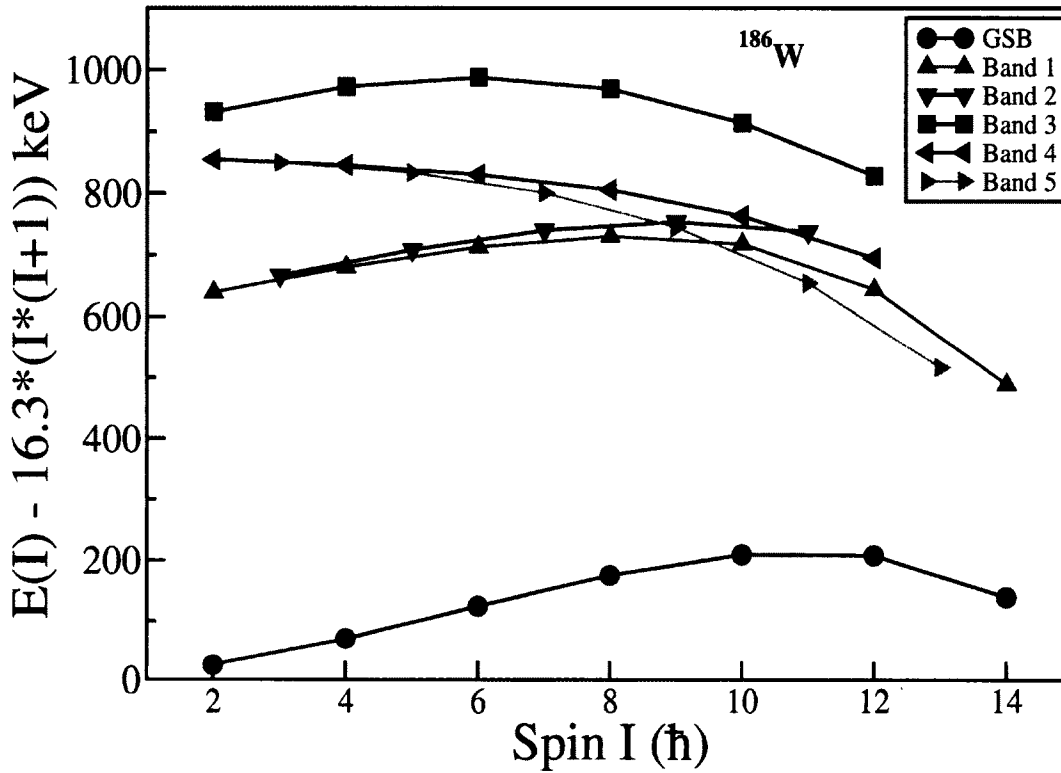
Figure 6.25: Excitation energies of members of the ground-state band, quasi-gamma, quasi-beta and octupole vibration bands in ^{186}W as a function of spin. To enhance band interaction effects, the energy of a reference rotor with $E_{ref} = 16.3*I(I+1)$ keV is subtracted from the level energies.

The kinematic moment of inertia versus rotational frequency (ω) for each spin state (I) is plotted for all the bands in ^{186}W is shown in Fig. 6.26. As in the excitation energy plot, this also shows that the even-spin gamma band has the same character as the odd-spin partner up to spin $8\hbar$ ($\hbar\omega \approx 0.25$ MeV). Beyond $8\hbar$, it upbends, which could be due to it mixing with an unobserved band with higher $J^{(1)}$, which is also higher than the $J^{(1)}$ of ground-state band. The measured

MOI for prolate g band (i.e. ground-state band) starts at about $24.5\hbar^2$ MeV^{-1} and reach $33.4\hbar^2$ MeV^{-1} at the highest rotational frequency. Where as for even-spin gamma-vibrational band it is $37\hbar^2$ MeV^{-1} at the highest rotational frequency.

Following the analysis thread of Ref. [26], assuming rigid rotation, MOI for oblate g band can also be obtained by $J_{oblate} = [(1 - 0.3\beta)/(1 + 0.3\beta)]J_{prolate}$ [15], where $J_{prolate} = 24.5\hbar^2$ MeV^{-1} and quadrupole deformation parameter, β, is 0.23. According to the trend in this region [72, 73, 74], MOI of the s bands are indicated at twice the respective values for the g bands. This gives MOI of 21.5, 43, $49\hbar^2$ MeV^{-1} for oblate g and s and prolate s bands, respectively. If the MOI parameter for the even-signature gamma vibrational band plateaued around $43\hbar^2$ MeV^{-1}, it would be consistent with the conjectured oblate band behavior in ^{180}Hf. The present data limits further discussion of this topic.
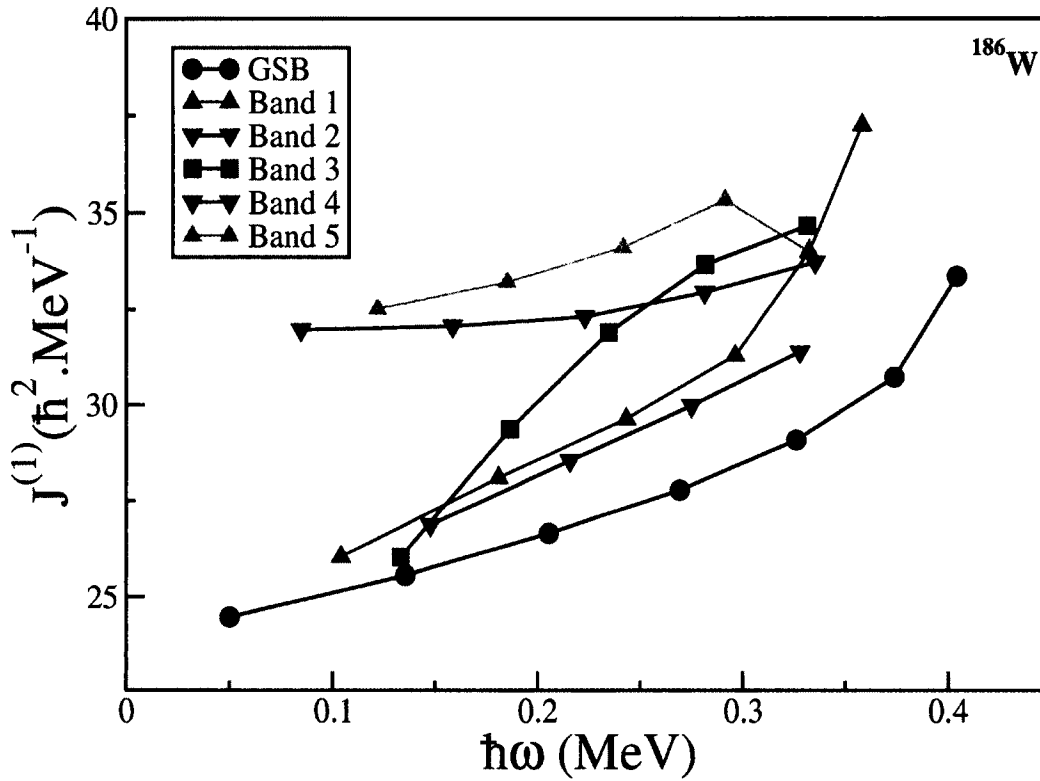
Figure 6.26: Kinematic moment of inertia $J^{(1)}$ versus rotational frequency (ω) for the $K^\pi = 0^+$ (Band 3), 2^+ (Bands 1 and 2), 2^- (Bands 4 and 5) bands in ^{186}W.

6.3.3 Triaxial softness around N = 112

The evolution from axially-symmetric deformed prolate shapes around the doubly midshell nucleus $^{170}_{66}$Dy$_{104}$ [75] towards spherical, doubly magic nucleus $^{208}_{82}$Pb$_{126}$ is predicted to pass through a region of triaxial gamma-soft and oblate nuclei [76]. The nuclear level structure and electromagnetic properties of Yb, Hf, W, Os and Pt isotopes have been experimentally and theoretically studied to show

both the characteristics for triaxiality and γ softness [77, 78].

Fig. 6.27 (a) shows the systematics of the low-lying states in even-even tungsten isotopes with N = 108 -> 116, where a monotonic decrease in the energy of the 2_γ^+ state relative to the yrast 2^+ states in this isotopic chain points to increasing γ-soft behavior with the increase in neutron number. This trend is also observed in the isotones when going from $^{186}_{74}\text{W}_{112}$ to $^{190}_{78}\text{Os}_{112}$, as shown in Fig. 6.27 (b).

The ratios of $E(4_1^+)/E(2_1^+)$ = 2.27 for ^{184}W and 2.22 for ^{186}W, decrease with increasing neutron number along the W isotopic chain, moving away from the perfect axial rotor limit of 3.33. This indicates increasing nonaxial behavior with increasing neutron number. This provides a motivation to investigate γ-vibrational bands in this region and establishes ^{186}W as a nuclei of interest in order to explore such physics phenomena.
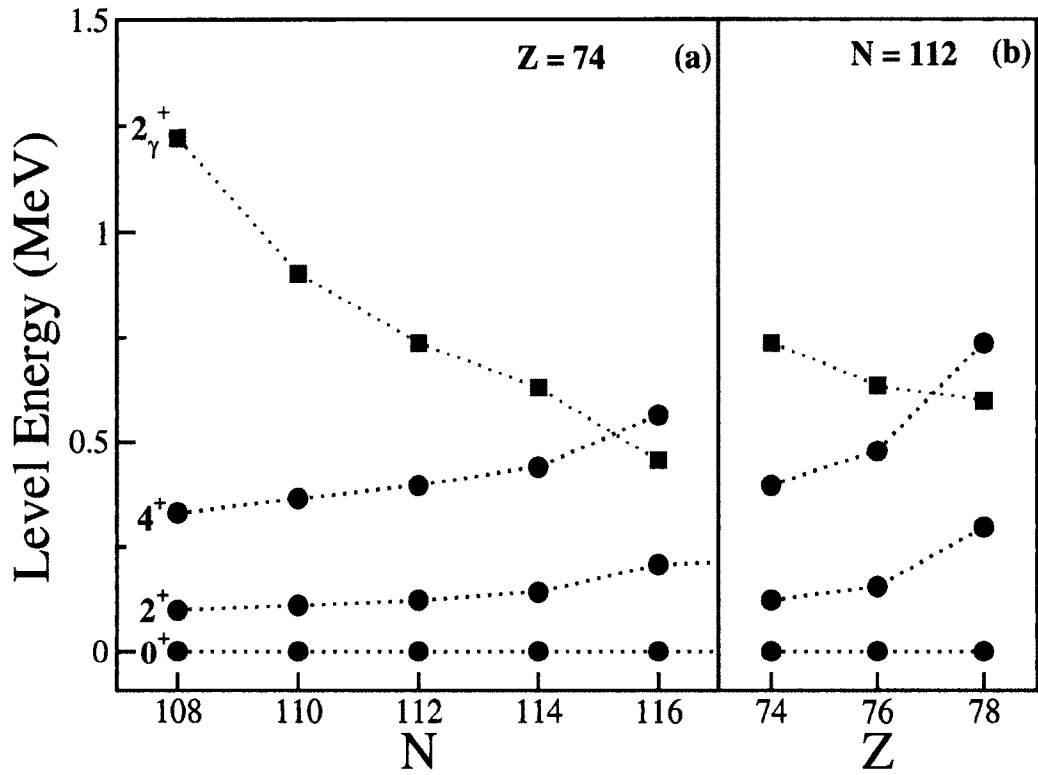
Figure 6.27: Energies of the lowest γ-vibrational levels (2^+_γ, 3^+_γ, 4^+_γ) in (a) Z = 74 isotopes and (b) N = 112 isotones, relative to the ground state. The 2^+ and 4^+ levels of the ground-state band are also included.

The odd-even energy-level staggering in a γ-band, analyzed in a framework of a ground-state band and a γ-band interaction, can provide an insight into the nature of the nuclear triaxiality (soft or rigid) [79]. This approach involves extracting the staggering parameter of the band, defined for spin I as

$$S(I) = E(I) - \frac{[E(I-1) + E(I+1)]}{2} \qquad (6.1)$$

Where E(I) stands for the energy of state I belonging to the γ-band. The ground-state band and quasi γ-vibrational band energies, together with the energy staggering parameter S(I), are shown in Fig. 6.28, where staggering is observed to increase with spin.
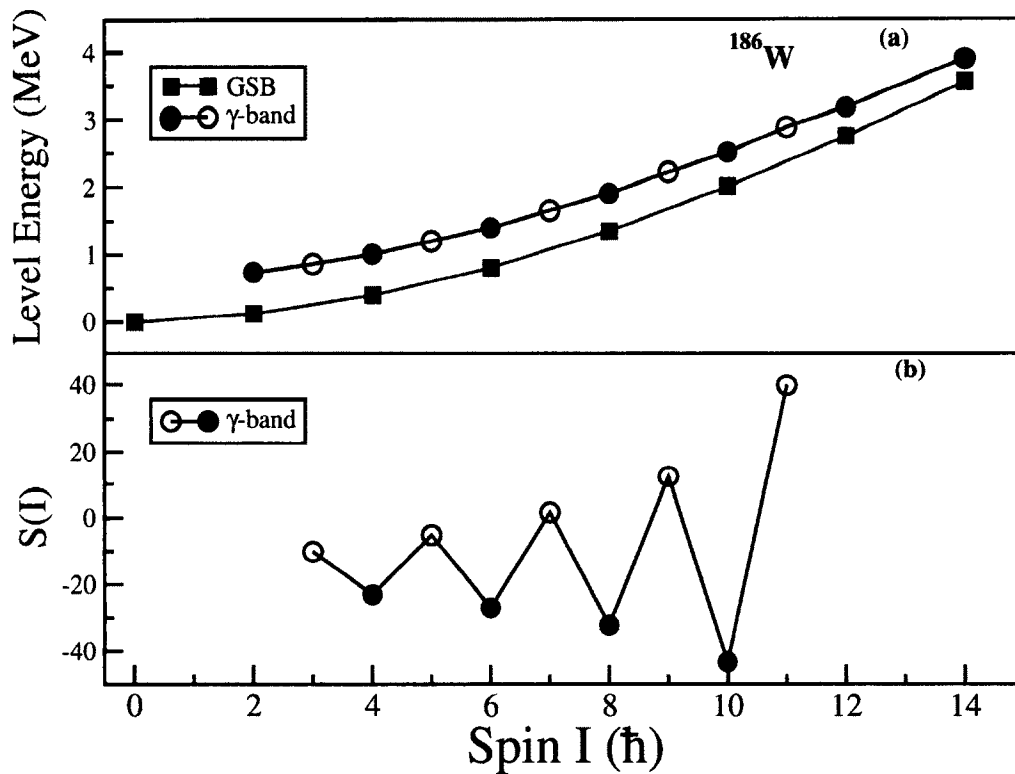
Figure 6.28: a) Level energies of the ground-state band and γ-vibrational band in ^{186}W, as a function of spin. (b) The staggering parameter, S(I), for γ-vibrational band as a function of spin.

While the γ-bands are not so well developed in lighter or heavier tungsten isotopes or in N = 112 isotones, the amplitude of the staggering effect in ^{186}W

is compared to ^{178,180}Hf, as shown in Fig. 6.29. The variation of staggering factor S(I) shows strong odd-even staggering or signature splitting for the γ-band in ^{180}Hf, in contrast with the neighboring ^{178}Hf nucleus, where odd-even staggering is observed to stay fairly constant up to spin 15. While increased staggering typically implies increased triaxiality, the explanation for ^{180}Hf case comes from the mixing of the even-spin signature of the γ-band with another even-spin band at intermediate spins (Band 4 in Fig. 3.2), where an interchange of character at the highest spins was observed [25]. Although no such additional even-spin band was found in ^{186}W, with the odd signature of γ-vibrational band extended in the current experiment, the S(I) values for ^{186}W seem to follow the staggering pattern in ^{180}Hf quite closely. This provides continued support to the possibility of a mixing of the even signature partner of the gamma vibrational band in ^{186}W with an unobserved positive parity even spin oblate band, where the higher lying members of the observed gamma vibrational band may already be changing character towards an oblate collective rotation scenario.
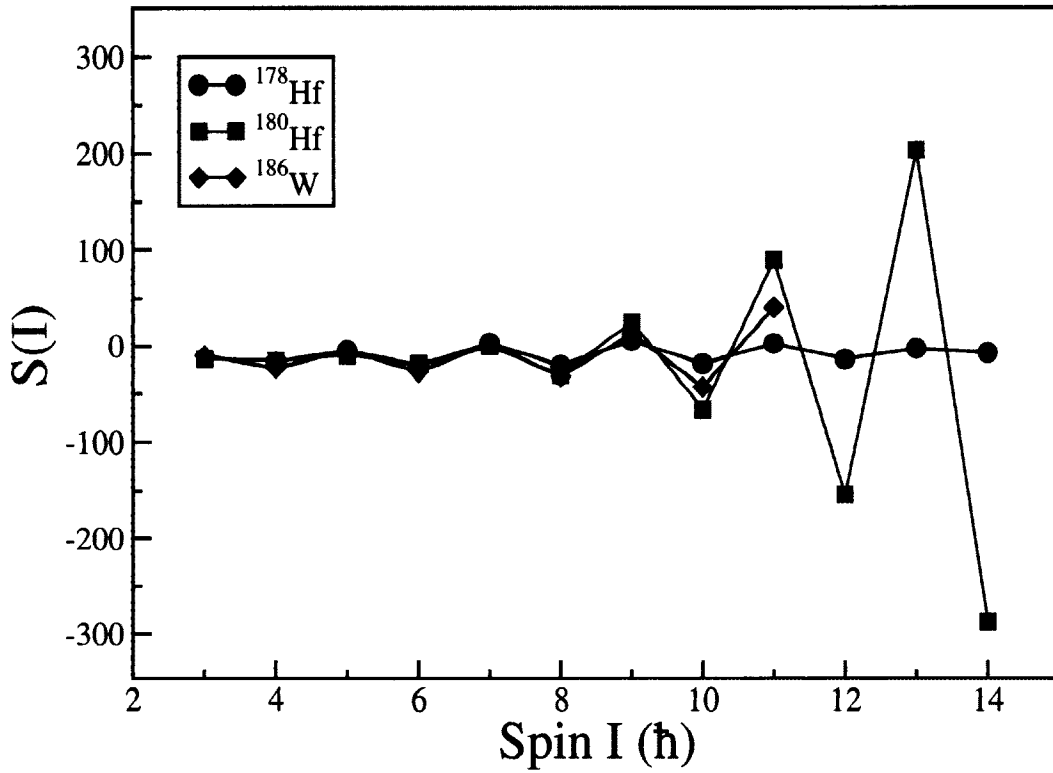
Figure 6.29: Odd-even staggering in γ-vibrational bands in ^{178}Hf, ^{180}Hf and ^{186}W.

6.4   Band Structure in ^{185}W, Z = 74, N = 111

To compare the evolution of high spin states built on $\nu 3/2^-[512]$ Nilsson state, excitation energy of all known states in isotones (even-Z, N = 111) in the neighborhood to ^{185}W are plotted in Fig. 6.30.
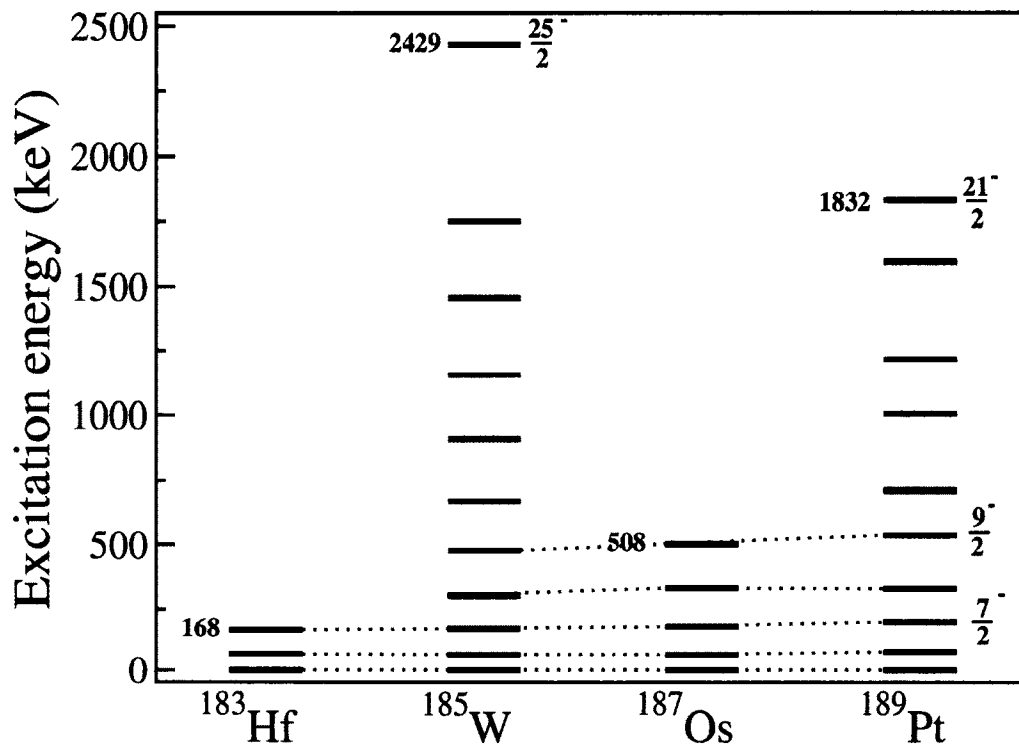
Figure 6.30: Excitation energies of known excited states built on $3/2^-$[512] bandhead in the even-Z, N = 111 isotones around ^{185}W. Red levels in ^{185}W are new from present work.

In addition, a plot of excitation energies of the ground state bands in ^{185,187}W (N = 111, 113) is shown in Fig. 6.31, highlighting the new states observed in ^{185,187}W. Both ground state bands in these two nuclei are built on the same configuration. The next lower odd-N neighbor, ^{183}W, has a different ground state configuration, and is excluded from this discussion. The new states in odd-W isotopes observed in the present work provide no surprises, and document the gradual

increase in deformation as one moves away from the Z = 82 and N = 126 magic numbers and approaches mid-shells.
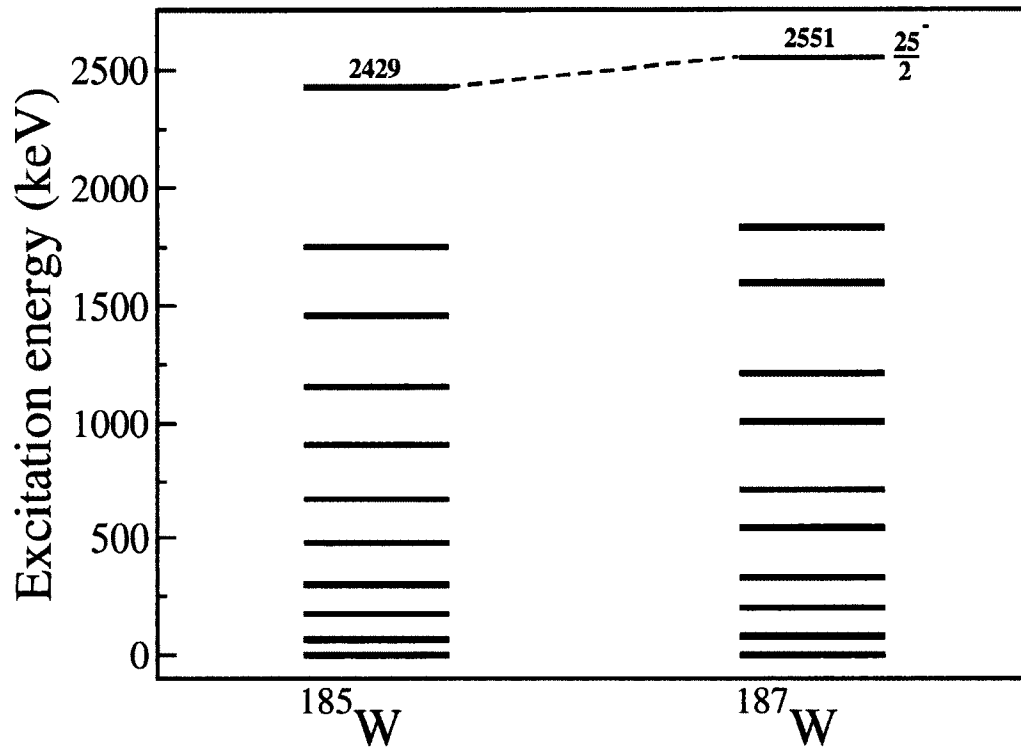
Figure 6.31: Excitation energies of ground state bands for A = 185 and A = 187 tungsten isotopes. Red levels are new from present work.

In Fig. 6.32, the kinematic moment of inertia, $J^{(1)}$, is plotted against rotational frequency for the ground state bands in $^{185,187}W$ nuclei and compared to their respective even-even $^{184,186}W$ cores (dotted lines). From this plot, it is evident that in going from ^{185}W to ^{187}W at low frequencies, the kinematic moment of

inertia trend tracks the behavior of their respective even-even cores. The $\alpha = -1/2$ signature of ^{187}W, is seen to have higher kinematic moment of inertia as compared to its signature partner.
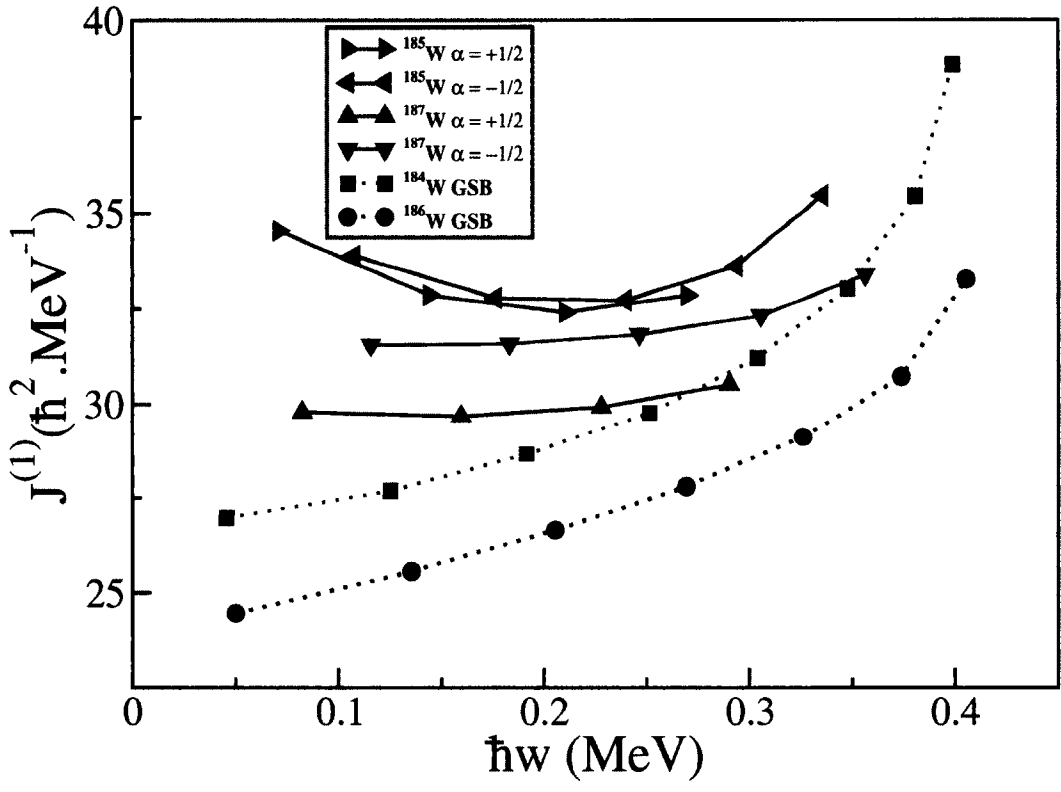
Figure 6.32: Kinematic moment of inertia $J^{(1)}$ as a function of rotational frequency of the ground state bands in $^{184-187}$W nuclei.

The experimental alignments (i_x) for $^{184-187}$W are plotted as a function of rotational frequency (ω), as shown in Fig. 6.33. Here the Harris parameters $J_0 = 24.5\ \hbar^2\ \mathrm{MeV}^{-1}$ and $J_1 = 42\ \hbar^3\ \mathrm{MeV}^{-4}$, obtained to ensure that the ground-state

band of ^{186}W has approximately zero alignment at low rotational frequency, are used.
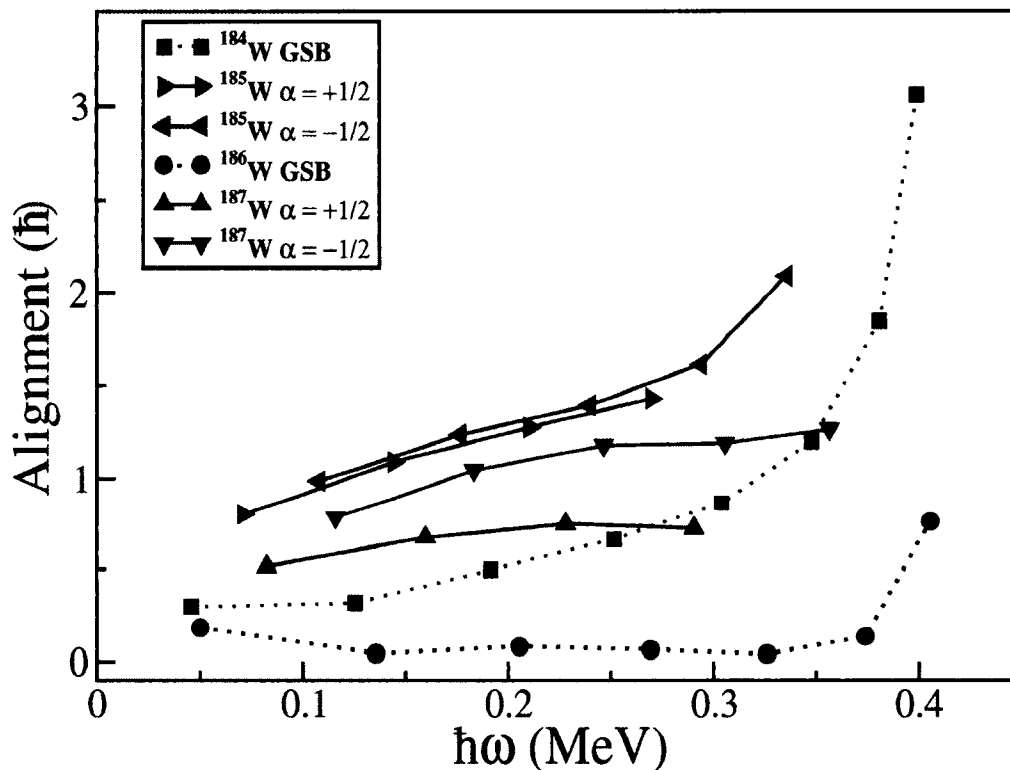
Figure 6.33: Experimental alignments, i_x, as a function of rotational frequency, ω, for the ground state bands of $^{184-187}$W. Data are taken from Ref. [80] [81] for ^{184,186}W. Harris parameters $J_0 = 24.5\ \hbar^2$ MeV^{-1} and $J_1 = 42\ \hbar^3$ MeV^{-4} are used.

As discussed earlier, the even-A nuclei all exhibit alignment or begin aligning at $\hbar\omega$ around 0.38 MeV, consistent with Woods-Saxon predictions for the breaking of a pair of $\nu i_{13/2}$ quasi-neutrons.

With newly identified transitions in ^{185}W, both signature partners of the ground

state band in this nucleus continue to follow each other till about 0.3 MeV/$\hbar$ rotational frequency, where a slight upbend in alignment for the $\alpha = -1/2$ signature is seen. The alignment plot also brings out signature splitting of the ^{187}W nucleus. To quantitatively compare the signature splitting, defined in equation 6.1 a staggering parameter, S(I), which characterizes the degree of splitting between the energies of the $\alpha = +1/2$ and $\alpha = -1/2$ signature components of a band, was extracted for the ground state rotational bands in $^{183-187}$W, as shown in Fig. 6.34. In comparison with ^{183,185}W, ^{187}W GSB shows a significantly larger signature splitting.
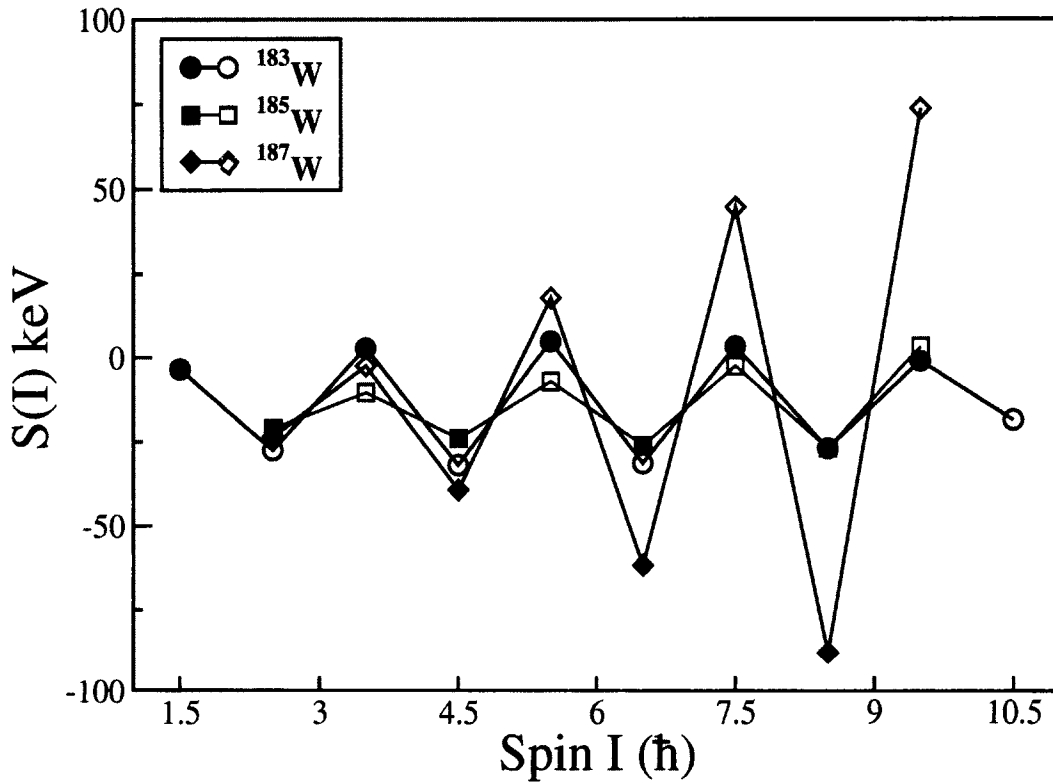
Figure 6.34: Signature splitting of the $1/2^-$ [510] bands in ^{183}W and of $3/2^-$ [512] bands in ^{185,187}W (this work). The filled (opened) symbols correspond to the $\alpha = +1/2$ ($\alpha = -1/2$) signature.

As discussed earlier in Section 6.3.3 and Fig. 6.27 for even-even W isotopes, an increase in softness towards triaxial shapes is indicated by sharply dropping energies of the gamma vibrational bands. For odd-A nuclei, the role of the odd particle in polarizing the core towards triaxiality has been discussed at length in the literature, and specifically for ^{187}W [68] [69]. With the new data on ^{185}W from the present work to compare with, one can infer a sudden marked increase in

133

gamma softness for the N=113 nucleus ^{187}W from the staggering plots, compared with the N=111 and N=109 isotopes of W. Thus, for W isotopes at least, the nucleus ^{185}W seems to define a boundary for the onset of gamma softness. This is also consistent with cranking calculations (Fig. 3.4) that predict a transition from prolate to triaxial shapes for moderate spins along the yrast line for ^{186}W.

Chapter 7

Summary and Future Work

The main aim of this thesis project was to investigate the predicted prolate to oblate shape transition at high spins in ^{186}W, a neutron-rich stable isotope of tungsten. A thorough search, using different spectroscopic techniques, was unsuccessful in extending the prolate yrast structure in this nuclei beyond the known states. Many previously unreported vibrational states have been established for ^{186}W, and a comprehensive level scheme was built from the coincidence analysis. A discussion of triaxiality in this nucleus was provided, based on the extended γ-vibrational band. The excitation energies of new levels in this band and their odd-even staggering trends were compared to the known γ-vibrational energy levels in neighboring isotopes and isotones.

Transfer reaction products were also analyzed for various nuclei neighboring ^{186}W. The yrast band in ^{185}W built on $\nu 3/2^-[512]$ Nilsson state, was extended to higher spins. A comparison of kinematic moment of inertia $J^{(1)}$, experimental

135

alignments $i_{(x)}$ and staggering trends in the yrast bands of ^{183}W, ^{185}W and ^{187}W, define ^{185}W as a nucleus that marks a boundary above which significant gamma softness is observed.

Whereas, the new results have expanded our knowledge of high-spin collective structures in ^{185,186}W nuclei, the unsuccessful attempt at populating high spin states in ^{186}W yrast band still poses a question. The experiment suffered from low statistics (more than an order of magnitude compared to a previous similar experiment on ^{180}Hf) for unexpected experimental limitations. In order to better understand the reaction mechanism, the Q-value of the reaction was used to extract yield for Coulomb excitation and the observed γ-ray yields were compared to predictions from the Coulomb excitation code GOSIA. This comparison shows that higher beam energy (800 MeV), should bring in more angular momentum to excite the high spin states in this nucleus. Further, similar calculations were carried out to compare and predict the possibility of using heavier ^{208}Pb beam as a binary reaction partner on ^{186}W target. This comparison indicated that Pb+W combination would be a more potent combination to excite high spins states in ^{186}W, where 1404MeV ^{208}Pb beam gave 20% higher yields for 14^+ excited state. For future experiments, heavier beams, like uranium and thorium, should also be explored in detail, which would allow the observation of high spin states and explore the theoretical predicted shape change.

For the future experiments, γ-ray tracking array like GRETINA/GRETA with high efficiency, high segmentation and thus high spatial resolution for Doppler

correction, and excellent background rejection, should be considered for improved

data quality.

Part 2

Optimizing Hole Mobilities for Gamma-Ray Tracking

Chapter 8

Position Sensitive HPGe Detectors

Gamma-ray spectroscopy, plays a central role in obtaining experimental information necessary for understanding nuclear structure. In order for a gamma ray to be detected, it must interact with detector material, and that interaction must be recorded. Detectors based on high-purity germanium (Ge) with their excellent energy resolution and efficiency are commonly used for nuclear spectroscopy studies.

In the last decade, significant progress has been made in the development of producing position-sensitive Ge-based detectors with fine spatial sensitivity. The position measurement of gamma-ray interaction events in all three dimensions includes substantial technical challenges, ranging form the fine electrode segmentation with efficient charge collection to building robust algorithms to get best spectroscopic performance of the detectors. Despite these challenges, new arrays such as the Advanced GAmma Tracking Array (AGATA) [82] and Gamma Ray

Energy Tracking In-beam Nuclear Array (GRETINA) [83] have been built for nuclear science based on highly segmented germanium crystals and are currently being used successfully.

As gamma rays interact at random depths within the detector, the depth of interaction in these detectors is obtained from the difference in the arrival time of the electron at an electrode on one side of the detector and that of the holes at an electrode on the opposing detector surface. This separate detection of the electron and hole collection, and hence knowledge of their precise velocities, is crucial to this technique which is aided by the segmented electrodes. This chapter presents the basic aspects of Ge-based position-sensitive detectors.

8.1 HPGe Detectors

In most γ-ray detector applications, solid material is used. The use of solid, rather than gas-filled, detectors allows the size of the detector to be smaller, because of the higher density of solids. This advantage comes at the cost of more challenging charge collection. Scintillation detectors can be built from solid material, but the large energy required to produce the charge carriers responsible for light generation ($\sim$100 eV) and the consequent small number of carriers created by the γ-ray interaction results in a very poor energy resolution ($\sim$10%). Semiconductor materials, in which the number of generated charge carriers is much larger, provide the best energy resolution performance.

Among the semiconductors, germanium is the material of choice for γ-ray detection. Germanium has larger atomic number (Z=32) than silicon (Z=14) and therefore a larger attenuation coefficient. Furthermore, the smaller energy gap (at T= 0K, E_g = 0.75 eV, which compares to E_g = 1.17 eV for silicon) results in a better resolution (~0.3 %). Germanium has a diamond crystal lattice, with properties varying along the crystallographic directions.

Current technology allows for the manufacture of large High Purity Germanium (HPGe) crystals in different configurations, such as: planar (rectangular or cylindrical) and Coaxial (true or closed-end coaxial). A semiconductor radiation detector is operated as a p-n junction under reverse bias. An example of a biased coaxial HPGe detector using a n-type (excess pentavalent impurities) crystal is shown in Fig. 8.2. For n-type coaxial geometry the n^+ and p^+ electrical contacts are provided on the two surfaces of the germanium cylinder. To reverse bias the detector, positive voltage is applied to the n^+ contact with respect to the p^+ surface. The depletion region, begins at the n^+ edge and extends deeper into the p region. The voltage is increased until the detector is fully depleted. Impurity concentration of reduced value up to 10^{10} atoms/cm^3 helps in attaining larger active detection region.

When an energetic particle strikes a semiconductor, bound electrons in the valence band gain energy via one of the interaction mechanisms like, photoelectric effect, Compton scattering of photon or pair production. In the photoelectric effect the incident γ-ray is totally absorbed by an atomic electron with the resulting

photo-electron having energy

$$E_e = E_\gamma - E_{BE}, \qquad (8.1)$$

where E_γ is the γ-ray energy and E_{BE} is the binding energy of the atomic shell where interaction occurs. This is an elastic scattering, which mainly involves the K shell and hence the most tightly bound electrons. The process leaves behind an ionized atom. The Compton scattering involves inelastic scattering of γ-rays from free electrons. After the collision a γ-ray of reduced energy is obtained, together with an electron that shares energy and momentum with the photon in the collision. The energy of the scattered photon ($h\nu$) is given by [85]:

$$h\nu = h\nu_0/[1 + h\nu_0/m_0c^2(1 - \cos\theta)] \qquad (8.2)$$

where $h\nu_0$ is the energy of the incident photon, m_0c^2 the rest mass of the electron and θ the angle of scattering. The third process of importance is pair production, where the incident γ-ray photon is completely absorbed, with a creation of a positron-electron pair whose total energy is equal to $h\nu$, the energy of photon. So we can write

$$h\nu = (T_+ + m_0c^2) + (T_- + m_0c^2), \qquad (8.3)$$

where m_0c^2 is again the rest mass of the electron and T_+ and T_- represent the kinetic energies of the positron and electron, respectively. If the energy gained by the electron is higher than the band-gap, they move to the conduction band,

142

leaving behind holes. When a voltage is applied to opposite electrodes, the free electron-hole pairs feel the electrostatic force of the applied field. They start to drift towards the contacts and induce an electric signal at the corresponding electrode, as shown in Fig. 8.2.

True coaxial   Closed-ended coaxial

p^- contact ——▶
n^+ contact ——

n-type coaxial detector
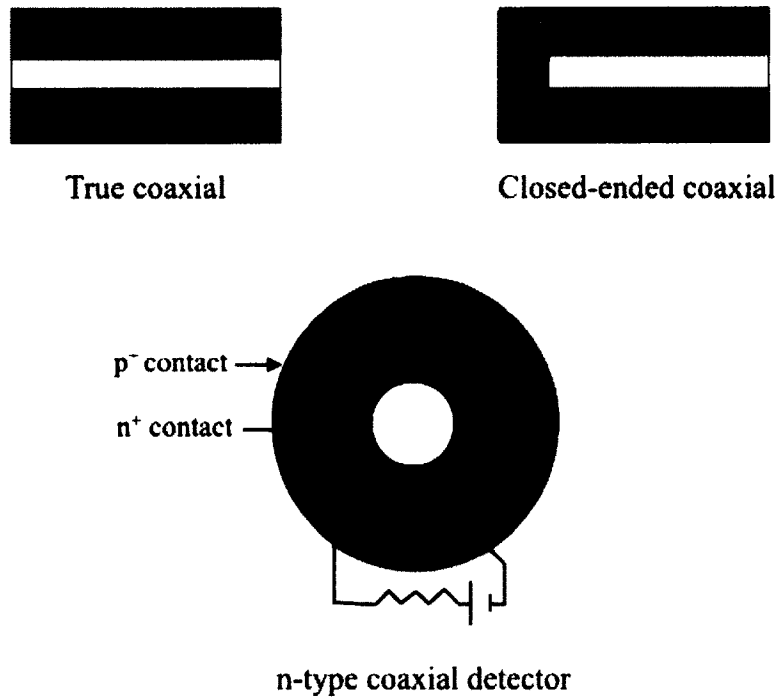
Figure 8.1: Coaxial HPGe detector configuration.

The combination of high stopping power, large sensitive volume and better energy resolution make these detectors unique among its kind. HPGe based advanced detectors and methods of data analysis, where determination of γ-ray interaction position is crucial, is attained by a two-dimensional segmentation of the

143

detector surface. This enables a three-dimensional position sensitivity through the analysis of pulse shapes, as explained in the next section.

8.2 Pulse Shape Analysis

The value of potential at any point inside a detector of defined geometry is found by solving the Poisson equation:

$$\nabla^2 \phi(r) = -\frac{\rho(r)}{\epsilon} \tag{8.4}$$

where $\rho(r)$ = en, is the space charge density, e is the electron charge and $\epsilon = \epsilon_0 \epsilon_r$ is the dielectric constant with $\epsilon_r = 16$ for a germanium detector, n is the impurity concentration. After calculating the potential map in the detector, the electrostatic field can then be found using:

$$E(r) = -\nabla \phi(r). \tag{8.5}$$

For a simple coaxial geranium detector with inner and outer radii of r_1 and r_2, the electric field is given by:

$$E(r) = \frac{\rho r}{2\epsilon} - \frac{1}{r} \left[\frac{V + \frac{\rho}{4\epsilon}(r_2^2 - r_1^2)}{ln\frac{r_2}{r_1}} \right] \text{ [86]} \tag{8.6}$$

where V is the applied reverse voltage. A current I(t) is induced inside the detector because of the drift of electrons and holes towards the electrodes. This induced

current is determined by the charge amplitude Q_0, the weighting field $E_w(r)$, and the charge drift velocity $v_{e,h}(r) = dr/dt$:

$$I(t) = Q_0 E_w(r) \frac{dr}{dt}. \qquad (8.7)$$

The weighting field E_w of an electrode is defined as the electric field calculated by solving the Poisson equation 8.4, taking a potential 1 Volt on the considered electrode and zero on all the other electrodes of a segmented detector [87].

When this induced current is integrated over the long time constant of the measuring circuit, it gives the corresponding induced charge $Q(t)$. For a coaxial geometry with electric field given by equation 8.6, the induced charge is,

$$Q(t) = \frac{Q_0}{ln\frac{r_2}{r_1}} \left[ln(1 + \frac{v_e t_e}{r_0}) - ln(1 - \frac{v_h t_h}{r_0}) \right] \quad [86] \qquad (8.8)$$

where r_0 is the position where the charges are created and t_e and t_h are the electron and hole collection times respectively. The instantaneous charge reaches its maximum value Q_0 when both the electrons and holes are collected at their respective electrodes. The induced charge is thus a function of both the electron and hole mobility which implies that the signal has two components, one corresponding to the drift of electrons and the other related to the drift of holes, as shown in Fig. 8.3. This feature is exploited by the Pulse Shape Analysis (PSA) algorithms in order to determine the location of the γ-ray hit. The amplitude of a pulse corresponding to a particular interaction point is proportional to the energy absorbed at that point.
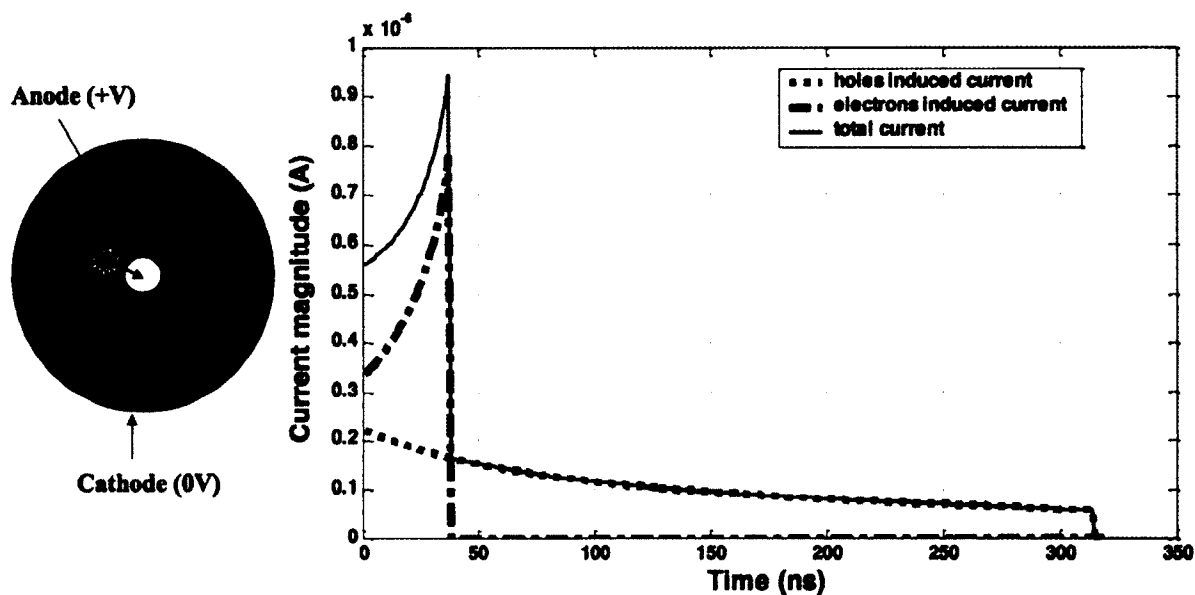
Figure 8.2: The moving charges induces a signal on the detector's electrode. Here, for a coaxial detector signal is shown to be summed contribution of electrons and holes.

Pulse Shape Analysis in a co-axial HPGe detector

The shape of the net charge pulse from either of the electrodes in a coaxial germanium detector provides information about the radial interaction position [86]. Fig. 8.4 shows an example of three different interaction points labelled as 1, 2 and 3 inside a coaxial HPGe detector. For net charge signals resulting from γ-ray interactions occurring in the vicinity of either of the electrodes, the pulse rises slowly because either the electrons or the holes have to travel a longer distance. Although both the pulses (1) and (3) have long rise time, they have different shapes because of different dominant charge clouds (holes in one case and electrons in the other). When the interaction takes place in the middle of the detector active volume the

pulse rises faster as electrons and holes have to travel the same distance. The radial interaction information is thus extracted from the net charge signal.
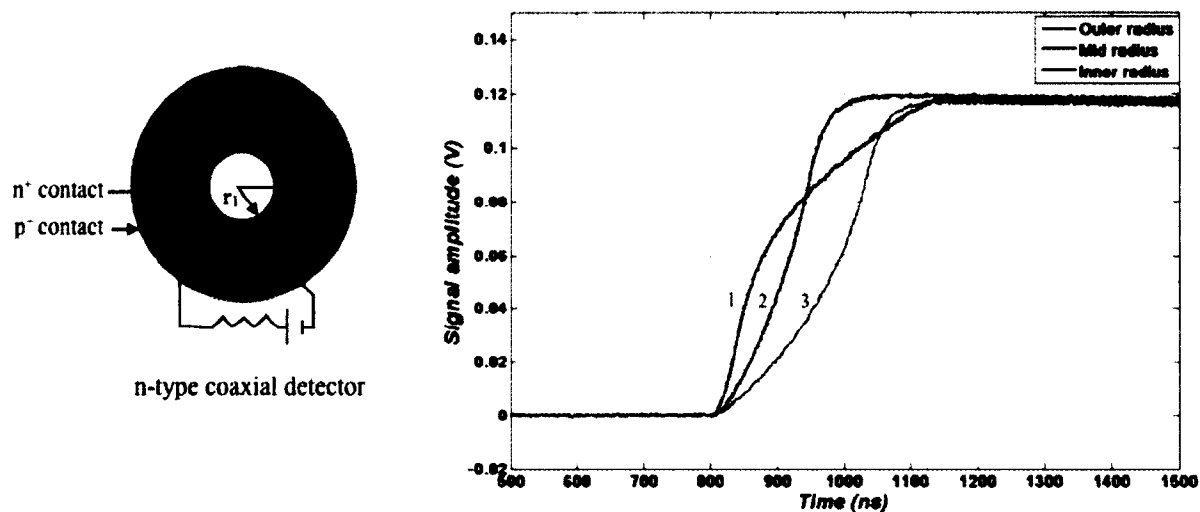
Figure 8.3: Calculated detector signals from co-axial detector with 3 interactions at different radii.

Contact segmentation and azimuthal information

If the electrodes on the germanium detector are segmented, separate pulses are obtained from each segment. The position sensing can be extended beyond just the radial coordinate by comparing the size of the individual electrode signals [44]. For a photon striking a segmented detector, two types of signals are available: (1) the net charge signal from the segment hit by the γ-ray and (2) the transient induced signals from the neighboring segments, also called mirror signals. The motion of the charges in the segment hit by the gamma ray induces a charge in the neighboring segment. The transient signals therefore have non-zero values only

for the time when the charge is drifting in the segment hosting the interaction. Transient signals carry azimuthal position information.

This is illustrated in Fig. 8.5 (a, b, c) for the case of an GRETINA crystal, which is a 36 fold segmented germanium detector. The highlighted part of the detector (b), shows the main segment (γ, 3), where three events takes place and rest are the adjacent segments from where mirror signals are collected. The pulse shapes (c) shows that the mirror charge signal amplitude will be higher if the interaction takes place close to the boundary of two segments and the amplitude decreases as the distance of the interaction point from the segment boundary increases.

From the above discussion of the charge pulses from a segmented coaxial detector, it is evident that the rise time and the shape of signals from a net charge collecting segment gives information about the radial interaction position, while azimuthal information is given by analyzing the transient signals. The charge drift velocity is a key parameter which directly affects the variation of the observed signals, as discussed in the next section.
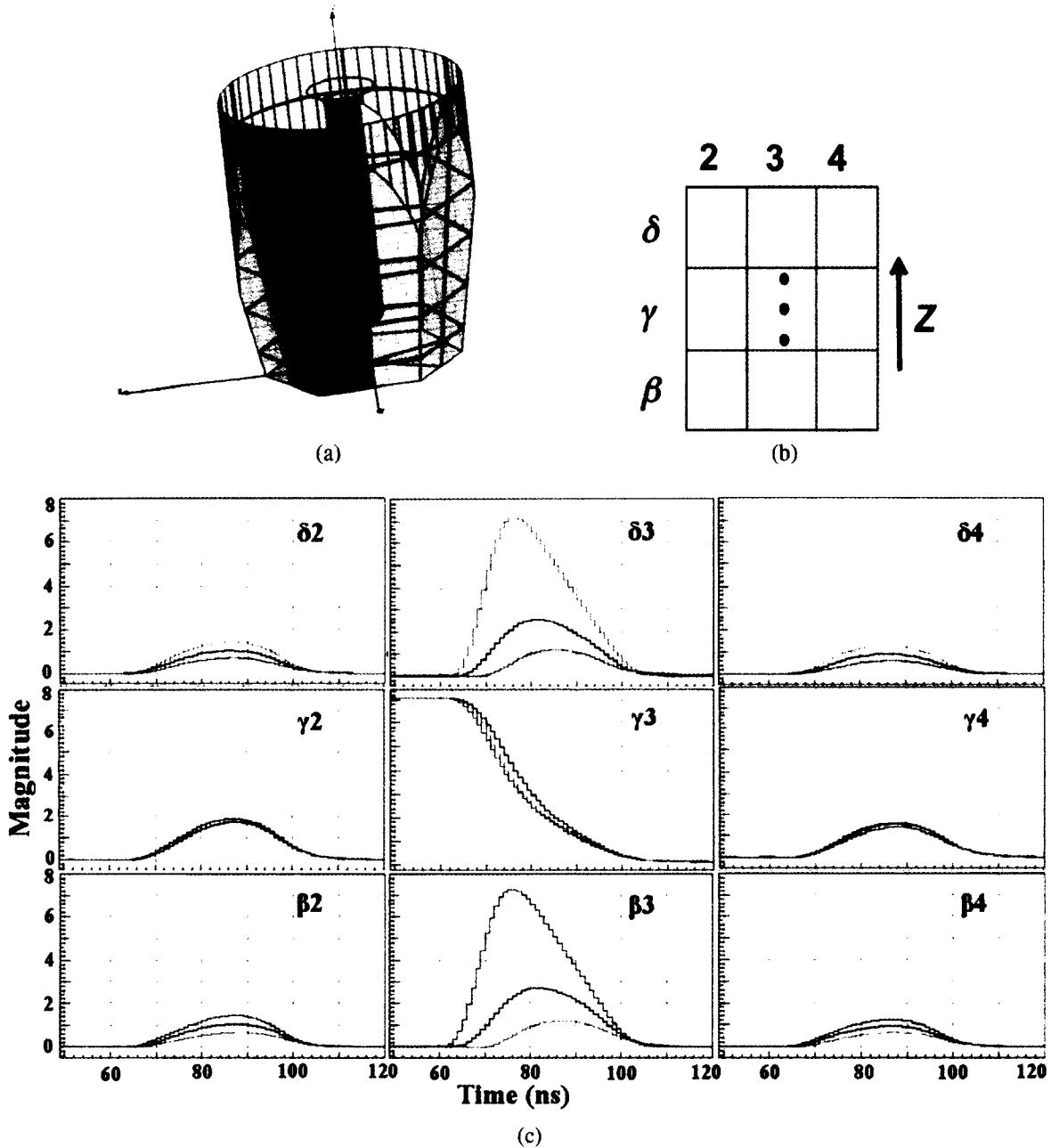
Figure 8.4: (a) 36-fold HPGe GRETINA detector. (c) Example of charge signals corresponding to three different interaction positions in segment 3 (as shown in (b)). For each interaction position, the net charge signals from contact $\gamma 3$, corresponding to a fully absorbed γ-ray, and the respective transient charge signals induced on the eight adjacent segments are shown.

Charge Mobility

At low-to-moderate values of the electric field intensity at a position r in the detector, the drift velocity $v_{e,h}(r)$ of either the electron or the hole is approximately proportional to the electric field, E(r). The corresponding proportionality factor is defined as a quantity called mobility of the charge carrier.

$$v_{e,h}(r) = \mu_{e,h}(r)E(r) \qquad (8.9)$$

At higher electric field values, the drift velocity increases more slowly with the field. Eventually, a saturation velocity is reached which becomes independent of further increase in the electric field. The conductivity in Germanium is anisotropic, i.e. the mobility of electrons and holes varies depending on the direction of the applied electric field with respect to the direction of lattice vectors.

The investigation of charge carrier drift velocities in germanium crystals at high electric fields and low temperature, and its influence on the charge collection process in HPGe detectors has been area of continuous and active interest for a long time. The major part of the experimental results reported in the previous works have been obtained with either the time-of-flight technique or other techniques, like Hall effect, which are based on the measurement of the time that electrons or holes created by a suitable ionizing radiation spend to cross a known thickness of sample under the effect of an applied electric field E [88]. These techniques give mobility parameters which are not affected by trapping and de-

trapping effects. Therefore they are less useful, especially in the case of germanium based detectors, where such effects are present [89].

The experimental evidence for the dependence of pulse shapes in closed-end HPGe detectors on the electron drift velocity anisotropy has been clearly established, as well as its influence on the signal processing methods required to perform the PSA [90]. In contrast to the electrons, for which a lot of theoretical as well experimental studies have been carried out in the past, for holes no direct applicable description of the anisotropic mobility exists in literature. This is due to the rather complicated mathematical description of germanium valence band [91]. A quantitative determination of hole mobility parameters is difficult and away from the purpose of the present work. In section 9.3, a methodology to determine the currently used values of these parameters for GRETINA detector is given.

8.3 Detector Operational Characteristics

Pre-amplifier

The total amount of free charge produced in a detector by a typical gamma-ray interaction is too small to be accurately measured. In order to operate a detector it must be coupled with electronics components to process and record the charge produced. To raise the magnitude of the signal to an appreciable level,

and minimize the effect of electronic noise picked up between the detector and measurement electronics, preamplifier circuitry is employed [86].

If pulse shape information is to be used to extract the position of interaction, it is necessary to preserve the signal shape as much as possible. For this purpose, a charge sensitive preamplifier with high gain and low noise is typically used. In a charge-sensitive preamplifier, the charge carried by the incoming pulse is first integrated on a capacitor and then removed by a slow discharge through a resistive feedback network. The output pulse amplitude is proportional to the charge produced by the γ-ray interaction. The time constant (RC) determines the decay rate of the output pulse [92].

Cross-talk

The complex electronics of segmented detectors imposes limitations on the size of the preamplifiers and the length of connection wires. One of the most common problem is capacitive coupling between detector crystal and individual channels associated with its electronics [93] [94]. This results in crosstalk between the channels whereby a real signal on any channel can produce an induced transient signal on each of the others. The shape of the induced signal has two components, one proportional to the magnitude of the real signal and one proportional to the differential of this signal [95]. Electronics should be designed and shielded in order to minimize this effect, which directly affects the pulse shape analysis.

An overview of state-of-the-art for pulse shape analysis to extract 3D position information of a γ-ray interaction in segmented GRETINA detector array is presented in the next chapter.

Chapter 9

Ingredients of Gamma-Ray Tracking

In the last decade, unprecedented R&D efforts have been made world-wide to achieve a number of technical advances which make it possible to construct a gamma-ray detector using the new idea of gamma-ray energy tracking. These are: fabrication of highly segmented HPGe detectors, fast digital electronics, and fast signal analysis algorithms, coupled with increased computing power. In this chapter, a brief overview of gamma ray tracking and its various components in context to GRETINA HPGe array will be discussed.

9.1 Highly Segmented HPGe Detectors

The Gamma Ray Energy Tracking In-Beam Nuclear Array (GRETINA), the first stage of the (future) Gamma-Ray Energy Tracking Array (GRETA), is composed of seven detector modules, each with four high purity germanium crystals, each of which is segmented into 36 electrically isolated elements [96], with six

154

longitudinal and six transverse outer electrical contacts, as shown in Fig. 9.1.

There are two crystal types (A and B) corresponding to the two different irregular hexagonal shapes needed to approximate a spherical surface. Hence seven four-crystal modules (Quads) are referred to in this thesis as Q1, Q2, . . . , Q7 and their individual crystals as Q1A1, etc. Each HPGe crystal is closed-ended, n-type with a tapered hexagonal shape designed to fit in a spherical shell arrangement consisting of about 120 of these detectors. The length of the crystal is 9 cm, the diameter at the back is 7 cm and the maximum diameter at the front is 4.4 cm. The angle of the taper is 10°. The inner core has a length of 7.5 cm and diameter of 1 cm.The six longitudinal boundaries are located in the middle of the flat sides of the hexagonal shape. The width of the transverse segments starting at the front (the narrow side) are 7.5, 7.5, 15, 20, 25 and 15 mm, respectively. The thicknesses of the layers were chosen to distribute the number of the interactions more equally among the segments for the γ-rays coming from the front and to allow the study of the influence of different thicknesses on the transient-signal sensitivity. The Ge crystal resides in a 1 mm thick aluminum can of the same shape as the crystal. This can is separated from the crystal by 1 mm to simulate a close packing of individually encapsulated detectors.The 37 FETs for the 36 segments and the central channel are located and cooled in the same vacuum as the crystal. Cold FETs provide low noise which is important for optimizing the energy and position resolution. The charge-sensitive preamplifiers are positioned on a cylindrical motherboard next to the vacuum feed throughs in the back of the detector. These

preamplifiers and their mount are designed to be of small size, fast rise-time, low noise, and excellent response properties. More details on the GRETA prototype detector and the preamplifiers can be found in [96, 97].
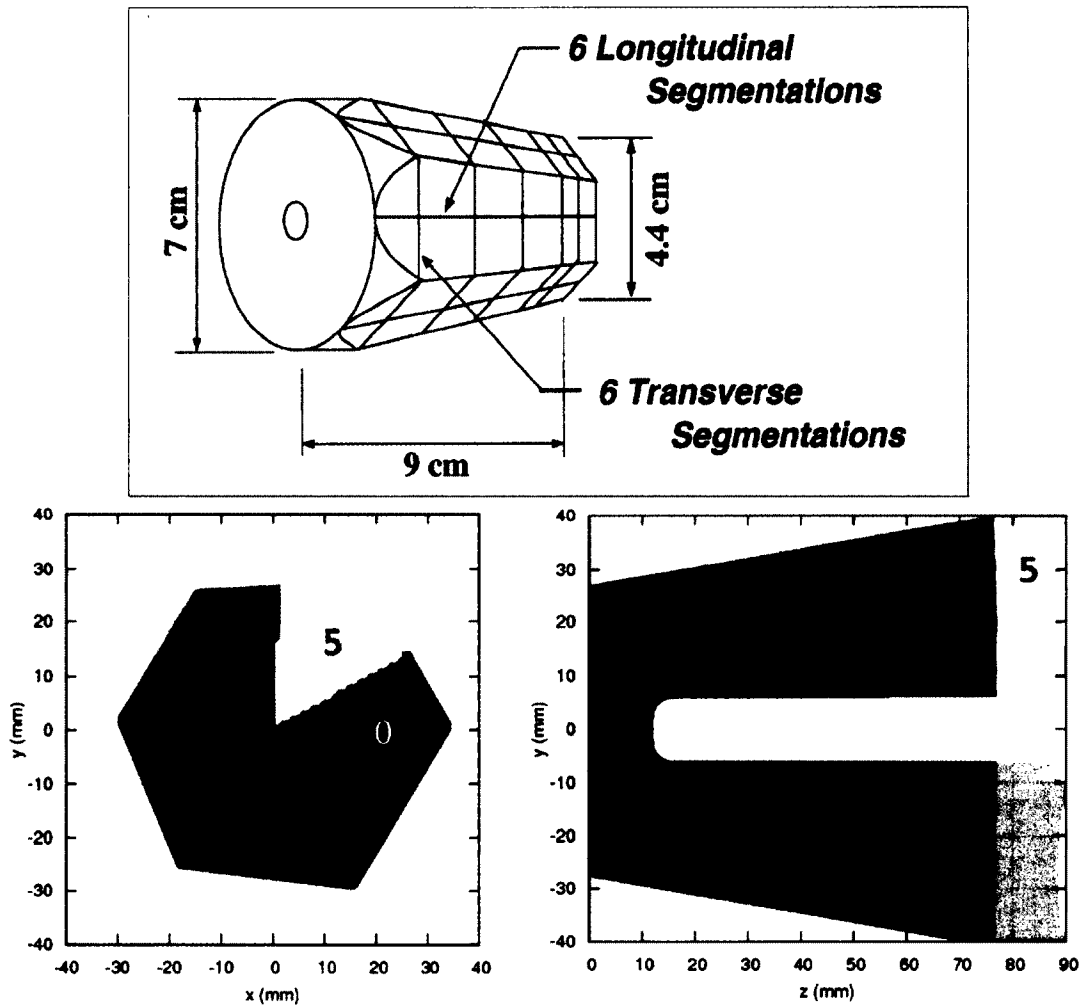
Figure 9.1: The upper part shows GRETINA prototype detector with its tapered hexagonal shape and the arrangement of the 36 segments [96]. The lower part shows schematic representations of an asymmetric GRETINA detector. The image on the left shows a slice through z = 0 mm while the plot on the right shows the longitudinal segmentation by slicing through x = 0 mm [98].

156

9.2 Digital Electronics and Data Storage

In addition to the highly segmented Ge detectors, the effective working of such an array requires digital sampling electronics to extract energy, time, and position information from the detectors output signals using pulse-shape analysis methods. The detector module components include charge sensitive amplifiers as assembled inside the enclosure to instrument each of the 36 segments and the central contact. The gamma ray interaction with the germanium crystal induces charge on the segments and central contacts. The amplifiers integrate this charge and drive an analog voltage to the GRETINA front end electronics. Two custom designed modules, the Digitizer/Digital Signal Processing (DSP) and the Trigger Timing and Control (TTC), compose the electronics of the GRETINA. Fig. 9.2 shows a block diagram of the GRETINA Electronics and Computing system.
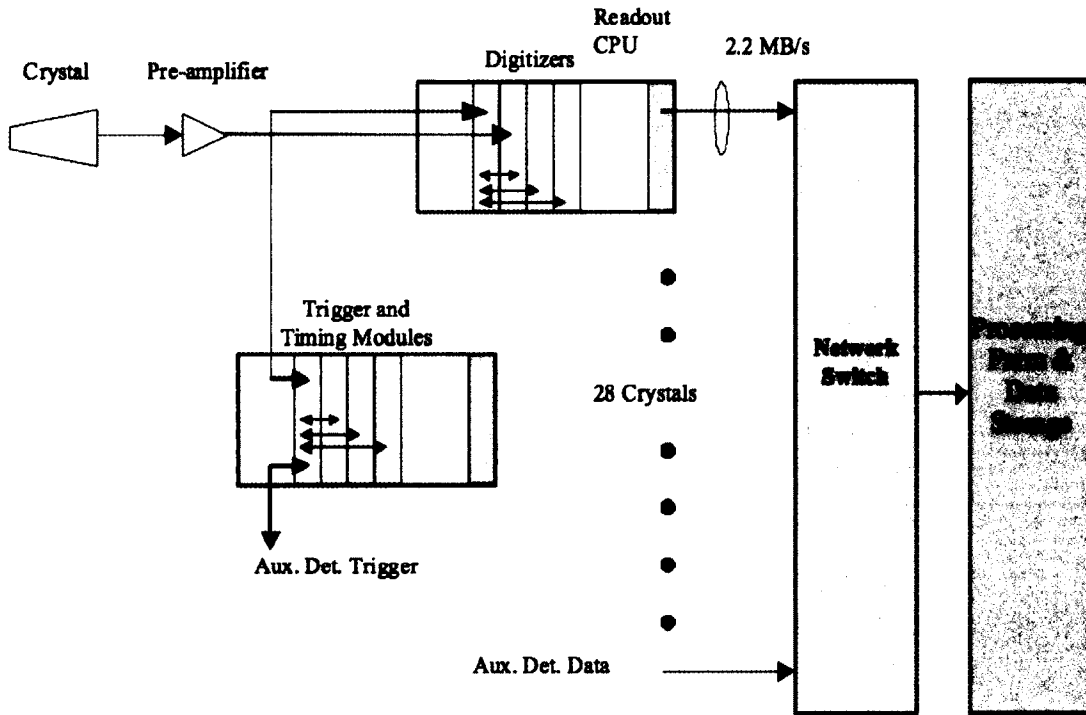
Figure 9.2: Block diagram of GRETINA electronics and computing system [99].

Each Digitizer/DSP and TTC module is implemented using two field programmable gate arrays (FPGA): one is a smaller FPGA, which controls the VME interface and has a steady configuration, and the other is a large FPGA which executes the module specific algorithms. The large on-board FPGA drives an energy, leading-edge time, and constant-fraction time from the input signal providing the functionality of conventional analog electronics system [100]. Readout and control of the digitizer is done over a VME bus. The TTC module supports three triggering modes: internal or self-trigger, external trigger, and validation trigger, which makes it efficient and flexible triggering system. The data acquisition sys-

tem includes 100MHz 14-bit digitizer modules and trigger modules [101].

9.3 Signal Decomposition

To extract the position information from the obtained pulse shapes in real-time, they have to be compared to shapes already known for each point of the detector. In principle, the shapes can be experimentally registered, using tightly collimated γ-ray sources and requiring for a Compton scattered γ-ray to have a coincidence with an external collimated detector. It has however been shown that these are extremely lengthy measurements if the required position resolution is of $\approx$ 2mm [102, 103]. The only viable way is then to calculate these pulse shape. The methodology for generating a basis of pulse shapes, varying according to the position of the charge generating interactions, and determining the interaction position using pulse shape analysis is in place for GRETINA and is discussed in the following subsections.

9.3.1 Raw basis

The pulse shape calculations are performed by the software codes structured in a progressive way, starting from the crystal geometry to characterize and up to the generation of the expected pulse shapes at the contacts, as described in Ref. [104].

Electric field and weighting potential

The electric field intensity influences the charge carriers drift velocity. There-fore, its distribution in the Ge volume is important in defining detectors response characteristics like rising time, signal forming, etc. The electric field inside the detector and the weighting potential for each outer segment contact are calcu-lated using either the finite element method or relaxation method (Fieldgen soft-ware [105]). The weighting potential is an artificial potential which measures the capacitive coupling between the electrodes and the moving charge [87]. It is cal-culated by solving the Laplace equation (i.e. Poisson's equation with zero space charge density) with unit voltage on the considered electrode and zero voltage on all the others. In the calculations, both the geometry and the material properties of the detector are carefully taken into account, including the space charge den-sity profile provided by the detector manufacturer. Fig. 9.3 shows electric filed and weighting potential calculated for a GRETINA detector. The solution for the electric field and weighting potential is tabulated on a mm grid.

The electric field is used to calculate the drift path of electron and holes for a given start position on the grid by using the following relation for velocity:

$$v(E(r) = \mu(T, E(r), \varepsilon, \vartheta)E(r) \tag{9.1}$$

In this calculation, electric field is interpolated between the grid points and a given time interval t of (e.g.) 2 ns, small enough to prevent discontinuities in the drift
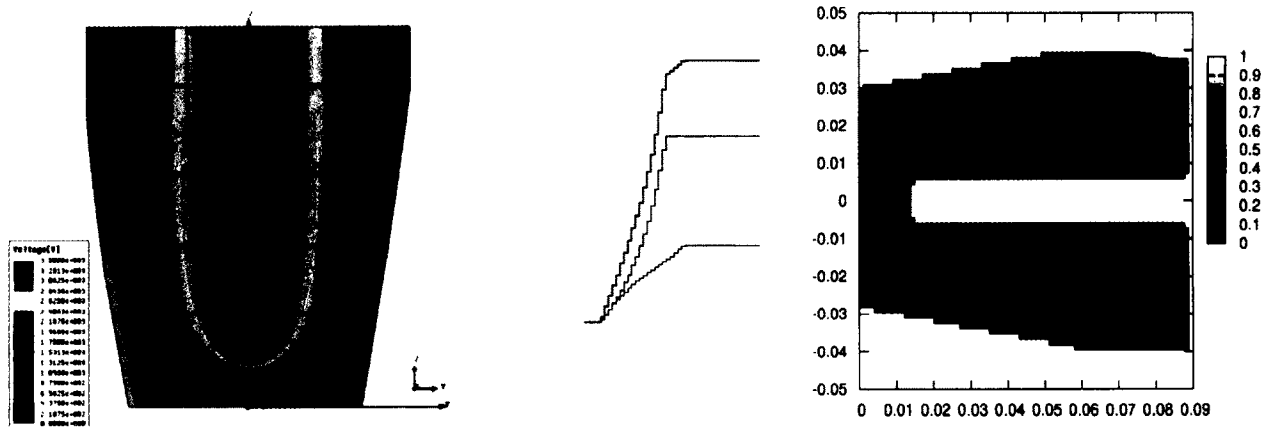
Figure 9.3: Left: Electric field for n-type coaxial GRETINA detector, where electric filed strength is seen to be decreasing as we move away from the positively charged core. Right: Weighting potential for GRETINA, where one segment is at potential 1V and rest are at 0V [106].

velocity. Here mobility μ is not only a function of the temperature (T) and electric field but depends also on the angle between the drift direction and the crystal orientation (ε) and the angle between the electric field and the crystal orientation (ϑ). The temperature, electric field strength and crystal orientation dependence for the magnitude of the mobility of electrons and holes in germanium and the anisotropy in the magnitude of electron and hole velocities for GRETINA detectors is implemented using a parameterization discussed in next section.

Drift velocity parameterization for GRETINA

A drift velocity model which is based on calculation of the drift velocities of electrons and holes, for any magnitude and direction of field, from the known drift velocity (either measured or calculated) along the three major Ge crystal axes, is used in the pulse shape calculation programs for creating the GRETINA basis [107]. This model also include the temperature dependence of the drift veloc-

ity which reduces at higher temperature due to the increasing of scattering with the lattice vibration. Drift velocities for electron and holes in high-purity Ge ($|N_D$ - $N_A|$) $\leq 10^{10}$cm^{-3} has been deduced for a wide range of temperatures $77 \leq T \leq 100°K$ and field $1 \leq E \leq 5000$ V/cm applied parallel to <100>, <110>, <111> crystallographic directions, given in Table 9.1.

Table 9.1: Tabulated are the drift velocity parameters [mm/ns] of electrons and holes along the three principal Ge crystal axis <100>, <110>, <111> currently used in GRETINA basis generation. Hcorr and Ecorr gives the temperature dependence correction coefficients for respective drift velocities [107].

E [V/cm]	e100	e110	e111	h100	h110	h111	Hcorr	Ecorr
0	0.0	0.0	0.0	0.0	0.0	0.0	-3.0	-2.1
100	0.027	0.027	0.027	0.036	0.033	0.031	-2.349	-1.748
160	0.038	0.039	0.0386	0.047	0.043	0.040	-2.04	-1.57
240	0.0490	0.050	0.048	0.056	0.051	0.048	-1.72	-1.36
300	0.055	0.055	.0525	0.06	0.055	0.0525	-1.533	-1.225
500	0.074	0.07	0.065	0.072	0.065	0.062	-0.984	-0.832
600	0.081	0.077	0.069	0.077	0.069	0.065	-0.82	-0.70
750	0.089	0.086	0.073	0.081	0.073	0.069	-0.657	-0.581
1000	0.101	0.095	0.078	0.086	0.077	0.073	-0.505	-0.461
1250	0.109	0.102	0.0825	0.089	0.08	0.076	-0.426	-0.397
1500	0.116	0.106	0.086	0.0925	0.082	0.078	-0.380	-0.360
1750	0.119	0.111	0.087	0.095	0.084	0.08	-0.352	-0.337
2000	0.122	0.113	0.088	0.097	0.086	0.082	-0.332	-0.321
2500	0.125	0.1167	0.091	0.1	0.088	0.084	-0.310	-0.302
3000	0.1275	0.1175	0.0925	0.1025	0.091	0.086	-0.297	-0.292
3500	0.1283	0.1183	0.0928	0.1036	0.093	0.091	-0.289	-0.285
4000	0.1288	0.1188	0.0930	0.1041	0.0945	0.093	-0.284	-0.281
4500	0.1291	0.1191	0.0932	0.1045	0.096	0.095	-0.281	-0.278
5000	0.1293	0.1193	0.0933	0.1047	0.097	0.096	-0.278	-0.276

Signal generation

The knowledge of the charge trajectory and weighting fields allows the signal shape to be derived. For each crystal, a simulation is performed where a unit charge is placed at a given point in the crystal and the net and transient currents induced on each of the 36 segment contacts are calculated (Siggen software [108]). This procedure is carried out on a grid of points, as shown in Fig. 9.4, whose spacing reflects the sensitivity of the detector. Fig. 9.5 shows logic scheme of a pulse shape calculation software. The set of these simulated pulse shape signals is termed a "basis".
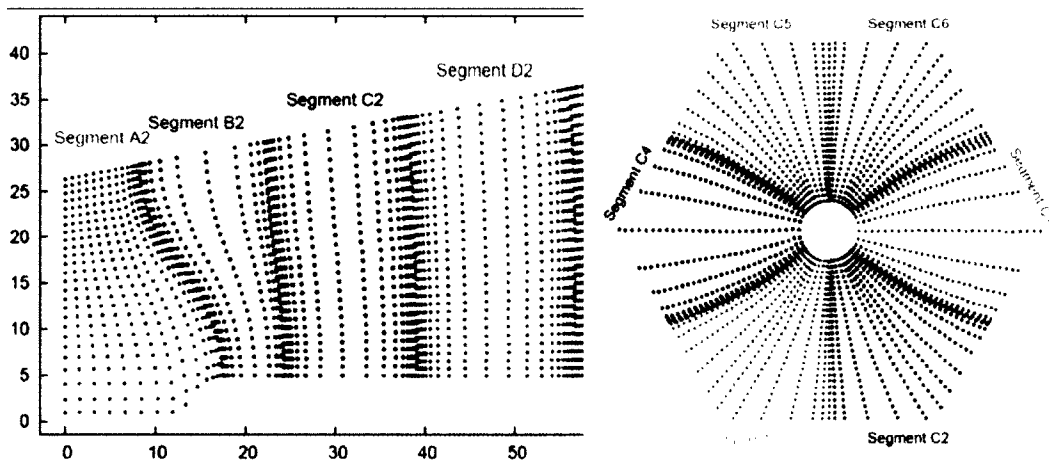
Figure 9.4: A fraction of the grid points used in the non-uniform GRETINA basis grid is shown [109].
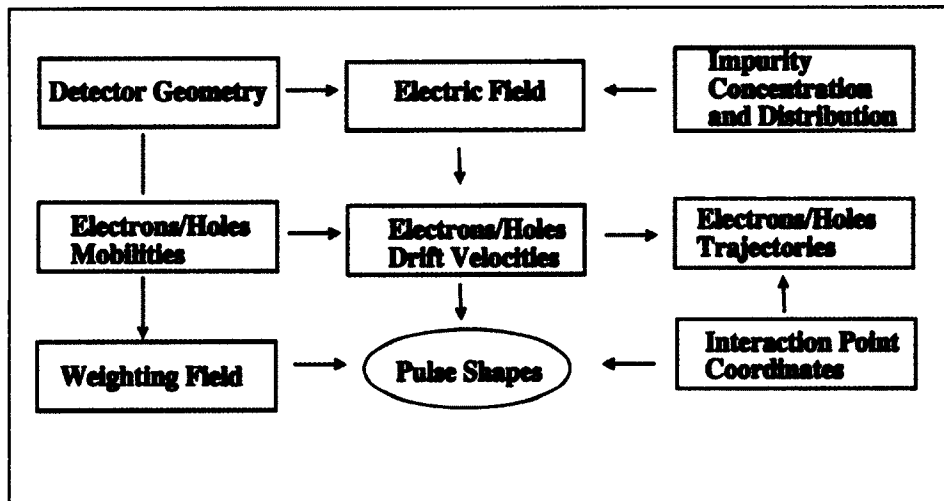
Figure 9.5: Flow chart showing the basic steps used to compute the expected signal shape.

9.3.2 Detector response corrected basis

The simulation for creating a "basis" library involves the geometry of the crystal, the bias voltage, charge carrier drift velocities and a model of the net charge distribution arising from crystal impurities. This idealized model of the crystal is not sufficient when applied to real signals, since corrections must be made for detector and electronic-response characteristics such as preamplifier shaping, relative time delays, and integral and differential cross-talk. Fig. 9.6 shows a side view of GRETINA quad housing and followed by the various electronics. Through source measurements, these signals are then corrected for the preamplifier response as well as integral and differential cross-talk between segments. Fig. 9.7 gives various steps, starting from comparing signal traces measured using a ^{60}Co source to a simulation, and then fitting the required parameters.

Experimental data are collected using a digital acquisition system, with a ^{60}Co

source placed at a distance from the detector front face. The same source and detector arrangement are modeled using GEANT4, and the signals from the gamma-ray interactions are reconstructed from an electric field simulation. The events, from both datasets, for which all of the deposited energy is confined to a single segment are then identified and organized according to segment number. The signals from each segment are aligned and a mean response is formed for each [110].
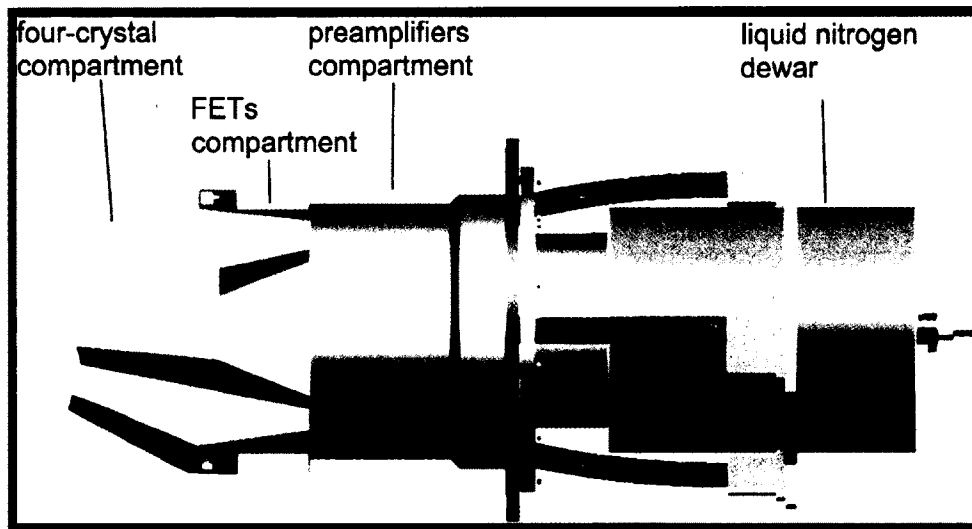
Figure 9.6: A side-view drawing of the GRETINA detector module [110].

For the fitting procedure, the signals from each GRETINA segment, which are read out by 37 pre-amplifiers, connected to 36 segment electrodes and one core electrode, are concatenated in a single pulse train called "superpulse" (Fig. 9.8). A fitting routine, which include integral and differential crosstalk, relative delays between channels and preamplifier shaping, then compare the calculated signals to a set of experimental signals and provide a value for the goodness-of-fit (chi-

squared difference) between them.
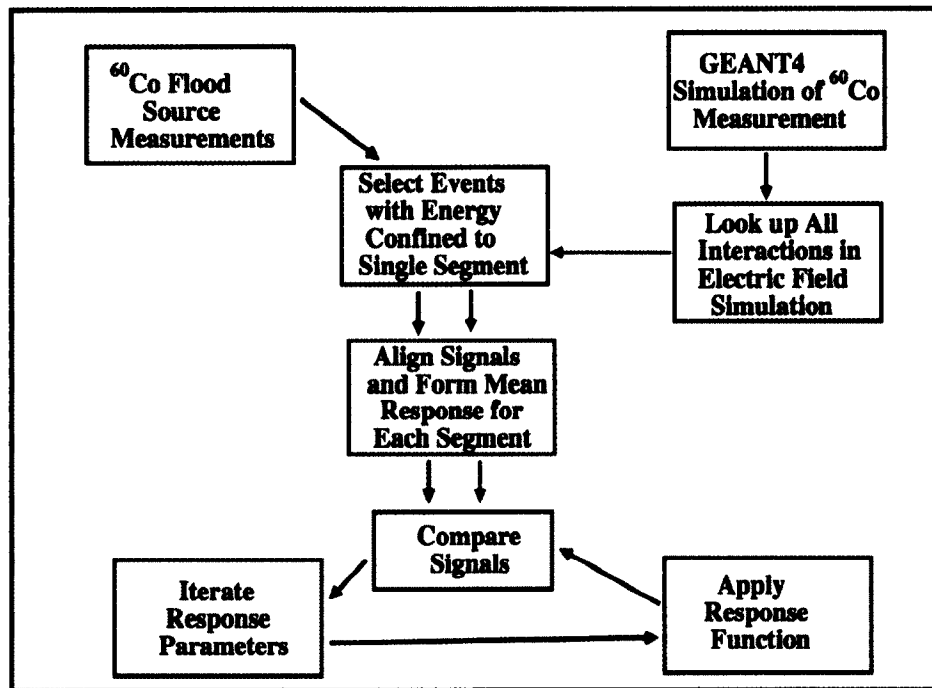
Figure 9.7: The steps for extracting detector response parameters.

The extracted parameters from the superpulse fitting procedure are applied to the "raw basis", which now will have detector responses.
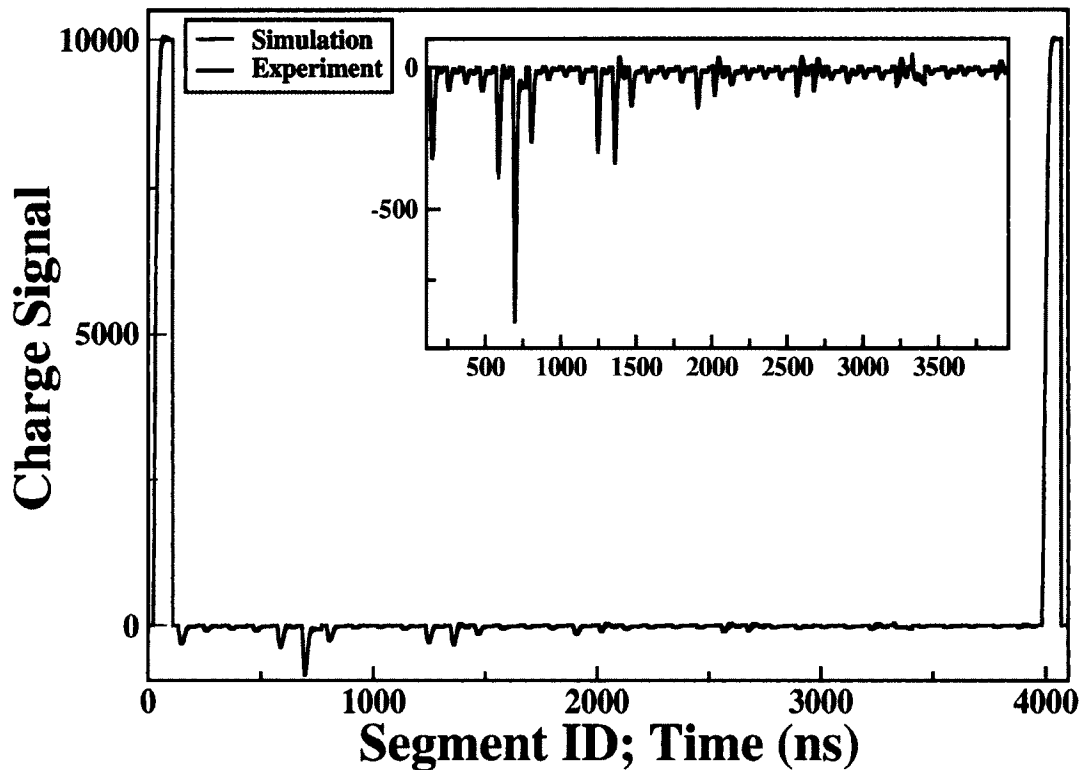
Figure 9.8: A superpulse fit for concatenated traces from 36 segments and central contact from the front face of the detector. Red: generated using the simulated raw basis and Blue: measured in a prototype crystal. Inset highlights the cross talk effects in the measured traces (Blue).

As it is likely that multiple interactions occur within a crystal, the signal decomposition process fits the observed waveform from each crystal segment with a linear combination of these pre-calculated detector response corrected basis signals. The GRETINA decomposition algorithm uses a two-step process which starts with an adaptive grid search for one and two interactions per segment followed by a sequential quadratic programming (non-linear least-squares) fit which

167

allows multiple interactions in multiple segments within a crystal [109, 111, 112]. This process occurs on an event-by-event basis in real time to extract the position and energy of γ-ray interactions.

9.4 Tracking principle

When a γ-ray hits a germanium detector it can deposit some or all of its energy in the detector via three main different mechanisms, as explained in Section 8.1. The most likely mechanism is a Compton scatter where the γ-ray deposits part of its energy to create a charge cloud proportional to the energy lost and then scatters at an angle determined by the incident energy and the lost energy. The γ-ray now does one of three things: it either leaves the detector (depending on scatter angle and the location of the first Compton scatter), or it goes on to lose all its remaining energy by photo-absorption somewhere in the detector, or it loses part of its energy in another Compton scatter where part of the remaining gamma-ray energy is absorbed, releasing another charge cloud. Typically a gamma ray deposits energy in 3 or 4 places within a detector by 2 or 3 Compton scatters and a final photo-absorption. At each of these 3 or 4 interaction sites a charge cloud of electrons and holes is created (Fig. 9.9). The charge carriers are transported towards either the cathode or the anode under the influence of the detector's bias voltage.
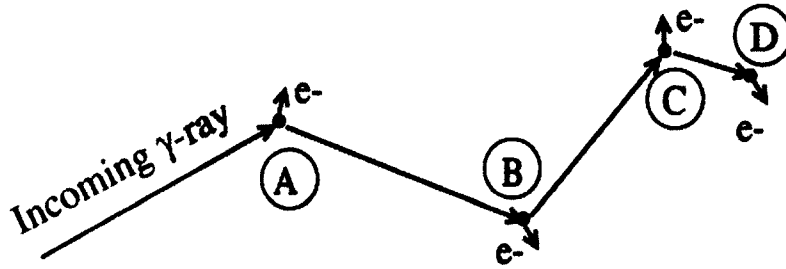
Figure 9.9: Pictorial representation of series of interaction points for a γ-ray entering in a detector volume, where it undergoes 3 Compton scatters at points A, B and C, releasing charge proportional to its energy loss at each point, before losing all its remaining energy at point D by photo-absorption.

Gamma-ray tracking is a technique which correlates and reconstructs the multiple interactions of a single γ-ray in a segmented germanium (Ge) detector or in an array of such detectors. The tracking process uses the energies and positions of the interaction points produced by the signal decomposition to determine the scattering sequence for a particular γ-ray. The locations of A, B, C and D are determined based on the segmentation of the Ge detector, pulse shape analysis and finally on the robustness of signal decomposition code [113].

Tracking algorithms

Different codes have been developed by the GRETINA collaboration to track events based on Compton scattering, pair-production and photo electric interac-

169

tions [114]. These rely on the fact that although points A, B, C and D in the diagram above can be ordered in 24 different ways, only 1 of these sequences will obey the Compton scattering formula (Equation: 8.2) relating the energy deposited at A, B and C to the angle between the scattered and the incoming γ-ray. The initial approach carried out to build the tracks can be either: Back-tracking and forward-tracking algorithms [115]. Back-tracking starts with the reconstruction of the interaction sequence taking as the initial point the last interaction. It is assumed that a photoelectric absorption has taken place and then it goes back trying to reconstruct the path of the ray until the initial source is reached. Conversely, forward-tracking codes make a clusterization of the interaction points according to their relative angular separation in order to assign each cluster to a given γ-ray. The starting point is the emitting source and then the algorithm follows all the interactions until the photon is fully absorbed in the detector.

Gamma-ray tracking technology opens up two new areas of detection physics: firstly by better Doppler broadening correction and secondly the design of efficient 4π gamma ray detector arrays (germanium shells) without the need for conventional escape suppression shields. To sum up this detection concept, whose success depends on the quality of the position information, has five main advantages over existing γ-ray detector arrays:

- Increase in efficiency due to proper summing of scattered γ-rays and no solid angle lost to suppressors.

170

- Good peak-to-background ratio using tracking plus Compton rejection.

- Excellent position resolution - better Doppler correction.

- Polarization sensitivity - from the angular distribution of the first scattering.

- High counting rate per crystal - due to the large number of segments.

The central part of GRETINA is the Ge detector modules, one of which is shown in Fig. 9.1. These modules have been under extensive performance tests, including energy, time and position resolution measurements, as well as pulse rise time and cross talk properties. The position resolutions, which is a critical parameter for the overall performance of the array, as measured using collimated sources and data analyzed with the latest signal decomposition and tracking algorithms, are about 5 mm depending on location of the interaction point in the crystal [116] [117].

The next chapter presents the use of GRETINA's current state-of-the-art for basis generation, sginal decomposition and tracking algorithms to explores its position resolution sensitivity to charge carrier drift velocities, which are integral part of signal decomposition.

Chapter 10

Detector Characterization and Result

Interpretation

GRETINA depends on sophisticated digital signal processing, which consists of decomposition algorithms, for the information it needs to track gamma rays, and therefore require these to be accurate and efficient in calculating energy and position of an interaction. This chapter presents a Monte Carlo (MC) and experimental characterization of a GRETINA germanium (Ge) detector with an aim to check sensitivity of signal decomposition codes, specifically to the hole mobility parameter.

10.1   Experiment: ^{137}Cs Source Run at NSCL

GRETINA is designed to move from laboratory to laboratory to take advantage of unique capabilities at different facilities. It arrived at National Supercon-

172

ducting Cyclotron Laboratory in early 2012 for its first science campaign. At NSCL, initial experiments were carried out with the goals such as 1) source calibration measurements 2) use of the results of an end-to-end analysis to determine the detector position resolution and the accuracy of signal decomposition and 3) to demonstrate the feasibility of using time stamps to correlate GRETINA data with data from S800 mass spectrograph.

Data from the source calibration runs were used for the analysis. To check the performance of GRETINA signal decomposition codes a ^{137}Cs source run was analyzed. To further check working of currently available tracking code, as discussed in chapter 9, the interaction points given by decomposition were used as an input. A first look at the tracked experimental data points out that decomposition seems to favor center and the edges of crystal, as shown in Fig. 10.1.

(a)
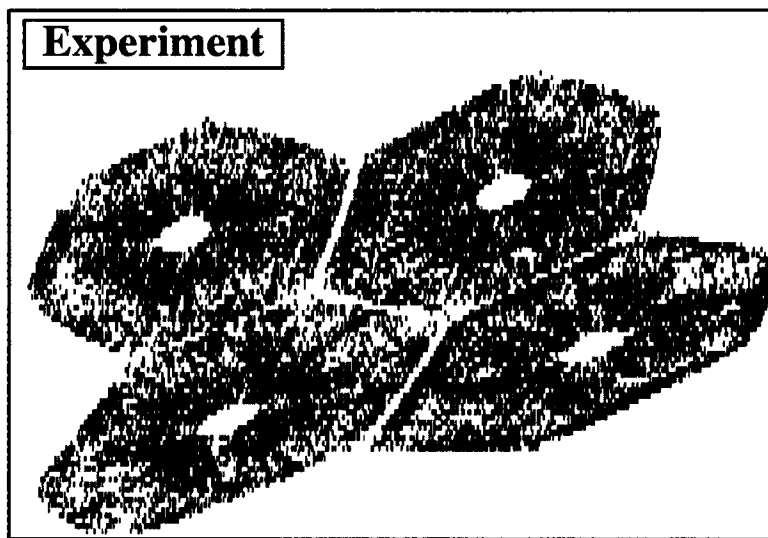
(b)

Figure 10.1: Upper panel (a) shows a single GRETINA quad. Lower panel (b) shows the interaction points determined from the signal decomposition algorithm for one such GRETINA quad.

174

10.2 Simulation: ^{137}Cs Source Run Using GEANT4

To further investigate this atypical accumulation of events, the MC simulations were performed with UCGretina, a GEANT4 simulation of the GRETINA setup [118]. The geometry of the asymmetric GRETINA detectors are defined in this package as they are described in the detector's technical documentation. To compare the results with the above experiment, an open ^{137}Cs source was placed at same distance and simulations were carried out to collect interaction points and energy of the gamma rays (shown in Fig. 10.2 (a)). A tracking code utility was then used to convert this information to an output format similar to as given by decomposition process. As shown in Fig. 10.2 (b), the simulated events as deduced from these algorithms are evenly spread. These inferred interaction points were then further used to test the tracking codes.
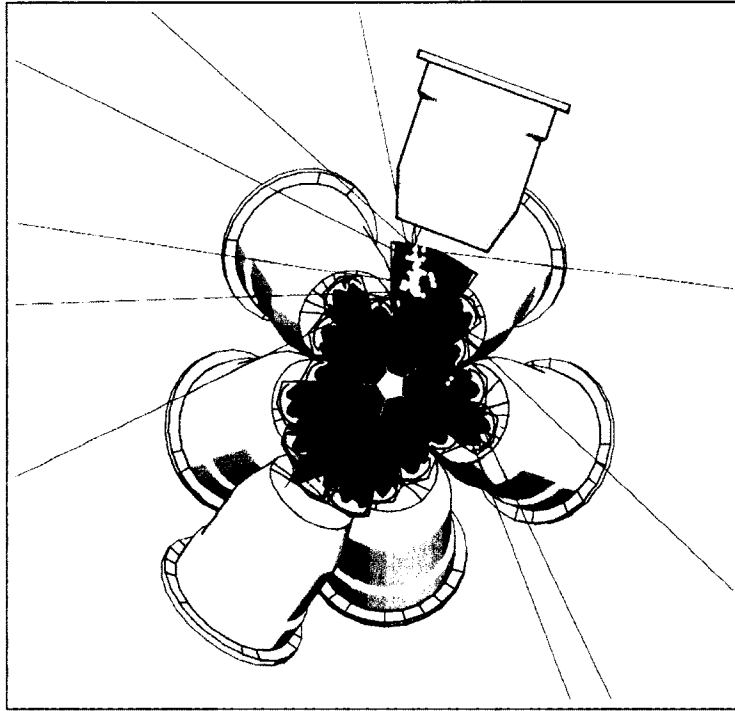
(a)
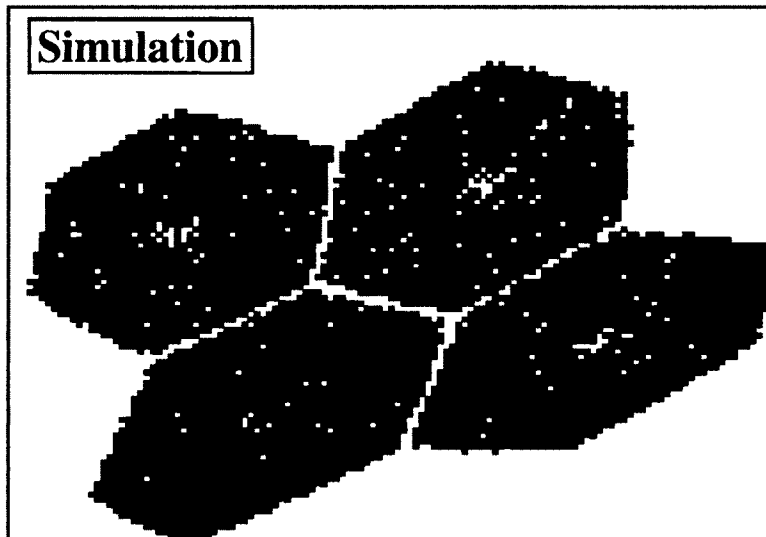
(b)

Figure 10.2: Upper panel (a) shows the GRETINA quads as simulated by the GEANT4 package. Lower panel (b) shows the interaction points determined from the tracking algorithm for one such quad.

176

10.3 Comparison Between Experimental and Simulation

The distribution of all events, deduced by the tracking code, along the GRETINA crystal z-axis for the ^{137}Cs source simulations and experiment, is shown in Fig. 10.3 (a) and (b), respectively. Whereas, the distribution of these inferred interactions along the crystal z-axis drop-off with the depth as expected for both the cases, clustering near segment edges are conspicuous for the experimental data.
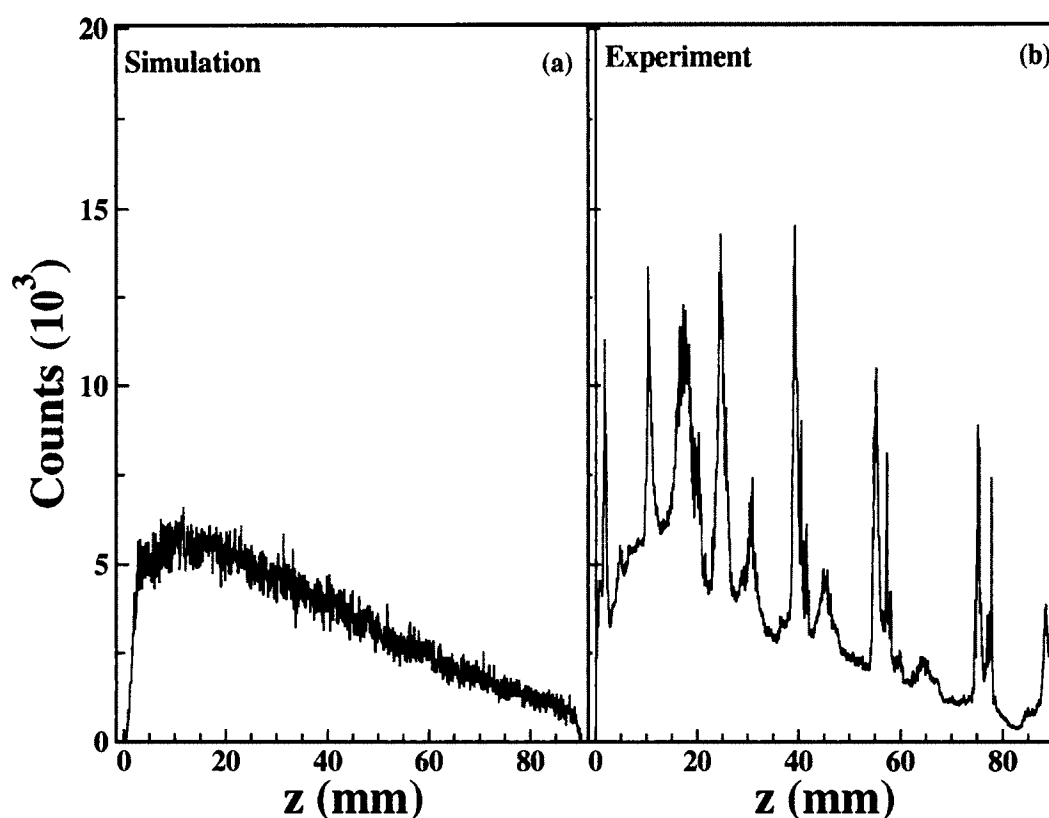
Figure 10.3: The distribution of all events, deduced by the tracking code, along the GRETINA crystal z-axis for the ^{137}Cs source simulations and experiment, in (a) and (b), respectively. The distribution profile of events for simulations show exponential fall-off as expected from the attenuation of γ-rays in HPGe.

From this comparison, it can be inferred that there is a problem in signal decomposition output when looking at experimental data. Possible reasons for this effect of accumulation of events on the segment edges and the center are discussed in this section and the need to investigate the drift velocity parameters is identified.

10.3.1 Possible explanations

Charge sharing

Charge sharing between two neighboring segments for events that should instead be seen by only one of them, poses a challenge in segmented germanium detectors. An interaction within the crystal releases a cloud of electron-hole pairs. The electrons will all drift towards the non-segmented core contact. The situation for the holes is different if the interaction took place in the vicinity of the segmentation lines. In fact, since neighboring segments have nearly the same potential, the transverse component of the electric field in the vicinity of the segmentation lines is quite weak. Therefore, the holes released by the interactions close to that area will travel slowly and, by diffusion, will be shared between the segments. Furthermore, part of them will not be collected within the time of the energy-processing shaper, resulting in some false signals [119]. This effect in terms of effective size of segmentation lines of an AGATA crystal has been discussed in detail in Ref. [120].

Cross talk

Given the 36-fold electrical segmentation of the outer electrode, and even disregarding the aspect related with pulse shape analysis, the operation of the GRETINA crystals is much more demanding than that of non-segmented detectors. In addition to the difficulty of managing 36 + 1 high-resolution channels instead of just a single core, there is the complication of the unavoidable cross-talk among the 37 channels. Furthermore, it is known from the previous studies [102] [121] from the development of Ge-strip detectors and HPGe segmented detectors that the segmentation produces undesirable effects on the energy spectra which should be understood and corrected. It is therefore essential to optimize the data analysis to include these effects in order to reach the best possible performance.

Drift velocities

The drift velocity is an essential input to the calculation of the pulse shapes which are used in the signal decomposition algorithms to determine the position of the interaction points. The drift length of the GRETINA Ge detector has a maximum distance of 35 mm. Thus to maintain an accuracy of 1 mm in position, it is necessary (though perhaps not sufficient) to know the drift velocity with an accuracy of $1/35 \approx 3\%$ in all three dimensions (i.e. 3% in magnitude and 2° in direction).

As mentioned in section 9.3, the hole mobilities and hence their drift velocities are not very well determined, and could very well be responsible for the observed anomalies in determining interaction points. A quantitative determination of hole mobility parameters is difficult and outside the scope of the present work. In the following section, a unique approach to determine the appropriate values of these parameters for GRETINA detector is presented. The experimental measurements and simulations, which were carried out with an aim to ascertain the effect of hole mobilities on GRETINA position resolution are discussed in subsequent sections.

10.4 Varying Hole Mobility: Response of Superpulse Fit

The first task in this work was to optimize the charge drift velocity parameters by adjusting the hole mobilities and minimizing chi-square in the superpulse fitting, which is used to extract detector response parameters. The hole mobility was scaled, as shown in Fig. 10.4, over an appropriate range around its currently used parameters (Table 9.1). Using these scaled parameters, "raw" bases were created for a range of scaled hole mobilities, from 30% less to 30% more than the current used values, in 5% steps.
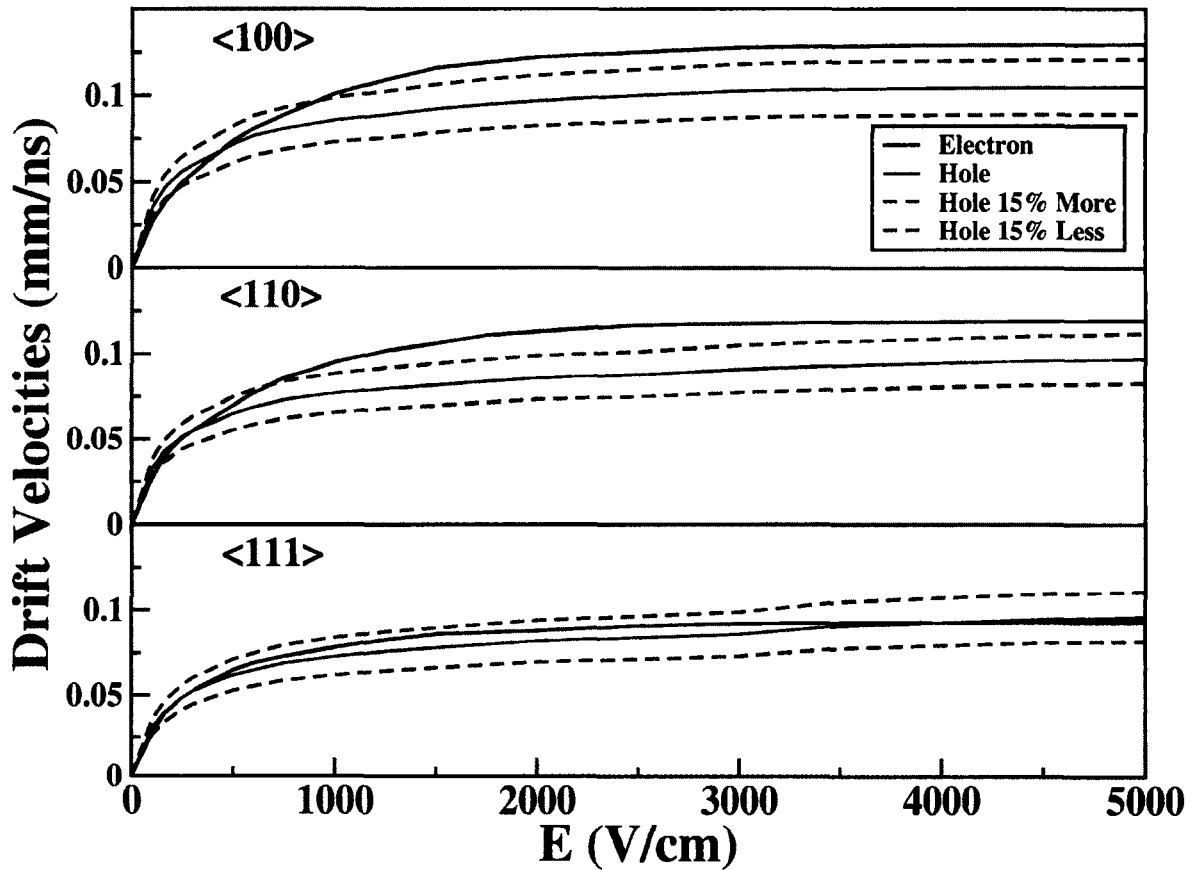
Figure 10.4: Solid lines show the drift velocities of electrons and holes along the three principal Ge crystal axis (<100>, <110>, <111>) as a function of the electric field, as currently used for GRETINA. Dashed lines show hole velocities scaled by ±15%.

Not all parameters involved in this superpulse fitting procedure, however, are truly independent. This was evident from initial findings where chi-sqaure values were rigorously extracted for Q1A1 (Fig. 10.5) and Q4A8 (Fig. 10.5) detectors. Where the chi-square minima is found to be around the current parameters for Q1A1 and about 15% above these accepted parameters for Q4A8.
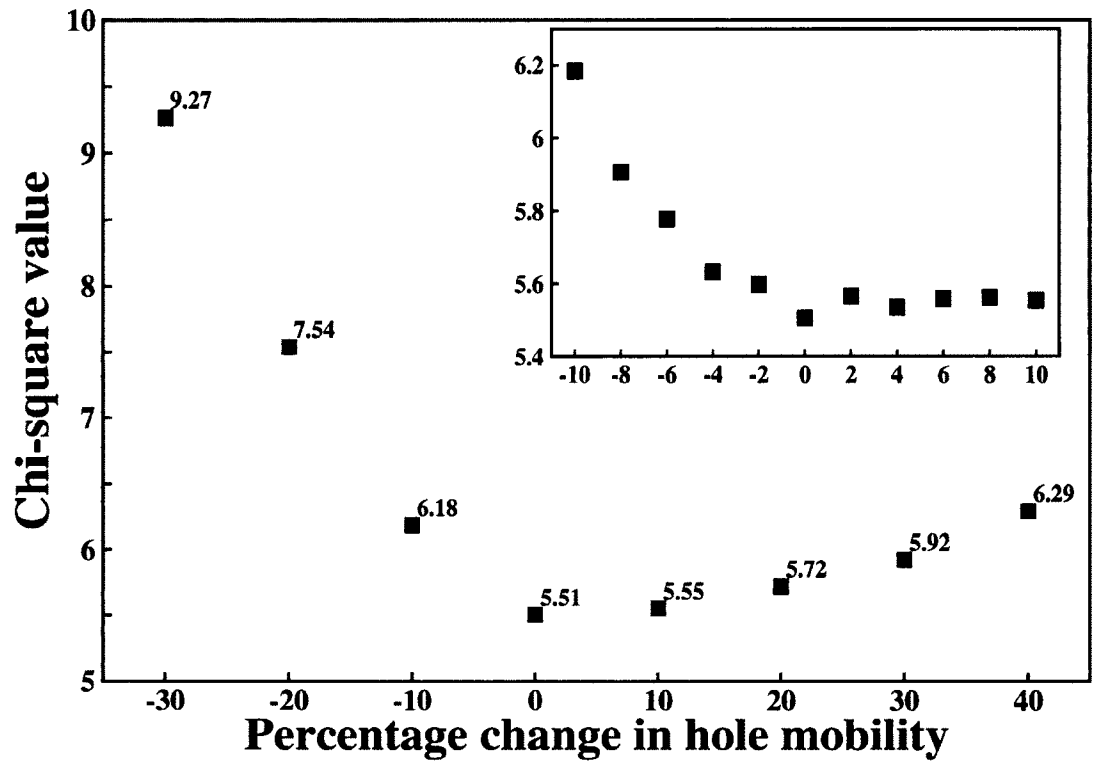
Figure 10.5: Chi-square values for varied hole mobility, when preamplifier rise time compensates for the changes, for Q1A1 GRETINA detector. The inset shows a finer grid of 2% variation around the possible (i.e with 0%) minima.
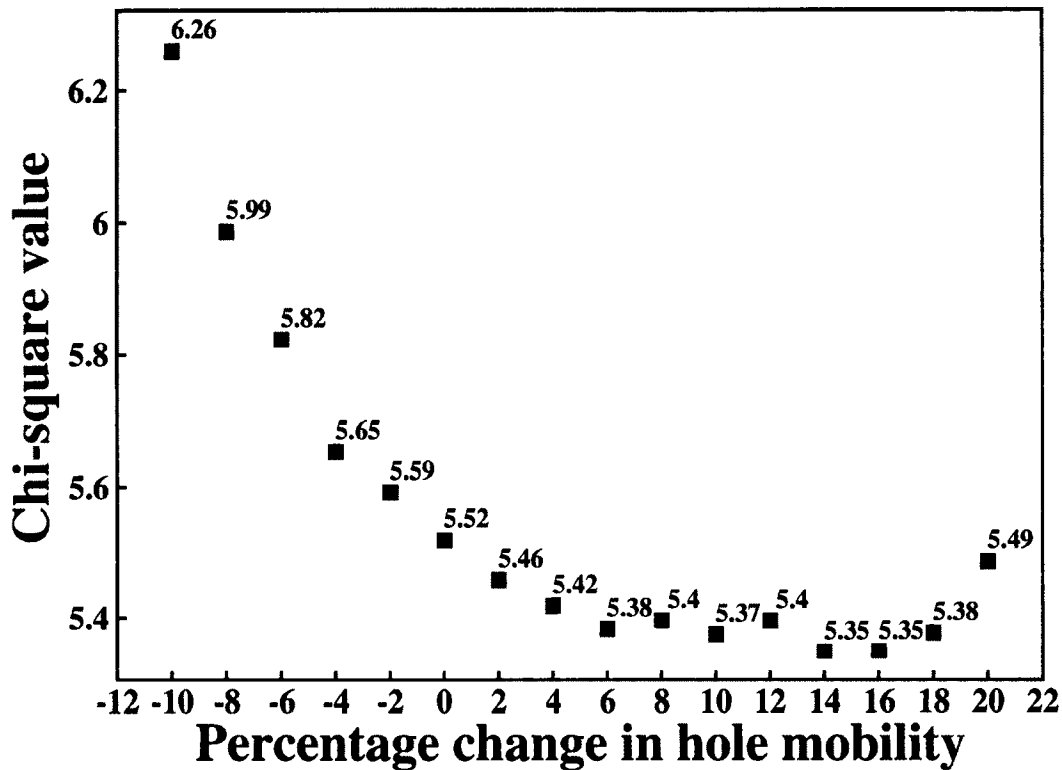
Figure 10.6: Chi-square values for varied hole mobility, when preamplifier rise time compensates for the changes, for Q4A8 GRETINA detector.

The pre-amplifier response rise time parameters, τ, values for each segment corresponding to mobility change, as given in table: 12.9, in particular, are found to be correlated with hole mobility. This is also clearly evident from Fig. 10.7, where the average τ value for all segments is seen to track the percentage change in hole mobility. The effects of the rise time changes counteract the effects of hole mobility changes in the fitting procedure.
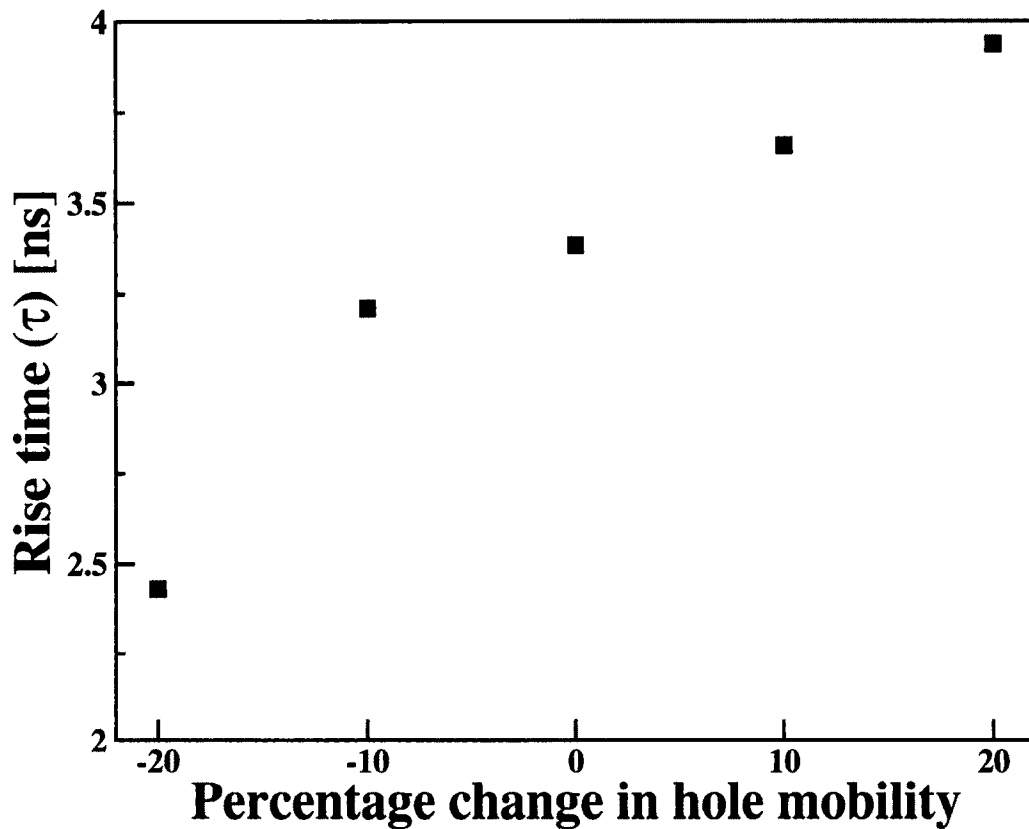
Figure 10.7: Average preamplifier rise time vs scaled hole mobilities.

Thus, in order to extract the specific effect of hole mobility changes, con-
strained fits were performed with the pre-amplifier response rise time parameters
fixed. The results, as shown in Fig. 10.8, indicate that there is a shallow minimum
in the χ^2, centered around hole mobilities that are $\approx 15\%$ lower than the current
parameters in use.
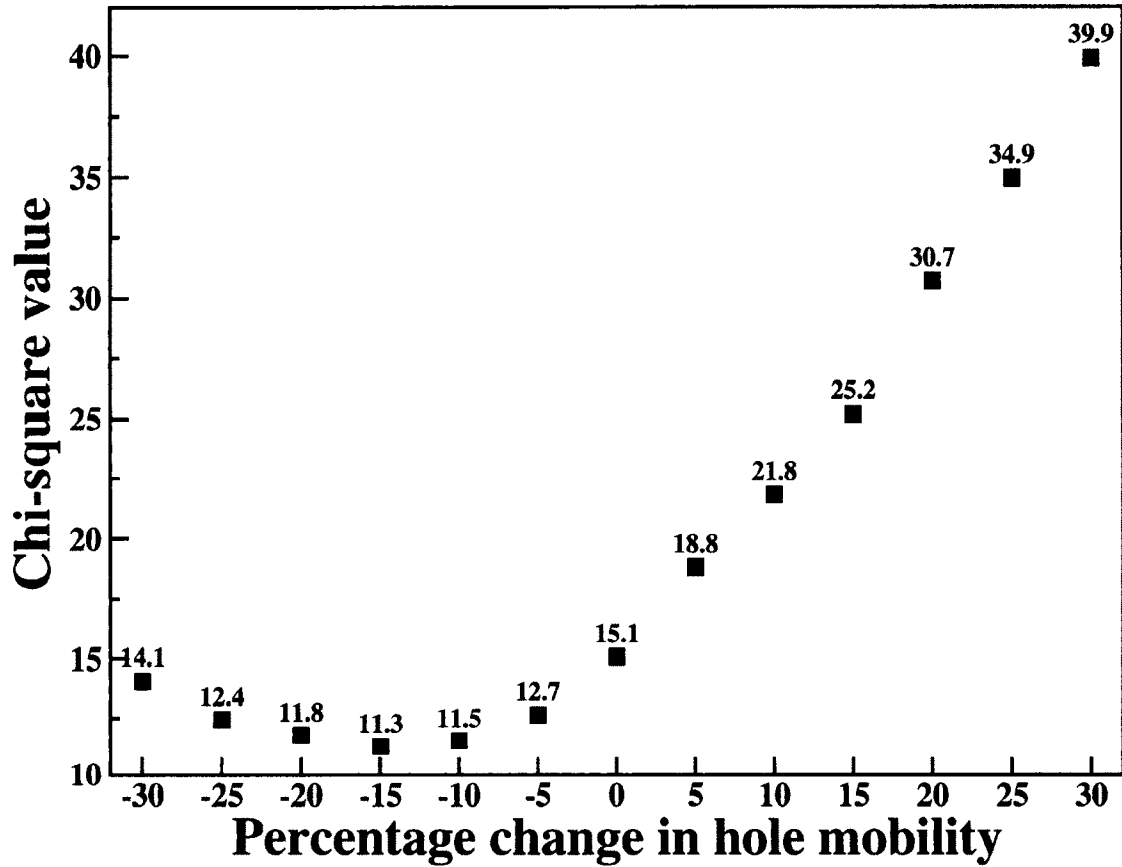
Figure 10.8: Scaling hole mobility to find χ^2 from superpulse fit.

The extracted parameters from this super-pulse fitting procedure are now applied to the "raw" basis to obtain a basis that now has been corrected for detector responses. Subsequently, signal decomposition algorithms compare measured signals to linear combinations of these simulated signals. As there are typically multiple interaction points in a given crystal for an incident photon, the best fit from this process provides the location and relative charge deposited at these interaction points.

10.5 Experimental Studies

While minimizing χ^2 in the superpulse fitting procedure optimizes the relevant parameters, the real test lies in the position resolution obtained in experiments. Therefore, the effect of a change in hole mobility on position resolution of the detector was investigated by analyzing a collimated 2 mm diameter "pencil" beam [110] of 662 keV γ-rays from a ^{137}Cs source. The beam generates a set of events and the scatter of inferred first interaction points about the collimated photon beam locus provides an experimental measure of the position resolution.

The GRETINA Q4A8 detector and cryostat was placed vertically downwards on a steel mount, as shown in Fig. 10.9. A 1mCi ^{137}Cs source was then placed in the lead collimator facing front face of the detector and other background sources were removed as far as possible from the detector. The electronics arrangement and data acquisition was the same as that used for GRETINA experiments, as discussed in chapter 3. GRETINA digitizers were used to digitize the signals from all 37 detector channels at a sampling rate of 100 MHz.
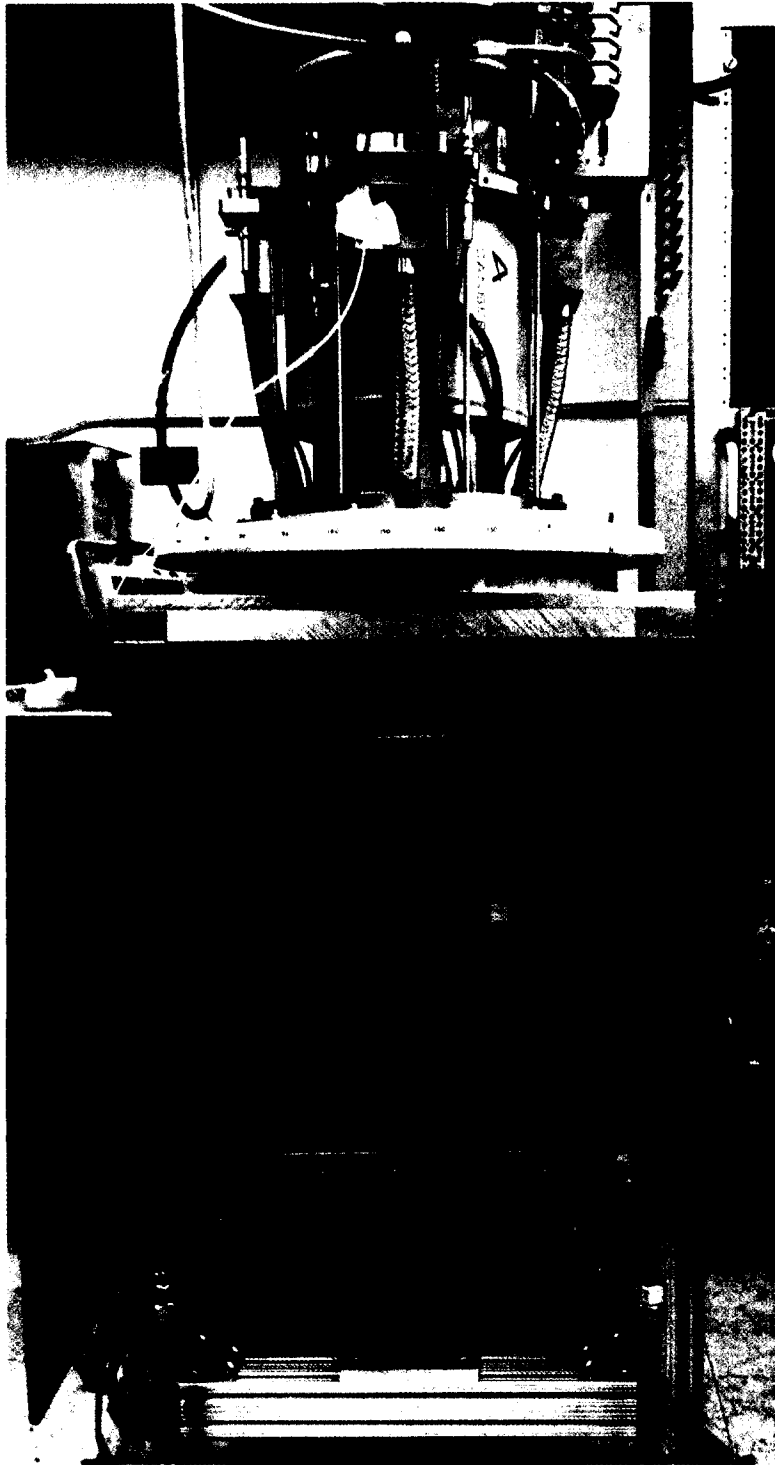
Figure 10.9: Experimental setup at LBNL detector characterization lab, where a ^{137}Cs source is mounted on a collimator. The LBNL scanning table was able to move the lead assembly, containing a collimated 1mCi ^{137}Cs source in the x-y plane. The steel support frame held the GRETINA Q4A8 cryostat in position along with its large LN2 storage dewar.

187

The pencil beams were collimated to enter the Q4A8 segment face at specific locations as shown in Fig. 10.10, where the segments are labeled A-F in azimuthal direction and the dashed lines indicate the segment boundaries. The dots indicate 7 different collimator locations whose x-y coordinates are given in table: 10.1. Five of these were spaced out at radial distances of 6, 12, 17, 22 and 30 mm from the cylindrical axis of symmetry of the detectors at a fixed x position of zero in the coordinate system shown. To explore azimuthal variations, three additional locations were chosen at varying x positions of 0, -3.5 and -7.5 mm at a fixed y position of 12 mm.
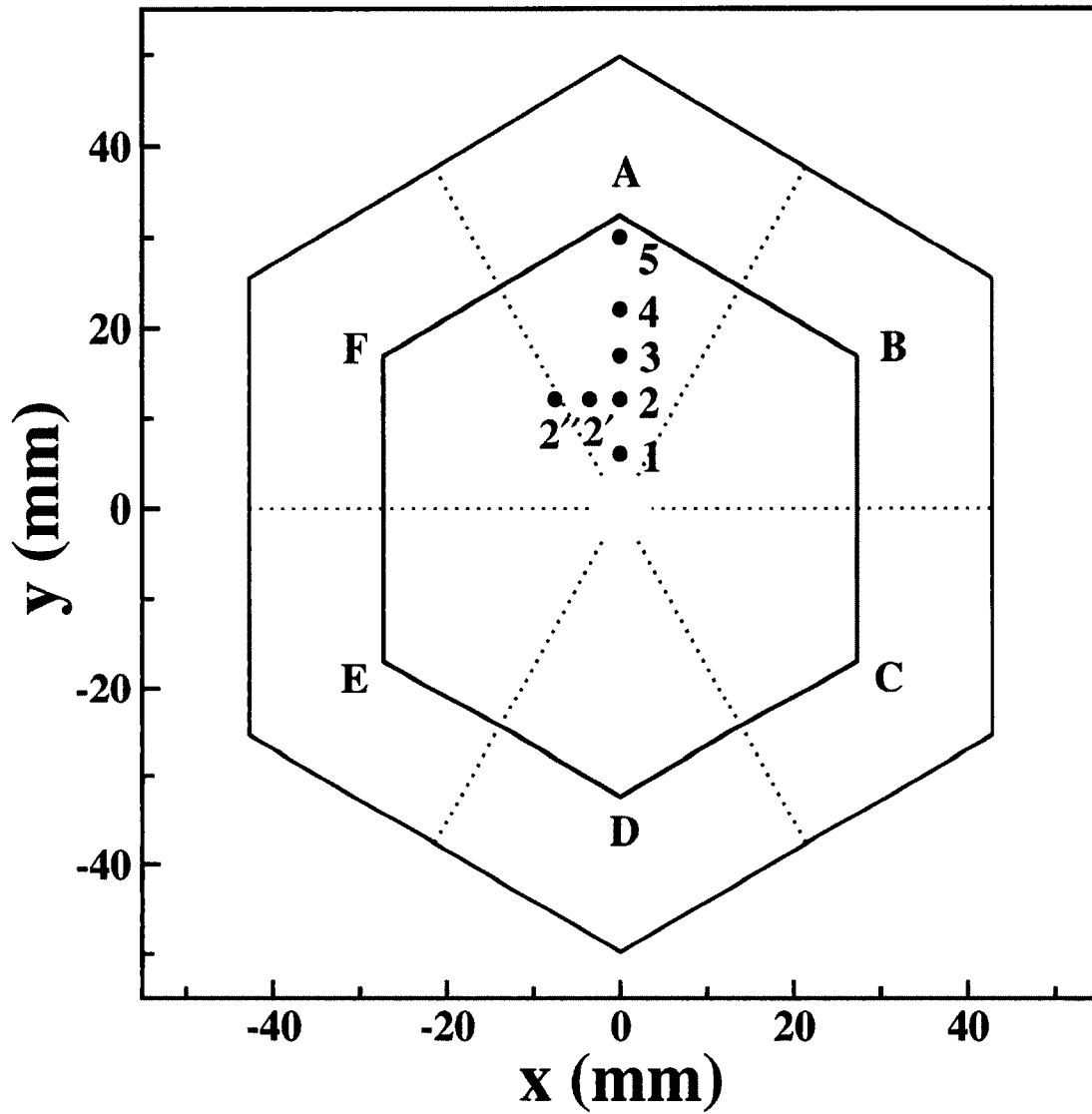
Figure 10.10: Coordinate system used for the position sensitivity measurement (Q4A8 GRETINA detector). The segments are labeled A-F in azimuthal direction and the dashed lines indicates the segment boundaries. Black dots indicate 7 different collimator locations, where the pencil beam measurements were carried out.

Table 10.1: Collimation points and their corresponding x-y coordinates (in mm) in the crystal axis where its center is at (x,y) = (0,0).

Collimation point	X	Y
1	0	6
2	0	12
3	0	17
4	0	22
5	0	30
2′	-3.5	12
2″	-7.5	12

In order to determine the position resolution, two conditions are imposed on the events considered: they are limited to a single interaction point (when using the decomposition algorithm) and the energy of this interaction is required to be greater than 300 keV. Such an analysis was performed on detector Q4A8, where a typical pencil beam for this crystal was reconstructed by the decomposition algorithm, under the above conditions.

10.5.1 Pencil beam along the radial line

To analyze whether reasonable variations in hole mobilities might affect the position resolution of the detectors perpendicular to the beam, the results for two different hole mobilities, one with currently used values, and the other 15% less than the currently used values, are compared for the five radially varying points in Fig. 10.11 and Fig. 10.12. The collimation of the source is clearly evident in the two-dimensional x vs z and y vs z plots. The centroids of the peaks in the

y vs z plot reproduce the actual radial distances of the collimator locations (to better than 1 mm). For all but point 1, there is no significant difference between the x or y position profiles obtained with the two different hole mobilities. This becomes more evident from Fig. 10.13, where y-projections are given for all the pencil beams at radial points. For point 1, the difference in peak positions between the two is ≈ 1.5 mm, where the typical FWHM of the position distribution is closer to ≈ 4 mm. The fact that point 1 is the only one out of the five positions that exhibits any noticeable dependence on the hole mobility can be understood from realizing that holes, which move away from the central axis, have to travel the farthest distance for point 1. Since point 1 is only 6 mm from the detector axis, the detector volume where a 15% change in hole mobility would be discernible is, therefore, a small fraction of the total active detector volume. Also shown in Fig. 10.14, are the x-projections whose centroid lies about the same point.
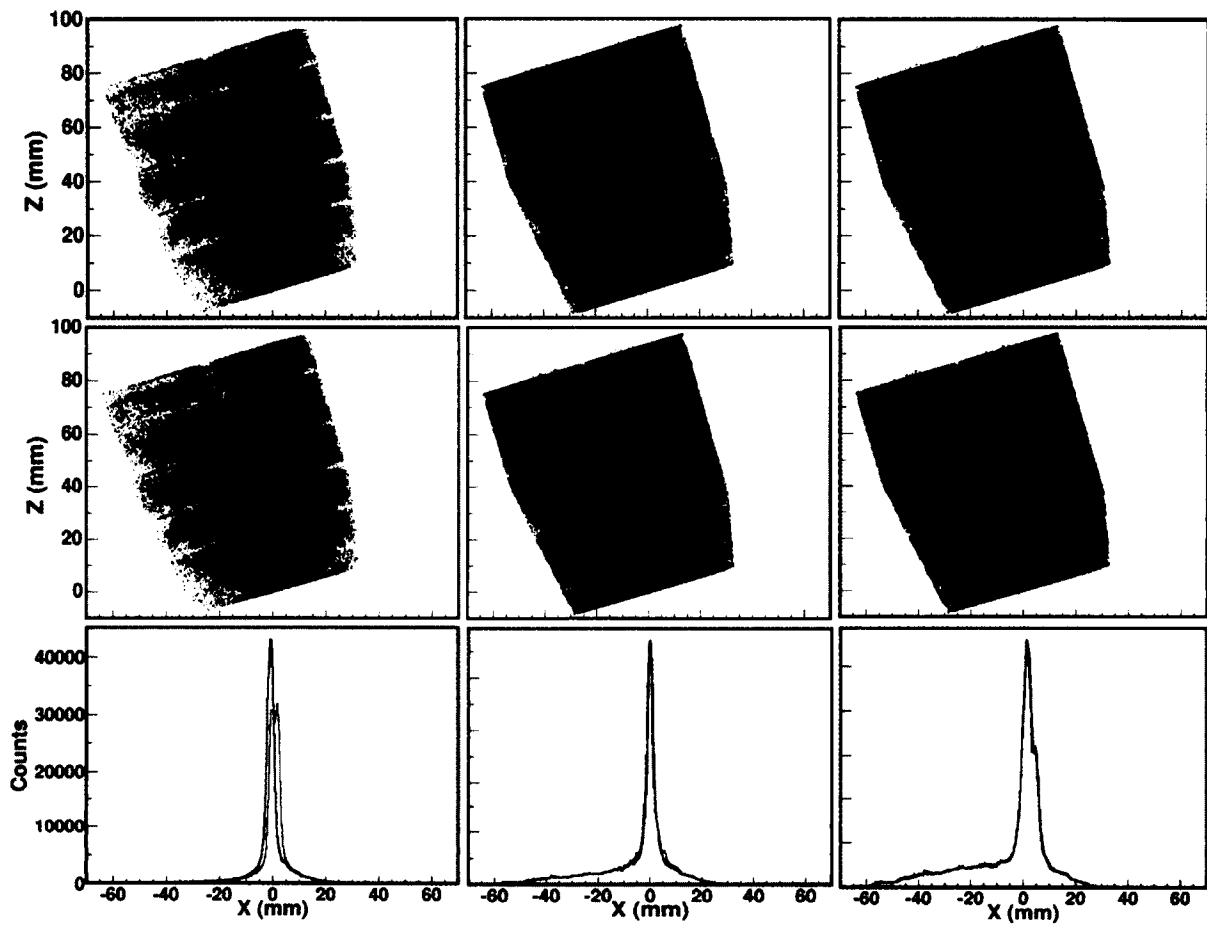
Figure 10.11: The upper panel shows 2D X-Z histograms for three different experimental pencil beams (from left: 1, 3, 5 collimation points (table: 10.1)) with current hole mobility parameters and corresponding 2D plots with 15% lowered parameters are shown in the middle panel. The overlaid projections in the lower panel are x-projections for these different mobilities, where color corresponds to their respective 2D plot frame.
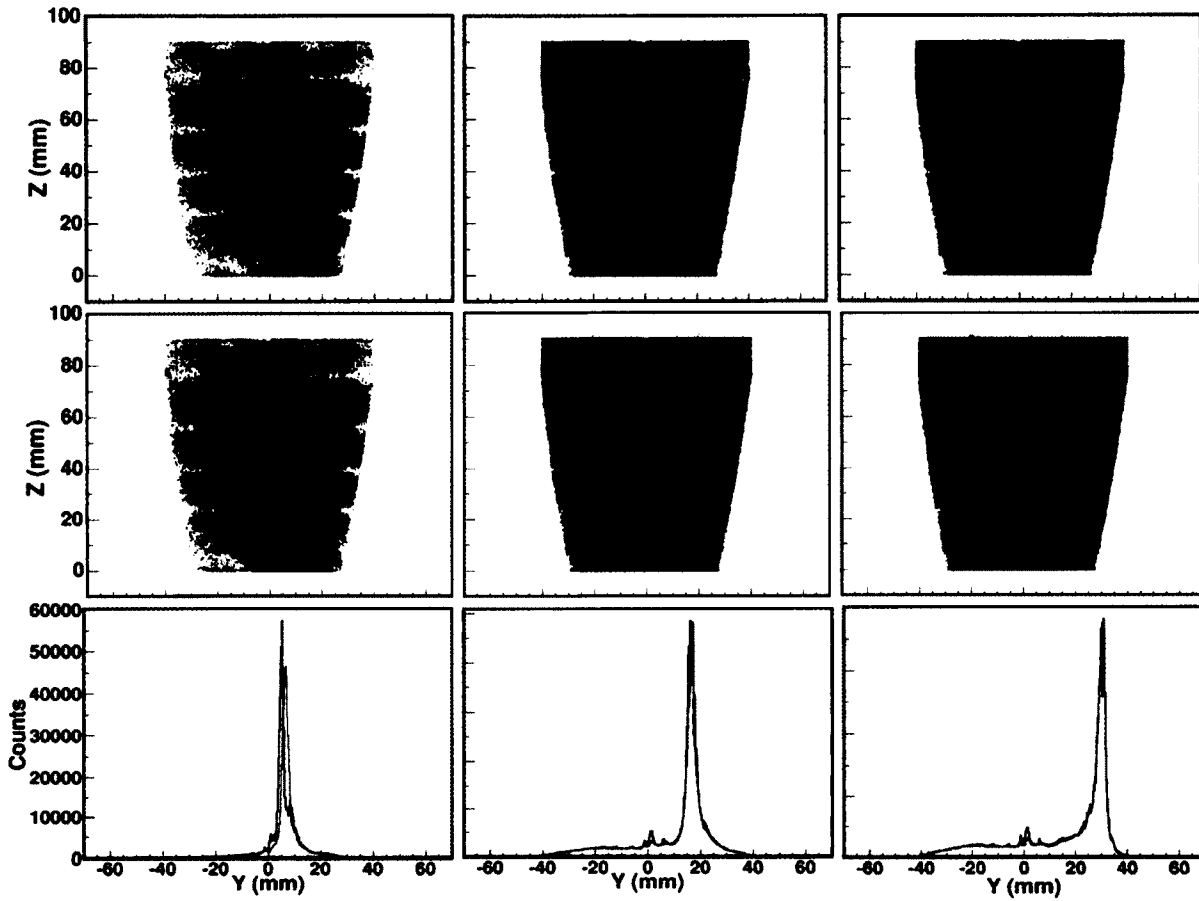
Figure 10.12: The upper panel shows 2D Y-Z histograms for three different experimental pencil beams (from left: 1, 3, 5 collimation points) with current hole mobility parameters and corresponding 2D plots with 15% lowered parameters are shown in the middle panel. The overlaid projections in the lower panel are y-projections for the different mobilities, where color corresponds to their respective 2D plot frame.
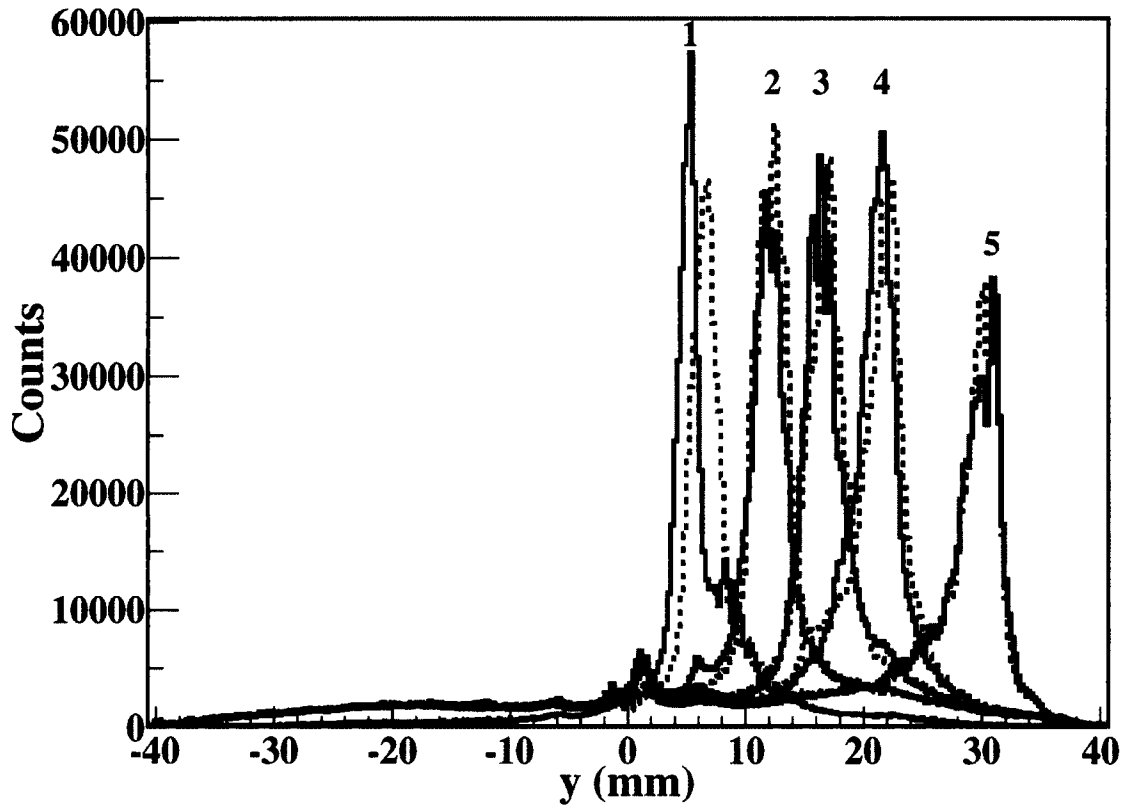
Figure 10.13: y-projections for all the radial points overlaid for current and 15% lowered hole mobility parameters.
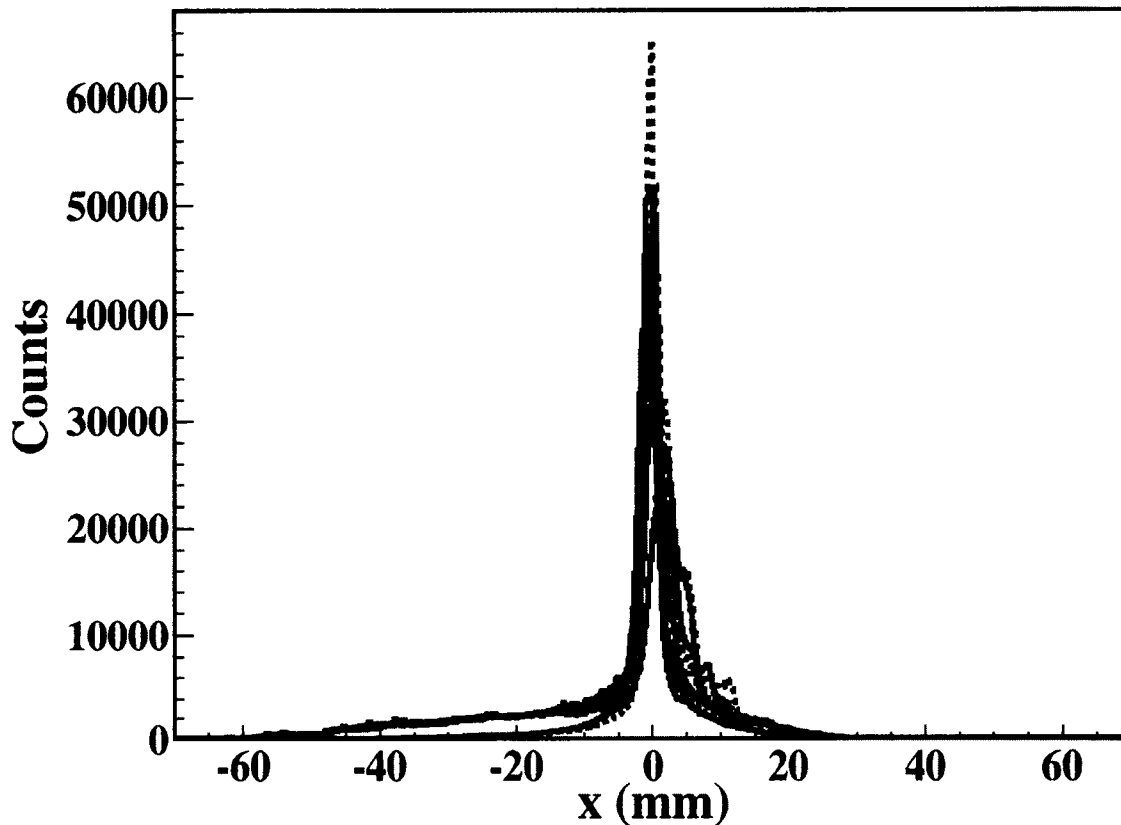
Figure 10.14: x-projections for all the radial points overlaid for current and 15% lowered hole mobility parameters.

10.5.2 Pencil beam along the azimuthal line

The azimuthal variation is explored, as shown in Figs. 10.15 and 10.16, for the points 2, 2′ and 2″. Here again, any difference in either the x or y projections for all three positions is below ≈1 mm. Since points 2′ and 2″ lie radially farther from the central axis compared to point 2, this underscores the earlier inference that the detector volume affected by 15% variations in hole mobility is indeed

195

restricted to a small detector volume around the central contact. To summarize
this, a plot of difference of collimation point coordinates and pencil beam x and
y projection's centroids for all the data points show that point 1 stands out with
maximum difference for either of the hole mobility (Fig. 10.17 and 10.18).
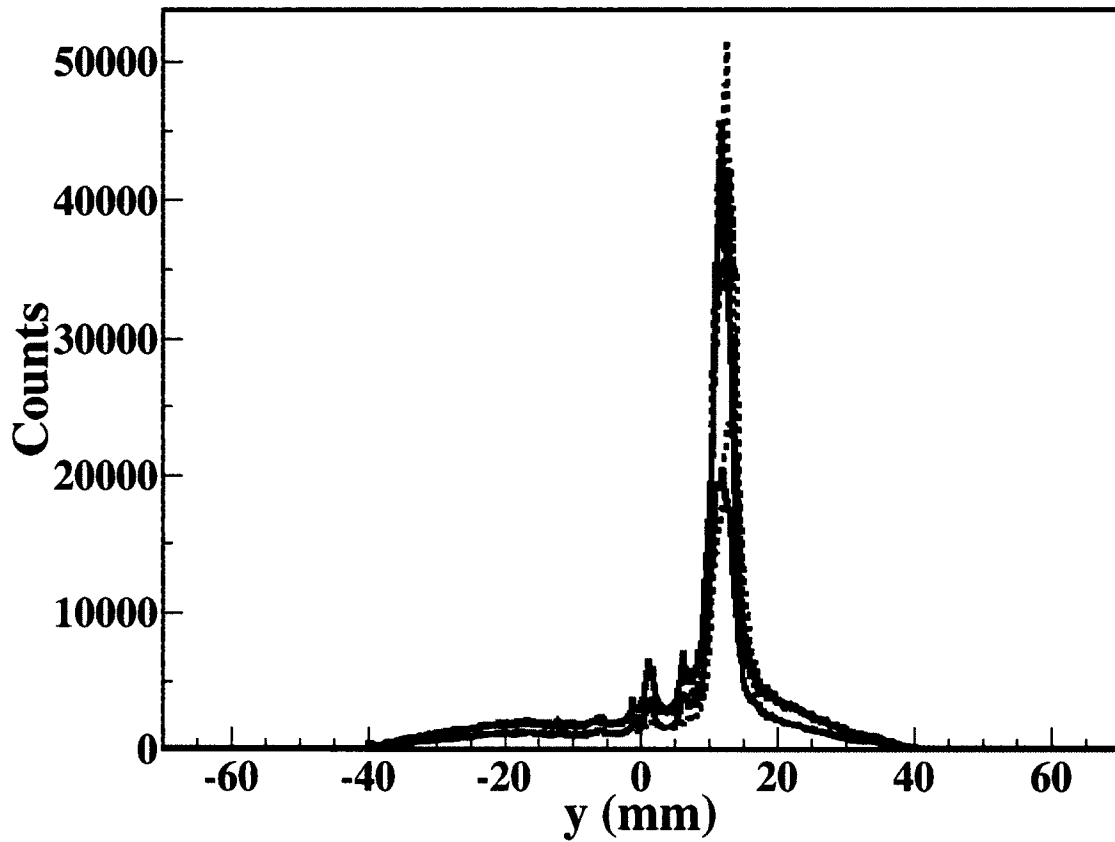
Figure 10.15: y-projections for all the azimuthal points overlaid for current and 15% lowered hole
mobility parameters.
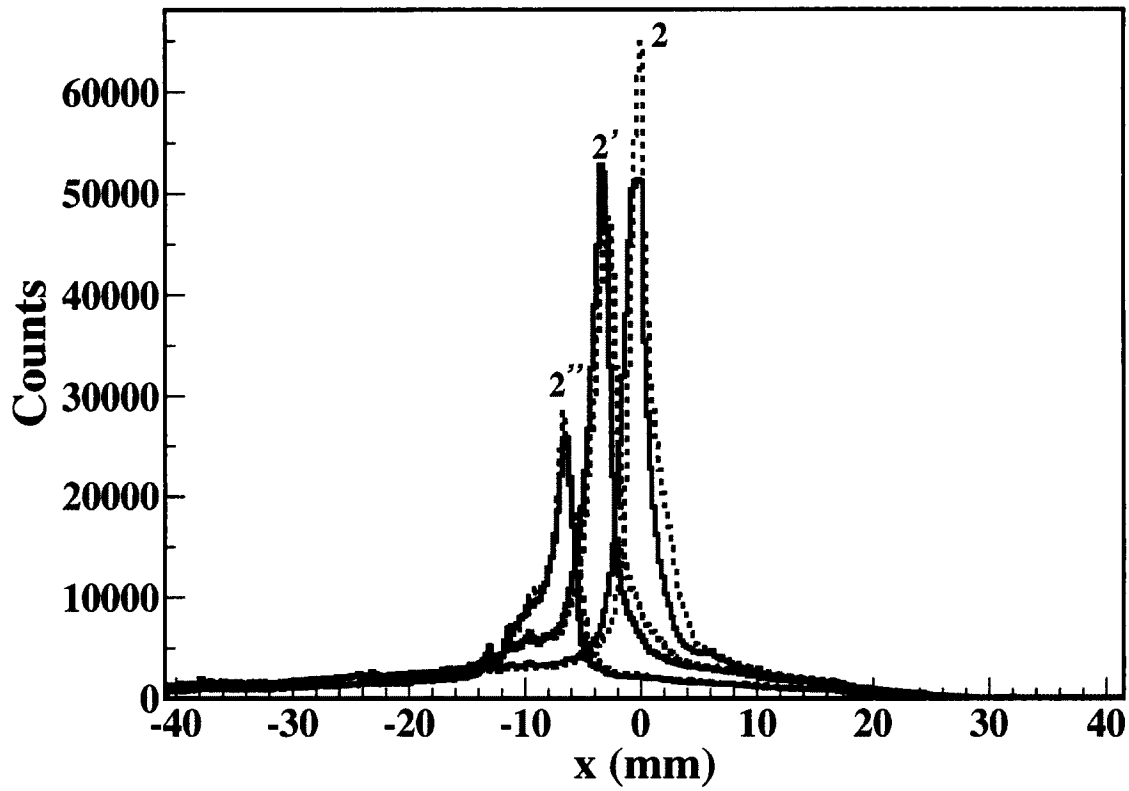
Figure 10.16: x-projections for all the azimuthal points overlaid for current and 15% lowered hole mobility parameters.
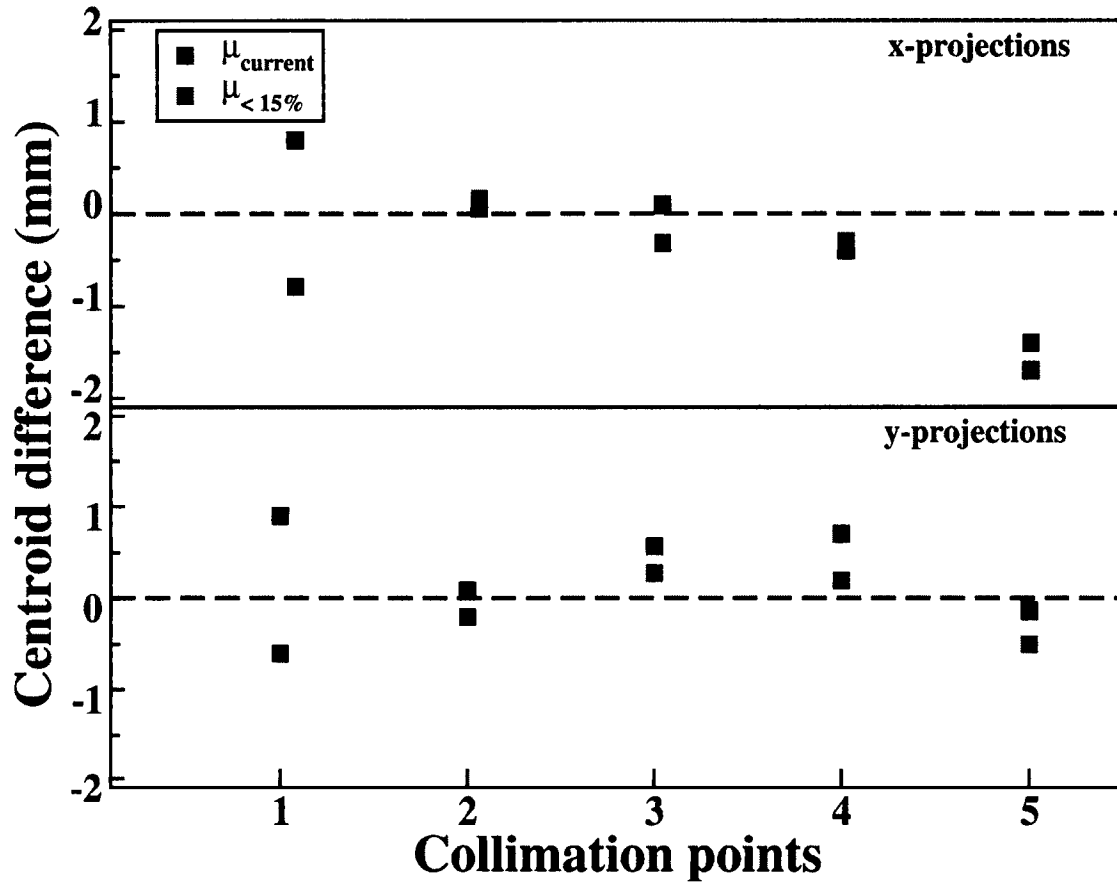
Figure 10.17: Difference of pencil beam x-y projection centroids from the collimation point coordinates for all the pencil beam collimation points (1, 2, 3, 4, 5) along the radial line.
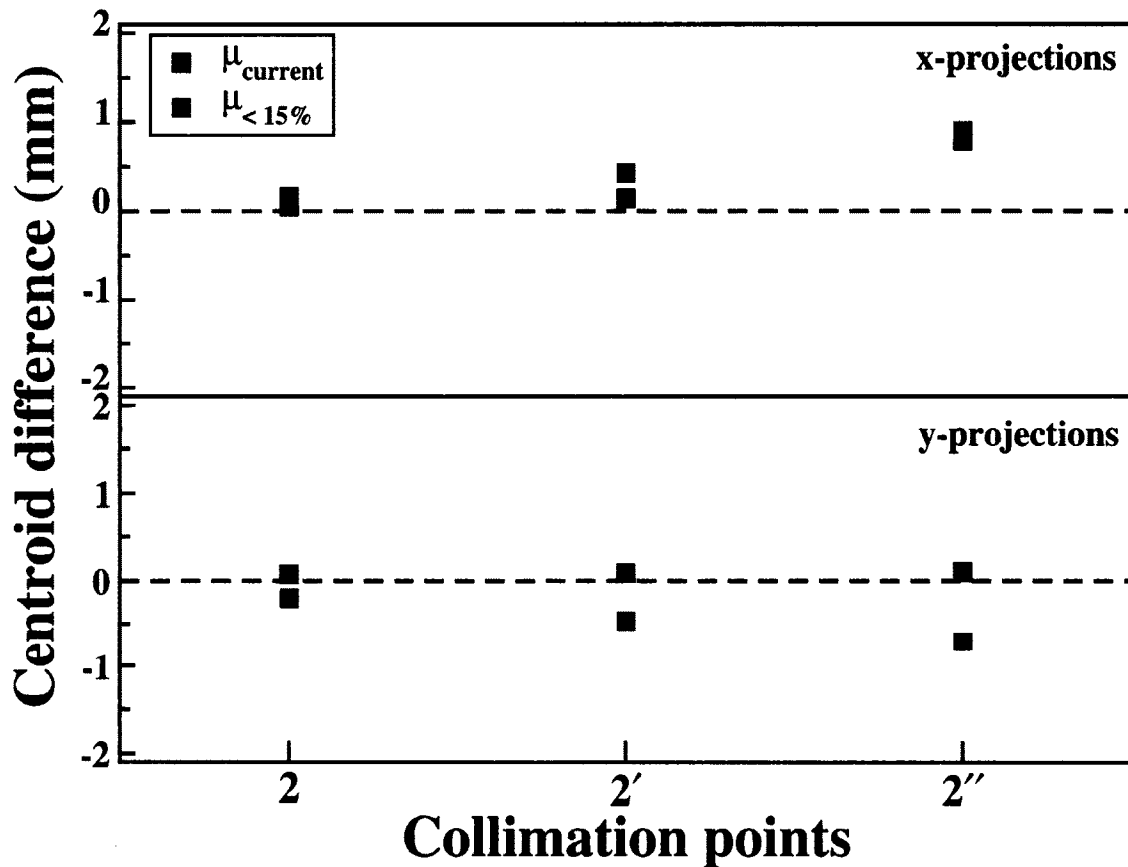
Figure 10.18: Difference of pencil beam x-y projection centroids from the collimation point coordinates for all the pencil beam collimation points (2, 2′, 2″) along the azimuthal line.

10.5.3 X-Y Projections as a function of detector depth

Since the above conclusions were based on the projections for all z, i.e. the entire depth of the crystal, x- and y-projections for six different z-windows were generated to explore whether a 15% variation in hole mobilities affected the posi-

tion reconstruction and resolution as the pencil beam travels deeper into the crystal (Figures 10.19 and 10.20). The first two z-slices near the front face show no discernible difference in their x- or y-projections for the two hole mobilities. Differences are observable for the deeper z-slices for collimation points 1 and 2 as the γ ray pencil beam reaches farther into the crystal. From collimation point 3 (shown in the figures) and higher, the centroids for the two mobilities essentially overlap. The reason for this may again lie in the fact that the crystals flare out with depth, and, therefore, the holes have to travel farther radially to reach their respective outer contacts.
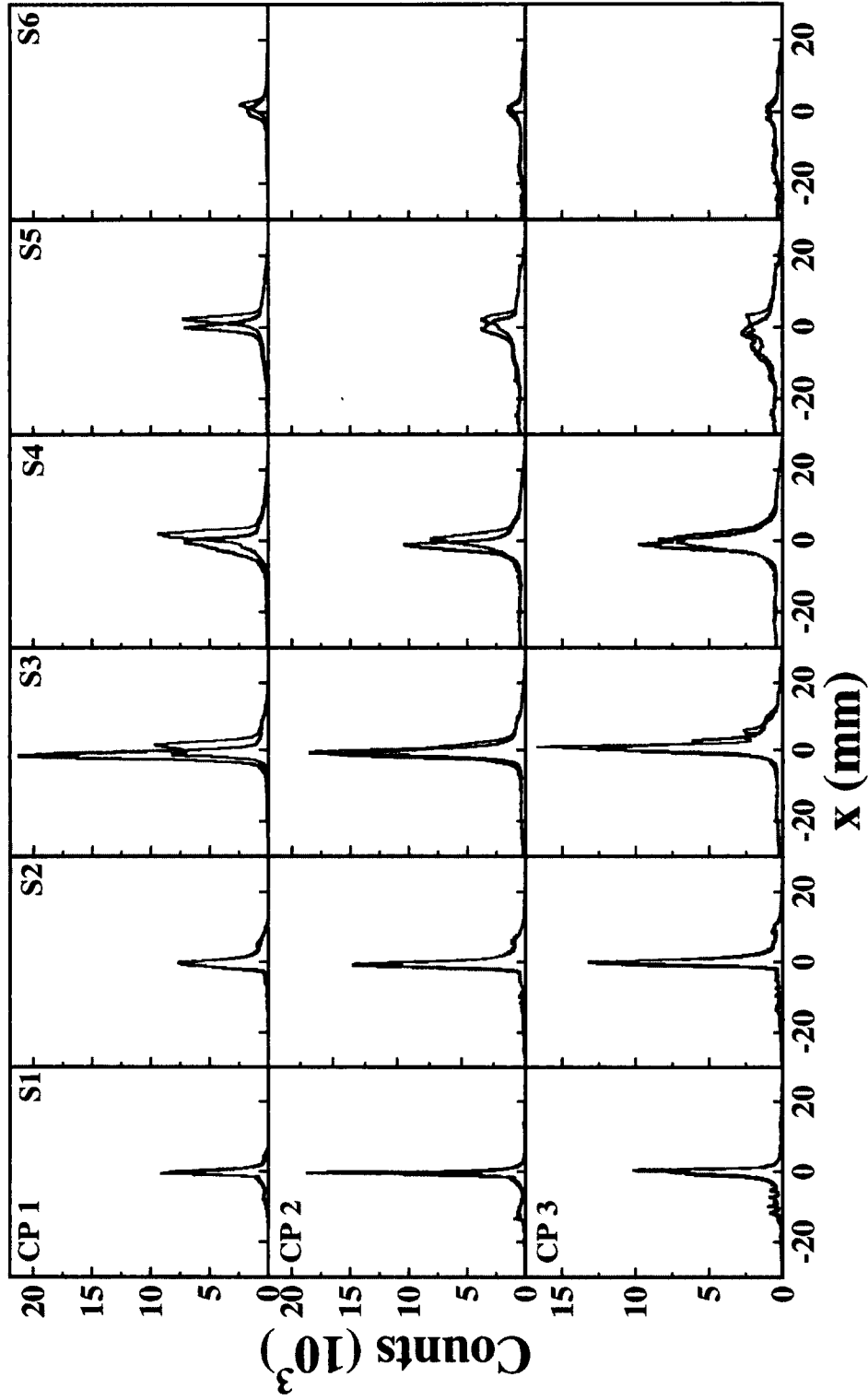
Figure 10.19: Comparing x projections for the pencil beams at collimation points 1 (top panel), 2 (middle) and 3 (lower) as a function of detector depth for no change in hole mobility (black) and 15% less (red). Here projections are given for all the six layers, starting from the detector front face.
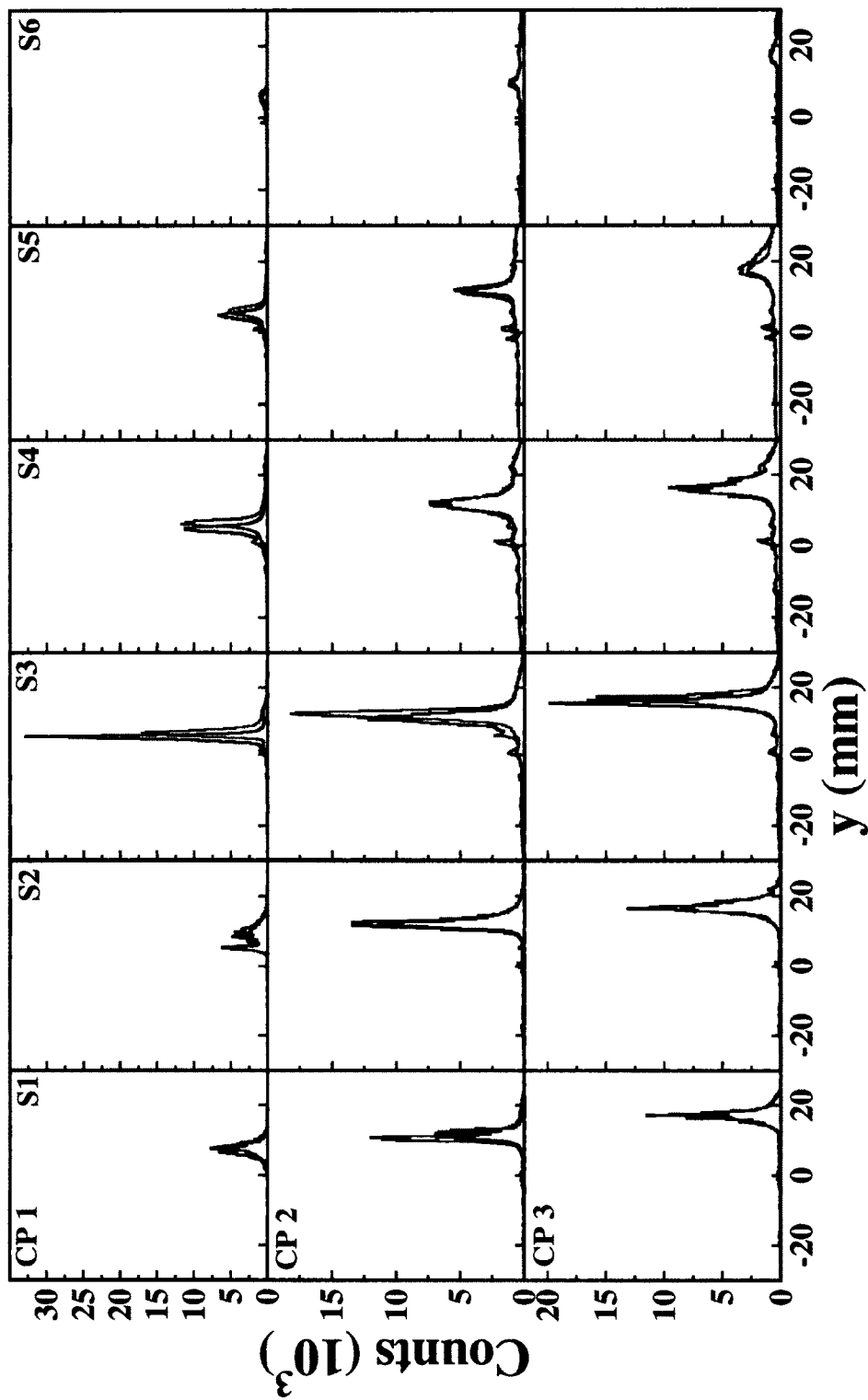
Figure 10.20: Comparing y projections for the pencil beams at collimation points 1 (top panel), 2 (middle) and 3 (lower) as a function of detector depth for no change in hole mobility (black) and 15% less (red). Here projections are given for all the six layers, starting from the detector front face.

202

10.6   Simulations of Pencil Beams

To investigate whether any of the above observations from the experimental pencil beam for varying hole mobilities is inherent in the data, or may arise from the analysis procedure itself, the same analysis was tested on a simulated pencil beam data set. This data set was created through a GEANT4 simulation, where pulse shapes for all the interaction points for a 2 mm uniform beam spot (positioned at x = 13 mm, y = -11 mm) were generated using the "basis". The positions were then reconstructed using the same signal decomposition codes used for the experimental data. The simulated data set, which is free from electronic effects, was analyzed and is compared with experimental results in an effort to isolate the dependence of position resolution on hole mobility.
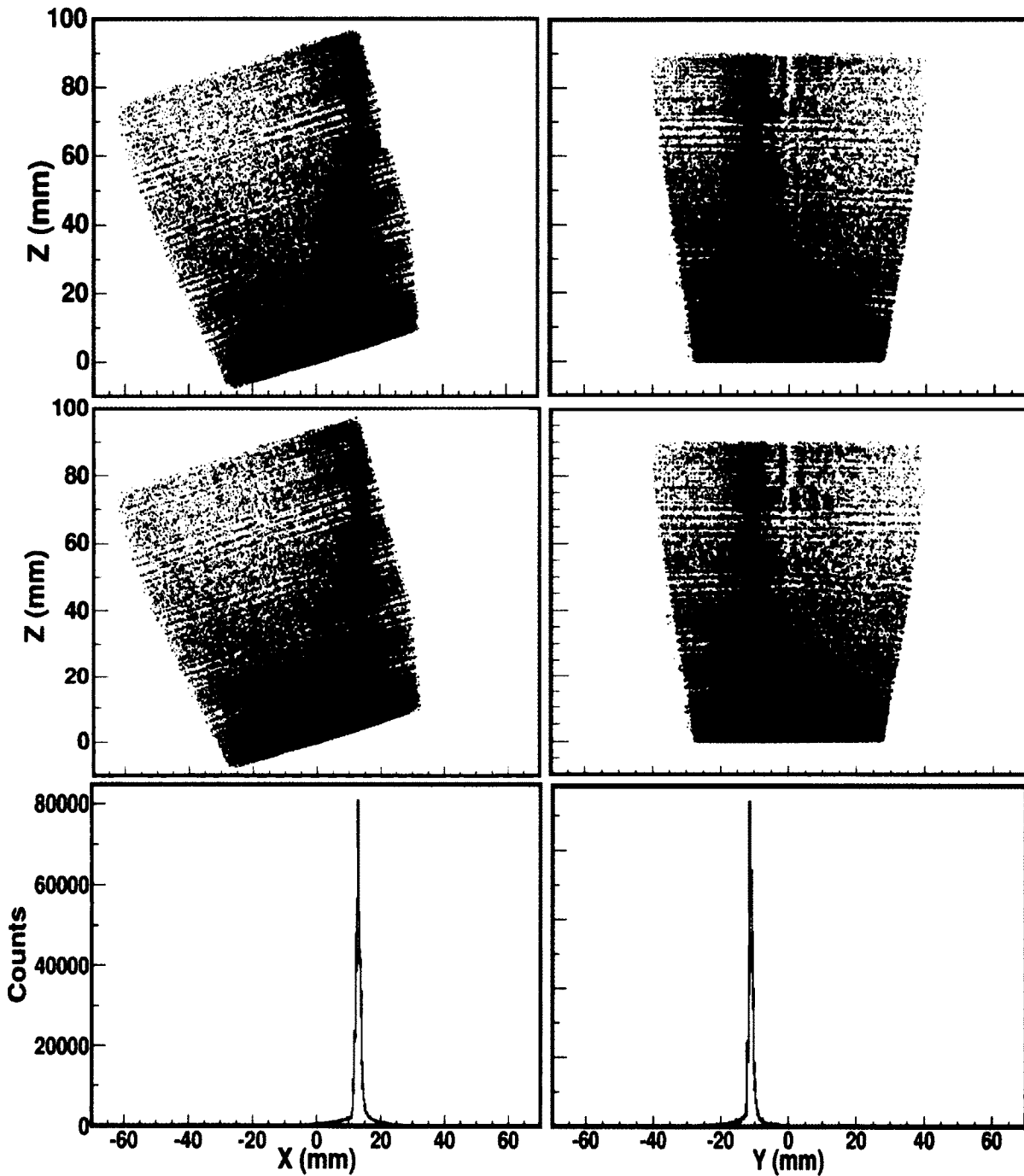
Figure 10.21: The upper panel shows 2D histograms (left: X-Z, right: Y-Z) of simulated pencil beams with current hole mobility parameters and corresponding 2D plots with 15% lowered parameters are shown in the middle panel. The overlaid projections in the lower panel are X (left) and Y (right) for the different mobilities, where color corresponds to their respective 2D plot frame.

10.7 Comparing Experimental and Simulated Pencil Beams

In the simulated data, there is no discernible difference in position resolution between the two hole mobilities that differ by 15%, either in the x or y projections (Figure 10.21). While in the experimental analysis, some artifacts, such as false hit events reconstructed away from the centroids (possibly due to cross-talk etc) are observed, the simulated data are quite clean in this regard. Again, neither data set shows significant variation between the two hole mobilities considered. This conclusion is borne out in Figure 10.22, where the ratio of counts reconstructed using the two different mobilities is shown as a function of interaction depth.

Thus, while the chi-square minimization from the super-pulse fitting procedure indicates a shallow minimum centered at hole mobility values 15% lower than currently in use, the reconstruction of the actual positions seems fairly insensitive to a 15% variation in hole mobilities, both for experiment and simulation. Therefore, hole mobilities can essentially be considered optimized for signal decomposition. Any outstanding challenges in position reconstruction, such as clustering effects near segment boundaries, need to focus on other parameters such as, e.g., electronic cross-talk, and/or improving tracking algorithms that isolate and identify individual γ-ray interaction points in an event.
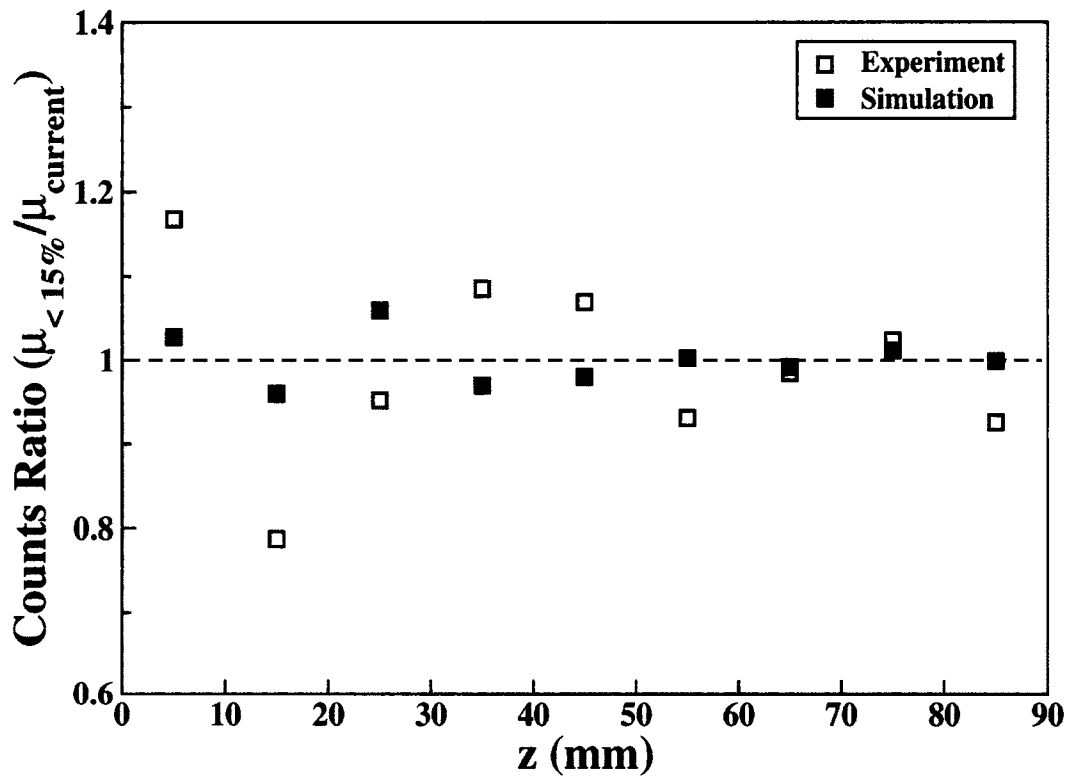
Figure 10.22: Comparing z-projections from experimental pencil beam data to simulated pencil beam data.

Chapter 11

Summary and Outlook

The position resolution of the interaction points is a key metric in the performance of the GRETINA spectrometer, which directly affects the efficiency and peak/total characteristics of the array. It also determines the effective energy resolution of the array when used with gamma-ray sources with high recoil velocities, where corrections for Doppler shifts is critical. The design requirement for GRETINA is a position resolution $\sigma < 2$mm RMS. While a number of parameters may affect the ultimate position resolution, this work specifically explores whether variations in hole mobility parameters is a significant contributor. The position reconstruction in signal decomposition algorithms is investigated for varying hole mobility parameters around the currently accepted values. The chi-square fits exhibit a shallow minimum in the hole mobility, centered at $\approx 15\%$ less than currently used values. Calibration data on position resolution is analyzed for two hole mobility parameters, at and 15% less than the currently accepted value, to-

gether with simulations that isolate the signal decomposition dependence from electronics cross-talk. The results exclude hole mobility as a significant parameter in play for addressing remaining challenges in reconstructing gamma-ray interaction points in GRETINA. The position resolution should, however, be examined more critically through experimental studies of collimated pencil-beams for clean single-scattered events in a well defined three-dimensional position in the crystal via coincidence scanning techniques.

Chapter 12

Appendix

Table 12.1: Internal conversion coefficients for γ-ray transitions in the ^{186}W level scheme.

E_γ (keV)	Internal Conversion Coefficient (α)	Error
122.6	1.768	0.025
268.8	0.1187	0.0017
273.9	0.112	0.016
335.0	0.0615	0.0009
373.6	0.0454	0.0007
391.3	0.0398	0.0006
412.7	0.0344	0.0005
455.5	0.0267	0.0004
470.2	0.0245	0.0004
506.0	0.0204	0.0003
540.0	0.01738	0.00025
564.3	0.01565	0.00022
567.2	0.01546	0.00022
608.0	0.01312	0.00019

Table 12.1 - continued

E$_\gamma$ (keV)	Internal Conversion Coefficient (α)	Error
653.2	0.01113	0.00016
660.0	0.01088	0.00016
667.1	0.01062	0.00015
675.0	0.01034	0.00015
737.0	0.00852	0.00012
740.0	0.00844	0.00012
748.5	0.00824	0.00012
811.5	0.00693	0.0001
922.0	0.00531	0.00008
1176.0	0.00327	0.00005
1276.4	0.00281	0.00004

Table 12.2: DCO ratios for 15 γ-rays in the ^{186}W level scheme.

E_γ (keV)	Gated on E_γ (keV)	R_{DCO}	Error	Multipolarity	Band$_i$ → Band$_f$
122	273	0.916	0.004	Quad	GSB → GSB
273	122	0.893	0.004	Quad	GSB → GSB
309	273	0.8	0.07	Di	5 → 1
315	273	0.68	0.06	Di	5 → 1
390	122	1.08	0.03	Quad	1 → 1
412	273	1	0.003	Quad	GSB → GSB
412	122	1	0.007	Quad	GSB → GSB
539	273	1.097	0.005	Quad	GSB → GSB
539	122	1.141	0.013	Quad	GSB → GSB
567	335+455	1.1	0.07	Quad	2 → 2
652	273	1.155	0.009	Quad	GSB → GSB
652	122	1.124	0.024	Quad	GSB → GSB
739	335+455	0.641	0.019	Di	2 → GSB
748	273	1.124	0.021	Quad	GSB → GSB
801	273	0.641	0.013	Di	2 → GSB
801	335+455	0.62	0.024	Di	2 → GSB
812	273	1.02	0.08	Quad	GSB → GSB
884	122	1	0.04	Quad	1 → GSB
902	273	1.02	0.08	Quad	3 → GSB
1001	273	1.02	0.024	Quad	1 → GSB

Table 12.3: The relative total intensity (i.e corrected for efficiency and internal conversion) and error of each transition of interest in ground state band of ^{186}W, as extracted from γ-γ matrix with no Q-value and scattering angle conditions.

E_γ (keV)	Spin ($\hbar$)	Intensity at 800 MeV Beam Energy	Error	Intensity at 725 MeV Beam Energy	Error
123	2^+	4.66E+04	4.21E+02	4.77E+04	4.31E+02
274	4^+	3.25E+04	4.67E+02	3.24E+04	4.67E+02
413	6^+	1.98E+04	1.54E+01	1.98E+04	1.52E+01
540	8^+	1.49E+04	1.32E+01	1.74E+04	1.23E+01
653	10^+	6.39E+03	5.96E+00	7.57E+03	8.86E+00
748	12^+	1.03E+02	8.43E-01	1.36E+02	9.86E-01
812	14^+	2.15E+01	4.17E-01	2.88E+01	5.04E-01
830	16^+	9.70E-01	1.90E-01	1.23E+00	2.55E-01

Table 12.4: The relative total intensity (i.e corrected for efficiency and internal conversion) and error of each transition of interest in ground state band of ^{186}W, as extracted from γ-γ matrix with Q-value and scattering angle conditions as explained in the text.

E_γ (keV)	Spin ($\hbar$)	Intensity at 800 MeV Beam Energy	Error	Intensity at 725 MeV Beam Energy	Error
123	2	3.70E+04	3.35E+02	2.94E+04	2.66E+02
274	4	2.65E+04	3.82E+02	1.94E+04	2.79E+02
413	6	1.59E+04	1.22E+01	1.21E+04	1.00E+01
540	8	9.52E+03	8.53E+00	5.82E+03	6.53E+00
653	10	3.43E+03	5.76E+00	1.78E+03	4.12E+00
748	12	4.93E+01	6.03E-01	1.96E+01	3.84E-01
812	14	8.97E+00	2.81E-01	2.42E+00	1.51E-01
830	16	5.36E-01	1.75E-01	2.06E-01	1.31E-01

Table 12.5: GOSIA calculations: γ-ray yield for ^{136}Xe beam of 800 MeV energy on the ^{186}W target for the scattering angles range of 20° to 47°.

NI	NF	II	IF	YIELD	NORM YIELD
11	10	20	18	8.11E-09	1.06E-11
10	9	18	16	1.37E-06	1.79E-09
9	8	16	14	1.55E-04	2.01E-07
8	7	14	12	1.18E-02	1.53E-05
7	6	12	10	5.07E-01	6.60E-04
6	5	10	8	12.532	1.63E-02
5	4	8	6	159.27	2.07E-01
4	3	6	4	712.33	9.26E-01
3	2	4	2	1245.6	1.62E+00
2	1	2	0	768.92	1

Table 12.6: GOSIA calculations: γ-ray yield for ^{136}Xe beam of 725 MeV energy on the ^{186}W target for the scattering angles range of 20° to 47°.

NI	NF	II	IF	YIELD	NORM YIELD
11	10	20	18	4.04E-10	4.40E-13
10	9	18	16	1.08E-07	1.18E-10
9	8	16	14	1.86E-05	2.03E-08
8	7	14	12	2.19E-03	2.38E-06
7	6	12	10	1.42E-01	1.55E-04
6	5	10	8	5.3174	5.79E-03
5	4	8	6	103.05	1.12E-01
4	3	6	4	682.52	7.43E-01
3	2	4	2	1537.5	1.6746
2	1	2	0	918.14	1

Table 12.7: GOSIA calculations: γ-ray yield for ^{208}Pb beam of 1404 MeV energy on the ^{186}W target for the scattering angles range of 20° to 47°.

NI	NF	II	IF	YIELD	NORM YIELD
8	7	14	12	2.06E+04	4.65E-05
7	6	12	10	4.76E+05	1.08E-03
6	5	10	8	6.12E+06	1.38E-02
5	4	8	6	4.65E+07	1.05E-01
4	3	6	4	1.93E+08	4.35E-01
3	2	4	2	5.57E+08	1.26E+00
2	1	2	0	4.43E+08	1

Table 12.8: GOSIA calculations: γ-ray yield for ^{208}Pb beam of 1287 MeV energy on the ^{186}W target for the scattering angles range of 20° to 47°.

NI	NF	II	IF	YIELD	NORM YIELD
8	7	14	12	5.47E+03	1.03E-05
7	6	12	10	1.82E+05	3.42E-04
6	5	10	8	3.35E+06	6.31E-03
5	4	8	6	3.50E+07	6.59E-02
4	3	6	4	1.75E+08	3.29E-01
3	2	4	2	5.77E+08	1.09E+00
2	1	2	0	5.31E+08	1

Table 12.9: Tabulated are the preamplifier rise time (τ) values for all 36 segments with varied hole mobilities, from super pulse fit.

Less 15%	Less 10%	Current parameters	More 10%	More 15%
5.31	5.39	5.12	5.05	5.08
5.89	5.91	5.81	5.84	5.87
4.79	4.96	4.91	4.93	5.02
4.75	4.72	4.51	4.5	4.57
4.37	4.67	4.39	4.43	4.5
4.19	4.54	4.31	4.39	4.53
2.75	3.64	3.6	3.71	3.85
3.45	3.99	4.39	4.68	4.95
2.34	2.84	3.25	3.56	3.81
2.66	3.36	3.5	3.71	3.88
2.48	3.33	3.43	3.56	3.7
1.46	2.46	2.72	2.93	3.17
2.34	3.44	3.54	3.79	4
2.74	3.41	4.04	4.38	4.69
2.28	2.71	3.23	3.59	3.89
2.42	2.97	3.19	3.38	3.58
2.08	3.32	3.68	3.97	4.16
1.43	2.77	3.09	3.58	3.99
2.28	3.28	3.7	3.91	4.19
2.18	2.66	3.35	3.73	4.15
2.51	2.52	3.12	3.42	3.75
1.67	3.06	3.37	3.48	3.61
2	2.89	3.44	3.82	4.23
1.99	3.34	3.62	4.13	4.61
2.57	2.53	3.07	3.33	3.6
2.39	2.18	2.1	2.7	3.08
0.41	1.98	2.15	2.37	2.64
4.05	3.44	3.5	3.42	3.56
1.74	3.04	3.52	4.09	4.55
1.95	3.09	3.28	3.87	4.35
1.28	1.58	1.72	2.31	2.84
-3.22	1.43	1.79	2.16	2.51
3.23	3.11	2.78	2.78	3.02
-0.43	2.22	2.6	2.85	3.1
1.61	2.45	2.27	2.91	3.53
1.6	2.37	1.71	2.43	3.19

215

Bibliography

[1] R. R. Hilton and H. J. Mang. *Phys. Rev. Lett.*, 43:1979–1981, Dec 1979.

[2] U.S. Tandel *et al*. Collective oblate rotation at high spins in neutron-rich ^{180}Hf. *Phys. Rev. Lett.*, 101:182503, Oct 2008.

[3] I-Yang Lee. The GAMMASPHERE. *Nuclear Physics A*, 520(0):c641 – c655, (1990).

[4] K. S. Krane. *Introductory Nuclear Physics*. 2nd Ed. John Wiley and Sons, Inc., (1987).

[5] A. Bohr and B. Mottelson. *Nuclear Structure, Vol. 2*. World Scientific, 2nd ed., 1998.

[6] R S Mackintosh. The shape of nuclei. *Reports on Progress in Physics*, 40(7):731, 1977.

[7] C. J. (Kim) Lister and Jonathan Butterworth. Nuclear physics: Exotic pear-shaped nuclei. *Nature*, 497:190–191, 2013.

[8] G. Andersson *et al*. Nuclear shell structure at very high angular momentum. *Nuclear Physics A*, 268(2):205 – 256, 1976.

[9] S. G. Nilsson. *Dan. Mat. Fys. Medd., 29, 3*. 1955.

[10] B. Singh *et al*. Table of superdeformed nuclear bands and fission isomers. *Nuclear Data Sheets*, 97(2):241 – 592, 2002.

[11] DR Inglis. Particle derivation of nuclear rotation properties associated with a surface wave. *Physical Review*, 96(4):1059, 1954.

[12] R Bengtsson and S Frauendorf. Quasiparticle spectra near the yrast line. *Nuclear Physics A*, 327(1):139–171, 1979.

[13] M. J. A. de Voigt, J. Dudek, and Z. Szymański. High-spin phenomena in atomic nuclei. *Rev. Mod. Phys.*, 55:949–1046, Oct 1983.

[14] Aage Bohr and Ben R Mottelson. Single-particle and collective aspects of nuclear rotation. *Physica Scripta*, 24(1B):71, 1981.

[15] RM Diamond and FS Stephens. Nuclei at high angular momentum. *Annual Review of Nuclear and Particle Science*, 30(1):85–156, 1980.

[16] Ingemar Ragnarsson and Sven Gvsta Nilsson. *Shapes and shells in nuclear structure*. Cambridge university press, 2005.

[17] J. P. Davidson. Rotations and vibrations in deformed nuclei. *Rev. Mod. Phys.*, 37:105–158, Jan 1965.

[18] X. Wang. Exotic collective excitations at high spin: Triaxial rotation and octupole condensation. *PhD thesis*, 2007.

[19] Raymond K. Sheline. Vibrational states in deformed even-even nuclei. *Rev. Mod. Phys.*, 32:1–24, Jan 1960.

[20] Lawrence Wilets and Maurice Jean. Surface oscillations in even-even nuclei. *Physical Review*, 102(3):788, 1956.

[21] AS Davydov and GF Filippov. Rotational states in even atomic nuclei. *Nuclear Physics*, 8:237–249, 1958.

[22] EL Church and J Weneser. Nuclear structure effects in internal conversion. *Annual review of nuclear science*, 10(1):193–234, 1960.

217

[23] BrIcc v2.3S Conversion Coefficient Calculator. http://bricc.anu.edu.au/.

[24] T Kibédi, TW Burrows, MB Trzhaskovskaya, Philip M Davidson, and Charles William Nestor. Evaluation of theoretical conversion coefficients using BrIcc. *NIM A*, 589(2):202–229, 2008.

[25] E. Ngijoi-Yogo *et al.* Collective rotation and vibration in neutron-rich ^{180,182}Hf nuclei. *Phys. Rev. C*, 75:034305, Mar 2007.

[26] U. S. Tandel. Investigating Shape Evolution and Delayed Nucleon Alignment in the Heaviest Stable Isotope of Hafnium. *M.S. Thesis*, 2007, University of Massachusetts, Lowell, MA, USA.

[27] Tord Bengtsson. *Nuclear Physics A*, 512(1):124 – 148, 1990.

[28] E. Monnand, J. Blachot, and A. Moussa. Désintégration radioactive du ^{186}Ta. *Nuclear Physics A*, 134(2):321 – 335, 1969.

[29] B. P. Pathak, K. S. N. Murty, S. K. Mukherjee, and S. C. Gujrathi. Decay of ^{186}Ta to levels in ^{186}W. *Phys. Rev. C*, 1:1477–1490, Apr 1970.

[30] S. C. Gujrathi and S. K. Mark. Levels of ^{186}W from the decay of ^{186}Ta. *Canadian Journal of Physics*, 51(3):241–256, 1973.

[31] H Karwowski, S Majewski, B Pietrzyk, L Wencel, and J Jastrzebski. Nanosecond isomers in ^{186}W. *Journal de Physique*, 36(6):471–474, 1975.

[32] J. de Boer, G. Goldring, and H. Winkler. Multiple coulomb excitation of rotational levels in even-even nuclei. *Phys. Rev.*, 134:B1032–B1046, Jun 1964.

[33] F.K. McGowan *et al.* Coulomb excitation of ^{182,184,186}W and ^{166}Er with ^{4}He and ^{16}O ions. *Nuclear Physics A*, 289(1):253 – 268, 1977.

[34] W.T. Milner *et al.* Coulomb excitation of ^{182,184,186}W, ^{186,188,190,192}Os and ^{192,194,196,198}Pt with protons, ^{4}He and ^{16}O ions. *Nuclear Physics A*, 177(1):1 – 32, 1971.

[35] R. Kulessa *et al.* Angular momentum dependence of the quadrupole deformation in ^{182,184,186}W. *Physics Letters B*, 218(4):421 – 426, 1989.

[36] C Wheldon *et al.* Opening up the A≈180 K-isomer landscape: inelastic excitation of new multi-quasiparticle yrast traps. *Physics Letters B*, 425(3-4):239 – 245, 1998.

[37] ATLAS Beam-Line Layout. https://www.phy.anl.gov/airis/layout.html.

[38] I-Yang Lee. Gammasphere. In *Exotic Nuclear Spectroscopy*, pages 245–258. Springer US, 1990.

[39] F.S. Goulding *et al.* GAMMASPHERE: Overview of detector and signal processing system. In *Nuclear Science Symposium and Medical Imaging Conference Record, 1995., 1995 IEEE*, volume 1, pages 432–436, Oct 1995.

[40] PJ Nolan, FA Beck, and DB Fossan. Large arrays of escape-suppressed gamma-ray detectors. *Annual review of nuclear and particle science*, 44(1):561–607, 1994.

[41] AM Baxter *et al.* Compton-suppression tests on Ge and BGO prototype detectors for GAMMASPHERE. *NIM A*, 317(1):101–110, 1992.

[42] M Devlin, LG Sobotka, DG Sarantites, and DR LaFosse. Simulated response characteristics of Gammasphere. *NIM A*, 383(2):506–512, 1996.

[43] FS Goulding *et al.* GAMMASPHERE-timing and signal processing aspects of the BGO Compton shield. *Nuclear Science, IEEE Transactions on*, 41(4):1135–1139, 1994.

[44] IY Lee, MA Deleplanque, and K Vetter. Developments in large gamma-ray detector arrays. *Reports on Progress in Physics*, 66(7):1095, 2003.

[45] I-Yang Lee and John Simpson. AGATA and GRETA: the future of gamma-ray spectroscopy. *Nuclear Physics News*, 20(4):23–28, 2010.

[46] Gammasphere. http://nucalf.physics.fsu.edu/ riley/gamma/gamma3.html.

[47] J.T. Anderson *et al.* A digital data acquisition system for the detectors at gammasphere. In *Nuclear Science Symposium and Medical Imaging Conference (NSS/MIC), 2012 IEEE*, pages 1536–1540, Oct 2012.

[48] Digital Gammasphere. https://www.phy.anl.gov/atlas/workshop14/eq/DGS.pdf.

[49] Cary N. Davids and James D. Larson. The argonne fragment mass analyzer. *NIM B*, 40-41, Part 2:1224 – 1228, 1989.

[50] D.G. Sarantites *et al.* The microball: Design, instrumentation and response characteristics of a 4π-multidetector exit channel-selection device for spectroscopic and reaction mechanism studies with Gammasphere. *NIM A*, 381(2-3):418 – 432, 1996.

[51] M.W Simon, D Cline, C.Y Wu, R.W Gray, R Teng, and C Long. CHICO, a heavy ion detector for Gammasphere. *NIM A*, 452(1-2):205 – 222, 2000.

[52] Chico. http://www.pas.rochester.edu/~cline/chico/chico.html.

[53] DGSSort. http://www.phy.anl.gov/gammasphere/doc/DGSSort/.

[54] ROOT Data reduction package. http://root.cern.ch/drupal/.

[55] Agda and Artna-Cohen. Nuclear data sheets for A = 152. *Nuclear Data Sheets*, 79(1):1 – 276, (1996).

[56] YA Akovali. Nuclear data sheets for A = 243. *Nuclear Data Sheets*, 103(3):515–564, 2004.

[57] RadWare. http://radware.phy.ornl.gov/.

[58] D.C Radford. ESCL8R and LEVIT8R: Software for interactive graphical analysis of HPGe coincidence data sets. *NIM A*, 361(1-2):297 – 305, 1995.

[59] T. Czosnyka, D. Cline, C.Y. Wu, A.B. Hayes, P Napiorkowski, and N. Warr. COULOMB EXCITATION DATA ANALYSIS CODES; GOSIA. 2008.

[60] Kurt Alder, Aage Bohr, Torben Huus, Ben Mottelson, and Aage Winther. Study of nuclear structure by electromagnetic excitation with accelerated ions. *Reviews of modern physics*, 28(4):432, 1956.

[61] A Winther and J De Boer. A computer program for multiple Coulomb excitation, reprinted in K. Alder and A. Winther, Coulomb excitation, 1966.

[62] Kurt Alder and Aage Winther. *Coulomb excitation: a collection of reprints*. Academic press, 1966.

[63] A. Krämer-Flecken *et al.* Use of DCO ratios for spin determination in γ-γ coincidence measurements. *NIM A*, 275(2):333 – 339, 1989.

[64] T. Shizuma *et al.* High-spin states in ^{182}W. *Nuclear Physics A*, 593(2):247 – 280, 1995.

[65] D.L. Bushnell *et al.* States in ^{184}W via neutron capture and beta-decay excitations. *Phys. Rev. C*, 11:1401–1421, Apr 1975.

[66] T.R. Saitoh *et al.* Collective and intrinsic structures in ^{183}W. *Nuclear Physics A*, 660(2):171 – 196, 1999.

[67] V. Bondarenko *et al.* Low-spin mixed particle hole structures in ^{185}W. *Nuclear Physics A*, 762(3-4):167 – 215, 2005.

[68] V. Bondarenko *et al.* Nuclear levels in ^{187}W. *Nuclear Physics A*, 619(1-2):1 – 48, 1997.

[69] V. Bondarenko *et al.* Nuclear structure of ^{187}W studied with (n, γ) and (d, p) reactions. *Nuclear Physics A*, 811(1-2):28 – 76, 2008.

[70] T. Shizuma *et al.* One-quasiparticle bands in neutron-rich ^{187}W. *Phys. Rev. C*, 77:047303, Apr 2008.

[71] C M. Baglin. Nuclear data sheets for A = 186. *Nuclear Data Sheets*, 99(1):1 – 196, 2003.

[72] B. Crowell *et al.* High-K isomers in ^{176}W and mechanisms of K violation. *Physical Review C*, 53(3):1173, 1996.

[73] DM Cullen *et al.* High-K decays and lifetime measurements in ^{172}Hf. *Nuclear Physics A*, 638(3):662–700, 1998.

[74] S. K Tandel *et al.* Search for strongly deformed structures and observation of multiple nucleon alignments in ^{174}W. *Phys. Rev. C*, 77:024313, Feb 2008.

[75] PH Regan *et al.* Structure of the doubly midshell nucleus $^{170}_{66}$Dy$_{104}$. *Physical Review C*, 65(3):037302, 2002.

[76] Krishna Kumar and Michel Baranger. Nuclear deformations in the pairing-plus-quadrupole model: (III). static nuclear shapes in the rare-earth region. *Nuclear Physics A*, 110(3):529 – 554, 1968.

[77] P. Sarriguren *et al.* Shape transitions in neutron-rich Yb, Hf, W, Os, and Pt isotopes within a Skyrme Hartree-Fock and BCS approach. *Phys. Rev. C*, 77:064322, Jun 2008.

[78] PD Stevenson *et al.* Shape evolution in the neutron-rich tungsten region. *Physical Review C*, 72(4):047303, 2005.

[79] NV Zamfir and RF Casten. Signatures of γ softness or triaxiality in low energy nuclear spectra. *Physics Letters B*, 260(3):265–270, 1991.

[80] Coral M. Baglin. Nuclear data sheets for A = 184. *Nuclear Data Sheets*, 111(2):275 – 523, 2010.

[81] Coral M. Baglin. Nuclear data sheets for A = 186. *Nuclear Data Sheets*, 99(1):1 – 196, 2003.

[82] S Akkoyun *et al.* AGATA - Advanced GAmma Tracking Array. *NIM A*, 668:26–58, 2012.

[83] I.Y. Lee *et al.* GRETINA: A gamma ray energy tracking array. *Nuclear Physics A*, 746(0):255 – 259, (2004).

[84] Anton Khaplanov. Position-sensitive germanium detectors for γ-ray tracking, imaging and polarimetry. *PhD thesis*, 2010.

[85] N Tsoulfanidis and S Landsberger. *Measurement and Detection of Radiation*. CRC Press; 3rd ed., (2010).

[86] G. F. Knoll. *Radiation detection and measurement*. John Wiley and sons, Third edition, 1999.

[87] Zhong He. Review of the shockley ramo theorem and its application in semiconductor gamma-ray detectors. *NIM A*, 463(1-2):250 – 267, 2001.

[88] M. Martini *et al.* Drift velocity and trapping in semiconductors: transient charge technique. *Applied Solid State Science*, 3:181–258, 1972.

[89] G. Ottaviani *et al.* Hole drift velocity in high-purity Ge between 8 and 220° K. *Journal of Applied Physics*, 44(6):2917–2918, 1973.

[90] L. Mihailescu *et al.* The influence of anisotropic electron drift velocity on the signal shapes of closed-end HPGe detectors. *NIM A*, 447(3):350 – 360, 2000.

[91] S. Bosi, C. Jacoboni, and L. Reggiani. Acoustic scattering in a two-band system and its application to hole transport properties in cubic semiconductors. *Journal of Physics C: Solid State Physics*, 12(8):1525–1531, 1979.

[92] J. D. Eskin *et al.* Signals induced in semiconductor gamma-ray imaging detectors. *Journal of Applied Physics*, 85(2):647–659, 1999.

[93] E. Gatti *et al.* A pulse-shape analysis approach to 3-D position determination in large-volume segmented HPGe detectors. In *Nuclear Science Symposium, 1999. Conference Record. 1999 IEEE*, volume 1, pages 346–351 vol.1, 1999.

[94] A. Pullia *et al.* Cross-Talk Limits of Highly Segmented Semiconductor Detectors. *Nuclear Science, IEEE Transactions on*, 58(3):1201–1205, June 2011.

[95] Bart Bruyneel *et al.* Crosstalk properties of 36-fold segmented symmetric hexagonal HPGe detectors. *NIM A*, 599(2-3):196 – 208, 2009.

[96] K. Vetter *et al.* Performance of the GRETA prototype detectors. *NIM A*, 452(1-2):105 – 114, 2000.

[97] M. Descovich *et al.* The position response of a large-volume segmented germanium detector. *NIM A*, 553(3):512 – 521, 2005.

[98] Ren Cooper. Position sensitivity in gamma-ray detectors. *Exotic Beam Summer School*, 2010.

[99] J. Anderson *et al.* Data acquisition and trigger system of the gamma ray energy tracking in-beam nuclear array (GRETINA). *IEEE Transactions on Nuclear Science*, 56(1):258–265, Feb 2009.

[100] M. Cromaz *et al.* A digital signal processing module for gamma-ray tracking detectors. *NIM A*, 597(2):233–237, 2008.

[101] S. Zimmermann *et al.* Implementation and performance of the electronics and computing system of the Gamma Ray Energy Tracking In-Beam Nuclear Array (GRETINA). In *Nuclear Science Symposium and Medical Imaging Conference (NSS/MIC), 2011 IEEE*, pages 596–601, Oct 2011.

[102] C. E. Svensson *et al.* Position sensitivity of the TIGRESS 32-fold segmented HPGe clover detector. *NIM A*, 540(2-3):348 – 360, 2005.

[103] A. J. Boston *et al.* Gamma-ray tracking: Characterisation of the AGATA symmetric prototype detectors. *NIM B*, 261(1):1098–1102, 2007.

[104] K. Vetter *et al.* Three-dimensional position sensitivity in two-dimensionally segmented HPGe detectors. *NIM A*, 452(1-2):223 – 238, 2000.

[105] http://radware.phy.ornl.gov/gretina/fieldgen. 2006.

[106] David Radford. Private communication.

[107] I-Yang Lee. GRETINA Technical Note: Electron and Hole Drift Velocity in Ge. *Document GRT-6-061112*, 2006.

[108] http://radware.phy.ornl.gov/gretina/siggen. 2006.

[109] I. Doxas *et al.* An approximate method for linear signal decomposition in γ-ray tracking detectors. *NIM A*, 580(3):1331 – 1337, 2007.

[110] S. Paschalis *et al.* The performance of the gamma-ray energy tracking in-beam nuclear array GRETINA. *NIM A*, 709(0):44 – 55, 2013.

[111] FCL Crespi *et al.* Application of the Recursive Subtraction Pulse Shape Analysis algorithm to in-beam HPGe signals. *NIM A*, 604(3):604–611, 2009.

[112] FCL Crespi *et al.* RS algorithm for 3D localization of γ interactions in segmented HPGe detectors: Tests with calculated and experimental signal

basis. In *Nuclear Science Symposium Conference Record (NSS/MIC), 2010 IEEE*, pages 908–910. IEEE, 2010.

[113] W. Gast *et al.* Digital signal processing and algorithms for gamma ray tracking. *IEEE Transactions on Nuclear Science*, 48(6):2380–2384, Dec. 2001.

[114] GRETINA project. http://www.phy.anl.gov/gretina.

[115] A. Lopez-Martens, K. Hauschild, A. Korichi, J. Roccaz, and J-P. Thibaud. γ-ray tracking algorithms: a comparison. *NIM A*, 533(3):454 – 466, 2004.

[116] M. Descovich *et al.* In-beam measurement of the position resolution of a highly segmented coaxial germanium detector. *NIM A*, 553(3):535 – 542, 2005.

[117] M. Descovich *et al.* GRETINA status and recent progress: The effect of neutron damage on energy and position resolution of the GRETINA detector. *NIM B*, 241(1-4):931 – 934, 2005.

[118] L. A. Riley. UCGretina GEANT4. *unpublished*.

[119] Mark S Amman and Paul N Luke. Position-sensitive germanium detectors for gamma-ray imaging and spectroscopy. In *International Symposium on Optical Science and Technology*, pages 144–156. International Society for Optics and Photonics, 2000.

[120] S. Aydin et al. Effective size of segmentation lines of an AGATA crystal, 2007.

[121] Bart Bruyneel *et al.* Crosstalk corrections for improved energy resolution with highly segmented HPGe-detectors. *NIM A*, 608(1):99 – 106, 2009.